UNIVERSITY OF LIVERPOOL

Conjugated Covalent Organic Frameworks with Novel Linkages for Energy and Environmental Applications

Yongjie Xu

July 2022

Supervisor: Prof. Andrew I. Cooper

Thesis submitted in accordance with the requirements of the

University of Liverpool for the Degree of Doctor of Philosophy

Abstract

Conjugated Covalent Organic Frameworks with Novel Linkages for Energy and Environmental Applications

By

Yongjie Xu

Department of Chemistry, University of Liverpool

Supervisor: Prof. Andrew I. Cooper FRS

The energy crisis and environmental destruction are the two major issues in our society that need to be solved urgently. Covalent organic frameworks (COFs) have been used for various energy and environmental applications such as electrodes or electrolytes for energy storage devices and sieves for the removal of heavy metal-ions from water. This is due to their good crystallinity and high surface area with tunable functionalities and pore sizes. However, traditional COF studies mainly focus on boronate- or imine-linked COFs that suffer from their unstable, non-conjugated linkages and bulk structures with poor processability, limiting their practical usage in energy and environment fields. COF linkage engineering is one of the most efficient and general strategies to prepare functional COF materials with high stability. This thesis will focus on the design and synthesis of new types of COF linkages that enhance conjugation, stability and processability for energy and environmental applications.

Fluorindine-linked COFs (FL-COFs) were prepared using a temperature gradient condensation. FL-COF showed a good crystallinity with ABC stacking mode from high-resolution electron microscopy and powder X-ray diffraction. We then

investigated the electrochemical performance as the electrode in supercapacitor and found that FL-COF achieved an excellent capacitance with both high energy and power densities, which are at the top-level among all the reported COF-based electrodes in supercapacitor. We ascribe this to the reversible four-electron redox processes and then the fast inter- and intra-layer charge transfer of the introduced fluorindine-linkages.

Multicomponent reactions can combine initial reversible covalent bond-forming steps with subsequent irreversible steps with high yield, high structural diversification and functionalization. Thus, we transferred this method to prepare stable and crystalline Quinoline-linked COFs (Qu-COFs) via a multicomponent Doebner reaction. Qu-COFs with different structures can be made by both one-pot synthesis and post-synthetic modification. The Qu-COFs showed good crystallinity and chemical stability and can be easily exfoliated to nanosheets under a mild base condition. We ascribe this to the unique quinoline-4-carboxylic acid linkages that reduce the π-π stacking interaction and provide active-sites for ion insertion that leads to the repulsion of the COF layers. Due to the more exposed active sites through exfoliation, these nanosheets exhibited excellent performance on cadmium capture from water, including high capacity, fast adsorption rate and good selectivity.

We also synthesised robust oligo-ethylene glycol-anchored Imidazole-linked COFs (IMD-COF-OEG-x) with three different lengths of oligo-ethylene glycol (OEG) chains using a multicomponent Debus-Radziszewski reaction. A change of stacking model from AA to ABC can be observed after the post-modification reaction due to the disturbance from the free OEG chains. IMD-COF-OEG-X was studied as a solid-state electrolyte for lithium-ion batteries. IMD-COF-OEG-3 showed a high lithium-ion conductivity (3.36×10^{-4} S cm^{-1} at 20 °C) with a high Li^{+} transference number (0.84), low activation energy (0.45 eV), high potential window (up to 5.1 V) and high stability during a Li plating-stripping cycling over 560 h. The 1D nanochannel of these COFs prevents the crystallisation of OEG chains and provides the pathway for lithium-ion transport while OEG chains induce the transport of lithium-ions and improve the carrier density in the nanochannels. Also, the micropore structure from ABC stacking model

with tert-butyl groups inside reduces the migration of cations to improve the lithium-ion transference number.

Acknowledgements

Firstly, I would like to thank my supervisor, Prof. Andrew I. Cooper, for giving me the opportunity to undertake research in his group. His immense knowledge and flexibility have allowed me much academic freedom to develop many new ideas. I would like to express my sincere gratitude to Dr. John Ward, for giving me a huge support with daily experiments, refining ideas, report writing, and general advice. He always is the first person I would like to ask for help and his suggestions always help me quite a lot. Thank you for all your supervision and it will guide me a lot for my future.

Many thanks go to all those I have collaborated with on this work, especially numerous people in Cooper group: Kewei Wang and Weiwei Zhang for ideas sharing and synthetic organic chemistry discussions, Haofan Yang for many kinds of characterization, Peiying Wang for experimental works, Rob Clowes for training in the use of numerous instruments, Lunjie Liu and Hui Gao for teaching me early electrochemistry, Zhongfu Pang, Zhiwei Fu and Xiaoyan Wang for COFs structure discussions, Linjiang Chen and Xue Wang for the simulation, Sriram Vijayakrishnan and Yang Bai for their help in experimental works in lab, Christopher Kane for his chemical compounds supporting. Special thanks to Yang Liu and Kai Wu from Sichuan University for their advises and also the helps of sample testing.

Also, I would like to thank other past and present members of the Cooper group for many helps in both work and life: Bonnie, Marc, Xiaofeng, Ming, Hongmei, Aiting, Xinxin, Jing, Liang, Boyu, Haiyan, Donglin, Wei, Qiang, Peng, Yu and Chengxi for giving a lot of help and discussion on research. I would like to thank the Leverhulme Research Centre for Functional Materials Design for providing funding for my research and living costs.

Special thanks to Peiying Wang for opening a new window and waking me the passions to the life out of the research. It could be a much more interesting experience of studying aboard if we could meet earlier. Great thanks also to my friends: Fuming Huang, Suofang Li, Ximin Shen and Xueyang Yang, my pride is to be your pride one day.

Finally, I extend my great appreciation to my friends and family for everything they've done for me during the last four years. In particular, thanks to my parents for your continuous love, understanding, and support. I couldn't be myself without you. The last bow is to my grandma, I waste you too much time for the long waiting and the day we are looking forward to is coming soon. Then your little boy would say: I'm back as a man and I'll never leave you again.

List of Publications

- **Yongjie Xu**, Yue Yong, Fanan Kong, Shijie Ren. "Direct Chemical Synthesis of Nitrogen-doped Graphynes with High Supercapacitance *via* a Cross-coupling Copolymerization Strategy". *Chem. Eng. J.* **2022**, 435, 135121.

- **Yongjie Xu**, Reiner Sebastian Sprick, Nick J. Brownbill, Frédéric Blanc, Qingyin Li, John W. Ward, Andrew I. Cooper, Shijie Ren. "Bottom-up Wet-chemical Synthesis of a Two-dimensional Porous Carbon Material with High Supercapacitance Using a Cascade Coupling/cyclization Route". *J. Mater. Chem. A*, **2021**, 9, 3303-3308.

- **Yongjie Xu**, Yang Liu, Xue Wang, Haofan Yang, Weiwei Zhang, John W. Ward, Andrew I. Cooper. "Base-mediated Exfoliation of Covalent Organic Frameworks Facilitated by Quinoline Linkages Installed by a Multicomponent Doebner Reaction". *In preparation.*

- **Yongjie Xu**, Xue Wang, Lunjie Liu, Hui Gao, Linjiang Chen, John W. Ward, and Andrew I. Cooper. "Fluorindine-Based Covalent Organic Framework Electrode Materials with High Supercapacitance and Energy Storage". *In preparation.*

- **Yongjie Xu**, Alex Neale, Haiyan Duan, Yang Liu, Haofan Yang, Peiying Wang, Xue Wang, Hui Gao, Aiting Kai, Rob Clowes, Laurence Hardwick, John W. Ward, Andrew I. Cooper "Oligoethylene Glycol-Anchored Imidazole-Linked COFs as Solid-State Li^+ Electrolytes". *In preparation.*

- Lunjie Liu, Michał A. Kochman, **Yongjie Xu**, Martijn A. Zwijnenburg, Andrew I. Cooper, Reiner Sebastian Sprick. "Acetylene-linked Conjugated Polymers for Sacrificial Photocatalytic Hydrogen Evolution from Water". *J. Mater. Chem. A*, **2021**, 9, 17242-17248.

- Weiwei Zhang, Linjiang Chen, Sheng Dai, Chengxi Zhao, Cheng Ma, Lei Wei, Minghui Zhu, Samantha Y. Chong, Haofan Yang, Lunjie Liu, Yang Bai, Miaojie Yu, **Yongjie Xu**, Xiao-Wei Zhu, Qiang Zhu, Shuhao An, Reiner Sebastian Sprick,

Marc A. Little, Xiaofeng Wu, Shan Jiang, Yongzhen Wu, Yue-Biao Zhang, He Tian, Wei-Hong Zhu, Andrew I. Cooper. "Reconstructed Covalent Organic Frameworks". *Nature*, **2022**, 604, 72-79.

- Kewei Wang, Zhifang Jia, Yang Bai, Xue Wang, Sophie E. Hodgkiss, Linjiang Chen, Samantha Y. Chong, Xiaoyan Wang, Haofan Yang, **Yongjie Xu**, Feng Feng, John W. Ward, Andrew I. Cooper. "Synthesis of Stable Thiazole-Linked Covalent Organic Frameworks via a Multicomponent Reaction". *J. Am. Chem. Soc.* **2020**, 142, 11131-11138.

- Hui Gao, Alex R. Neale, Qiang Zhu, Mounib Bahri, Xue Wang, Haofan Yang, **Yongjie Xu**, Rob Clowes, Nigel D. Browning, Marc A. Little*, Laurence J. Hardwick, and Andrew I. Cooper. "A Pyrene-4, 5, 9, 10-Tetraone-Based Covalent Organic Framework Delivers High Specific Capacity as a Li-Ion Positive Electrode". *J. Am. Chem. Soc.* **2022**, 144, 9434-9442.

Table of Content

List of Abbreviations

1D	One-dimensional
2D	Two-dimensional
3D	Three-dimensional
AFM	Atomic Force Microscopy
ASSBs	All-solid-state-batteries
BVE	Bruce-Vincent-Evans technique
C	Specific capacitance
C_2	Contact capacitance
CA	Chromoamperometry techniques
C_{cell}	Experimentally determined specific capacitance of two-electrode device
C_e	Final equilibrium concentration of metal ions
C_i	Initial concentration of metal ions
CLPs	Conjugated ladder polymers
CMPs	Conjugated microporous polymer
COFs	Covalent organic frameworks
CONs	Covalent organic nanosheets
CP-MAS	^{13}C cross-polarization magic angle spinning
C_s	Specific capacitance of each electrode of two-electrode device
CTFs	Covalent triazine frameworks
CV	Cyclic voltammetry
DBPT	2, 7-di-tert-butylpyrene-4, 5, 9, 10-tetraone
DCC	Dynamic covalent chemistry
DCM	Dichloromethane
DHQ	2, 5-dihydroxy-1, 4-benzoquinone
DLS	Dynamic light scattering
DMAc	Dimethylacetamide

DMF	N, N-dimethylformamide
DMTPA	2, 5-dimethoxy terephthalaldehyde
DSC	Differential scanning calorimetry measurement
DVB	Divinylbenzene
E	Energy density
E_a	Activation energy
EDLCs	Electric double layer capacitors
EIS	Electrochemical impedance spectroscopy
EW	Electrochemical window
FL-COF	Fluorindine-linked covalent organic framework
FT-IR	Fourier-transform infrared spectroscopy
GCD	Galvanostatic charge/discharge
HAT	2, 3, 6, 7, 10, 11-Hexaaminetriphenylene
HCPs	Hyper-crosslinked polymers
HR-MS	High resolution mass spectrometry
I	Discharge current
I_0	Initial current before polarization
ICP-OES	Inductively coupled plasma optical emission spectrometry
IMD-COF	Imidazole-linked covalent organic framework
I_s	Steady current value after polarization
ISEs	Inorganic solid electrolytes
IUPAC	International Union of Pure and Applied Chemistry
k_2	Pseudo-second-order rate constant of adsorption
K_d	Distribution coefficient
LEs	Liquid electrolytes
LiBs	Lithium-ion batteries
LSV	Linear scanning voltammetry
MCRs	Multicomponent reactions

MOFs	Metal organic frameworks
n-BuOH	1-Butanol
NH_4OAc	Ammonium acetate
NL-DFT	Nonlocal density functional theory
NMP	N-methylpyrrolidinone
NMR	Nuclear magnetic resonance
OCP	Open circuit potential
o-DCB	1, 2-Dichlorobenzene
OEG	Oligo-ethylene glycol
P	Power density
PAFs	Porous aromatic frameworks
PC	Propylene carbonate
PCPs	Porous coordination polymers
PEG	Poly-(ethylene glycol)
PEGDA	Polyethylene glycol acrylate
PIMs	Polymers of intrinsic microporosity
POCs	Porous organic cages
PXRD	Powder X-ray diffraction
Q_1	Constant phase element of double-layers
Q_e	Amount of metal ions adsorbed at equilibrium
Q_m	Saturate adsorption capacity
Qu-COFs	Quinolone-linked covalent organic frameworks
Qu-CONs	Quinoline-linked covalent organic nanosheets
R_0	Initial resistance value before polarization
R_1	Bulk resistance
R_2	Charge-transfer resistance
R_{CT}	Charge transfer resistance
R_s	Steady resistance value after polarization

SA_{BET}	Brunauer-Emmett-Teller specific surface area
SEM	Scanning electron microscopy
SPEs	Solid polymer electrolytes
SSEs	Solid-state electrolytes
ss-NMR	olid-state nuclear magnetic resonance
STM	Scanning tunnelling microscopy
t_+	Lithium-ion transference number
TAPB	1, 3, 5-tri(4-aminophenyl)benzene
TAPT	4, 4', 4''-(1, 3, 5-triazine-2, 4, 6-triyl)tribenzaldehyde
TEM	Transmission electron microscopy
TEMPO	2, 2, 6, 6-Tetramethyl-1-piperidinyloxy
TFB	1, 3, 5-triformylbenzene
T_g	Glass transition temperature
TGA	Thermogravimetric analysis
THF	Tetrahydrofuran
UV-Vis	UV-Visible absorption spectra
XPS	X-ray photoelectron spectroscopy
Δt	Total discharge time
ΔV	Potential drop during discharge
σ	Ionic conductivity

Chapter 1

Introduction

1.1 Porous Materials

Porous materials, a kind of multi-phase materials with a certain number and size of pore structures, are ubiquitous in nature (wood, bamboo and coral, etc.) and are also widely used in human society (cork stoppers, foam and sponges, etc.). Over the past several decades, porous materials have emerged as a hot topic of research interest in chemistry and materials science because of the unique structures for fundamental studies and the promising potential for various applications.

Porous materials are defined by International Union of Pure and Applied Chemistry (IUPAC): macroporous materials have the diameter of pores larger than 50 nm; mesoporous materials have the diameter of pores between 2 nm and 50 nm; microporous materials the diameter of pores less than 2 nm.[1] The term "nanoporous" has come to be used to refer to the materials with pores width less than 100 nm, which contains mesoporous and microporous materials.[2]

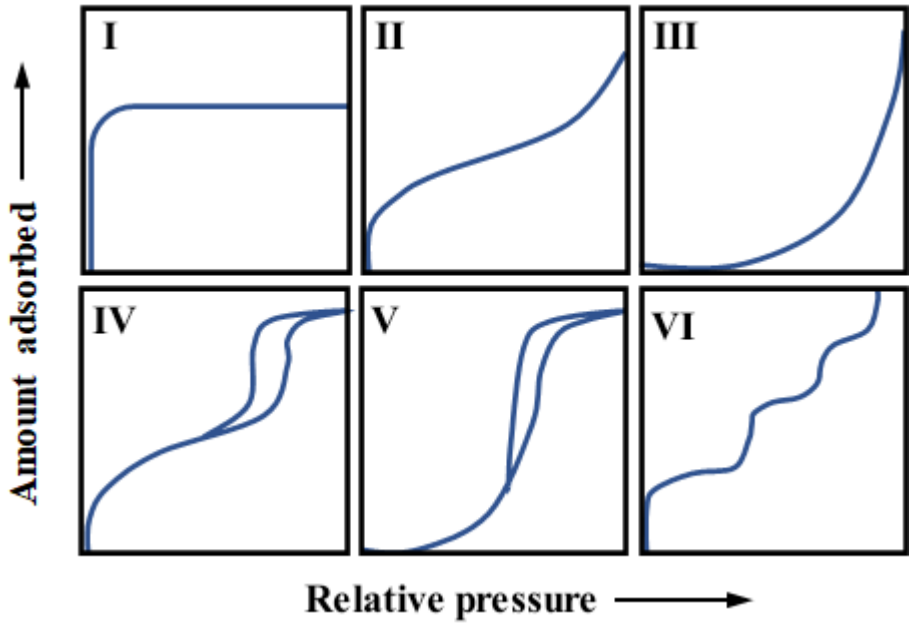

Figure 1.1 Types of reversible physisorption isotherms from different kinds of porous materials.

As significant properties of porous materials, surface area, pore volume and pore size distribution can be quantified by gas adsorption measurements. The majority of reversible physisorption isotherms can be classified into six main types (**Figure 1.1**).[1]

Type I isotherm shows a major adsorption at low relative pressure area, which is usually given by microporous materials. Macroporous or non-porous materials normally represent the Type II isotherm, which comes from unrestricted monolayer-multilayer adsorption. But if the interaction between adsorbate and adsorbent is weak enough, such a system can exhibit an unusual Type III isotherm. Type IV isotherms have different kinds of hysteresis loop, which is related to the capillary condensation of mesopores. Type V isotherm is similar to Type III isotherm, except a turning point, normally obtained from the water adsorption of mesoporous materials that have hydrophobic surfaces. Type VI isotherm exhibits the multiple steps of adsorption depending on the temperature and system, indicating a uniform non-porous surface. Different porous properties can significantly affect the performance of the porous materials in different applications.[3]

Other than the porosity, the chemical composition can also be used for the classification of porous materials, namely, porous inorganic materials, porous hybrid materials and porous organic materials.[4] They all have different arrangements in the solid state, resulting in either crystalline or amorphous materials that can be single molecular species or extended networks (**Figure 1.2**).[5]

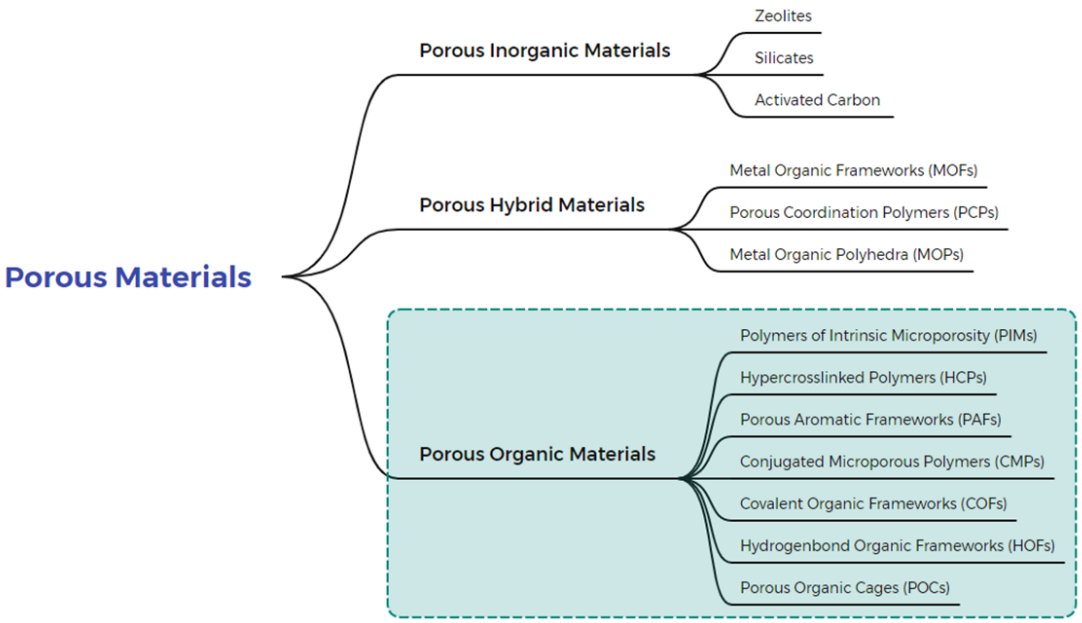

Figure 1.2 Summary of families of porous materials and their subcategories.

Porous inorganic materials, for example, zeolites, porous silicates or activated carbon are common to see in human society, especially in their use for the removal of pollutants in the water or air.[6] Among them, zeolite molecular sieves are a class of porous inorganic materials with regular pores or cage structures that are made by TO_4-kind of tetrahedra (T = Si, Al, P, etc.) as the basic building blocks connected by bridge oxygen co-deposition points. Zeolites have excellent hydrothermal stability and tuneable pore properties with large specific surface areas. However, the single synthesis conditions, the narrow pore size distribution, and the difficulty of functionalization have limited the potential usage of zeolites.[7]

Porous hybrid materials have inorganic-containing units, which can be called as porous coordination polymers (PCPs)[8] when they are amorphous or metal organic frameworks (MOFs)[9] when they are crystalline, respectively. MOFs, constructed with metal ions or clusters and organic ligands, exhibit repeating building units with a periodical arrangement. Compared to zeolites, MOFs offer significant advantages in the design and control of material structure and properties. The topologies and properties of MOFs can be controlled by selecting suitable building blocks, providing a material basis for a deeper understanding of the relationship between material structures and properties and opening a window for hot research of crystalline porous frameworks.[10] Recently, MOFs have been widely used in the fields of adsorption and separation, catalysis and optoelectronics. However, the backbone structure of MOFs materials is connected with the coordination bonds between metal and ligands, which makes them relatively sensitive to moisture, acids and bases, and thus are unstable in some cases.[11]

Compared with these inorganic-containing porous materials, there is a class of porous organic materials in which the backbone consists of only light elements (C, H, O, N, B, S), exhibiting higher chemical stability, better diversity of both preparation and performance and much more environment friendly.[5]

Due to the unique advantages like large specific surface area, tunable chemical structures, easy surface modification and good chemical stability, porous organic materials have developed rapidly as a rising material star during the last decade (**Figure 1.3**).[12] Unlike the insoluble porous polymer network, which is the most common form of porous organic materials, porous organic cages (POCs) are a kind of cage-like small molecules with a unique cavity.[13, 14] POCs have no formal intermolecular bonds and can therefore be dissolved in solvents and then dramatically improve the processability for different applications.[15]

Through the design of diverse reactive monomers and synthetic methods, porous polymer networks can be divided into the following main categories: polymers of intrinsic microporosity (PIMs),[16] conjugated microporous polymer (CMPs),[17] porous aromatic frameworks (PAFs),[18] hyper-crosslinked polymers (HCPs)[19] and covalent organic frameworks (COFs).[20]

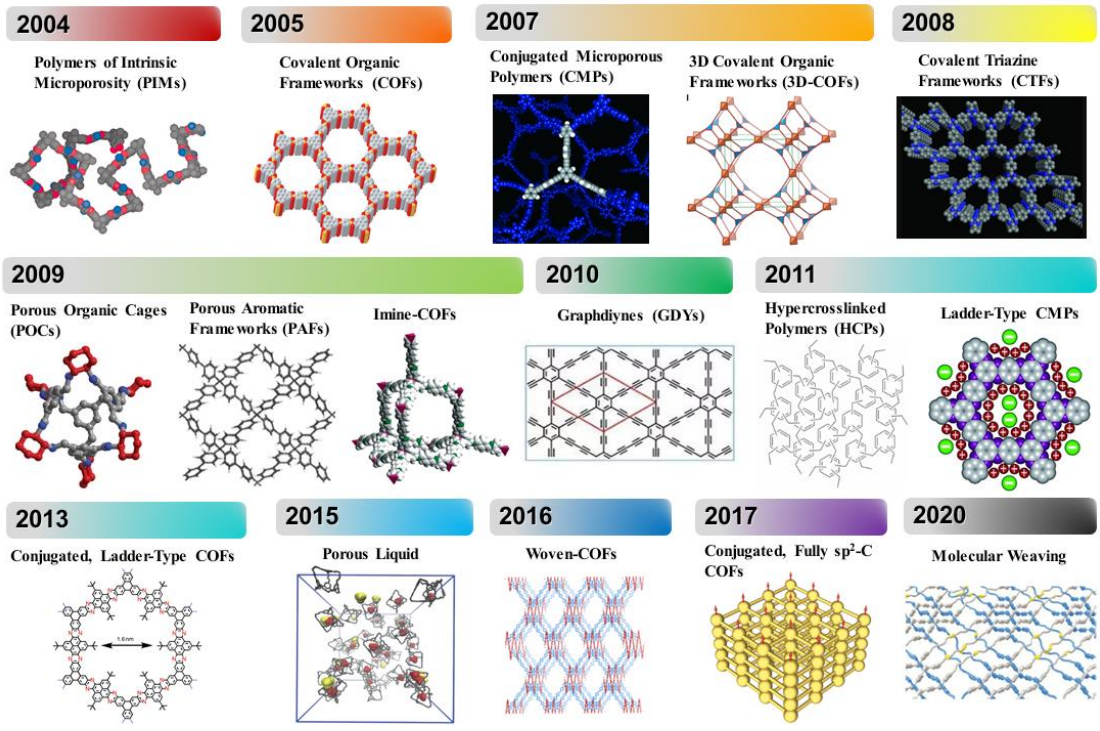

Figure 1.3 Selected advances in porous organic materials.

PIMs are a class of microporous polymers, in which the rigid structure and twisted chain structure in the backbone pack together inefficiently and provide porosity and

solubility, respectively. Thus, PIMs can be used to prepare membranes for separation.[21] HCPs are mainly made by a rapid Friedel-Crafts reaction, which have several advantages such as easy-designed, low-cost reagents and mild reaction conditions. Especially after the new strategy of external crosslinking developed since 2011, HCPs become the only successful industrialisation materials among all the kinds of porous organic polymers.[22] Due to the usage of the tetrahedral nodes like tetraphenylmethane, PAFs are used to show a topology similar to diamond and thus exhibit a rigid three-dimensional porous structure with both large surface area and pore volume, which makes them suitable for gas storage and separation.[23] Similar to PAFs, CMPs are also made by coupling reactions. However, CMPs are constructed by the direct linking of rigid aromatic building blocks, possessing an extended π-conjugation network.[24] Therefore, CMPs can combine high surface area with good optical or electronic properties, especially in the case of all-carbon construction CMPs like Graphynes or Graphdiynes.[25] In most examples so far, CMPs are amorphous materials because of the irreversible polymerizations controlled by a kinetic route. Some covalent triazine-based frameworks (CTFs) are also amorphous and have extended π-conjugation networks with microporosity that can be categorised as a kind of CMPs.[26] But some CTFs have crystalline structures as well when the selected synthetic methods are controlled by the thermodynamics, and these can be categorised as a kind of COF.[27] COFs are thermodynamic products formed by reversible chemistries, leading to the unique crystalline property among all the porous organic polymers. The large variety of molecular building blocks that can be coupled in this way allows the control of functionality and structure in COFs, and it is this structural diversity that has led to a rapid growth of interest in these materials since their discovery.[28] Recently, linkages engineering, conjugated structures with high stability, exfoliation towards thinner layers and even a molecular weaving strategy are on-going to push COFs towards a new direction.[29]

1.2 Covalent Organic Frameworks

Covalent Organic Frameworks (COFs) are a novel type of two- or three-dimensional crystalline porous polymers that allow the integration of organic building blocks into extended structures with atom precision, and form periodic skeletons with ordered nanopores. Due to the diversity of knots and linkers with different functional degrees and geometry, COFs can be designed into various topologies (**Figure 1.4**).[28]

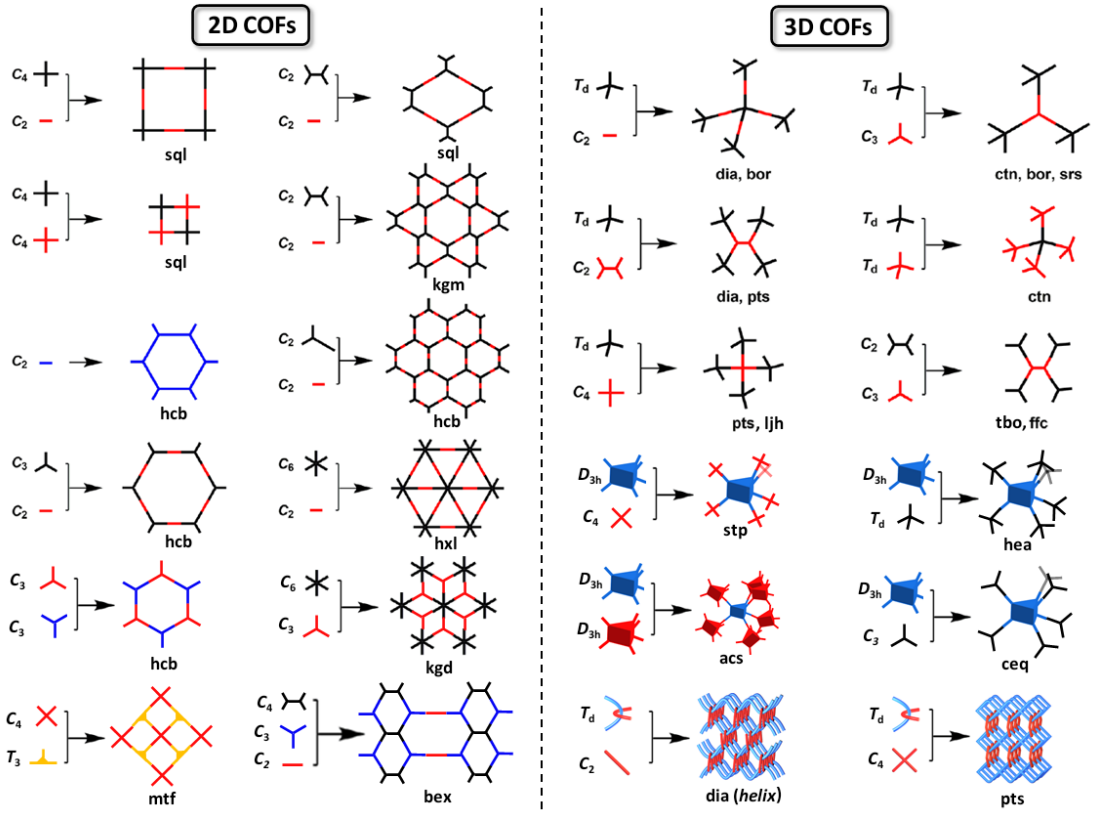

Figure 1.4 Basic topological diagrams for designing 2D COFs (left) and 3D COFs (right).

However, the essence of such periodic skeletons is to elaborate on the regularity of covalent bond formation and frameworks extending. Thus, the design principle, mainly the suitable synthetic methods and monomers, should be explored and followed to control and ensure the ordered growth of COFs during the polymerization.

1.2.1 Design Principle and Mechanistic Studies

The design principles used to synthesise COFs comes from the studies of MOFs, developed initially by Omar. Yaghi and his co-workers. COFs can be made by

following dynamic covalent chemistry (DCC) with reversible covalent bond linkages under thermodynamic control that provide the system with 'error checking' and 'self-healing' characteristics, leading to the most ordered products with the highest thermodynamical stability.[30]

Therefore, at the early stage, the strategy of improving crystallinity in solution-phase COFs synthesis is focused on reaction conditions: i) insoluble monomers to reduce reaction rate to minimize the defects in the structure; ii) increasing the temperature and time of reaction, leading to a thermodynamic dominated processes for further defect annealing.[31] Recently, several groups have worked on the mechanistic investigations, demonstrating a joint action of reversible and irreversible chemical and physical processes that are more than a simple self-healing of materials. Based on these new sights of crystalline COFs growth, some researchers have developed other methods which can introduce irreversible chemistries to produce COFs with novel structures.[32]

Recently, the general way to obtain crystalline COFs can be briefly defined into two main directions:[33] i) Dynamic covalent chemistry, which is the most common strategy for making COFs, including direct reversible reaction or amorphous-to-crystalline transition with continuous unit exchanges. ii) Extra interactions with the restriction of the degrees of freedom, including surface synthesis on template or interface, assembly with pre-organization and post-modification of the original COFs.

1.2.1.1 Dynamic Covalent Chemistry

Most covalent chemistry reactions are kinetically controlled, *i.e.*, the difference of free energy levels of the transition states during the reaction leads to the relative proportions of products. This is determined by the relative stabilities of the resulting products instead of the thermodynamically controlled reaction (**Figure 1.5**).[34] DCC is a reversible process that allows the formation and breakage of covalent bonds at a thermodynamic equilibrium with a drive force of achieving the lowest energy state of the reaction system. The thermodynamic equilibrium is relative to reaction conditions, like reaction medium (catalysts and solvents), physical factors (temperature, light,

electric, pressure, etc.), or the presence of stabilization sources (templates, metal ions, protons, etc.).[35]

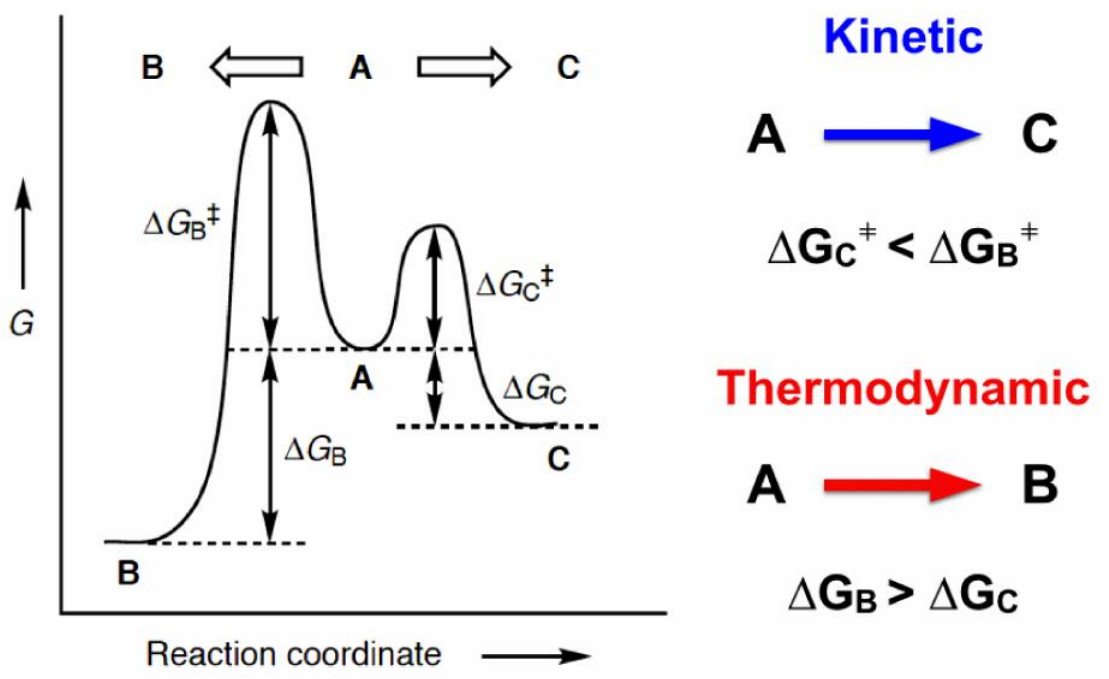

Figure 1.5 Free energy profile illustrating kinetic (A to C) versus thermodynamic (A to B) control of the product distribution. Most of covalent chemistry is irreversible and controlled by kinetic while most of supramolecular, co-ordination and dynamic covalent chemistry are reversible and controlled by thermodynamic control. (This figure is reprinted from ref. 34).

In typical COF synthesis, a crystalline COF structure is formed by a fast kinetic controlled polymerization following thermodynamic controlled defect-correction. The kinetical intermediate in the first step has two different understandings, namely, amorphous polymers or disordered COF nanosheets and the final crystalline COFs are formed through a defect-healing or layer-rearrangement, respectively (**Figure 1.6a**).[36] The former one is following a traditional DCC theory while the latter one is following a nucleation-elongation mechanism, wherein formed disordered nanosheets initially stack together with continued growth and rearrangement.[37] This is beneficial for designing some COFs with new linkages from irreversible reactions.

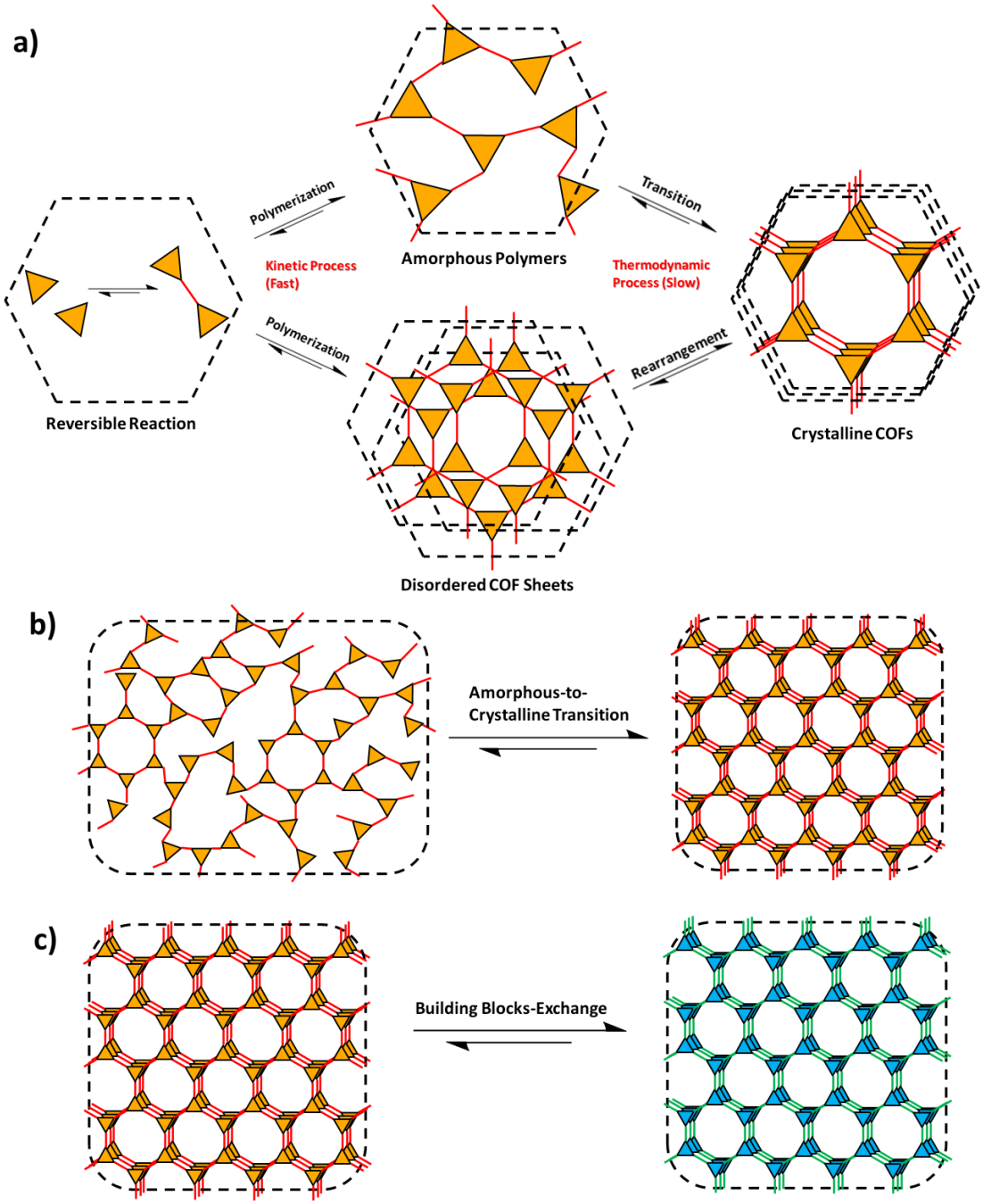

Figure 1.6 a) Crystalline COF formation from reversible reactions based on DCC mechanism: The kinetical intermediate (amorphous polymer or disordered COF sheets) is formed firstly through a fast polymerization and then a slow crystallization happens through self-healing. b) A transition from amorphous product to crystalline product can take place in suitable conditions through DCC. c) The exchange of either linkers or knots can take place in suitable conditions through DCC.

According to DCC, the defects caused by irregular arrays of reversible bonds inside the amorphous precursors can also be corrected by a second-step thermodynamic controlled recrystallization process, and then the energy-minima COFs can be obtained

through amorphous-to-crystalline transition (**Figure 1.6b**).[38] Similar to metathesis reactions, linkages or building blocks can be exchanged to form a new COF from the mother COF, extending a new method for preparing some COFs that are amorphous from direct synthesis (**Figure 1.6c**).[39] Also, based on this linker-exchange, the use of modulators for COF synthesis can reduce the reaction rate to improve the crystallinity and even achieve the growth of single-crystal COFs.

The formation of COFs also relies on the rigidity and directionality of building blocks, which limits the types of COF linkages. However, a range of reactions have been explored for COF synthesis. Except the early boronate-ester condensation and the recent Knoevenagel condensation, Schiff-base condensation for making COFs with imine bonds is appeared as the largest domination in this field because of a relative better balance between reversibility and stability (**Figure 1.7**).

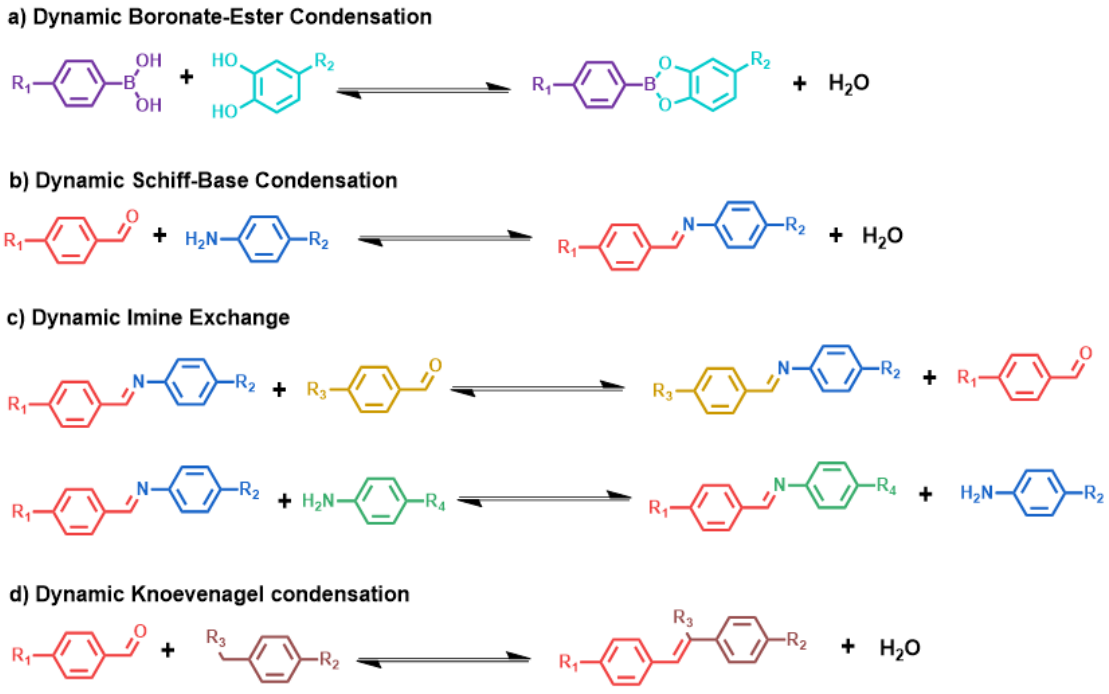

Figure 1.7 a) Dynamic condensation between the precursors of boronic acids and catechols to produce boronate-ester products; b) Dynamic condensation between the precursors of aldehydes and amines to produce imine products; c) Dynamic exchange between the imine and aldehydes or amines, respectively; d) Dynamic condensation between the precursors of aldehydes and acetonitriles to produce cyano-substituted olefin products.

Based on the DCC mechanism, for improving the crystallinity of COFs, it's important to adjust the thermodynamic equilibrium during the reaction. Thus, optimizing a suitable reaction condition with several key factors (reaction time, temperature, pressure, catalysts, concentration and the types and proportions of solvents) is necessary for COF synthesis.[40] Recently, solvothermal synthesis with co-solvents is still the most common method for the preparation of crystalline COFs. This method is general for most COFs preparation but has two disadvantages: long reaction time and usage of toxic solvents. Therefore, other methods are developed gradually, such as ionothermal synthesis,[41] microwave[42] or sonication synthesis,[43] mechanochemical synthesis,[44] and even rapid, room temperature synthesis[45] in aqueous solutions and ambient conditions (**Figure 1.8**). All of the methods above are aimed to reduce the cost of preparation (either reaction time or temperature), Simplifying the preparation process of COF materials.

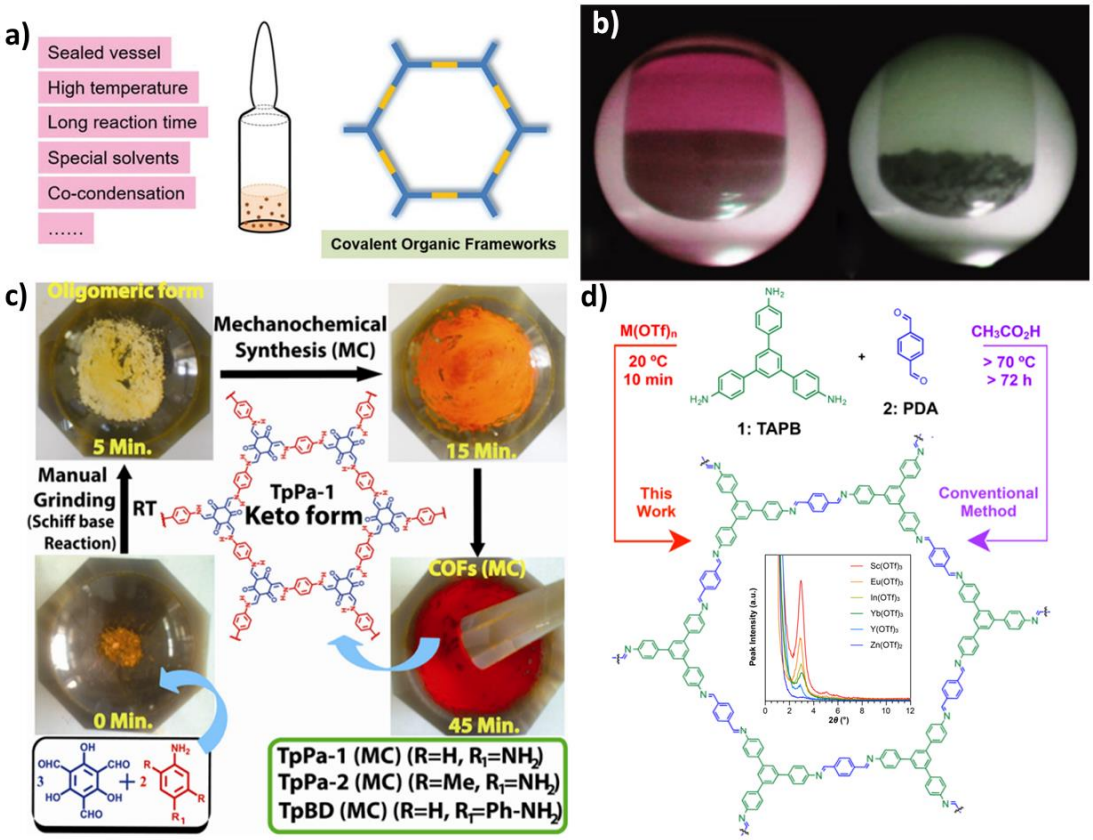

Figure 1.8 Different synthetic methods of CPF preparation: a) Solvo/iono-thermal synthesis; b) Microwave synthesis; c) Mechanochemical synthesis; d) Rapid, room temperature synthesis catalyzed by $M(OTf)_n$ under ambient conditions (This figure is reprinted from ref. 41-44).

Generally speaking, good reversibility means a related poor chemical stability in some specific conditions. The COFs made by DCC could have the problem in some real usage. Therefore, developing novel systems other than just DCC to achieve the introduction of irreversible linkages for improving the stability of COF materials is critical and on-going.

1.2.1.2 Systems with Extra interactions

Other than the self-healing of DCC, the reaction systems with some extra interactions can be well-designed to restrict the degree of freedom during the framework forming or control the arrangement of monomers and the sequence of bonds formation step by step for the growth of crystalline materials even under the irreversible conditions. This strategy has been used in other materials, such as the templating synthesis of 2D polymers[46] or mesoporous silica,[47] which normally only show ordered structure on a long-range scale. But through introducing interactions on a molecular level, the as-obtained COFs could show comparable high crystallinity with the DCC products but much higher stability. The main strategies of designing such reaction systems can be classified into three directions: the surface synthesis including any kinds of interface synthesis and templating synthesis (**Figure 1.9a**); pre-organization of monomers (**Figure 1.9b**); post-modification from an original crystalline COF material (**Figure 1.9c**).[33]

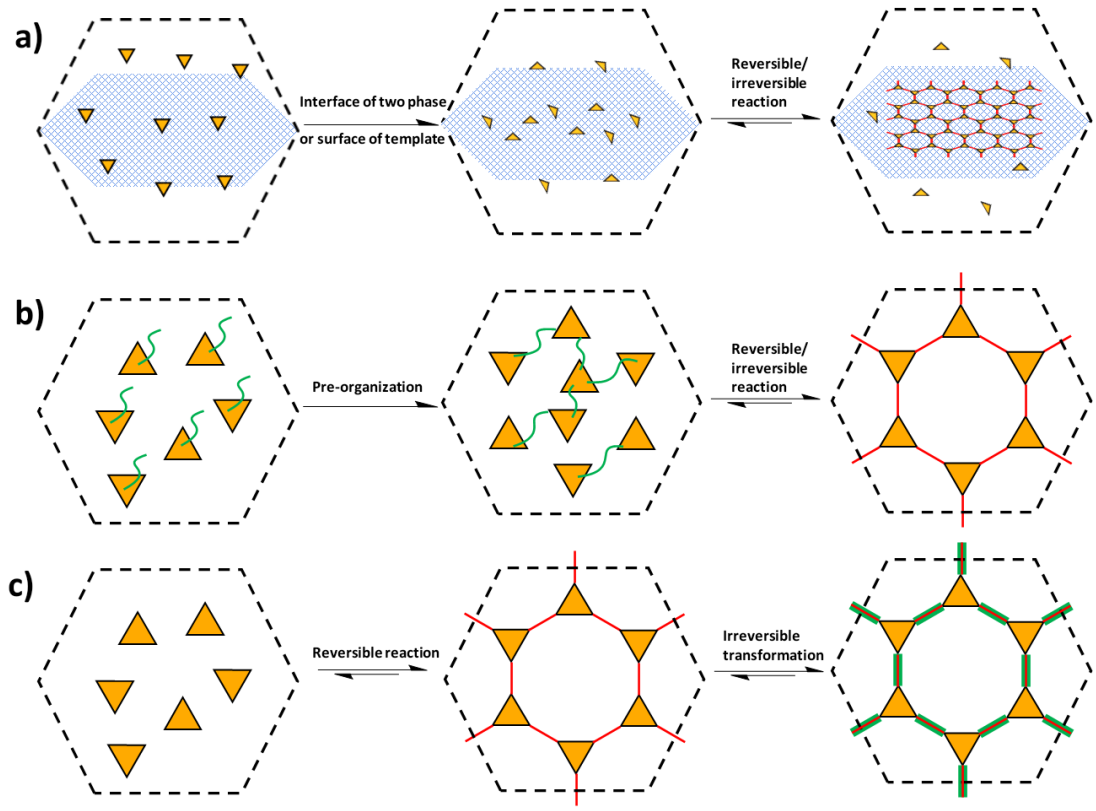

Figure 1.9 Different strategies of building reaction systems with extra interactions for obtaining crystalline COFs: a) Surface synthesis; b) Pre-organization of monomers; c) Post-modification from original crystalline COFs.

Surface synthesis. Surface synthesis can be used to control the products even during a dynamic process due to its unique characteristics: 1) inducing the diffusion and ordered stacking and alignment of precursors on surfaces; 2) restricting the direction of product growth to avoid the irregular extensions; 3) activation of precursors for reducing the energy to accelerate the coupling.[48] Mainly, the surface synthesis used in COF field is focus on the templating synthesis and interface synthesis.

Typically, solid substrates used in COF synthesis are not only catalysts for surface-metal-mediated coupling but also templates to avoid the random distribution and local aggregation of monomers, which are suitable for the growth of crystalline COFs by rigid monomers even from irreversible reactions. For example, crystalline 2D-COFs can be made from multiple-brominated monomers through an irreversible Ullmann coupling reaction on the surface of metal substrates, such as silver, gold (**Figure 1.10a**) or copper (**Figure 1.10b**).[49, 50] And the formation of COFs with regular pore structure

can be characterized clearly by scanning tunnelling microscopy (STM), proving the ordered topology structure of the as-made COFs. However, it's hard to get pure COFs from catalyst residue, limiting the products from some biological applications.

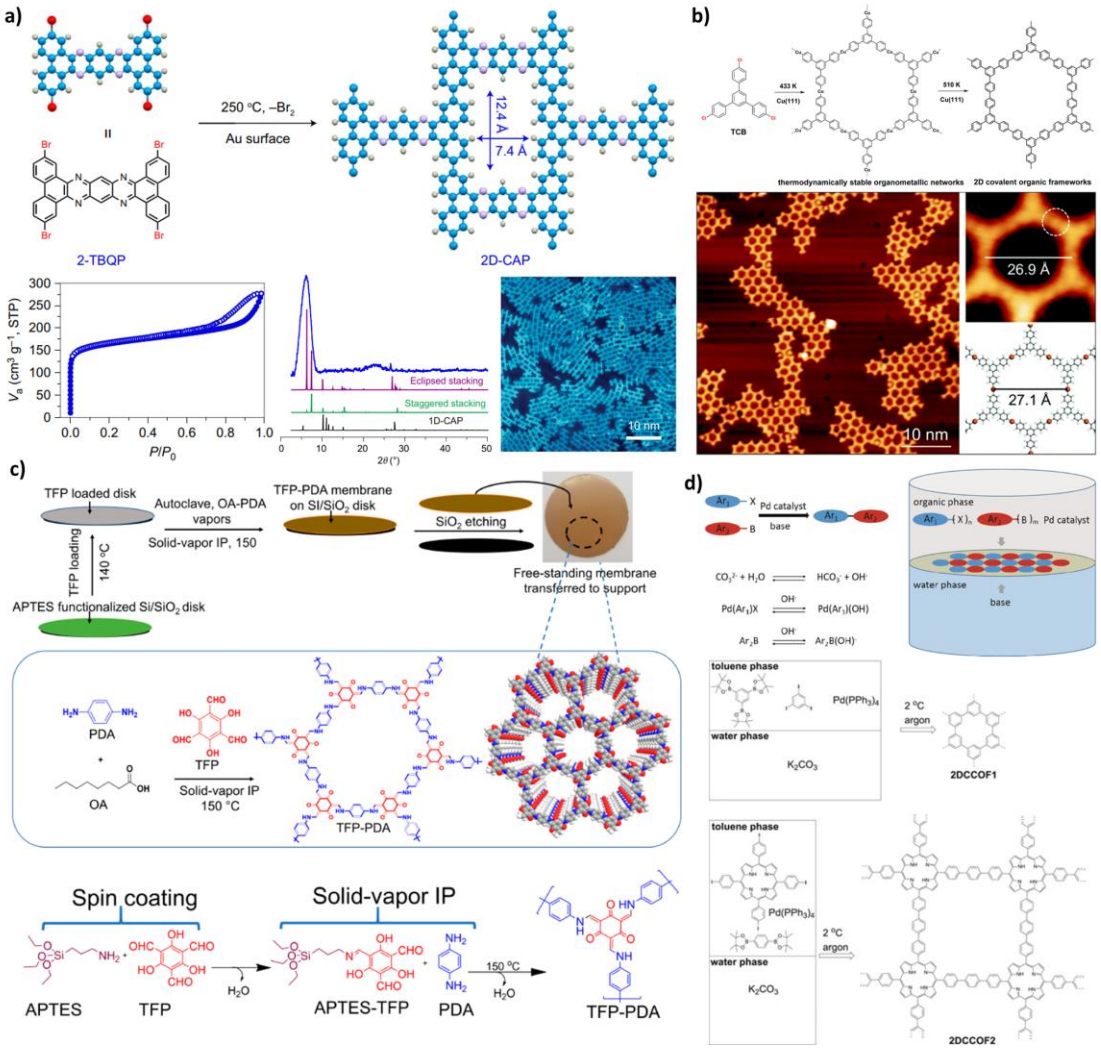

Figure 1.10 Crystalline COFs made from surface synthesis: a) 2D-CAP from Ullmann coupling on the surface of Au (111); b) 2D COFs from Ullmann coupling on the surface of Cu (111); c) TFP-PDA from Schiff-base reaction on the solid-vapor interface; d) 2D CCOF1&2 from Suzuki coupling on the liquid-liquid interface (This figure is reprinted from ref. 49-52).

By contrast, interface synthesis has been widely used to prepare films or nanosheets of COFs because it does not need crystalline or smooth substrates for supporting or harsh conditions for the reactions. This method usually requires the addition of separate monomers or catalysts within two phases that are not mutually soluble, respectively, thus ensuring that the reaction occurs and the growth of the product is restricted to the

interfacial region, leading to crystalline COF-based materials. The advantage of interface synthesis is the controllable thickness of products by simply controlling the concentration of the monomers. Without the substrates, the COFs at the interface can be transferred to any substrate after the polymerization, thus suitable for some specific applications. The common interface can be set-upped on the vapor-liquid, solid-vapor[51] (**Figure 1.10c**) or liquid-liquid[52] (**Figure 1.10d**). However, the yield of this method is not high enough, limiting the industrialization.

Pre-organization of monomers. Instead of forming the ordered structure under non-reversible conditions, a pre-organization strategy has been used to prepare crystalline materials by separating the steps into molecular arrangements and the further polymerization. Generally, the assembly and formation of pre-organized precursors can be induced by pre-designed weak bonds, such as non-covalently bonds, reversible co-ordination or covalent bonds.

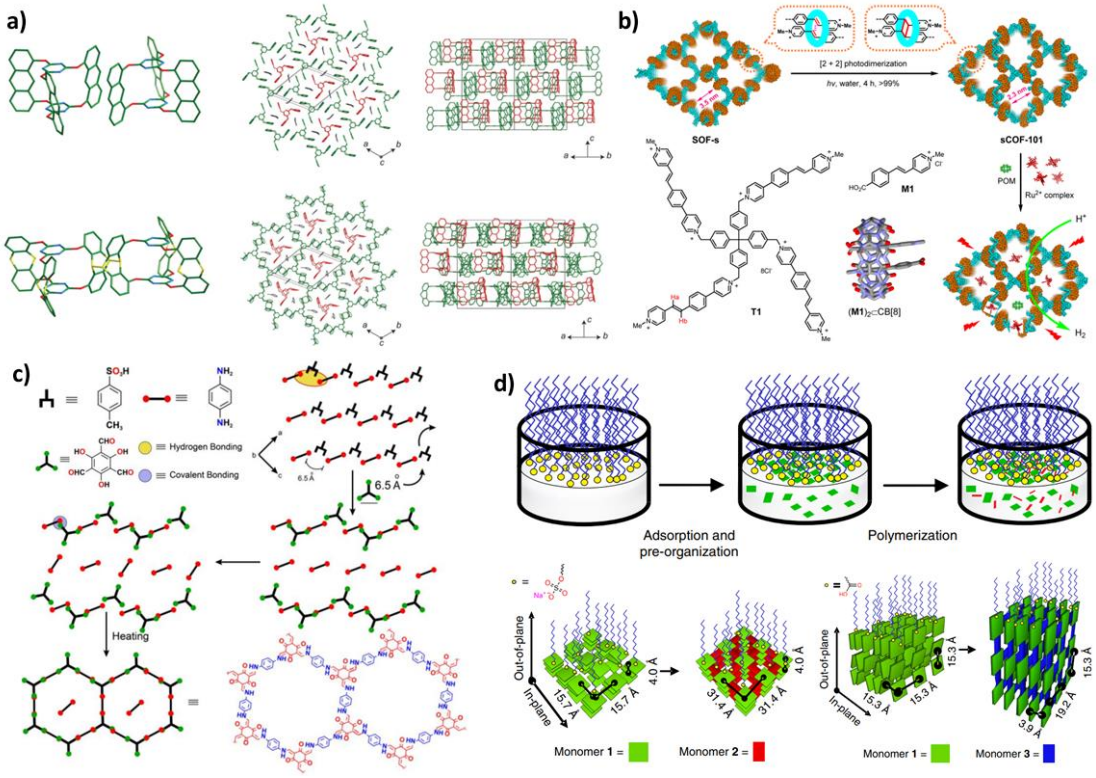

Figure 1.11 Crystalline COFs made from pre-organization strategy: a) 2D covalently connected polymer by a single-crystal-to-single-crystal transformation from photodimerization of the pre-organized propeller-shaped trianthracene; b) Pre-organized 3D supramolecular network (SOF-s) transforms into sCOF-101 by [2+2] photodimerization of the vinyl functional groups; c) Pre-

organization of monomers through the formation of a *p*-toluenesulfonic acid salt with the amine precursors; d) Pre-organization of monomers with different surfactants in the interfacial synthesis of imide-based COFs (both horizontally and vertically) (This figure is reprinted from ref. 53-56).

Single crystals that are ready for subsequent solid-state reactions can be used as an excellent template, for example, a pre-organized molecular crystal of propeller-shaped trianthracene, can be further transformed to a crosslinked 2D polymer, which is still a single crystal with same topology as before (**Figure 1.11a**).[53] Other than single crystals, a pre-organized 3D supramolecular network through host-guest chemistry can be transformed into a COF by [2+2] photodimerization of the vinyl functional groups (**Figure 1.11b**).[54] Constructing a *p*-toluenesulfonic acid salt with the amine precursors can be a general way to pre-organize the reaction system for imine-based COFs. (**Figure 1.11c**).[55] In the traditional liquid systems, the assembly of precursors can be induced by some weak interactions and also the influence of reaction conditions. By using different surfactants, the ordered stacking of monomers can be pre-organized at the air/water interface, leading to the oriented growth of 2D imide COFs with good crystallinity in either horizontal or vertical directions (**Figure 1.11d**).[56]

Post-modification of COFs. Different from the pre-organization strategy mentioned before, which is using small molecules as precursors in order to improve the crystallinity of products, post-modification of COFs is based on original crystalline COFs focusing on the enhanced chemical stability. As a contrast, the post-modification method is based on the ready frameworks that only need to consider the mild condition to avoid the loss of crystallinity instead of contrasting the crystal from small molecular precursors, which is much easier to achieve. The post-modification method can be simply classified into two categories: 1) Simple transformation of original linkage to another, such as the reduction from imine linkage to amine linkage or the oxidization from imine linkage to amide linkage[57] (**Figure 1.12a**). 2) Introducing additional connections between linkers intermolecularly or intramolecularly to achieve the formation of new linkages.

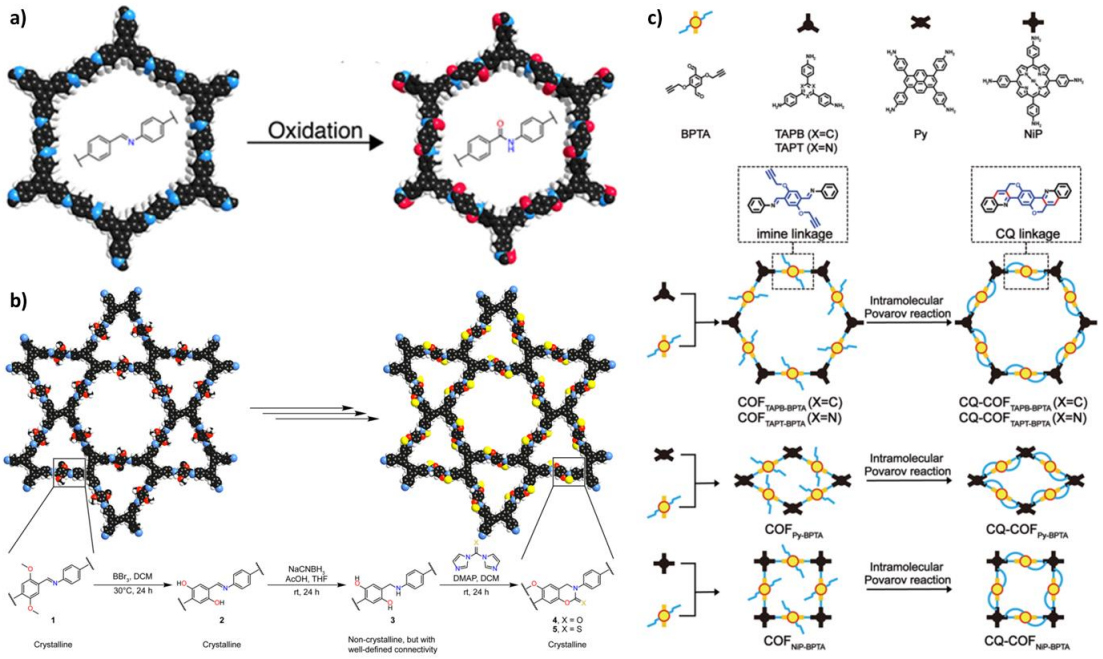

Figure 1.12 Crystalline COFs made from post-modification strategy: a) Amide-linked COFs from the oxidation from original imine-linked COFs; b) Carbamate- and thiocarbamate-linked COFs from a multiple-steps intermolecular post-modification reaction; c) Chromenoquinoline-linked COFs from an intramolecular Povarov reaction of imine-linked COFs (This figure is reprinted from ref. 57-59).

Normally, the former shows a higher generality as the building blocks do not need to be pre-designed with relative functional groups. The latter has more chance to introduce more specific linkages with unique properties, like higher conjugation. Post-synthetic locking can even be performed within multistep reactions and the crystallinity can be recovered even it is lost during one of the steps in the process (**Figure 1.12b**).[58] For intramolecuar post-modification, the functional groups need to be pre-connected with the suitable position of monomers, and an irreversible post-modification reaction occurs after the formation of frameworks and lock each linker to form a new COF with good stability (**Figure 1.12c**).[59] Post-modification strategy is one of the simplest and efficient method to get COFs with both high crystallinity and stability.

1.2.2 Linkages of Covalent Organic Frameworks

COFs can be designed with different topological diagrams in both 2D and 3D, which is controlled by constructing building blocks with different geometries (**Figure 1.13**). Generally speaking, in order to build a COF with extended network and rigid backbone,

the monomers should contain the following characteristics: 1) aromatic units to avoid the collapse of the skeleton; 2) at least two functional degrees for the crosslink of each linker; 3) functional groups for the unique properties.[40]

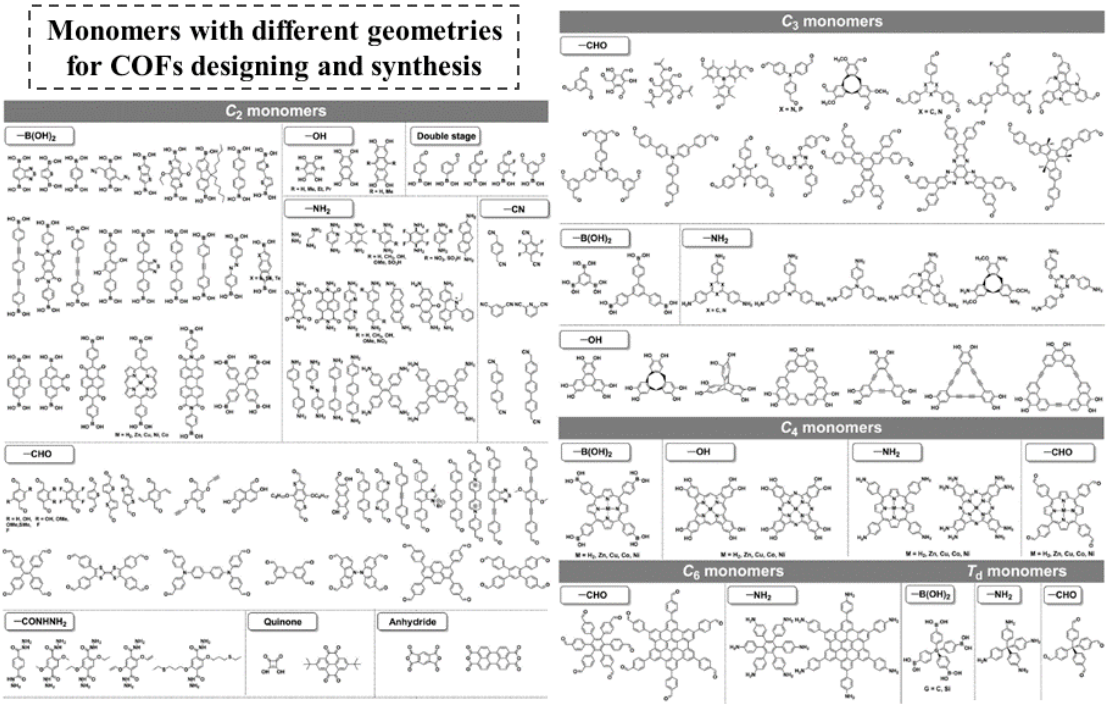

Figure 1.13 Some of the typical reported monomers with different geometries and reactive sites for the COFs designing (This figure is reprinted from ref. 40).

Other than topology and building blocks, the linkage is also the reason for the large diversity of COFs. Except for the first boronate-ester chemistry, many other reversible reactions and even some of the irreversible reactions are developed for preparing COFs gradually. Considering the conjugation, the linkages can be categorised into three classes: 1) Non-conjugated linkages; 2) Semi-conjugated linkages and 3) Fully-conjugated linkages (**Figure 1.14**). The different conjugated degrees of these linkages affect the semiconductor properties of COFs like their π-electronic distribution, electron delocalization, band gap, conductivity and thus optical or electrical applications.[40]

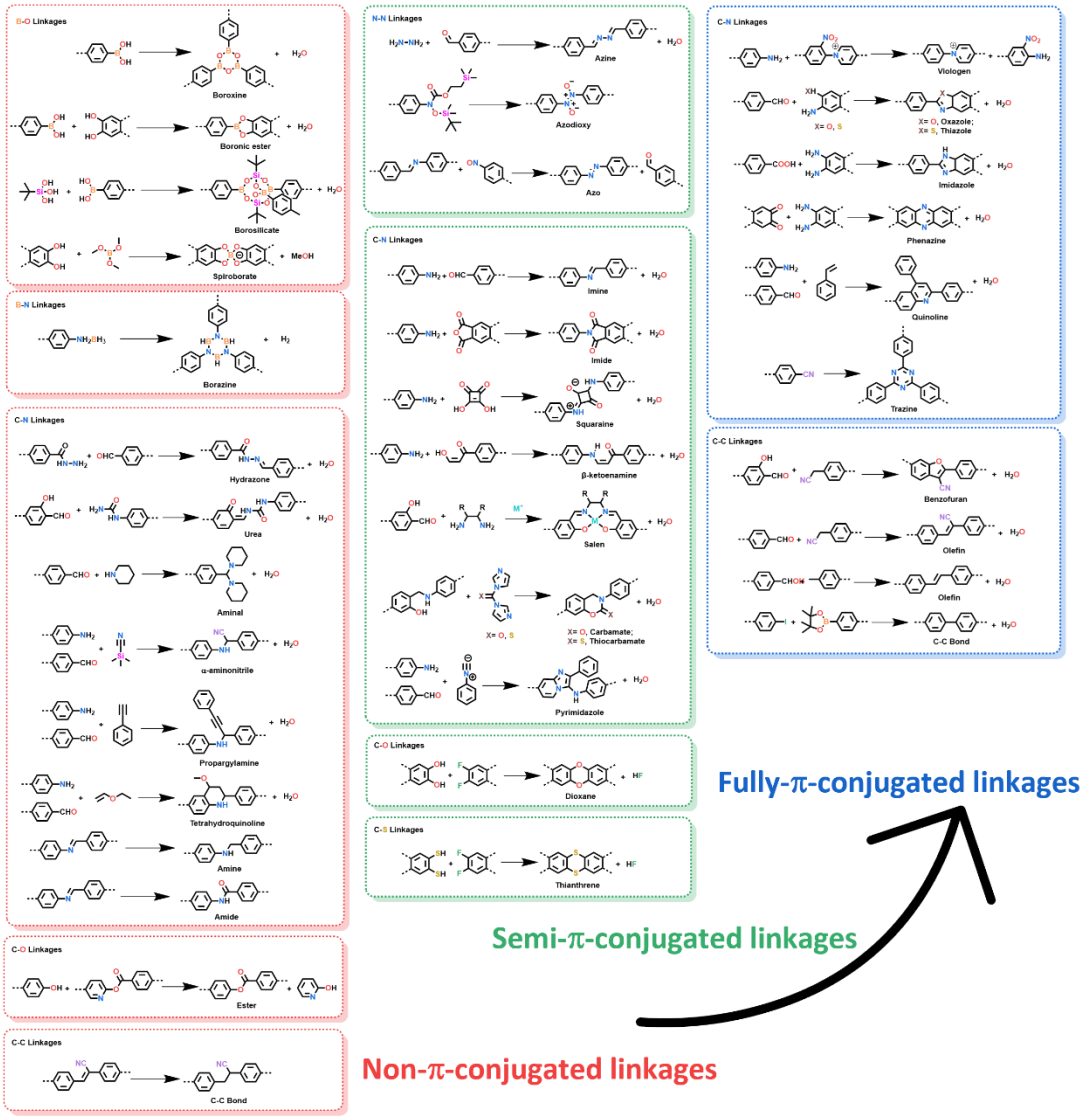

Figure 1.14 Various linkages explored for COF designing and synthesis.

On the other hand, the classification of COF linkages can be confirmed according to the composition and the corresponding polymerization chemistries. The linkages of COFs mainly rely on B-O, C-N or C-C bond formations while COFs with C-O, N-N, B-N and C-S based connection still have a few reported examples.

1.2.2.1 B-O Linkages

B-O linkages are the first type of COF linkages, which are usually obtained by self-polymerisation of boronic acid monomers (or boronic acid ester precursors) or by the condensation with hydroxyl-containing monomers (e.g. *o*-diol monomers or their acetal

precursors, silicone triol monomers, etc.).[60] These COFs can be prepared by a common solvothermal method with highly crystallinities, but they are quite unstable under even relatively mild conditions such as weak acids, bases or water vapour.

The most common B-O linkages of boron-based COFs are boroxyhexa-cycles and boronic esters. For example, COF-1 and COF-5 were first reported by Omar M. Yaghi's group in 2005.[60] The COF-1 with boron-oxygenated hexa-ring linkage was achieved by the trimerization of the boronic acid monomer (1, 4-benzenediboronic acid), while the COF-5 with boronic ester five-membered ring is obtained by the condensation of 1, 4-benzenediboronic acid and hexahydroxy-triphenylene. Both COF-1 and COF-5 were obtained by solvothermal methods and exhibited high crystallinity and specific surface area.

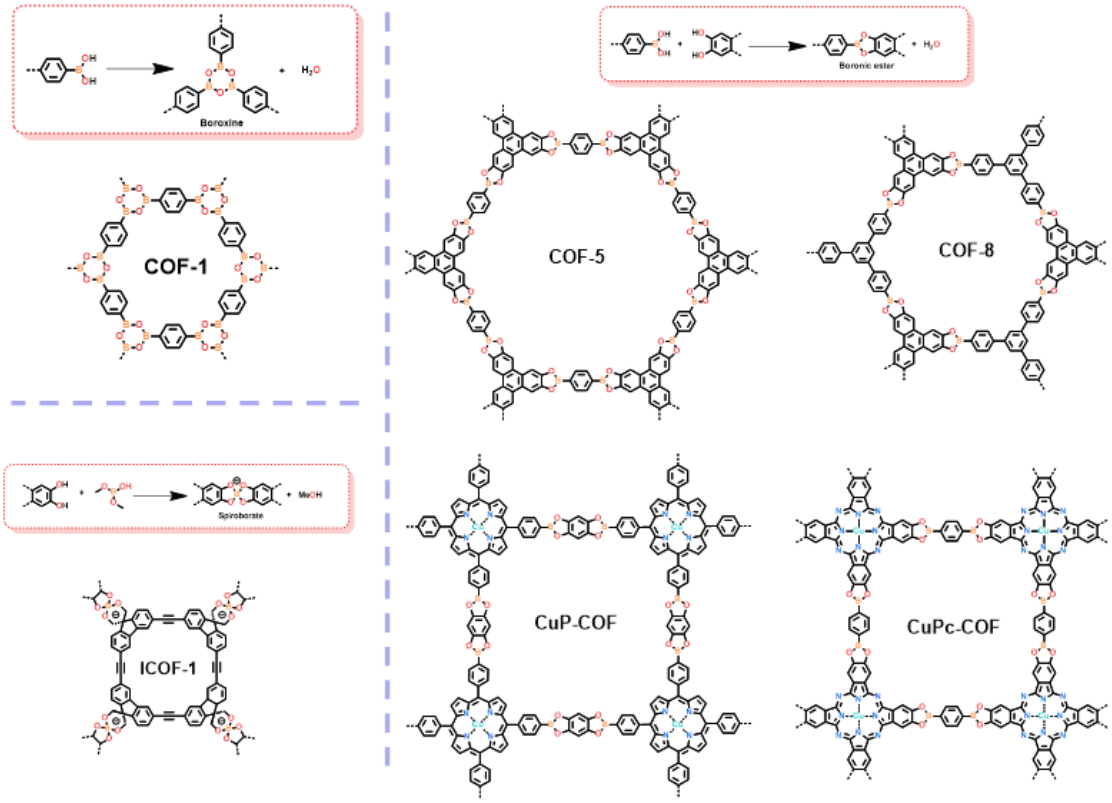

Figure 1.15 Representative examples of COF skeletons with various B-O linkages and their synthesis.

Since, a series of functionalised boron-based COFs with similar structures were reported by changing the building blocks, such as COF-8,[61] CuP-COF,[62] CuPc-COF[63]

and ICOF-1,[64] etc (**Figure 1.15**), which were found to have unique electrochemical and gas separation properties. However, due to their relatively poor chemical stability and especially their sensitivity to water vapour, the functionalization and application of these materials are still very limited. Notably, the crystallinity and specific surface area of boron-based COFs are generally higher than those of other similarly structured COFs materials due to the high reversibility of boron-based linkers and hence the prominent self-healing effect during the crystallization. Therefore, COFs based on B-O linkages can be promising in the specific fields of gas storage and adsorption, energy storage, and non-homogeneous catalysis if their stability can be improved.[65]

1.2.2.2 C-N Linkages

C-N linkages are the second class of COF linkages, which are successfully reported after B-O linkages and are the most intensively studied class of COF linkages up to date. Common C-N linkages of COFs include imines, triazines, amides, imides, etc.

Imine-based COFs are a kind of the most common and important COFs connected by imine bonds, which are usually formed by the acid-catalysed Schiff-base condensation of aromatic aldehydes (or precursors such as acetals) and amine monomers (or precursors such as imines). The first example of an imine-linked COF (COF-300) was reported by Omar M. Yaghi's group in 2009.[66] The COF-300 was obtained by the acetic acid-catalyzed solvothermal reaction of tetra(4-aminophenyl) methane with the tetrahedral configuration and linear terephthalaldehyde. Generally, the crystallinity and specific surface area of imine COFs are lower than those of similarly structured COFs based on B-O linkages, but their stability is significantly improved, leading to the far more widely studies than those COFs based on B-O linkages.

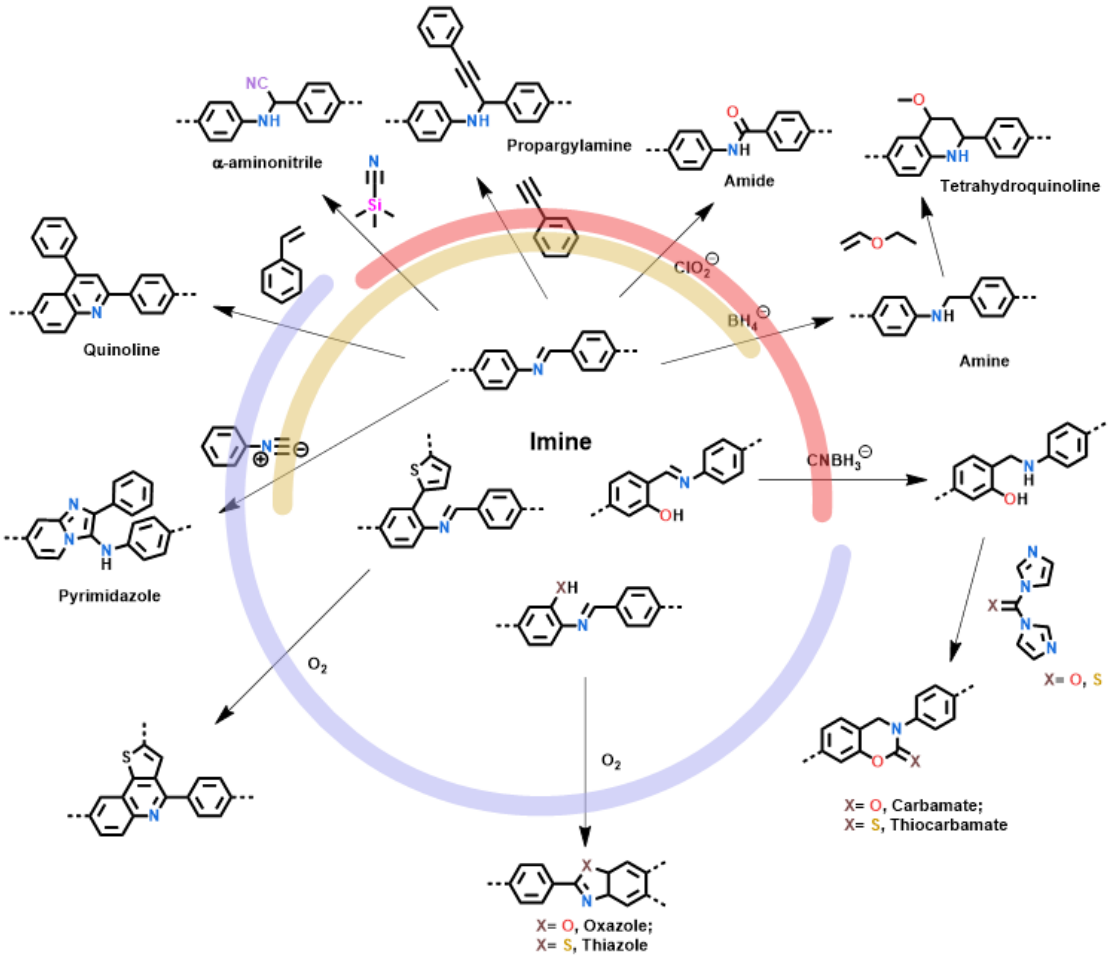

Figure 1.16 Overview of the C-N linkages based on the imine linkage. The different C-N linkages can be separated into these categories: Non-π-conjugated linkages (red) and π-conjugated linkages (blue), and reactions of novel C-N linkages that based on the unfunctionalized aromatic imine precursors with a high universality (yellow).

Due to the good reversibility of Schiff-base reaction for the forming of crystalline COF materials, the designing and preparation of various new linkages based on the initial imine bonds have emerged recently (**Figure 1.16**).[33] With a high generality, any unfunctionalized imine-linked COFs can be used for a further post-modification reaction and form new linkages, including quinoline-,[67] pyrimidazole-,[68] α-aminonitrile-,[69] propargylamine-,[70] amide-,[57] amine-[71] and tetrahydrquinoline-linkages.[72] While some of the reactions need specific building blocks either in amine or aldehyde monomers, such as the formation of an oxazole- or a thiazole-linkages from the ortho-hydroxy and ortho-thiol amines, respectively.[73] Another example is the oxidative cyclization of an imine-linked COF with pendant ortho-thiophene side-groups that forms an extended heterocyclic aromatic linkage.[74]

There are also some other reactions used to form COFs with different C-N linkages, and they can be classified as a kind of Schiff-base reaction broadly, including the reactions for making COFs with hydrazone-,[75] urea-,[76] salen-,[77] squaraine-,[78] β-ketoenamine[79] and aminal-linkages[80] (**Figure 1.17a-f and Figure 1.17k**). Among them, the β-ketoenamine-linked COFs that is first reported by Rahul Banerjee's group shows a much better stability due to an irreversible transformation to keto-enamine tautomerism from the initial enol-imine form.[81] Polyimide based COFs were first prepared by Qianrong Fang in 2014 through a condensation of amine and anhydride monomers with a following cyclization.[82] Due to the large number of exposed imide-linkages, these COFs have recently been widely investigated for lithium-ion batteries and other energy storage devices (**Figure 1.17g**). The nitrogen-containing heterocyclic linkages are another class of imine-based derivative linkages. Both six-membered heterocycles (phenazines,[83] quinolines) and five-membered heterocycles (imidazoles,[84] thiazoles, oxazoles) have been successfully introduced as linkages in COF synthesis (**Figure 1.17h and Figure 1.17j**). The phenazine linker is a six-membered aromatic ring with two nitrogen atoms in the *para*-position, formed by the condensation of *o*-diamine with an *o*-diketone monomers (or *o*-diol precursors). Generally speaking, COFs based on such nitrogen-containing heterocyclic linkages have high conjugated structures with tunable energy levels and high chemical stabilities. These materials are used in a large number of studies like energy storage and conversion.

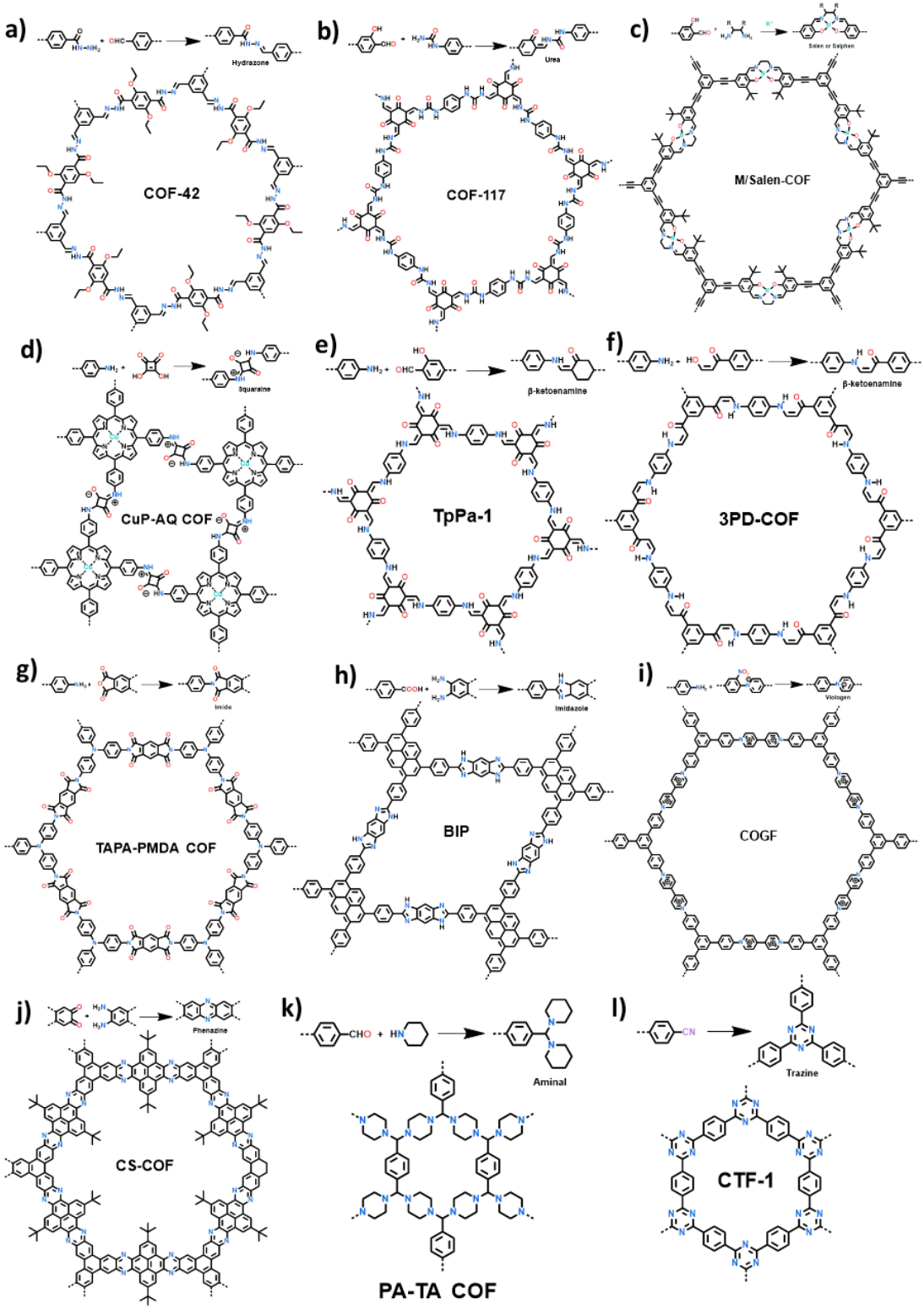

Figure 1.17 Representative examples of COF skeletons with various C-N linkages and their synthesis.

Covalent triazine frameworks (CTFs) are another important class of materials for COFs based on the triazine-ring, which belongs to the C-N linkages. CTF-1 was first reported

by Arne Thomas in 2008 through an ionthermal-induced trimerization reaction of cyanide monomers under high-temperature molten salt conditions ($ZnCl_2$, 400 °C) (**Figure 1.17l**).[85] CTF-1 has a moderate crystallinity with a BET surface area of 791 m^2 g^{-1}. Due to their high surface and conjugation, and good stability, CTFs have been widely used in research on electrochemical energy storage, electrocatalysis and photocatalysis. However, the low reversibility of the reaction and the harsh conditions for the trimerization of cyanide monomers cause their low crystallinity and specific surface area. To solve this problem, Bien Tan's group developed a novel method for the preparation of highly crystalline CTFs by the condensation of amidine monomers with aldehyde monomers (or hydroxyl precursors) (**Figure 1.18b**).[86, 87] Meanwhile, Jong-Beom Baek's group developed a pCTF-1 with ultra-high specific surface area (2034 m^2 g^{-1}) by the condensation of aromatic amides (**Figure 1.18c**).[88]

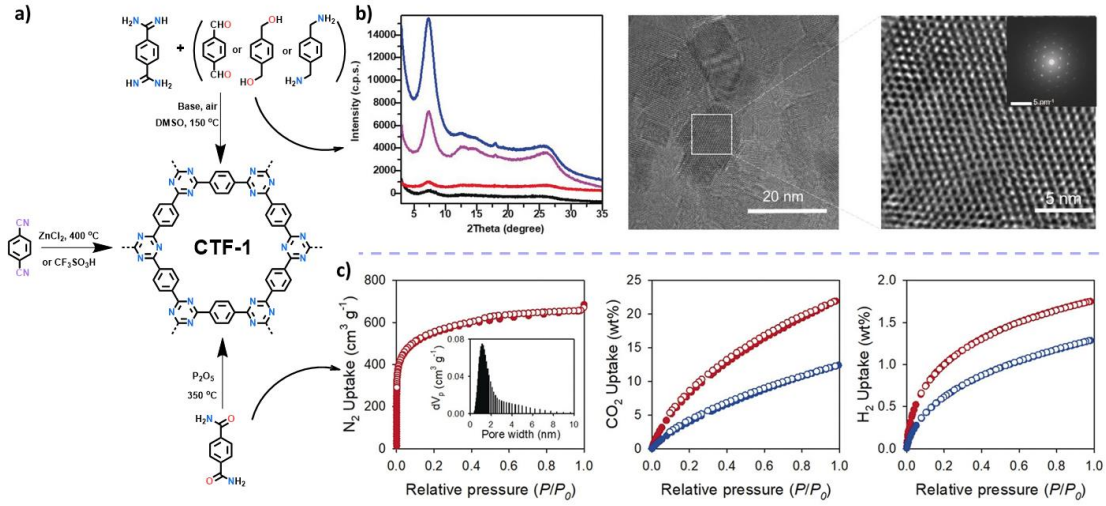

Figure 1.18 a) CTF-1 made by different synthetic routes; b) CTFs with high crystallinity *via* a condensation reaction between an aldehyde and an amidine dihydrochloride involving a Schiff base formation followed by a Michael addition; c) CTFs with high surface area *via* a phosphorus pentoxide (P_2O_5)-catalyzed direct condensation of aromatic amides (This figure is reprinted from ref. 85-88).

1.2.2.3 C-C Linkages

Although the COFs based on C-N linkages represented by imines and their derivative linkages have made great progress in terms of stability and application scope compared with COFs based on B-O linkages, they are still difficult to be chemically stable under

some harsh environments (e.g., higher concentrations of acids and bases) for a long time. In comparison, C-C linkages usually show a much better chemical stability but the main problem of this kind of materials is the poor reversibility, which is quite important for the forming of crystalline COF materials.[89] Currently, COFs based on C-C linkages are mainly focused on the C=C (carbon-carbon double bond) made by Knoevenagel condensation.

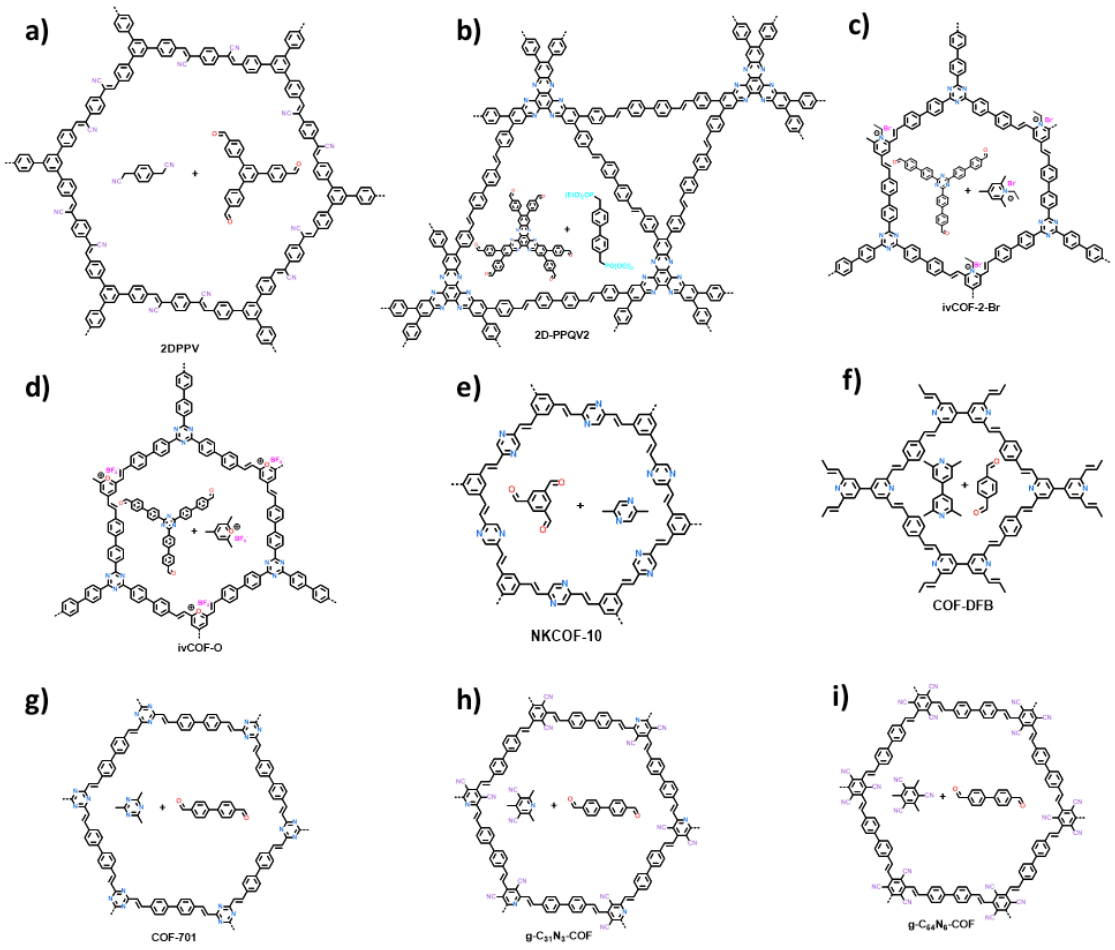

Figure 1.19 Representative examples of COF skeletons with various C-C linkages and their synthesis.

The first reported case is the COF called 2DPPV[90] from Fan Zhang's group in 2016 by using strong-base catalysed Knoevenagel condensation of aldehyde and benzylacetonitrile monomers, which is also called sp^2-C COF reported by Donglin Jiang's group in 2017 (**Figure 1.19a**).[91] From the reaction mechanism, the cyano-group in acetonitrile monomers is important for improving the activity of activated proton for the Knoevenagel condensation. Based on that, other methylene monomers with

enhanced active hydrogen were used to make C=C linkages without the substituted cyano-groups, for example, 2, 4, 6-trimethyl-1, 3, 5-triazine,[92] 3, 5-dicyano-2, 4, 6-trimethylpyridine,[93] 1, 3, 5-tricyano-mesitylene,[94] N-ethyl-2, 4, 6-trimethylpyridinium salts,[95] 2, 4, 6-trimethylpyrylium tetrafluoroborate[96] and 1, 4-bis (diethylphosphonomethyl) benzene[97] (**Figure 1.19b-i**). To enrich the diversity and improve the crystallinity of COFs based on C=C linkages, designing new monomers with high react activity is essential for the further research. Meanwhile, the COFs linked by C-C bonds can be made by palladium-catalysed coupling reaction.[98] However, it's more probable to get amorphous products instead because these reactions are typically kinetic-controlled reactions with poor reversibility. Therefore, other methods like surface synthesis need to be developed as a supplement for the growth of COF based on C=C linkages.

Compared with imine-based COFs, the COF based on C=C linkages have unique properties due to the high rigidity, high conjugation and good chemical stability of C-C linkages and can be explored to some specific applications, such as photocatalysis, fuel cells, supercapacitors and lithium-ion batteries.[99] Thus, it is convinced that more and more cases of COF materials with C-C linkages would be prepared in the future.

1.2.2.4 Other Linkages

In addition to the common B-O linkages, C-N linkages and C-C linkages discussed above, there are several other linkages reported for extending the diversity of COF synthesis though the generality of preparing these linkages is still limited.

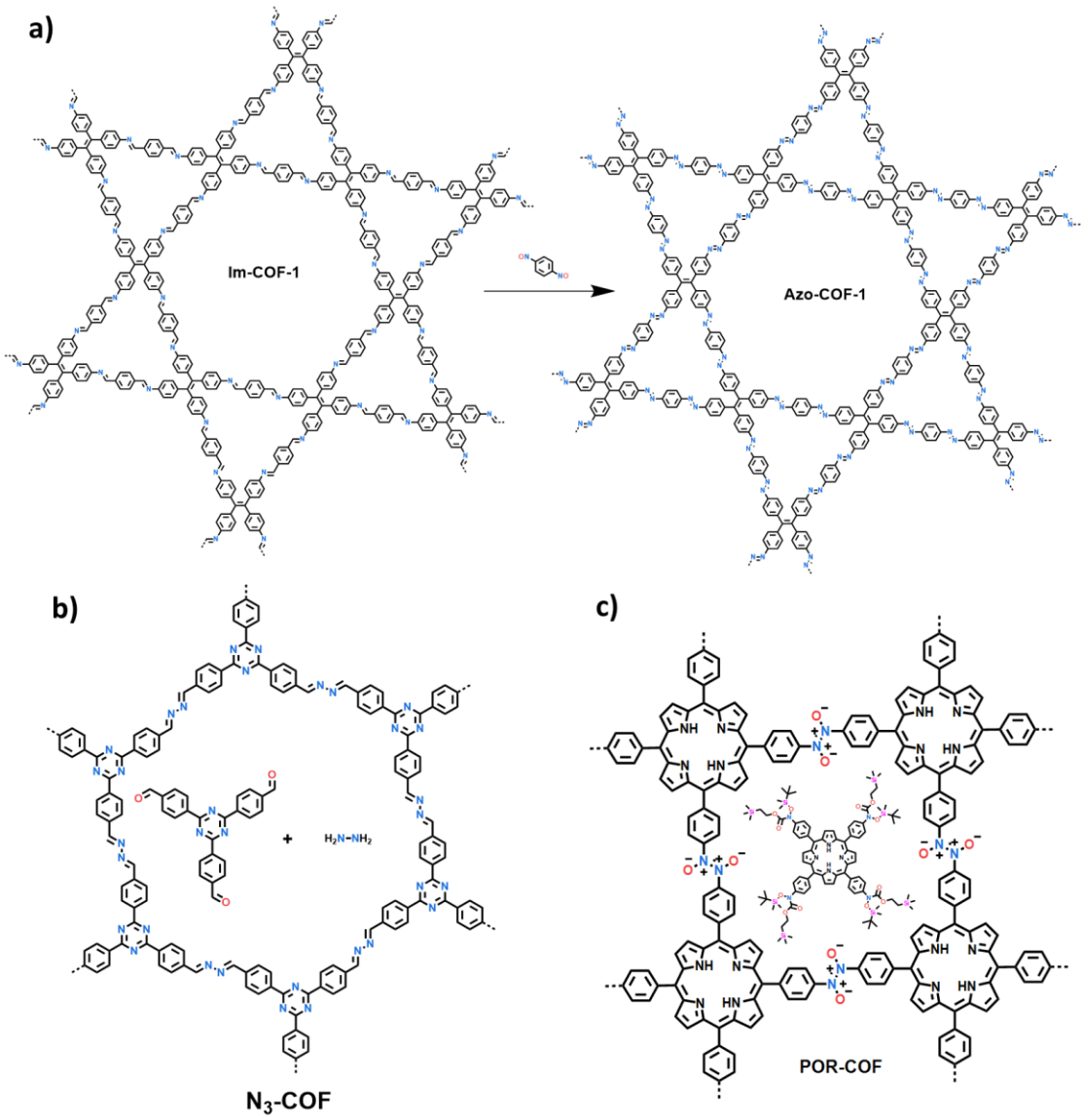

Figure 1.20 Representative examples of COF skeletons with various N-N linkages and their synthesis.

The reported N-N linkages contain azo-, azine- and azodioxy-linkage. The crystalline COFs with azo-linkage cannot be obtained by a direct condensation, so Xin Zhao's group develop a method to synthesize COFs with azo linkage on the basis of *in-situ* linker exchange, by which azo-linked COFs can be transformed from imine-linked COFs (**Figure 1.20a**).[100] Azine-linked COFs can be made by the condensation of hydrazine hydrate and aldehyde monomers. As one of the monomers containing the smallest building block size, azine-linked COFs usually have a smaller pore size and high stability, leading to the tunable properties for gas adsorption and photocatalysis (**Figure 1.20b**).[101] The COFs (NPN-x, x=1, 2, 3) with azodioxy-linkage were first

prepared in 2013 through the self-polymerisation of nitroso monomers and it was also the first example of COF single crystals that obtained successfully. Later in 2016, Gang Xu's group reported the preparation of a porphyrin-containing COF with azodioxy-linkage based on the protected aromatic hydroxylamine monomers (**Figure 1.20c**).[102] However, these COFs have not been able to attract sufficient attention, and relevant studies are relatively few because of their poor stability.

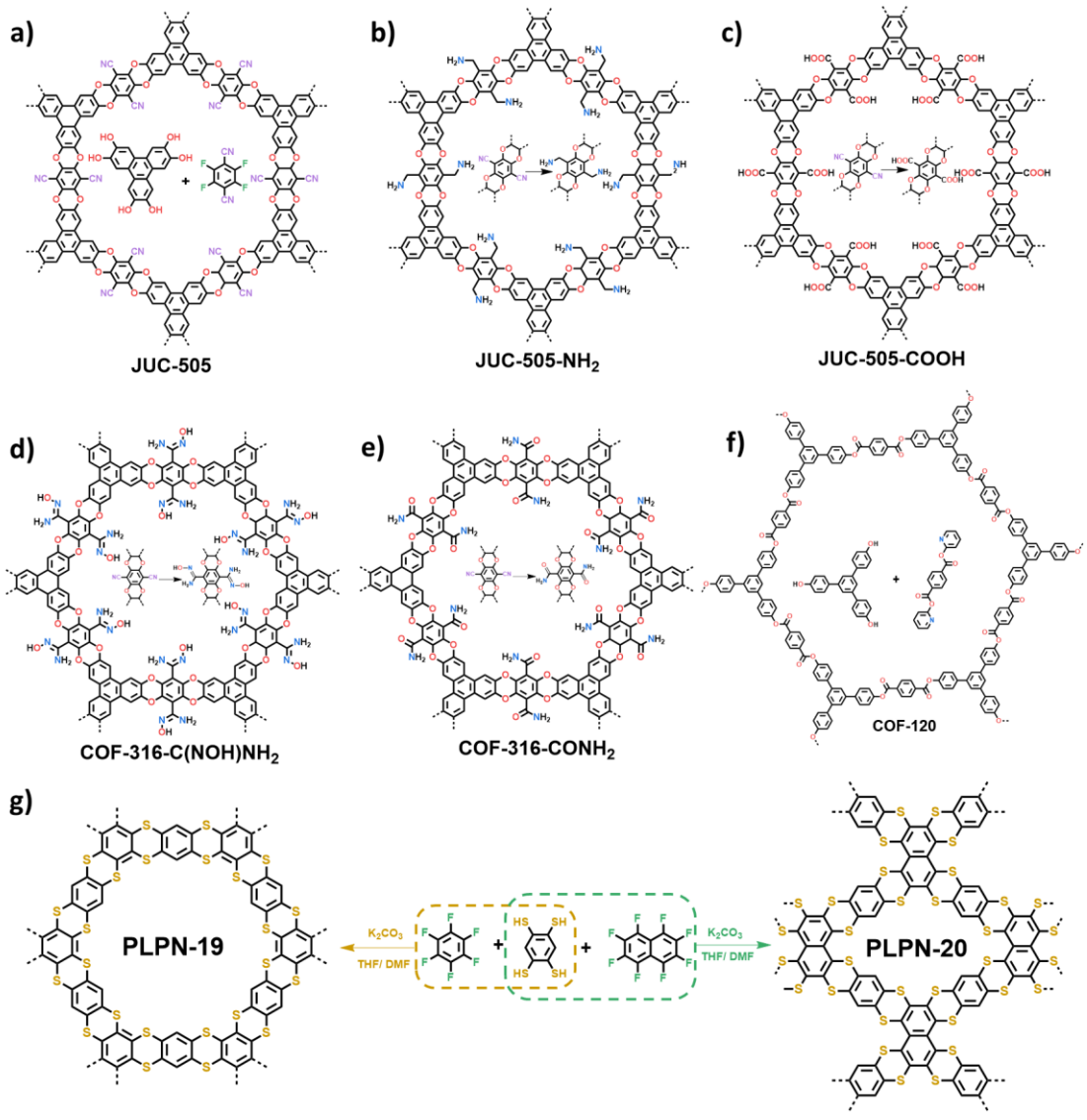

Figure 1.21 Representative examples of COF skeletons with various C-O and C-S linkages and their synthesis.

Up to now, COFs with C-O or C-S linkages have been studied for a relatively short time and therefore there are only a few instances. Polyarylether-based COFs that are

linked by dioxane were reported by Omar M. Yaghi (COF-316) and Qianrong Fang (JUC-505) in 2018 (**Figure 1.21a**).[37, 103] These linkers were prepared by a base catalysed aromatic nucleophilic substitution reaction (S_NAr) between *o*-diphenol and *o*-difluoro monomers. COF-316 and JUC-505 showed the crystallinity even though the cyclization of dioxin-ring is irreversible. The reason for the formation of ordered structures might be the rigidity of the building units and the strong directionality of the linkages. The high chemical stability of dioxane linkages allows these COFs to endure the harsh environments for some post-modification reactions to get a series of derivatives for different practical applications (**Figure 1.21b-e**). Another example of C-O linkages is the ester-linked COFs made by a transesterification reaction between di-functional degree 2-pyridinyl aromatic carboxylates and multiple-functional phenols, owning both high flexibility and high surface area and crystallinity, which is never reported in COFs field before (**Figure 1.21f**).[104] Also, COFs based on C-S linkages show the similar properties and can also be made from the dynamic self-correcting nucleophilic aromatic substitution, but the reaction activity of -SH is higher than the -OH which case the poorer reversibility and crystallinity of the obtained porous ladder polymer networks (**Figure 1.21g**).[105, 106]

To summarise, the design of COF materials with relatively rigid covalent bonds instead of fragile coordination bonds, significantly improves their chemical stability compared to MOFs materials and up to now there have been lots of COF linkages reported with different types. However, most of common COF materials are connected by reversible covalent bonds based on the dynamic covalent chemistry due to the requirements of the final crystallinity, and therefore their stability is still difficult to meet the practical usage. Thus, develop the novel linkages to improve the chemical stability of COFs materials while maintaining crystallinity and pore structure is currently one of the major goals for the future research in the COF field and this is one of our major goals in this thesis.

1.2.3 Morphology Control of Covalent Organic Frameworks

1.2.3.1 Polycrystalline Powders

Crystallinity is the key feature that distinguishes COFs from other porous organic polymers, including CMPs, HCPs, PIMs and PAFs. However, as a kind of cross-linked polymers that possess the feature of insoluble and fusible, the majority of COF materials can only be obtained as polycrystalline powders. Such polycrystalline powders are not benefit to either structure characterization or scale-up for industrial applications because the former needs large precise single crystal to avoid the disturb from the defects while the latter needs a good solubility or dispersibility for the further processing. Thus, the efficient way for the preparation of single crystals or nanosheets of COF materials is one of the important directions in the COF research area.

1.2.3.2 Single-Crystals

Single crystals are crystals in which the atoms are arranged in three dimensions regularly and periodically, consisting of the same continuous spatial lattice internally in the three-dimensional direction, and the arrangement of the masses in space is long-range ordered throughout the crystal. However, when the size of a single crystal is as small as nanometre scale or a few micrometres, it's usual to define their aggregates as polycrystalline powders.

Typically, a single crystal is defined with a size that meets requirement of the single crystal X-ray diffraction testing, which is normally around 10 to 50 μm, depending on the sources of X-rays. For many studies, polycrystalline samples can be used instead, but large single crystals of reasonable size are irreplaceable sometimes, because the orientation of the grains is disordered in polycrystals, so that the properties of the samples tested from polycrystalline samples can certainly be affected by the gaps between each polycrystals.

The growth of crystals can be divided into two stages: nucleation is the initial stage of the phase transition, *i.e.* the process of creating a nucleus. Growth is the process in

which the crystal continues to grow on the formed nucleus. The quality of the crystal mainly depends on the rate of both nucleation and crystal growth: when the rate of nucleation is greater than the rate of crystal growth, a large number of microcrystals tend to form and then aggregate, while when the rate of growth is greater than the rate of nucleation, the crystal tends to have defects. In other words, to grow a large single crystal, the rate of nucleation must be reduced, and at the same time, the rate of growth must not be controlled in order to obtain a crystal with good crystallinity.[107]

Similarly, single crystal is related to one of the most important and challenging issues of the COF field in revealing structural insights into functions and properties. However, the conditions of COF synthesis are usually intense and complex during the long-time solvothermal reaction, therefore, the report of general way for making single crystal COFs is still few.

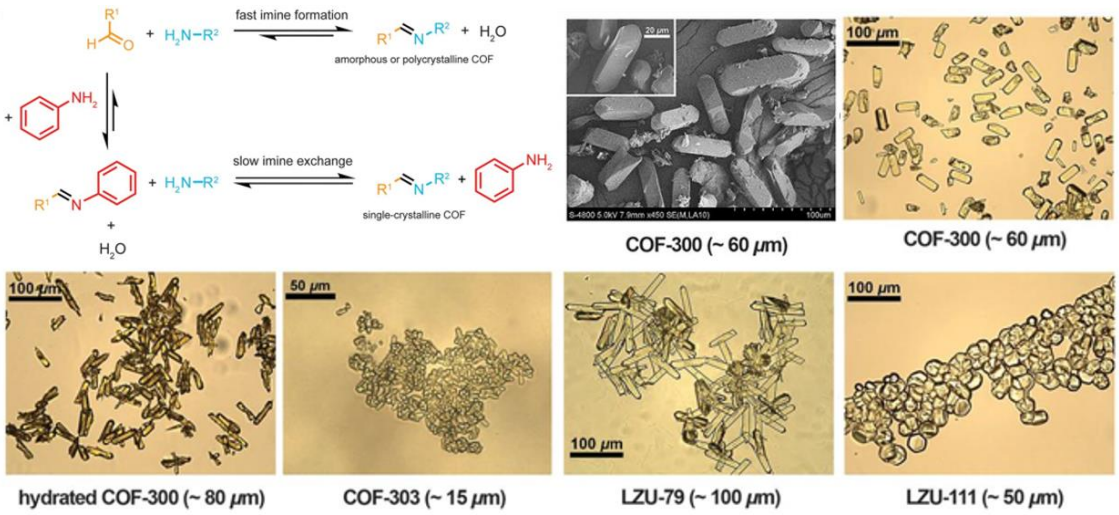

Figure 1.22 The mechanism of the formation of COF single crystals by using a modulation approach with anilines (This figure is reprinted from ref. 108).

In 2018, Wei Wang's group obtained a series of 3D imine COFs with single crystal structures by the use of aniline as the modulators during the synthesis (**Figure 1.22**).[108] In the absence of aniline, the situation is similar to the normal COF synthesis, *i.e.* the imine-formation equilibrium is shifted toward the product, amorphous or polycrystalline COFs, whose formation is governed by fast nucleation and limited crystal growth. In the presence of aniline, the formation of the terminal phenyleneimine

product is comparably fast followed by a slow imine exchange which enables the growth of single-crystalline COFs. However, this method needs a long time (more than 30 days), which limits the preparation of single crystal COFs in a large scale. Thus, the exploration of the efficient way to prepare single crystals of both 2D and 3D COFs is still ongoing.

1.2.3.3 Nanosheets

Unlike one-dimensional linear polymers, the rigid framework structure and limited solubility of COFs powders make them difficult to subsequently process. For some specific applications, these micro-crystalline COF powders have to be further moulded into different shapes. However, the moulding often results in non-homogeneous phases and therefore reduced properties due to their poor solubility. Improving the solubility and processability of COFs powders is an important direction for the further applications of COF materials.[109] For the 2D-COFs that are initially designed with a two-dimensional topology, allowing their own layers extension into the wanted morphology by some controlled methods theoretically. The exfoliation of 2D-COF powders to thinner covalent organic nanosheets (CONs) can effectively improve the dispersibility for the further processing. Moreover, due to their large ratio of surface-to-thickness and excellent nano-structural properties, CONs can be widely used in industrial applications including: (1) Adsorption and separation, where CONs play a key role in forming unique nano-structure for the high selectivity and efficiency; (2) Sensing, where the fluorescence, biocompatibility and electrochemical properties of CONs lead them to the high performance in signal transduction and conversion; (3) Energy storage and conversion, where the more exposed active centres and rapid charge transfer of CONs facilitate the energy storage in supercapacitors and batteries and also various photo- or electro-catalytic reactions.[110] Therefore, the preparation of CONs is imperative to realise the further usage of COFs. Up to date, some great works have been explored in the fabrication of monolayer or multilayer CONs by top-down or bottom-up strategies (**Figure 1.23**).[110]

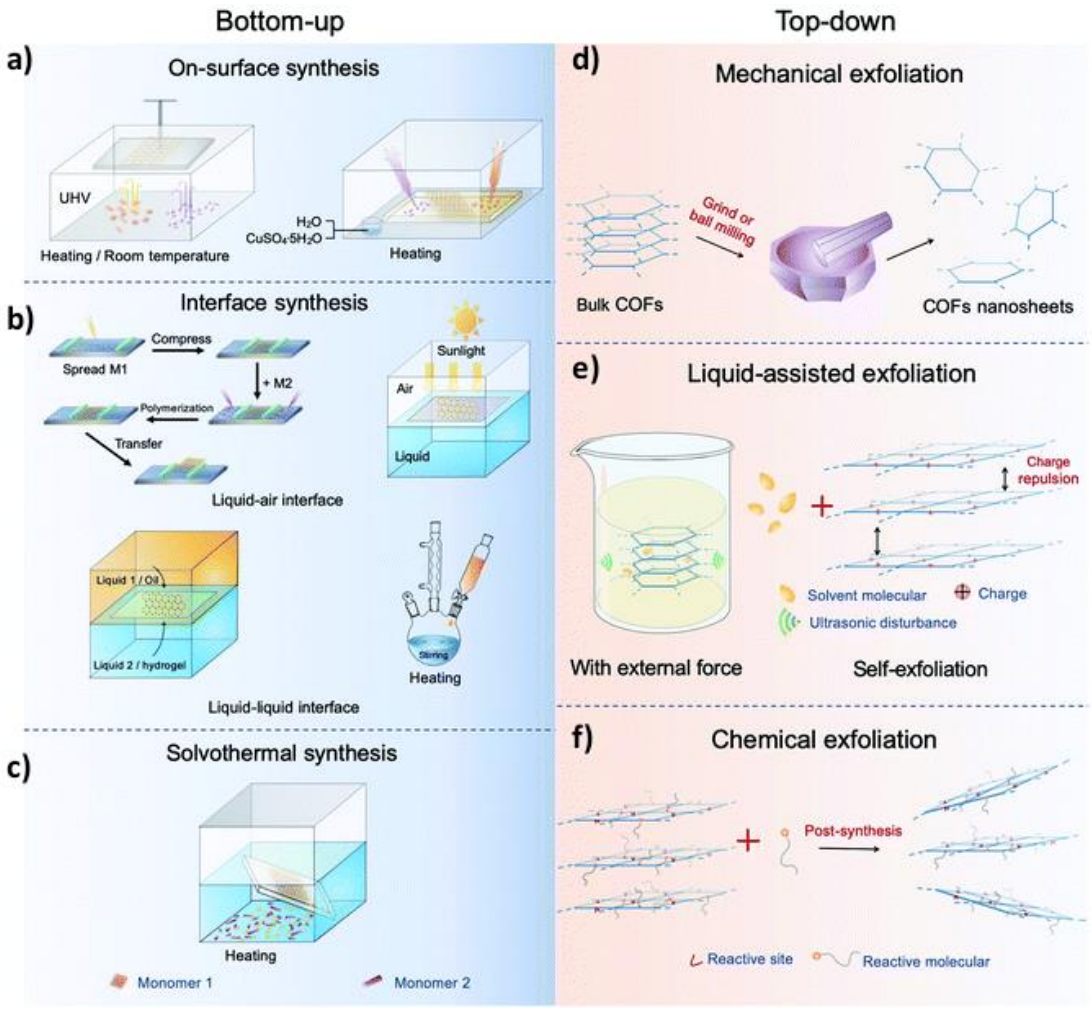

Figure 1.23 Diagram of the synthesis of CONs. The left represents the bottom-up method and the right is top-down synthesis (This figure is reprinted from ref. 110).

The bottom-up approach is usually associated with the selection of a functional coating on the surface, which has been widely used in the preparation of CONs (**Figure 1.23a-c**). The key to this strategy is to control the growth direction of the layers to avoid random expansion into three-dimensional bulk COF materials. So far, many highly oriented CONs have been synthesised by bottom-up methods on different substrates and interfaces. However, exploring suitable synthesis conditions to grow CONs is not easy while the substrate supported solvothermal method is still the most widely used method for the preparation of CONs. In addition, other excellent and simple methods have been used, including interfacial synthesis, room temperature steam-assisted conversion and synthesis under continuous flow conditions, which has been introduced in the previous section.

In contrast to the bottom-up synthetic method, the top-down strategy involves the simple preparation of exclusive monolayer/multilayer CONs from bulk COF powder materials, rather than growing CONs on a specific substrate or interface. The top-down strategy is relative simpler, more affordable, more straightforward and more general than the bottom-up approach, where the monomers are usually unique and expensive, and the synthetic process require the demanding conditions. 3D bulk COF polycrystalline powders with 2D layered structures that are stacked in layers along the vertical direction by the weak interaction forces such as van der Waals force. The top-down strategy is designed to break down the π-π interaction forces between COF layers by the internal or external forces, resulting in single-layer or multi-layers CONs. The top-down strategy contains various methods, including liquid phase assisted exfoliation, mechanical exfoliation, chemical exfoliation and self-exfoliation (**Figure 1.23d-f**). The difference between these different methods is the source and strength. For example, self-exfoliation methods rely on the internal forces primarily, whereas solvent-assisted exfoliation, mechanical exfoliation and chemical exfoliation are induced by external forces such as ultrasound, mechanical forces and charge repulsion.

Solvent-assisted exfoliation is a common method for the exfoliation of bulk COF materials into 2D-CONs. As the most commonly used exfoliation method, solvent-assisted exfoliation has many examples that are inspired by the success of ultrasonic exfoliation of graphene oxide materials in water (Hummers' method). Felix Zamora's group first used solvent-assisted exfoliation to obtain layered CONs with 10-25 layers (**Figure 1.24a**).[111] The π-π interaction forces between the COF layers can be weakened by the mechanical forces through the help from the suitable solvent, namely, the assisted action of ultrasound accelerates the insertion of solvent molecules into the COF layers, thereby increasing the layer spacing and thus weakening the interlayer π-π interaction forces. In addition, the solvent plays a quite important role in the exfoliation of the layered COF, not only to exfoliate the layers, but also to stabilise them into a nanosheet dispersion. In particular, the appropriate surface tension between the COF layers and the solvent is key to reducing the energy of system and increasing the

efficiency of exfoliation. Furthermore, the reaction time also influences the quality of the CONs. Normally, longer reaction time results in the thinner but smaller nanosheets.

Another effective method is mechanical exfoliation. Rahul Banerjee's group used solvent-free room temperature mechanochemical methods to prepare TpPa-1 and found that exfoliated CONs also existed in the product (**Figure 1.24b**).[112] It was shown that mechanical grinding can disrupt the strong π-π interaction forces between the COF layers. Thus, they further prepared a series of self-supported CONs made under the similar condition of grounding methanol dispersion of bulk COF materials. These self-supported CONs showed the thickness of 3-10 nm with good stability in both acid and base solution.

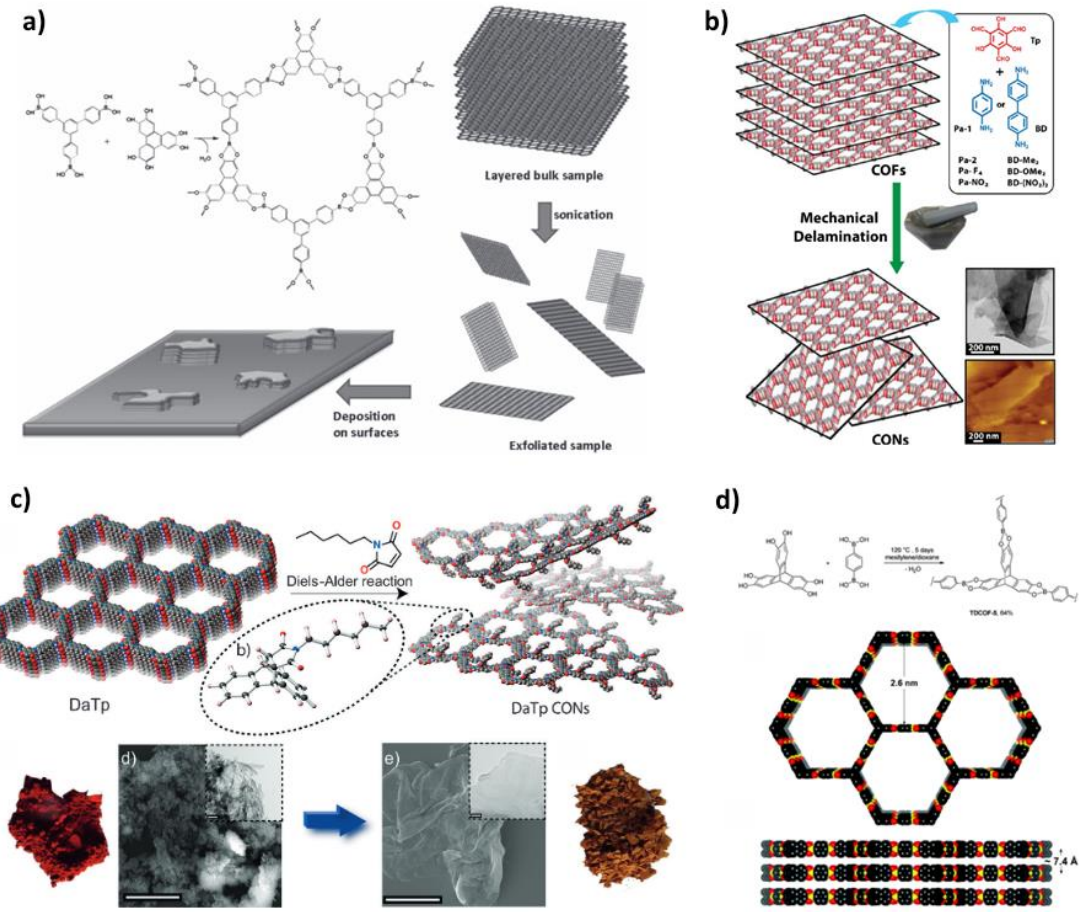

Figure 1.24 Various methods used for the COF exfoliation based on top-down strategy: (a) solvent-assisted exfoliation; (b) mechanical exfoliation; (c) chemical exfoliation and (d) self-exfoliation (This figure is reprinted from ref. 111-114).

Relatively speaking, chemical exfoliation and self-exfoliation are less common. For chemical exfoliation, it needs a pre-consideration of the monomer and chemical structure of COFs to introduce specific groups for the further exfoliation to prepare CONs. Considering the poor dispersion of the COFs, Khayum et al. synthesised anthracene-based COF via a [4 + 2] cycloaddition reaction, and further obtained self-supported CONs at the water/gas interface by the layer-by-layer assembly (**Figure 1.24c**).[113] Compared to the exfoliation with the help of external forces, the self-exfoliation method is more likely to rely on well-designed building blocks to induce an internal force for the exfoliation. For example, El Kaderi et al. reduced the π-π interaction forces between the prepared COF layers by the insertion of a triplet alkene unit. Then two methyl groups were introduced into the 9,10 position of the triplet genetic alcohol to further increase the distance between the COF layers, resulting in the exfoliation and the monolayer CONs (**Figure 1.24d**).[114] Furthermore, the ionic building blocks can not only initiate the self-exfoliation process but also act as target functional groups, which broadens the range of applications for CONs. The introduced functional groups not only avoid aggregation but also have a targeting function. But for the solvent-free mechanical exfoliation, toxic organic solvents are well avoided. Although each of these methods has its own advantages and has been successfully applied to the preparation of free-standing CONs, there are still some certain limitations that remain. Firstly, it is difficult to obtain monolayer nanosheets due to aggregation from layer stacking. On the other hand, the relatively low yields of CONs prevent their further applications.

For a short summary, the real applications of bulk powder COF are greatly limited due to its insolubility and poor processability. Therefore, in order to achieve better performance, it is essential to prepare CONs with large surface-to-thickness ratios by convenient ways. Also, CONs have great potential for some applications due to their more superior nanostructures, thinner layers and more exposed active sites. As mentioned above, various methods can be used to prepare CONs, however, different synthetic methods lead to different physical or chemical properties and thus suitable to

different applications. The main applications of CONs include energy storage, adsorption and separation, etc. Especially for energy storage, CONs with larger specific surface area, thinner layers, more accessible active sites and the unique electronic conductivity show a much better performance than the previous bulk COFs. Thus, preparing CONs efficiently is also another major target of our works.

1.2.4 Opportunities and Challenges

As mentioned above, due to a wide variety of building blocks and the diversity of linkages and topologies, the design and functional exploration of COFs have established an amazing foundation in both basic and application research over the past 15 years.

However, several challenges have still remained in the COFs research field: i) Stability: Normally, COFs are made by reversible reactions, which determine their forming linkages can be decomposed in some specific conditions. ii) Processability: Most reported porous organic polymers, including COFs, are obtained in the form of insoluble bulk powder, which has a poor processability to limit the further usage in many practical applications to a certain extent. iii) Structure characterization: Although there have been progresses in making single crystals, most COF materials are still synthesized as polycrystalline powders, which are too poor to further determine the structure accurately. A general way to get single crystals of COFs, and also the methods of characterization and modelling of such polycrystalline powders still need to be developed. iv) Application: Now there are many researchers exploring different applications on the academic level, but actually there is no such applications which are unique for COFs, or they would become interesting for industry. v) Industrialisation: Preparation of COFs scalable is still difficult recently, because traditional COFs synthesis needs long-time, high-temperature, inert environment and expensive monomers.

In this thesis, we focus on the new COF chemistry to explore the new linkages and extend the COF systems, and further try to partly solve some of the challenges mentioned above, including (i) Stability, ii) Processability and iv) Application).

1.3 Energy storage Devices

1.3.1 Electrochemical energy

Since the development of population, society and economy all over the world, the demand for energy is increasing urgently. However, there are two huge problems with the usage of non-renewable energy sources currently: 1) The over-exploitation of non-renewable energy sources, represented by coal, oil and natural gas, leads to an irreversible consumption. Thus, over-reliance on such fossil energy sources will therefore inevitably cause a slowdown in social development when they are run out in the future. 2) The inappropriate use of non-renewable energy sources has caused a series of environmental problems, such as air pollution and the greenhouse effect. These environmental problems have seriously affected the quality of our daily lives. Therefore, the development of new renewable energy technologies to deal with these two major issues of the 21st century, namely, the energy crisis and environmental issues, can no longer wait.

Electrochemical energy, a new type of energy with sustainable and environmentally friendly features, has emerged as one of the most promising substitutes for fossil energy. As the most mature and widely used energy conversion system, electrochemical energy storage devices can store and utilise new energy sources such as solar, tidal, geothermal and nuclear energy. Recently, the electrochemical energy storage devices are mainly focused on secondary batteries and supercapacitors.

1.3.2 Lithium-Ion Batteries and Supercapacitors

The rechargeable lithium-ion batteries (LiBs) we used today is a development from one-time lithium batteries. Primary lithium batteries use pure lithium metal as the anode. But lithium can deposit on the surface of the electrode unevenly during the discharge,

forming lithium dendrites that can easily puncture the separator and cause internal short circuits in the battery, therefore, lithium batteries are generally not rechargeable. Lithium-ion batteries, which are modified from lithium batteries, containing materials that can reversible extraction and insertion of lithium-ion as electrodes, an organic solution dissolved in lithium salts as the electrolyte and a polymeric barrier membrane as a separator to prevent short-circuiting by contact between the two electrodes.

In terms of the mechanism for achieving the reversible conversion of electrical and chemical energy, LiBs are batteries based on the differential concentration of lithium-ions. During the charging process of the LiBs, the cathode that is lithium-containing transition metal oxide (e.g. lithium cobaltate, lithium iron phosphate, etc.), undergoes an oxidation reaction for shedding lithium ions to the electrolyte under the action of an external voltage, and the lithium ions combine with the anode material (e.g. silicon, graphite, etc.) by the insertion of lattice or in the form of alloying, thereby converting electrical energy into chemical energy to achieve the energy storage. While during the discharging process, namely, electrons move along the external circuit to the cathode, the anode undergoes an oxidation reaction and lithium ions return from the anode to the cathode through the electrolyte, where they combine with electrons to re-form the lithium-containing compounds and release of electrical energy (**Figure 1.25b**).[115]

Supercapacitors are another type of electrochemical energy storage device. Compared to the batteries, it has the advantages of high power density, long cycle life, high safety and environmental friendliness. Supercapacitors have a good electrochemical reversibility because they do not have chemical reactions during charge and discharge process like batteries. According to the different energy storage mechanisms, supercapacitors can be divided into two categories: electric double layer capacitors (EDLCs) and pseudocapacitors.

Currently, EDLCs are widely used due to their fast charge-discharge performance, long cycle life and high safety. The theoretical basis of double electric layer supercapacitors is the classical interfacial electric double layer theory. When a working electrode is

inserted into the electrolyte, the positive and negative charges will generate on the surface of electrodes and the interface of electrolytes, respectively, thus creating a certain potential difference on the electrode surface. When two working electrodes are applied with a voltage less than the decomposition potential of the electrolyte, the positive and negative ions in the electrolyte will move towards the two electrodes respectively under the force from the electric field to form a tight electric layer, thus creating an electric double capacitance effect (**Figure 1.25a**).[115]

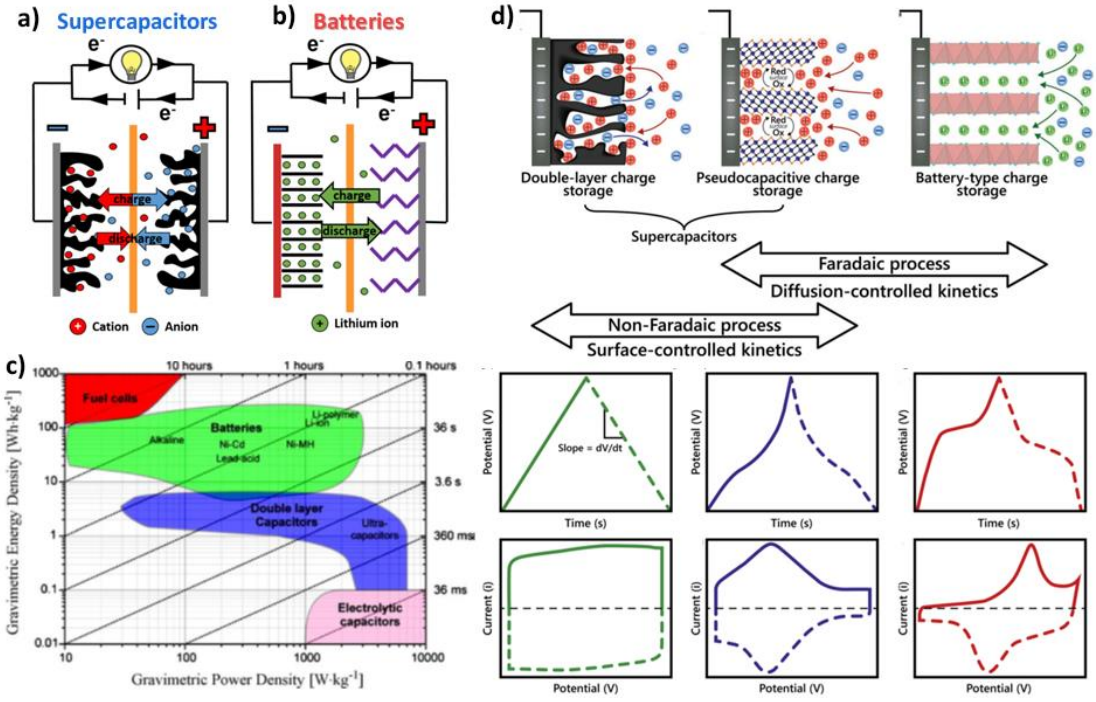

Figure 1.25 (a-b) Construction of supercapacitor and lithium-ion battery. (c) The Ragone plot presenting specific power and energy values reached by different energy storage devices. (d) Illustration of different charge storage process of EDLCs, pseudocapacitor and battery. (This figure is reprinted from ref. 115-116).

Pseudocapacitor, which is also called as a Faradaic quasi-capacitor, is based on a highly reversible chemical adsorption or redox reaction of an electroactive substance on the surface of electrodes, resulting in a capacitance related to the charging potential of the electrodes. The electroactive material undergoes a reversible Faradaic process from chemical adsorption or redox reaction for an electron transfer, which is similar in nature to the charge-discharge reaction of batteries. However, from a kinetic study of the reaction, the whole charging and discharging process shows a similar behaviour with

capacitors, i.e. the potential of the two electrodes is almost linear related to the current applied to the electrodes, which is different from the behaviour of batteries reaction (**Figure 1.25d**).[116] Thus, it can be considered that pseudocapacitance is a type of energy storage mechanism between the reactions of batteries and EDLCs. It is found that the pseudocapacitance is not only generated at the surface of the electrodes but also at a certain depth from the electrode surface, which greatly increases the utilisation of the active material in the device, so the specific capacity and energy density generated by the pseudocapacitance mechanism is higher than that of the electric double layer capacitance but with a relatively lower power density.

Both LiBs with high energy density and supercapacitors with high power density are important and attractive energy storage devices that we used and studied. From theoretical mechanistic studies to the technical assembly of devices, there are lots of directions for studying to improve their performances. But the key point is always focus on the materials of the components in the devices, mainly are electrodes and electrolytes, which need the suitable materials.

1.4 Electrodes in Supercapacitors

1.4.1 Organic Electrodes

According to the electric double layer theory, a larger the specific surface area of electrode material with a high conductivity can generate a higher the theoretical specific capacity. Therefore, porous materials especially porous carbon materials, are widely used as the electrode of EDLCs. However, unsuitable pore sizes can restrict the transport of electrolyte ions, so not all the specific surface area of electrodes can be used as electrochemical activated surface area. Therefore, how to regulate the inherent porous properties of the material to obtain a higher specific capacity is important for EDLCs. Meanwhile, pseudocapacitor have a relative higher energy density due to the reversible redox reactions of metal oxides or conducting polymers, but the dimensional stability of these materials is not high, so how to improve the power density and cycling

performance of pseudocapacitor while maintaining their high energy density is also a challenge.

Organic electrode materials have the advantage of being environmental-friendly, structurally diverse and flexible due to their natural abundance of non-metallic elements (e.g., C, H, O, N, S) and the large number of redox-active sites linked by covalent bonds, which gives it the potential to be used as an electrode material. Organic electrode materials include small organic molecules, polymers and other organic materials.

The functional groups containing N, O and S elements with isolated electron pairs or unsaturated covalent bonds in small organic molecules can combine cations, facilitating the electron transference, which leads to the electrical energy storage. However, the small organic molecules can be dissolved in the electrolytes, causing a fast attenuation of capacitance. Although the cyclic stability of the electrodes based on s can be enhanced by a further polymerisation, the poor utilisation of the active organic groups leads the polymeric materials with relatively low capacitance. The polymer-based electrodes contain a high theoretical capacity, but the irregular stacking of the polymer material hides the redox-active sites. Also, the poor conductivity of the organic electrode reduces the electron conducting, causing a large internal resistance.

1.4.2 Conjugated Ladder-Polymers as Electrode materials

Conjugated ladder polymers (cLPs) are a specific sub-type of ladder polymers where the fused rings in the backbone are π-conjugated. In addition, they are distinct from conventional conjugated polymers as the fused rings restrict the free rotation between the aromatic units within the backbone. In general, two distinct methods can be used to construct fully conjugated ladder polymers (**Figure 1.26a**).[117] One is single-step ladderization which constructs two strands of bonds simultaneously. The other approach relies on the post-polymerization process, which means the ladderization step happens when the side groups cyclize to form the fused rings. cLPs exhibit outstanding thermal and chemical stability. They possess strong π–π stacking interactions, fast intra-chain charge transport and long exciton diffusion length due to the loss of defects along

the fully coplanar backbones. In contrast to conventional conjugated polymers, cLPs maximize π-electron delocalization and are torsional defect-free, exhibiting a higher charge carrier mobility leading to better electronic performance (**Figure 1.26b**).[118]

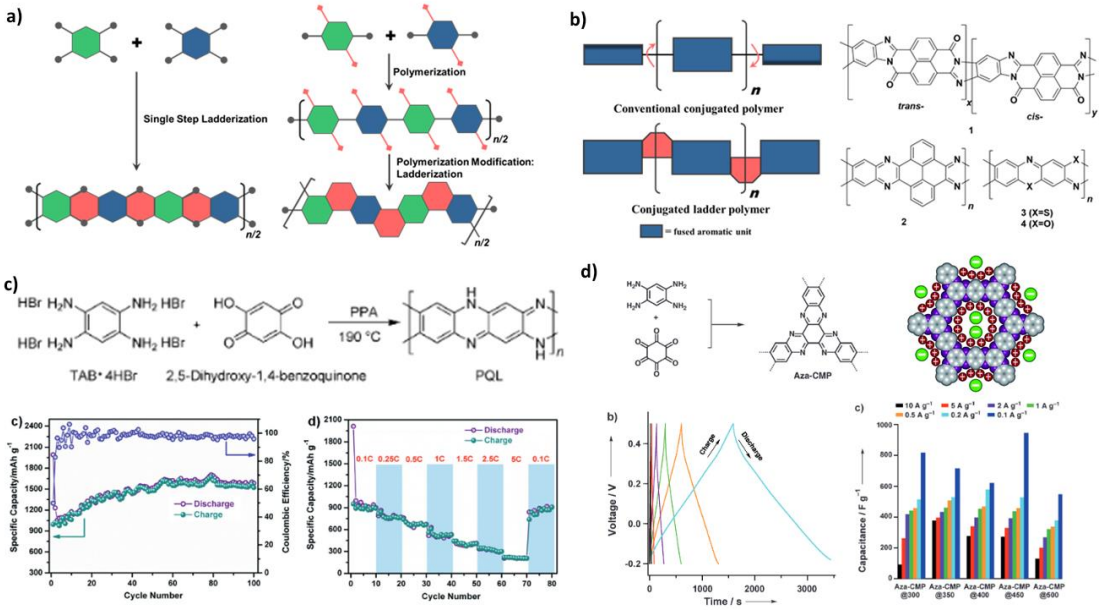

Figure 1.26 (a) Graphical synthetic approaches to construct cLPs: one-pot ladderization and post-ladderization. (b) Graphical representation of cLPs and conventional conjugated polymer with free torsional motions. (c) Synthesis and electrochemical performance of PQL-30 (d) Synthesis and electrochemical performance of Aza-CMP. (This figure is reprinted from ref. 117-120).

Qichun Zhang's group reported a ladder polymer with a large number of heteroatoms (N), serving as lithium-ion insertion sites (**Figure 1.26c**).[119] As the electrode material for a Li-ion battery, PQL-30 nanoparticles exhibited a larger capacitance of 1770 mAh g^{-1} at the charge rate of 0.05 C. The excellent electrochemical performances of cLPs promise their applications as excellent electrodes for LiBs.

When the cLPs form to a network, the larger surface area from porous structure can improve their performance as the electrode in supercapacitors. For instance, Donglin Jiang's group developed a ring-fused CMP for electric energy storage (**Figure 1.26d**).[120] Aza-CMP exhibits a high capacitance of 946 F g^{-1} at a current density of 0.1 A g^{-1}. The outstanding performance come from the structural features: (1) Conjugated fused CMP backbone, (2) Aza units in the skeletons has dipolar interaction with

electrolyte ions, (3) Optimized pore size that allow for fast ionic motion and (4) High surface areas for the formation of electric double layers.

1.4.3 Covalent Organic Frameworks as Electrode materials

As mentioned before, crystalline COFs are a kind of emerging porous organic materials with large surface areas and tunable chemical structures. Their structural tunability has enabled the development of COFs with redox-active building blocks, a suitable pore size, and a special pore environment, and is a promising direction for electrode materials in supercapacitors. Especially the 2D-COFs stacked by holy 2D nanosheets, which show a shorter pathway ion diffusion, more active surface, and open structures for faster electronic transport, compare to those non-porous materials (**Figure 1.27**).[121]

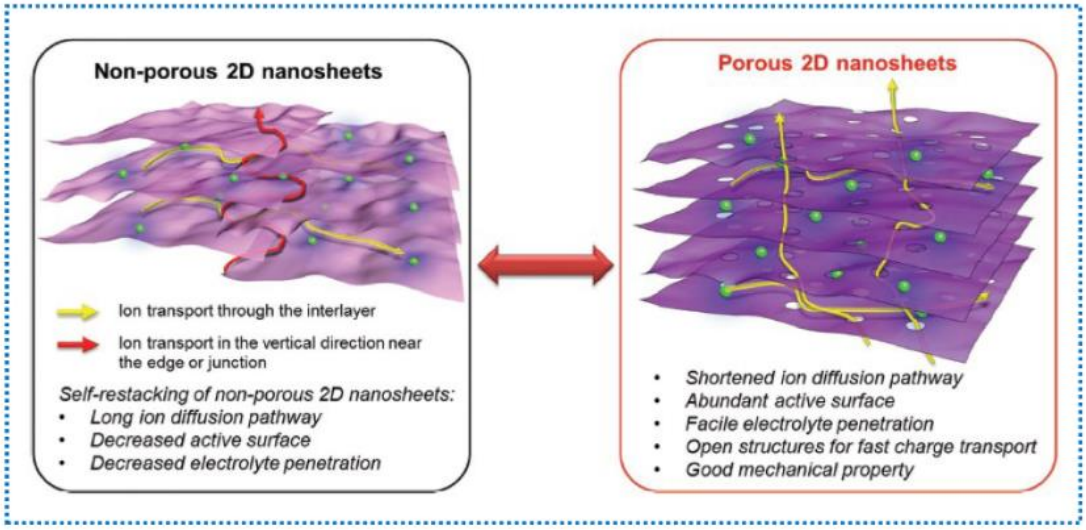

Figure 1.27 Advantages of porous 2D nanosheets for energy storage. (This figure is reprinted from ref. 121).

For example, 2, 2, 6, 6-Tetramethyl-1-piperidinyloxy (TEMPO), one of the electrochemical-active radical groups can be used as side groups, which endows the COFs with extra pseudocapacitive properties. As a general strategy, the TEMPO groups can be introduced by pore-surface engineering. Donglin Jiang's group used a click reaction as the post-modification to connect TEMPO on the pore walls of a porphyrin-based COFs ($[TEMPO]_x$-NiP-COFs). The $[TEMPO]_x$-NiP-COFs showed CV curves with a pair of redox peaks, which was come from the reversible switching of the neutral

TEMPO radical and its oxoammonium cation (**Figure 1.28a**).[122] The content of TEMPO could also be controlled by this method, and it was found that $[TEMPO]_{50\%}$-NiP-COFs showed the highest capacitance of 167 F g^{-1}, which is higher than many other redox-active MOFs. Furthermore, Bo Wang's group prepared exfoliated CONs and got better performance, indicating the exfoliation could be helpful for exposing more electrochemical-active sites for the enhanced capacitance (**Figure 1.28b**).[123]

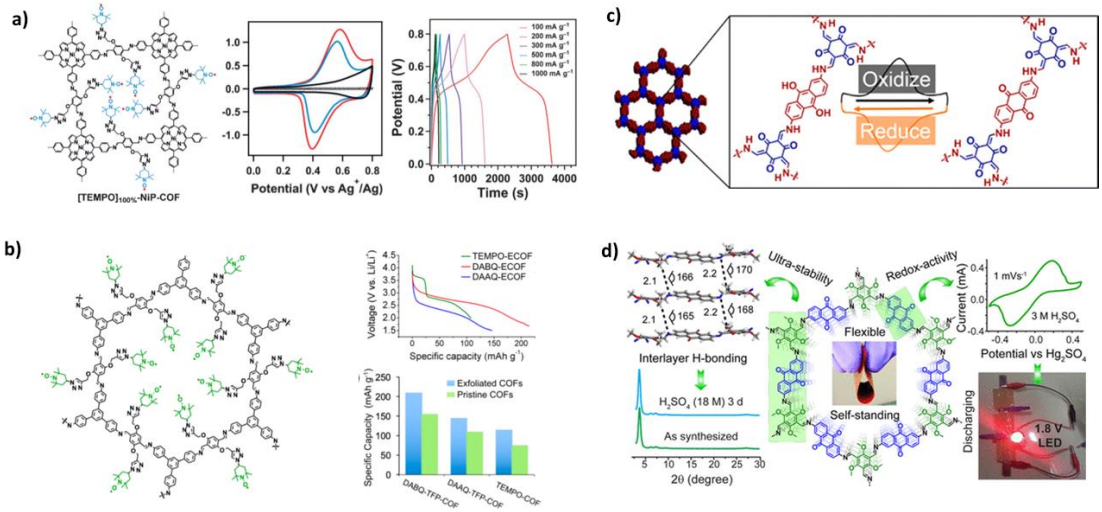

Figure 1.28 COFs for electrode materials: (a) 2D COFs with TEMPO as side groups. (b) Exfoliated CONs with TEMPO as side groups. (c-d) 2D COFs with anthraquinone as building blocks. (This figure is reprinted from ref. 122-125).

Also, anthraquinone and phenazine were used as the linkers to endow the COFs with pseudocapacity, respectively. William R. Dichtel's group introduced anthraquinone units into so called DAAQ-TFP COF in 2013 (**Figure 1.28c**).[124] Compared with the COF made by 9, 10-dihydroxyanthraquinone, DAAQ-TFP COF have a capacitance over 3 times larger with a stability over 5000 charge-discharge cycles. But owing to the random orient and poor conductivity, only 2.5% of electrochemical-active sites contributed to the capacitance. In 2018, Rahul Banerjee's group prepared a TpOMe-DAQ COF with both anthraquinone groups and intramolecular hydrogen bonds, which increased the distance between COF layers, and also endowed COF with high chemical stability (**Figure 1.28d**).[125] Thus, TpOMe-DAQ COF showed a higher capacitance of 169 F g^{-1} in the electrolyte of 3 M H_2SO_4 aqueous solution.

1.4.4 Opportunities and Challenges for COF-Based Electrode Materials

Over the past decades, lots of great works have been tried to explore the potential of COF materials for electrodes in energy storage devices for storing electricity, and COFs with redox-active sites show a promising performance so far.

However, the following issues should be solved for further development: 1) Enhancing the density of the exposed redox-active sites; 2) Increasing the electron conductivity for higher power density; 3) Balancing the density and porosity by structural optimization to utilize their pores and active sites efficiently; 4) High stability for widening potential windows, high temperature and various electrolytes, and also some theoretical studies need to be deeply investigated.

One of the efficient solutions to the issues (No. 1, 2, 4) above is to have a fully π-conjugated system connecting the redox sites. Conjugated ladder polymers have emerged as highly conductive polymers for energy storage applications with high charge carrier mobility due to their fully π-conjugated 2D aromatized skeletons. Based on that, we have designed a novel COF material that connected redox-active sites with pseudocapacitance properties through ladder-type connectivity for highly π-conjugated COF electrode materials with improved energy density and power density, which will be discussed in the **Chapter 2**.

1.5 Electrolytes in Lithium-Ion Batteries

1.5.1 Solid-State Electrolytes

The capacitance of LiBs is mainly determined by their electrode materials. High-performance LiBs therefore require the electrode materials with the properties of high capacity, good structural stability, high lithium-ion diffusion coefficient, long cycle life and low cost. However, the separator and electrolyte determine the stability and safety of LiBs. The first reason is that LiBs always suffer from the growth of lithium dendrites during cycling, and lithium dendrites can also puncture the separator and cause the volume expansion, leading to the poor electrochemical performance. Another reason is

the safety and pollution issues caused by the toxicity, leakage and explosions of organic liquid electrolytes.

To face with the increasing demands for various applications, all-solid-state-batteries (ASSBs) with solid-state electrolytes (SSEs) was considered as one of the most promising directions for the next generation batteries. As the instead of liquid electrolytes (LEs) to keep the devices with higher flexibility and higher safety, SSEs is certainly the key factor for the ASSBs, to which require for a broad potential window, low activation energy, high ion-conductivity and suitable mechanical strength. Thus, several parameters of SSEs from electrochemical testing are used for the evaluation: (1) Ionic conductivity (σ). The ionic conductivity is the most basic performance for SSEs and the value corresponds to the ability of SSEs to transport cations. (2) Lithium-ion transference number (t_{Li+}). Lithium-ion transference number affects whether there is a large concentration polarisation within the SSEs, effecting the performance of the batteries. (3) Potential window. For SSEs, the high electrochemical stability requires that they do not undergo reduction reactions at low potentials while do not undergo oxidation reactions at high potentials. This performance is usually tested using cyclic voltammetry (CV) and linear scanning voltammetry (LSV).

Based on the previous research, the challenges of solid-state batteries at this stage can be divided into the following areas: 1) Chemical stability. Chemical stability can be seen as the ability of materials for holding a stable interface before the charge-discharge process. 2) Electrochemical stability. Electrochemical stability is used to describe the changes in the battery material as well as the interface during the charge and discharge process. There is still decomposition of electrolytes and the continuous formation of inactive material at the interface at a high voltage. 3) Mechanical stability. Mechanical stability indicates the ability of solid-state electrolytes to avoid the remaining volume changes under an external force, which may be generated by the deformation of the electrode/electrolyte interface. The growth, cracking or crushing of lithium dendrite still exist during the cycling. 4) Thermal stability. Thermal stability means the ability to prevent the decomposition of electrolytes at high temperatures.

1.5.2 Polyethylene Glycol as Solid-State Electrolyte materials

Currently, there are two main categories of SSEs: Inorganic solid electrolytes (ISEs) and solid polymer electrolytes (SPEs). SPEs mainly contains a polymer matrix and lithium salts. The polymer matrixs have continuous polar groups such as -O-, =O, -S-, -N-, C=O or C=N, -P-, etc., which have the ability to dissolve lithium salts or form polymer-lithium salt complexes. The ideal polymer matrix for SPEs should have these basic standards: (1) Cation solvation properties. In order to facilitate salt dissociation, the interaction between polymer and cations must be strong enough (ensuring solubility of lithium salt through the cation solvation) but the lattice energy should be low enough (benefit for ion hopping from one coordination site to another); (2) Dielectric constant. The high dielectric constant of the polymeric body give rise to an effective charge separation of lithium salts, further leading to a high concentration of charge carriers. (3) Flexibility of the backbone. High flexibility of the backbone can reduce the energy barrier for bond rotation and promote segmental movement of the polymer chains. (4) High molecular weight. The polymer matrix also facilitates the processing of the SPE due to its good mechanical properties. Among all the SPEs, poly-(ethylene glycol) (PEG) is the most commonly used polymer matrix. In 1973, Wright and his colleagues first demonstrated that the composite of PEG and alkali metal salts could be used as an ionic conductor. Since then, SPEs containing a polymer matrix and lithium salts have attracted a great deal of attention as an important part of ASSBs.

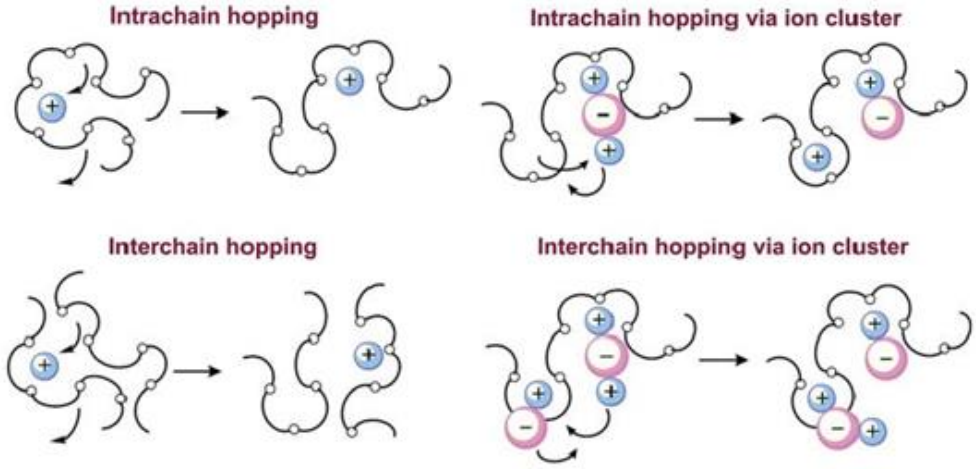

Figure 1.29 Mechanism of lithium transference in PEG-based SPE.

PEG can be used as one of the most prospective SPEs because it not only has a good processability and simple fabrication with large amount of industrial production but also has ethylene glycol chains to form Li-O bonds, which has a good compatibility with lithium salts as ion hopping sites to help the intermolecular transport of lithium ions. The properties of the lithium-ion conductivity in PEG derive from its specific molecular structure, where the EO unit is a good electron donor and PEG exhibits high chain flexibility. In the PEG matrix, Li^+ forms a coordination with the oxygen in the PEG chain, and during the Li-O bond continue breaks and forms, the successive rearrangement of segments allows a long-range transport of lithium (**Figure 1.29**).

It is worth noting that PEG is a semi-crystalline polymer and only amorphous region contribute to the lithium-ions transference. The glass transition temperature (T_g) of PEG is approximately 206 K, above which the proportion of amorphous phases may be higher than the crystalline state. When the temperature is under T_g, the limited free volume in numerous crystalline phases profoundly restrict the motion of lithium-ions. Therefore, PEG has a poor low lithium-ion conductivity, especially at room temperature, greatly limiting the application of PEG-based SPEs.

To address this issue, a series of methods have been developed including co-polymerization, cross-link, and preparation of composites with other polymers or plasticizers. Among all these methods, cross-link is an efficient strategy for the preventing the crystallinity of the ethylene glycol chains. Meanwhile, the mechanical strength as well as the thermal stability of the polymer electrolyte has been improved greatly.

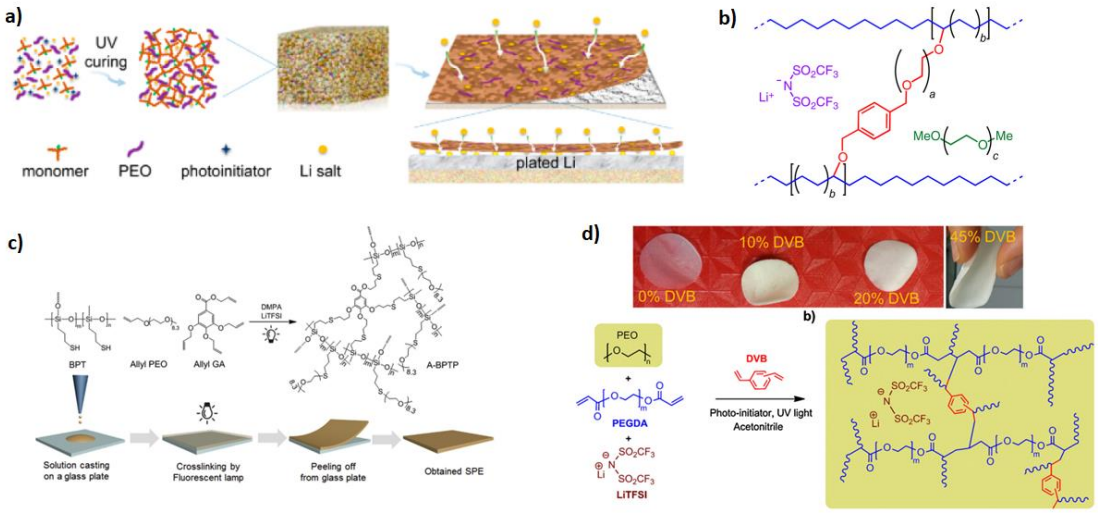

Figure 1.30 Examples for cross-linked PEG-based SPEs. (This figure is reprinted from ref. 126-129).

For the instance, Guo et al. prepared a cross-linked polymer of polyacrylate and PEG by photo-initiated polymerization (**Figure 1.30a**).[126] The cross-linked polymer had an interpenetrating cage structure in which PEG was bound, increasing the ionic conductivity to 2.2×10^{-4} S cm^{-1} with a high Young's modulus (12 GPa). In 2014, Coates et al. designed and prepared a polyethylene/PEO cross-linked SPE[127] (**Figure 1.30b**) that achieved an ionic conductivity of 1.0×10^{-4} S cm^{-1} at 25 °C with the addition of the plasticiser polyethylene glycol. This work also reveals that the suppression of Li-dendrites does not require an extremely high mechanical strength. However, the Li^+ transport in it needs to pass through nanoporous mesh PEG material, effectively reducing the formation of Li-dendrites. Lee et al. prepared another cross-linked SPE by photo-initiated polymerisation, which is shown in **Figure 1.30c**.[128] The electrolyte has an ionic conductivity of 4.0×10^{-4} S cm^{-1} at 60 °C with high thermal stability, and the electrolyte can withstand up to 250 °C without decomposition. In 2016, Armand et al. prepared a SPE by the cross-linking polyethylene glycol acrylate (PEGDA) with divinylbenzene (DVB) and blended it with PEG (**Figure 1.30d**).[129] DVB as the cross-linking agent effectively reduced the crystallinity of PEG, while the benzene rings in the DVB structure provided higher mechanical properties to the electrolyte film, and the ionic conductivity of the electrolyte reaches 1.0×10^{-4} S cm^{-1} at 70 °C.

These methods can improve the comprehensive performance of the modified PEG materials, especially the Li-ions conductivity at room temperature. Nevertheless, such amorphous cross-linked PEG networks still lack an oriented pathway for the diffusion of lithium ions, leading to unstable ion conductivity performance during a long-term cycling. Moreover, the heterogeneous status of amorphous electrolytes exhibits an unknown structure at the atomic level, interfering with the mechanism study of ion transport. Thus, the investigation of crystalline materials for efficient solid-state electrolytes is significant, and COFs can be a good candidate.

1.5.3 Covalent Organic Frameworks as Electrolyte materials

It is well-known that 2D-COFs are constructed by covalent bond-linked organic units in the plane while stacked by 2D layers to form the bulk 3D structure with oriented 1D nanochannels. Thus, compared to other typical solid-state conductors, COF-based SSEs can exhibit excellent ionic conductivity with a unique ion transfer mechanism after the precise designing with well-defined directed ion channels and continuous ion conduction sites.[130] The positive role of why COFs are considered as a kind of excellent SSEs can be defined into several aspects. The first advantage is the structure of COFs. COFs have insoluble backbones, supporting COF-based SSEs with high chemical, electrochemical and thermal stability. And these backbones are composed of light elements (C, H, N, O, B, etc.), which is important for improving the energy density. In addition, the rigid framework enables COFs to weaken the bad influence of low temperatures on ionic conductivity. Moreover, oriented 1D nanochannels of COFs can provide pathways for fast ion transference, thus reducing the ion diffusion energy barrier effectively. The second advantage comes from the tenability of COFs, leading to the simple introduction of functional groups from various building blocks and linkages, which endows COFs with specific functions for ionic conducting. These 1D nanochannels can interact with metal cations or anions or introduce host-guest systems to facilitate the dissociation of salts. Consequently, COF-based SSEs often have a high cation transfer number, reducing the adverse effects of concentration polarization. In addition to the good thermal and mechanical stability, low density, rich structural

tenability and high surface area with unique porosity, these abundant straight, continuous and aligned 1D nanochannels in 2D-COFs can promote ion transport due to the extended skeleton with ordered pore structure and stacking model. Based on the various building blocks and linkages used in COF chemistry, such 1D open nanochannels can be designed with satisfying pore shape and size, uniform distribution and tunable interface environment of the pore walls, leading to good compatibility with electrodes, low interface impedance and further high ion-conductivity. Also, COFs allow the post-modification with various functional groups onto their pore wall, providing chances for introducing functional groups.[131]

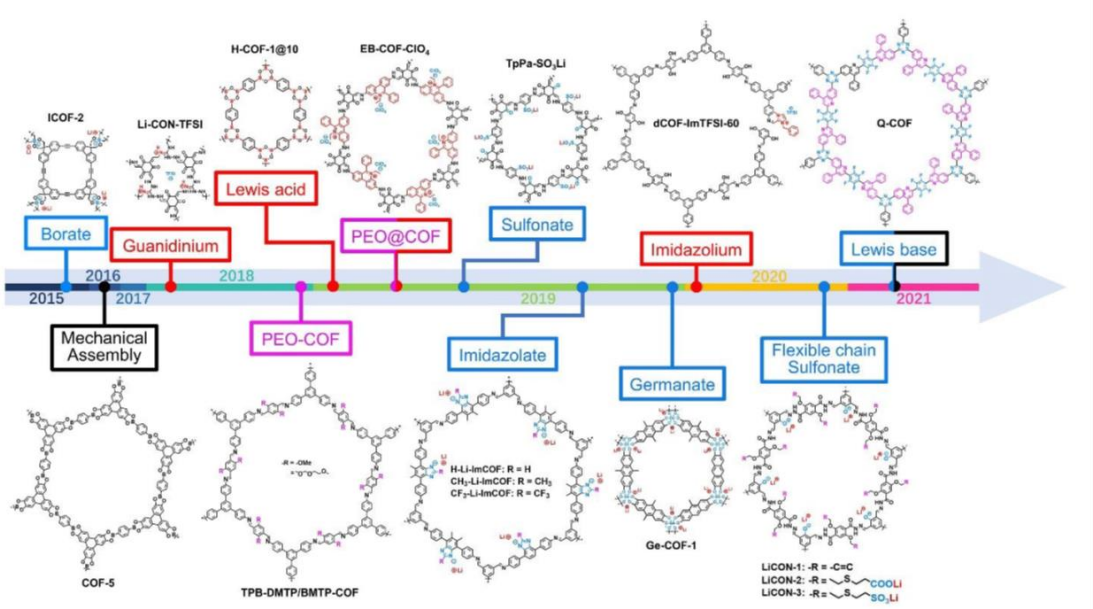

Figure 1.31 A brief chronology of the development of COF-based SSEs. The PEO@COF and PEO-COF represent the physical encapsulation and chemical anchoring of polymer chains in COFs pores, respectively. The black, purple, red and blue boxes indicate development of electroneutral, cationic (& Lewis acidic) and anionic (& Lewis basic) COF-based SSEs, respectively. (This figure is reprinted from ref. 132).

Recently, several works on COF-based polyelectrolytes have been reported, including ionic COFs (including cationic- and anionic-COFs) and COF/lithium-salt hybrid composites, showing a good potential in either proton conductivity in fuel cells or ion conductivity in batteries (**Figure 1.31**).[132] In 2018, Dongling Jiang's group reported the first example of electroneutral polyelectrolyte with oligo-(ethylene oxide) chains

grafted onto the channel walls and investigate it as SSE (**Figure 1.32a**).[133] Since that, Wei Zhang's group introduced imidazole units into COF linkers and the as-obtained anionic-COFs showed an outstanding Li-ions conductivity (7.2×10^{-3} S cm^{-1}) with low activation energy (0.10 eV), high Li-ions transference number (0.91), and wide potential window (4.5 V) (**Figure 1.32b**).[134] Liwei Chen prepared a guanidinium COF with a skeleton to split the Li salt ion anions through stronger dielectric screening and shield the Coulomb effect between ion pairs (**Figure 1.32c**).[135] Bo Wang's group reported the preparation of incorporating low-molecular-weight PEG into electroneutral-, anionic- and cationic-COFs and studied the Li-ions conductivity of different systems, which indicates that COFs hosted with non-electroneutral skeletons can be more conducive to enhancing Li-ion transport (**Figure 1.32d**).[136]

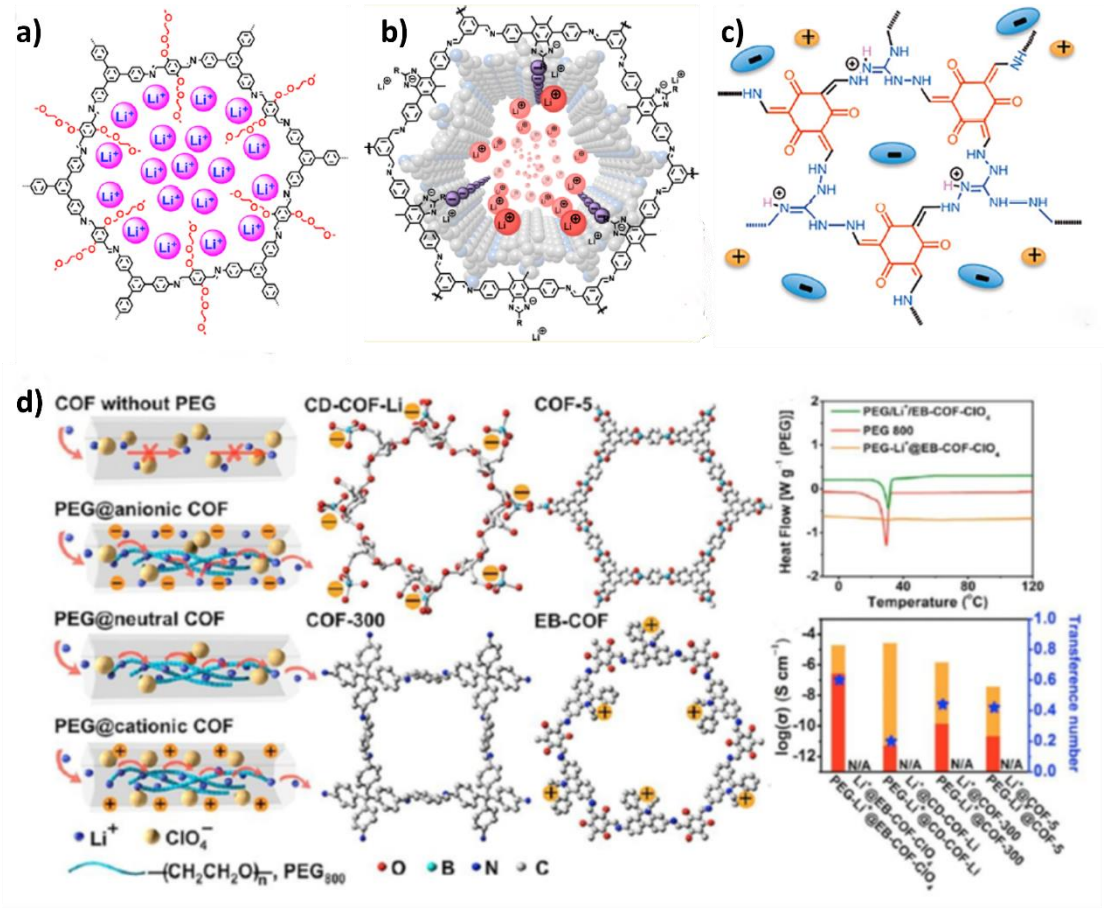

Figure 1.32 Examples for COF-based SSEs: (a) electroneutral-COF, (b) anionic-COF, (c) cationic-COF. (d) Schematic illustrations of the study of Li ion transport in different COF/ PEG systems. (This figure is reprinted from ref. 133-136).

1.5.4 Opportunities and Challenges for COF-Based Solid-State Electrolyte Materials

Though great progress has been achieved in the field of COF-based SSEs, several challenges in the research of both fundamentals and applications still require to be solved in the future. First of all, the mobile Li-ions in the nanochannels are concentrated at the position that is quite near pore walls of COFs, reducing the carrier density, which causes low ion conductivity, especially at room temperature. Also, ion transport in the COF electrolytes often has a large diffusion energy barrier, especially when the narrow nanochannel is designed for reducing cation transference number. In addition, the structure-property relationships are still unclear in the COF-based SSE system. Moreover, the enrichment of perpendicular nanochannels is beneficial for the Li-ions transport, but it's different for the COFs processing to get oriental pathways in the membranes at the macro level. Finally, most of the reported electrolyte-used COF materials are connected by imine or borate bonds, which are not stable enough during either SSEs preparation or electrochemical testing, which may have an unclear influence on the performance. Therefore, we have designed a series of novel COF-based SSEs to address the issues mentioned above, which will be discussed in the **Chapter 4**.

1.6 Covalent Organic Frameworks as Adsorbent for Metal Ions Uptake

Currently, water pollution is one of the environmental issues that need to be addressed. The main pollutants in water are heavy metal ions and organic pollutants. Unlike organic pollutants, heavy metal ions are not biodegradable and tend to accumulate in organisms, causing toxicity to most creatures. As one of the heavy metals, cadmium is not an essential element for humans. In general, excessive intake of cadmium can lead to cadmium poisoning in humans. When the water is polluted by cadmium, it can be enriched in organisms and enter the human body through the food chain, causing chronic poisoning. The biological half-life of cadmium is 10-30 years, and the bio-concentration effect is significant. Long-term intake of cadmium-containing water can

cause chronic kidney toxicity. Meanwhile, cadmium ions replace calcium ions in the bones, thus preventing the normal deposition of calcium on the bones and leading to chondromalacia.

Adsorption is a cost-effective treatment method for the removal of heavy metal ions from wastewater. It removes metal ions mainly through the interaction between the porous solid adsorbent and the metal ions, causing the adherence of metal ions to the surface of the porous adsorbent. It is a simple, cost-controllable and widely adaptable method, which is gradually gaining more and more attention. The adsorption and removal of heavy metal ions offers a great deal of flexibility in the design and operation of the adsorbent materials and adsorption equipment. In addition, the adsorption process is sometimes reversible, allowing for regeneration and reuse of the material.

In the last decades, COF-based adsorbents have received increasing attention due to their large specific surface area, adjustable surface chemistry, good mechanical rigidity, uniform pore size distribution and ease of regeneration.

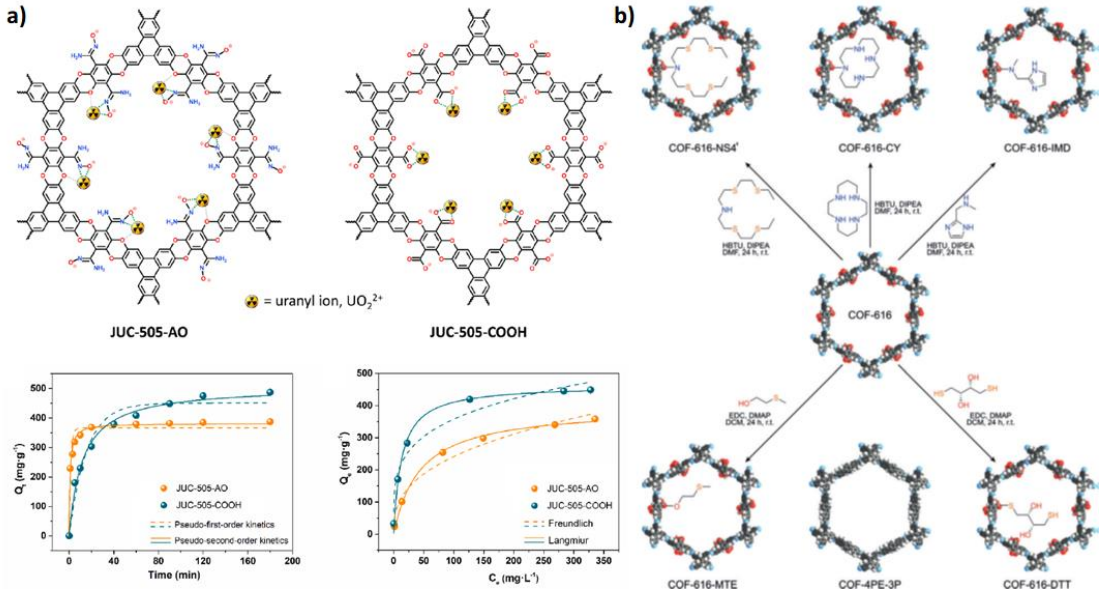

Figure 1.33 Examples for COF-based adsorbent materials: (a) JUC-505 family for selective uranium extraction, (b) COF-616 family for a series of metal ions removal. (This figure is reprinted from ref. 137-138)

To enhance the adsorption capacity of metal ions, modification of COF materials with the definite functional groups becomes an important method. The additional

introducing absorption process can be explained by the coordination bond, hydrogen bond, electrostatic interaction, chelation effect and ion exchange. Liu et al. prepared a COF with cyano-units (JUC-505) and further obtained the amidoxime and carboxyl functionalised COFs (JUC-505-AO and JUC-505-COOH)[137] by a simple hydrolysis. Both COFs showed a good performance of selective uranium extraction from aqueous solution with the maximum adsorption capacities of 395 mg g^{-1} and 464 mg g^{-1}, respectively (**Figure 1.33a**). Yaghi's group also reported a series of imine COFs (COF-616 family)[138] with different side groups by the post-synthetic modifications. With the high density of chelating groups anchored onto the backbone, these modified COF-616 can be utilized to remove different heavy metal ions (Pb^{2+}, Hg^{2+}, Cu^{2+}, Zn^{2+}) efficiently from water (**Figure 1.33b**).

Although COF-based adsorbents have many attractive properties, there are still some challenges that limit their wide usage:[139] 1) Traditional COFs made by reversible reactions have poor stability in water solution. Thus, the adsorption capacity can be diminished after the decomposion of the COF linkages. 2) The active-sites that grafted on the COFs cannot been fully used when COF layers stack closely. Thus, improving the stability of COF materials and expose more active-sites by exfoliation are important for the further designing of COF-based adsorbents, and our related works based on that will be discussed in the **Chapter 3**.

1.7 Characterization Techniques

1.7.1 Nuclear Magnetic Resonance

Nuclear Magnetic Resonance (NMR) is a quantum magnetic physics property based on the atomic scale. Nuclear spin and spin angular momentum are intrinsic features of a nucleus with an odd number of protons or neutrons. By applying a high magnetic field to the sample, devices frequently employ low temperature superconducting magnets to see atoms *via* NMR. Under the influence of the applied magnetic field, the magnetic fields of the nuclear spins themselves are re-organised, and the majority of the spins are in a low energy state. Applying an additional electromagnetic field to interfere with the

transfer of the low energy spins to a higher energy state, and then back to equilibrium to release the radio frequency, which is the NMR signal. This process can be used for molecular science research, such as molecular structure and dynamics.

Solid-state samples are the subject of investigation in the analytical method known as Solid-state nuclear magnetic resonance (ss-NMR). The rapid motion of molecules in liquid samples averages out the various interactions (such as chemical shift anisotropy and dipole-dipole interactions) that cause the NMR spectrum to broaden, resulting in a high-resolution liquid NMR spectrum; in contrast, the rapid motion of molecules in solid samples is constrained, and the presence of various interactions (such as chemical shift anisotropy) causes the spectrum to broaden severely, limiting the resolution of the solid NMR technique. As a result, ss-NMR method have lesser resolution than liquid NMR techniques.

Cross Polarization (CP) and Magic Angle Spinning (MAS) are two key method of ss-NMR. The former can greatly enhance the signal from ^{13}C through a cross-polarization from abundant nucleus (such as ^{1}H) to dilute nucleus (such as ^{13}C). In MAS technique, high-speed rotation of the sample tube is performed about an axis that forms a magical angle (54.7°) with the major nuclear field. To attain high resolution in solid nuclear magnetic spectra, the MAS efficiently averages out the numerous anisotropic interactions. The range of rotating speeds is 0-80 kHz.

1.7.2 Powder X-ray Diffraction

PXRD is a measurement that is used to ascertain whether a material has a crystalline or defective structure. If the wavelength of the radiation is similar to the distance between the lattice stripes, the sample is exposed to X-rays and scatters in a specular manner. When the angle of incidence and the angle of scattering are identical, and the path lengths of the two waves are an integer multiple of the wavelengths, constructive interference between the waves that are scattered from the crystalline material can occur. This is based on Bragg's Law ($2d \sin \theta = n\lambda$, where d is distance, n is a positive integer,

and λ is the wavelength of the incident wave), which describes the condition on the scattering angle (θ) for constructive interference to be at its strongest.[140]

1.7.3 Thermogravimetric Analysis

Thermogravimetric Analysis (TGA) calculates sample mass as temperature rises over time. Phase changes or breakdown can be learned from the measurement. You may utilise a number of gases, including air and N_2. TGA may be used to assess the degree of carbonisation at various temperatures when operating in the N_2 environment.

1.7.4 Elemental Analysis

Elemental analysis can be used to determine the elemental composition (carbon, hydrogen, nitrogen, and sulfur elements) of the organic samples quantitively. This is performed by burning the sample in an excess of oxygen and collecting the complete combustion products: CO_2, H_2O, NO_x, and SO_2, with the masses used to calculate the composition of the sample.

1.7.5 Fourier-transform Infrared Spectroscopy

Fourier-transform infrared spectroscopy (FT-IR) is a technique used to analyse the chemical structure of samples by obtaining infrared absorption and emission spectra of solids, liquids or gases. FT-IR can identify the chemical bonds and functional groups contained in organic molecules based on the location, types and intensity of characteristic absorption peaks.

1.7.6 Raman Spectroscopy

Raman spectroscopy provides structural information of samples by observing the vibrational, rotational, and other low-frequency modes. This is performed by illuminating a sample with a laser beam. The laser beam interacts with the various nodes in the system, resulting in the shift of the energy of the laser photons, giving information about the vibrational modes. For carbon or organic materials, the disordered (*D*) and graphitic (*G*) bands can be monitored at ~1350 cm^{-1} and ~1590 cm^{-1}, respectively. The *2D* band at ~2650 cm^{-1} is usually observed in materials with a few layers.[141]

1.7.7 X-ray Photoelectron Spectroscopy

X-ray Photoelectron Spectroscopy (XPS) is a technique that measures the surface elemental composition and electronic state of the elements in a material. This is performed by irradiating a material with X-rays and simultaneously measuring the kinetic energy and number of electrons that escape from the depth of 0 to 10 nm from the surface of the material. Peaks from a single element can then be quantified and partitioned into different bonding states using a table of binding energies, allowing the environment of the element to be probed within the material. Compared to elemental analysis, XPS has advantages of quantifying oxygen and metal contents.

1.7.8 Scanning Electron Microscopy

Scanning Electron Microscopy (SEM) is used to investigate the surface morphology of materials by a focused electron beam. An electron beam is accelerated and focused onto the surface of samples and the reflected electrons are detected for the output of image information. By scanning the electron beam and detecting the variation of the number of reflected electrons, morphology can be constructed. The measurement requires the sample to be conductive because the non-conductive sample collects charge from the electron beam which causes image artefacts to appear. Thus, organic samples usually need to be coated with an ultrathin layer of an electrically conductive metal (such as gold) by low-vacuum sputter coating.

1.7.9 Transmission Electron Microscopy

Transmission Electron Microscopy (TEM) is used to investigate the structure of samples by transmitting a beam of electrons through the samples. The electron beam passes through and have the interaction with the sample to form an image. The energy of the electron beam of TEM is much larger than SEM due to collecting the beam transmits through the samples and thus the samples usually need to be thin enough.

1.7.10 Inductively Coupled Plasma Optical Emission Spectroscopy

ICP-OES is used to detect the content of metal ions. An inductively coupled plasma is used to produce excited atoms and ions from the sample that emits electromagnetic radiation at characteristic wavelengths to a particular metal element. The concentration of the metal elements can also be determined by the intensity of the emissions.

1.7.11 Gas Adsorption

Adsorption is defined as the enrichment of molecules, atoms, or ions in the vicinity of an interface. There are two types of adsorption: physisorption and chemisorption. Physisorption means gas is brought into contact with a surface of adsorbent through attractive intermolecular forces (van der Waals), which is a physical process.[1] Other molecular interactions, like polarisation, can also adjust geometric and electronic properties of the gas and the surface of adsorbent, changing the behaviour of adsorption.

Gas adsorption measurements are used to characterise the porous properties of materials, including surface area, pore size distribution and pore volume. The characterisation method is used to measure the adsorption of supercritical gases or various subcritical fluids (*e.g.*, N_2 at 77 K, CO_2 at 273 K and H_2 at 77 K). Modelling simulation have been developed, such as density functional theory (DFT) and Monte-Carlo simulations, which allows more accurate porosity structural analysis from the adsorption isotherm, which has relationship between the amount of gas adsorbed and the equilibrium pressure of the gas at constant temperature.[1]

Adsorption processes of micropores always take place at low relative pressures, the extent of which depends on the size of the gas molecules, the shape of the micropores and the interaction between them. Adsorption in mesopores happens through multiple stages. Monolayer adsorption initially happens where all the gas molecules are in contact with the surface to form a single gas molecular layer. Then multilayer adsorption occurs where the gas is continue filled in and in contact with the single gas molecular layer that formed before. This is followed by capillary condensation, where

the gas changes to a liquid-like phase in the pores at a pressure less than the saturation pressure (P/P_0 = 0.5) of the bulk liquid.[1]

The analysis of pore sizes across the micropore and mesopore range requires experiments that span over a wide range of pressures starting below 1 Pa. Thus, gas sorption is usually carried out with special instruments in the relative pressure range $10^{-7} \leq P/P_0 \leq 1$, which ensures the sample tube and manifold can be evacuated to very low pressures.[1] The amount of un-adsorbed gas in the effective void volume (dead space) should also be tested. This can be achieved by using a non-adsorbing gas such as helium to measure the dead space under the operating conditions. Before the gas adsorption measurement, the samples should be degassed to remove all impurities to improve the accuracy of the test.

There are two major models used to describe the adsorption process: the Langmuir model and the Brunauer-Emmett-Teller (BET) model.[142] The Langmuir model is a simple model, which explains the monolayer adsorption by assuming the adsorbate behaves as an ideal gas under isothermal conditions. The BET model is an extension of the Langmuir model which considers the situation of multilayer adsorption, and has a theoretical foundation based on three assumptions: 1) Gas molecules can be absorbed onto a solid in numerous layers. 2) There is no interaction between the adsorbed layers. 3) Langmuir's theory of adsorption holds for each monolayer. The BET equation form is:

$$1/\{v\times[(P_0/P)\text{-}1]\} = (c\text{-}1)/(v_m\times c)\times(P/P_0)+1/(v_m\times c)$$

where c is the BET constant, defined as:

$$c = \exp\{(E_1-E_L)/RT)\}$$

where E_1 is the heat of adsorption for the first layer and E_L is the heat of adsorption for the rest multilayers.

The BET method is the most widely used procedure for evaluating the surface areas, but it still has some weaknesses based on its theoretical foundations. BET theory

assumes the surface is homogeneous, thus differences between the surface and lateral adsorbate-adsorbate interactions are ignored. Therefore, high energy sites will be occupied at lower relative pressures, resulting in nonlinearity of BET plots at $P/P_0 <$ 0.5. Also, BET theory has its suitable relative pressure range from 0.05 to 0.35. This is because the pressure is too low to establish a multilayer or even monolayer physisorption equilibrium when the relative pressure is less than 0.05, while when the relative pressure is larger than 0.35, the multilayer physisorption equilibrium can be disrupted by the significant capillary condensation. And this range is also suitable for two criteria that Rouquerol suggested, namely, c must be positive and theusage of the BET equation must be limited to the range where the term $v(1-P/P_0)$ increases with the relative pressure continuously.[142]

1.7.12 Electrochemical Measurements

1.7.12.1 Cyclic Voltammetry

Cyclic voltammetry (CV) can be used for the understanding of charge transfer mechanisms and is an important experimental criterion for quantifying the electrochemical performance of active materials. The CV curves depend on a variety of parameters such as scan rate, temperature, electrodes, and electrolytes.[143]

Potential windows are chosen to avoid irreversible electrode and electrolyte reactions, such as solvent decomposition and irreversible redox reactions on the electrodes. This avoids over-oxidation and/or over-reduction so that we only record current from the capacitive potential range of the material.

The specific capacitance (C_{sv}) of a material can be calculated by CV using the following equation:

$$\mathcal{C}_{sv} = (q_a + q_c) / (2ms \times \Delta V)$$

where q_a and q_c represents the anodic and cathodic charge integrated from the positive and negative sweeps of the CV, m is the mass loading of active material, s is the potential scan rate and ΔV corresponds to the potential window.

1.7.12.2 Galvanostatic charge-discharge

Galvanostatic charge-discharge (GCD) applies a constant current to charge or discharge to evaluate the rate of potential increase (charging) or decrease (discharging). A triangular charge-discharge shape is the typical behaviour for constant charge and discharge of supercapacitive materials with good reversibility while battery and pseudocapacitor have specific platforms which is come from the redox reactions.[144]

The specific capacitance (C_{sc}) of a material can be calculated by GCD using the following equation:

$$C_{sc} = (I \times t)/(V \times m)$$

where I is the discharge current, t is discharge time, V is the discharge voltage, and m is the mass loading of active material.

Coulombic efficiency is used to evaluate the efficiency of discharge of the device when a certain charge has been transferred into a system through an electrochemical reaction. Coulombic efficiency normally decreases when undesirable side reactions occur. Coulombic efficiency of a system can be calculated from GCD curves using the following equation:

$$\eta = t_d/t_c \times 100\%$$

where t_d is the discharge time and t_c is the charge time.

1.7.12.3 Electrochemical impedance spectroscopy

In order to perform electrochemical impedance spectroscopy (EIS), an alternating current electrode is used. A tiny amplitude alternating signal is applied, and the electrode's return to its stationary state is then observed.[145] The ESR, which contains multiple components including the resistance of the electrolyte and active material as well as the interface resistance of active material/ current collector, is revealed by the real part of the impedance at a given frequency. The Nyquist plot of an energy storage device typically contains a semi-circle and then a vertical step towards Z". The plot

gives information about the solution resistance (R_s) and the charge transfer resistance (R_{ct}).

R_s is related to the bulk solution resistance which depends on the conductivity of the electrolyte. R_{ct} can be divided into components for electrical and ionic resistance. The electronic resistance is a result of the interaction between the active material and the current collector as well as the intrinsic electronic conductivity of the carbon particles. Ionic resistance, which depends on the conductivity of the electrolyte, the material's porous structure, and the thickness of the active material, is the resistance of the electrolyte within the pores of the electrode. The interfacial charge-transfer resistance and dispersed capacitance are very minimal, suggesting good capacitive responses, if the semicircle is tiny, imperfect, or absent. The internal resistance (R_{int}) of the device can be estimated from the intersection between the low frequency section crossing the X-axis and the region immediately after the semicircle.

1.8 Project Overview

The core aim of this project is to synthesize a series of novel fused-ring-linked COFs with high conjugation for energy and environmental applications; specifically, fluorindine-linked COF for supercapacitive energy storage (**Chapter 2**), exfoliated quinoline-linked COF for heavy metal removal (**Chapter 3**), and imidazole-linked COF for solid-state electrolytes (**Chapter 4**).

As discussed above, crystalline COFs have some unique properties that are different from either linear polymers or amorphous porous organic polymer and can be well-designed for energy and environmental applications. The good combination of crystallinity and porosity endows COFs with abundant, periodical aligned homogeneous pores and the corresponding tunnels, leading to an excellent host system for the adsorption, transport, separation of specific guest molecules, and thus COFs show a great potential in heavy metal uptake or ion conductive. Also, the good tunability of COFs allow a target molecular design for the linkers and linkages or a further post-modification based on the side chains or pore engineering, endowing COFs

with various functionalities for photo- or electro-based applications like energy storage and conversion. However, several key issues have still constrained the development of the further COF research: (1) Most reported COFs with known linkages are typical organic materials with a poor conductivity, limiting the usage for application based on electrochemical properties. (2) Most reported COFs with known linkages are usually obtained in the form of insoluble bulk powder, which has a poor processability to limit the further usage in many for practical applications. (3) Most reported COFs with known linkages show poor stability for a further post-modification, which restricts the diversity and functionality of COF materials. To address the above issues, designing and synthesis of crystalline COFs with novel linkages hold great promise to the further fundamental and application studies for COF research in the future.

Introducing redox-active sites into COF materials can efficiently improve the energy density of electrodes for supercapacitive energy storage. However, most of these redox-active sites are introduced to the linkers or side chains in the pores of COFs and connected to the skeleton by single bonds. The poor conductivity limits the electronic transport, leading to a low power density. Thus, we want to design a novel conjugated linkage of COFs according to the concept of ladder polymers. The reaction for COF synthesis contains an initial reversible step and a following irreversible cyclization to confirm the formation of framework and good conjugation and stability. Moreover, this novel linkage can combine the redox-site and ladder structure to improve the energy density and power density, respectively, which is helpful for the performance as the electrode material in supercapacitiors. This work will be discussed in **Chapter 2**.

Preparing the thinner CONs exfoliated from bulk COF powders enhances the dispersibility of materials in common solvents, improving the processability and usability of COF materials. However, the most reported COFs focus on the imine-linkage, which is not stable in most of exfoliation conditions. Thus, we want to design a novel linkage with a much more stable structure and active site to further attract ions, leading to a charge repulsion for the exfoliation. On the other hand, based on the previous work in **Chapter 2**, cyclization-containing multiple-steps reaction can

improve the stability and conjugation of COFs, but it can also reduce the crystallinity of COFs. So that the method for novel COF synthesis we selected here is a multicomponent reaction. The method similar with Hummers' method was be used for the exfoliation of COFs and the heavy metal uptake properties of the exfoliated CONs were investigated. This work will be discussed in **Chapter 3**.

The oriented 1D nanochannels stacked by the regular pores in 2D-COFs are benefit to support pathways for fast ion-transport. However, most known linkages don't have reactive sites and enough stability for a post-modification, which can be designed to increase the concentration of target ions for SSEs. Here we want to design a novel linkage that is stable enough and has sites for a further anchoring of oligomer chains to accelerate the ion conduction. By combining the advantages of both COFs and linear polymers, COF can inhibit the crystallization of oligomer chains while oligomer chains can improve ionic concentration and conduction in the COF nanochannels. The full battery tests based on this well-designed COF SSE were also investigated. This work will be discussed in **Chapter 4**.

1.9 References

1. Thommes, M.; Kaneko, K.; Neimark, A. V.; Olivier, J. P.; Rodriguez-Reinoso, F.; Rouquerol, J.; Sing, K. S., Physisorption of gases, with special reference to the evaluation of surface area and pore size distribution (IUPAC Technical Report). *Pure Appl. Chem.* **2015,** *87* (9-10), 1051-1069.
2. Zaworotko, M. J., Nanoporous structures by design. *Angew. Chem., Int. Ed.* **2000,** *39* (17), 3052-3054.
3. Barbour, L. J., Crystal porosity and the burden of proof. *Chem. Comm.* **2006,** (11), 1163-1168.
4. Slater, A. G.; Cooper, A. I., Function-led design of new porous materials. *Science* **2015,** *348* (6238).
5. Dawson, R.; Cooper, A. I.; Adams, D. J., Nanoporous organic polymer networks. *Prog. Polym. Sci.* **2012,** *37* (4), 530-563.

6. Chaoui, N.; Trunk, M.; Dawson, R.; Schmidt, J.; Thomas, A., Trends and challenges for microporous polymers. *Chem Soc Rev.* **2017,** *46* (11), 3302-3321.

7. Tao, Y.; Kanoh, H.; Abrams, L.; Kaneko, K., Mesopore-modified zeolites: preparation, characterization, and applications. *Chem. Rev.* **2006,** *106* (3), 896-910.

8. Kondo, M.; Yoshitomi, T.; Matsuzaka, H.; Kitagawa, S.; Seki, K., Three-Dimensional Framework with Channeling Cavities for Small Molecules:{[M2 (4, 4′-bpy) 3 (NO3) 4]· xH2O} n (M= Co, Ni, Zn). *Angew. Chem., Int. Ed.* **1997,** *36* (16), 1725-1727.

9. Long, J. R.; Yaghi, O. M., The pervasive chemistry of metal–organic frameworks. *Chem Soc Rev.* **2009,** *38* (5), 1213-1214.

10. O'Keeffe, M., Design of MOFs and intellectual content in reticular chemistry: a personal view. *Chem Soc Rev.* **2009,** *38* (5), 1215-1217.

11. Furukawa, H.; Cordova, K. E.; O'Keeffe, M.; Yaghi, O. M., The chemistry and applications of metal-organic frameworks. *Science* **2013,** *341* (6149), 1230444.

12. Lee, J. S. M.; Cooper, A. I., Advances in Conjugated Microporous Polymers. *Chem. Rev.* **2020,** *120* (4), 2171-2214.

13. Tian, J.; Thallapally, P. K.; McGrail, B. P., Porous organic molecular materials. *CrystEngComm* **2012,** *14* (6), 1909-1919.

14. Zhang, G.; Presly, O.; White, F.; Oppel, I. M.; Mastalerz, M., A permanent mesoporous organic cage with an exceptionally high surface area. *Angew. Chem., Int. Ed.* **2014,** *53* (6), 1516-1520.

15. Zhang, G.; Mastalerz, M., Organic cage compounds–from shape-persistency to function. *Chem Soc Rev.* **2014,** *43* (6), 1934-1947.

16. McKeown, N. B.; Makhseed, S.; Budd, P. M., Phthalocyanine-based nanoporous network polymers. *Chem. Comm.* **2002,** (23), 2780-2781.

17. Jiang, J. X.; Su, F.; Trewin, A.; Wood, C. D.; Campbell, N. L.; Niu, H.; Dickinson, C.; Ganin, A. Y.; Rosseinsky, M. J.; Khimyak, Y. Z., Conjugated microporous poly (aryleneethynylene) networks. *Angew. Chem., Int. Ed.* **2007,** *46*, 8574-8578.

18. Ben, T.; Qiu, S., Porous aromatic frameworks: Synthesis, structure and functions. *CrystEngComm* **2013,** *15* (1), 17-26.

19. Xu, S.; Luo, Y.; Tan, B., Recent development of hypercrosslinked microporous organic polymers. *Macromol Rapid Commun.* **2013,** *34* (6), 471-484.

20. Feng, X.; Ding, X.; Jiang, D., Covalent organic frameworks. *Chem Soc Rev.* **2012,** *41* (18), 6010-6022.

21. McKeown, N. B.; Budd, P. M., Polymers of intrinsic microporosity (PIMs): organic materials for membrane separations, heterogeneous catalysis and hydrogen storage. *Chem Soc Rev.* **2006,** *35* (8), 675-683.

22. Li, B.; Gong, R.; Wang, W.; Huang, X.; Zhang, W.; Li, H.; Hu, C.; Tan, B., A new strategy to microporous polymers: knitting rigid aromatic building blocks by external cross-linker. *Macromolecules* **2011,** *44* (8), 2410-2414.

23. Ben, T.; Ren, H.; Ma, S.; Cao, D.; Lan, J.; Jing, X.; Wang, W.; Xu, J.; Deng, F.; Simmons, J. M., Targeted synthesis of a porous aromatic framework with high stability and exceptionally high surface area. *Angew. Chem., Int. Ed.* **2009,** *48* (50), 9457-9460.

24. Vilela, F.; Zhang, K.; Antonietti, M., Conjugated porous polymers for energy applications. *Energy Environ. Sci.* **2012,** *5* (7), 7819-7832.

25. Ivanovskii, A., Graphynes and graphdyines. *Prog. Solid. State Ch.* **2013,** *41* (1-2), 1-19.

26. Ren, S.; Bojdys, M. J.; Dawson, R.; Laybourn, A.; Khimyak, Y. Z.; Adams, D. J.; Cooper, A. I., Porous, fluorescent, covalent triazine-based frameworks via room-temperature and microwave-assisted synthesis. *Adv. Mater.* **2012,** *24* (17), 2357-2361.

27. Wang, K.; Yang, L. M.; Wang, X.; Guo, L.; Cheng, G.; Zhang, C.; Jin, S.; Tan, B.; Cooper, A., Covalent triazine frameworks via a low-temperature polycondensation approach. *Angew. Chem., Int. Ed.* **2017,** *56* (45), 14149-14153.

28. Geng, K. Y.; He, T.; Liu, R. Y.; Dalapati, S.; Tan, K. T.; Li, Z. P.; Tao, S. S.; Gong, Y. F.; Jiang, Q. H.; Jiang, D. L., Covalent Organic Frameworks: Design, Synthesis, and Functions. *Chem. Rev.* **2020,** *120* (16), 8814-8933.

29. Liu, Y.; Ma, Y.; Zhao, Y.; Sun, X.; Gándara, F.; Furukawa, H.; Liu, Z.; Zhu, H.; Zhu, C.; Suenaga, K., Weaving of organic threads into a crystalline covalent organic framework. *Science* **2016,** *351* (6271), 365-369.

30. Rowan, S. J.; Cantrill, S. J.; Cousins, G. R.; Sanders, J. K.; Stoddart, J. F., Dynamic covalent chemistry. *Angew. Chem., Int. Ed.* **2002,** *41* (6), 898-952.

31. Diercks, C. S.; Yaghi, O. M., The atom, the molecule, and the covalent organic framework. *Science* **2017,** *355* (6328), eaal1585.

32. Li, Y. S.; Chen, W. B.; Xing, G. L.; Jiang, D. L.; Chen, L., New synthetic strategies toward covalent organic frameworks. *Chem Soc Rev.* **2020,** *49* (10), 2852-2868.

33. Haase, F.; Lotsch, B. V., Solving the COF trilemma: towards crystalline, stable and functional covalent organic frameworks. *Chem Soc Rev.* **2020,** *49* (23), 8469-8500.

34. Corbett, P. T.; Leclaire, J.; Vial, L.; West, K. R.; Wietor, J.-L.; Sanders, J. K.; Otto, S., Dynamic combinatorial chemistry. *Chem. Rev.* **2006,** *106* (9), 3652-3711.

35. Lehn, J.-M.; Eliseev, A. V., Dynamic combinatorial chemistry. *Science* **2001,** *291* (5512), 2331-2332.

36. Ding, S.-Y.; Wang, W., Covalent organic frameworks (COFs): from design to applications. *Chem Soc Rev.* **2013,** *42* (2), 548-568.

37. Zhang, B.; Wei, M.; Mao, H.; Pei, X.; Alshmimri, S. A.; Reimer, J. A.; Yaghi, O. M., Crystalline dioxin-linked covalent organic frameworks from irreversible reactions. *J. Am. Chem. Soc.* **2018,** *140* (40), 12715-12719.

38. Xiong, Z.; Sun, B.; Zou, H.; Wang, R.; Fang, Q.; Zhang, Z.; Qiu, S., Amorphous-to-Crystalline Transformation: General Synthesis of Hollow Structured Covalent Organic Frameworks with High Crystallinity. *J. Am. Chem. Soc.* **2022,** *144* (14), 6583-6593.

39. Li, Z.; Ding, X.; Feng, Y.; Feng, W.; Han, B.-H., Structural and dimensional transformations between covalent organic frameworks via linker exchange. *Macromolecules* **2019,** *52* (3), 1257-1265.

40. Liu, R. Y.; Tan, K. T.; Gong, Y. F.; Chen, Y. Z.; Li, Z. E.; Xie, S. L.; He, T.; Lu, Z.; Yang, H.; Jiang, D. L., Covalent organic frameworks: an ideal platform for designing ordered materials and advanced applications. *Chem Soc Rev.* **2021,** *50* (1), 120-242.

41. Maschita, J.; Banerjee, T.; Savasci, G.; Haase, F.; Ochsenfeld, C.; Lotsch, B. V., Ionothermal Synthesis of Imide-Linked Covalent Organic Frameworks. *Angew. Chem., Int. Ed.* **2020,** *59* (36), 15750-15758.

42. Campbell, N. L.; Clowes, R.; Ritchie, L. K.; Cooper, A. I., Rapid microwave synthesis and purification of porous covalent organic frameworks. *Chem. Mater.* **2009,** *21* (2), 204-206.

43. Gan, S.-X.; Jia, C.; Qi, Q.-Y.; Zhao, X., A facile and scalable synthetic method for covalent organic nanosheets: ultrasonic polycondensation and photocatalytic degradation of organic pollutants. *Chem. Sci.* **2022**, *13*, 1009-1015.

44. Biswal, B. P.; Chandra, S.; Kandambeth, S.; Lukose, B.; Heine, T.; Banerjee, R., Mechanochemical synthesis of chemically stable isoreticular covalent organic frameworks. *J. Am. Chem. Soc.* **2013,** *135* (14), 5328-5331.

45. Matsumoto, M.; Dasari, R. R.; Ji, W.; Feriante, C. H.; Parker, T. C.; Marder, S. R.; Dichtel, W. R., Rapid, low temperature formation of imine-linked covalent organic frameworks catalyzed by metal triflates. *J. Am. Chem. Soc.* **2017,** *139* (14), 4999-5002.

46. Cai, S. L.; Zhang, W. G.; Zuckermann, R. N.; Li, Z. T.; Zhao, X.; Liu, Y., The organic flatland—Recent advances in synthetic 2D organic layers. *Adv. Mater.* **2015,** *27* (38), 5762-5770.

47. Fang, X.; Zhao, X.; Fang, W.; Chen, C.; Zheng, N., Self-templating synthesis of hollow mesoporous silica and their applications in catalysis and drug delivery. *Nanoscale* **2013,** *5* (6), 2205-2218.

48. Shen, Q.; Gao, H.-Y.; Fuchs, H., Frontiers of on-surface synthesis: from principles to applications. *Nano Today* **2017,** *13*, 77-96.

49. Liu, W.; Luo, X.; Bao, Y.; Liu, Y. P.; Ning, G.-H.; Abdelwahab, I.; Li, L.; Nai, C. T.; Hu, Z. G.; Zhao, D., A two-dimensional conjugated aromatic polymer via C–C coupling reaction. *Nat. Chem.* **2017,** *9* (6), 563-570.

50. Wang, C.-X.; Chen, J.-L.; Shu, C.-H.; Shi, K.-J.; Liu, P.-N., On-surface synthesis of 2D COFs on Cu (111) via the formation of thermodynamically stable organometallic networks as the template. *Phys. Chem. Chem. Phys.* **2019,** *21* (24), 13222-13229.

51. Khan, N. A.; Zhang, R.; Wu, H.; Shen, J.; Yuan, J.; Fan, C.; Cao, L.; Olson, M. A.; Jiang, Z., Solid–vapor interface engineered covalent organic framework membranes for molecular separation. *J. Am. Chem. Soc.* **2020,** *142* (31), 13450-13458.

52. Zhou, D.; Tan, X.; Wu, H.; Tian, L.; Li, M., Synthesis of C− C Bonded Two-Dimensional Conjugated Covalent Organic Framework Films by Suzuki Polymerization on a Liquid–Liquid Interface. *Angew. Chem., Int. Ed.* **2019,** *58*, 1376-1381.

53. Kory, M. J.; Wörle, M.; Weber, T.; Payamyar, P.; Van De Poll, S. W.; Dshemuchadse, J.; Trapp, N.; Schlüter, A. D., Gram-scale synthesis of two-dimensional polymer crystals and their structure analysis by X-ray diffraction. *Nat. Chem.* **2014,** *6* (9), 779-784.

54. Gao, Z.-Z.; Wang, Z.-K.; Wei, L.; Yin, G.; Tian, J.; Liu, C.-Z.; Wang, H.; Zhang, D.-W.; Zhang, Y.-B.; Li, X., Water-soluble 3D covalent organic framework that displays an enhanced enrichment effect of photosensitizers and catalysts for the reduction of protons to H_2. *ACS Appl. Mater. Interfaces* **2019,** *12* (1), 1404-1411.

55. Karak, S.; Kumar, S.; Pachfule, P.; Banerjee, R., Porosity prediction through hydrogen bonding in covalent organic frameworks. *J. Am. Chem. Soc.* **2018,** *140* (15), 5138-5145.

56. Liu, K.; Qi, H.; Dong, R.; Shivhare, R.; Addicoat, M.; Zhang, T.; Sahabudeen, H.; Heine, T.; Mannsfeld, S.; Kaiser, U., On-water surface synthesis of crystalline, few-layer two-dimensional polymers assisted by surfactant monolayers. *Nat. Chem.* **2019,** *11* (11), 994-1000.

57. Waller, P. J.; Lyle, S. J.; Osborn Popp, T. M.; Diercks, C. S.; Reimer, J. A.;Yaghi, O. M., Chemical conversion of linkages in covalent organic frameworks. *J. Am. Chem. Soc.* **2016,** *138* (48), 15519-15522.

58. Lyle, S. J.; Osborn Popp, T. M.; Waller, P. J.; Pei, X.; Reimer, J. A.; Yaghi, O. M., Multistep solid-state organic synthesis of carbamate-linked covalent organic frameworks. *J. Am. Chem. Soc.* **2019,** *141* (28), 11253-11258.

59. Ren, X.-R.; Bai, B.; Zhang, Q.; Hao, Q.; Guo, Y.; Wan, L.-J.; Wang, D., Constructing Stable Chromenoquinoline-Based Covalent Organic Frameworks via Intramolecular Povarov Reaction. *J. Am. Chem. Soc.* **2022,** *144* (6), 2488-2494.

60. Cote, A. P.; Benin, A. I.; Ockwig, N. W.; O'Keeffe, M.; Matzger, A. J.; Yaghi, O. M., Porous, crystalline, covalent organic frameworks. *science* **2005,** *310* (5751), 1166-1170.

61. Babarao, R.; Jiang, J., Exceptionally high CO2 storage in covalent-organic frameworks: Atomistic simulation study. *Energy Environ. Sci.* **2008,** *1* (1), 139-143.

62. Feng, X.; Liu, L.; Honsho, Y.; Saeki, A.; Seki, S.; Irle, S.; Dong, Y.; Nagai, A.; Jiang, D., High-rate charge-carrier transport in porphyrin covalent organic frameworks: switching from hole to electron to ambipolar conduction. *Angew. Chem., Int. Ed.* **2012,** *51*, 2618-2622.

63. Ding, X.; Feng, X.; Saeki, A.; Seki, S.; Nagai, A.; Jiang, D., Conducting metallophthalocyanine 2D covalent organic frameworks: the role of central metals in controlling π-electronic functions. *Chem. Comm.* **2012,** *48* (71), 8952-8954.

64. Du, Y.; Yang, H.; Whiteley, J. M.; Wan, S.; Jin, Y.; Lee, S. H.; Zhang, W., Ionic covalent organic frameworks with spiroborate linkage. *Angew. Chem., Int. Ed.* **2016,** *55* (5), 1737-1741.

65. Kubo, Y.; Nishiyabu, R.; James, T. D., Hierarchical supramolecules and organization using boronic acid building blocks. *Chem. Comm.* **2015,** *51* (11), 2005-2020.

66. Uribe-Romo, F. J.; Hunt, J. R.; Furukawa, H.; Klock, C.; O'Keeffe, M.; Yaghi, O. M., A crystalline imine-linked 3-D porous covalent organic framework. *J. Am. Chem. Soc.* **2009,** *131* (13), 4570-4571.

67. Li, X.; Zhang, C.; Cai, S.; Lei, X.; Altoe, V.; Hong, F.; Urban, J. J.; Ciston, J.; Chan, E. M.; Liu, Y., Facile transformation of imine covalent organic frameworks into ultrastable crystalline porous aromatic frameworks. *Nat. Commun.* **2018,** *9* (1), 1-8.

68. Liu, J.; Yang, T.; Wang, Z.-P.; Wang, P.-L.; Feng, J.; Ding, S.-Y.; Wang, W., Pyrimidazole-Based Covalent Organic Frameworks: Integrating Functionality and

Ultrastability via Isocyanide Chemistry. *J. Am. Chem. Soc.* **2020,** *142* (50), 20956-20961.

69. Li, X.-T.; Zou, J.; Wang, T.-H.; Ma, H.-C.; Chen, G.-J.; Dong, Y.-B., Construction of covalent organic frameworks via three-component one-pot Strecker and Povarov reactions. *J. Am. Chem. Soc.* **2020,** *142* (14), 6521-6526.

70. Wang, J.-C.; Kan, X.; Shang, J.-Y.; Qiao, H.; Dong, Y.-B., Catalytic asymmetric synthesis of chiral covalent organic frameworks from prochiral monomers for heterogeneous asymmetric catalysis. *J. Am. Chem. Soc.* **2020,** *142* (40), 16915-16920.

71. Liu, H.; Chu, J.; Yin, Z.; Cai, X.; Zhuang, L.; Deng, H., Covalent organic frameworks linked by amine bonding for concerted electrochemical reduction of CO2. *Chem* **2018,** *4* (7), 1696-1709.

72. Li, C.; Ma, Y.; Liu, H.; Tao, L.; Ren, Y.; Chen, X.; Li, H.; Yang, Q., Asymmetric photocatalysis over robust covalent organic frameworks with tetrahydroquinoline linkage. *Chinese J. Catal* **2020,** *41* (8), 1288-1297.

73. Waller, P. J.; AlFaraj, Y. S.; Diercks, C. S.; Jarenwattananon, N. N.; Yaghi, O. M., Conversion of imine to oxazole and thiazole linkages in covalent organic frameworks. *J. Am. Chem. Soc.* **2018,** *140* (29), 9099-9103.

74. Wang, Y.; Liu, H.; Pan, Q.; Wu, C.; Hao, W.; Xu, J.; Chen, R.; Liu, J.; Li, Z.; Zhao, Y., Construction of fully conjugated covalent organic frameworks via facile linkage conversion for efficient photoenzymatic catalysis. *J. Am. Chem. Soc.* **2020,** *142* (13), 5958-5963.

75. Uribe-Romo, F. J.; Doonan, C. J.; Furukawa, H.; Oisaki, K.; Yaghi, O. M., Crystalline covalent organic frameworks with hydrazone linkages. *J. Am. Chem. Soc.* **2011,** *133* (30), 11478-11481.

76. Zhao, C.; Diercks, C. S.; Zhu, C.; Hanikel, N.; Pei, X.; Yaghi, O. M., Urea-linked covalent organic frameworks. *J. Am. Chem. Soc.* **2018,** *140* (48), 16438-16441.

77. Li, L.-H.; Feng, X.-L.; Cui, X.-H.; Ma, Y.-X.; Ding, S.-Y.; Wang, W., Salen-based covalent organic framework. *J. Am. Chem. Soc.* **2017,** *139* (17), 6042-6045.

78. Nagai, A.; Chen, X.; Feng, X.; Ding, X.; Guo, Z.; Jiang, D., A Squaraine-Linked Mesoporous Covalent Organic Framework. *Angewandte Chemie* **2013,** *125* (13), 3858-3862.

79. Rao, M. R.; Fang, Y.; De Feyter, S.; Perepichka, D. F., Conjugated covalent organic frameworks via michael addition–elimination. *J. Am. Chem. Soc.* **2017,** *139* (6), 2421-2427.

80. Jiang, S.-Y.; Gan, S.-X.; Zhang, X.; Li, H.; Qi, Q.-Y.; Cui, F.-Z.; Lu, J.; Zhao, X., Aminal-linked covalent organic frameworks through condensation of secondary amine with aldehyde. *J. Am. Chem. Soc.* **2019,** *141* (38), 14981-14986.

81. Kandambeth, S.; Mallick, A.; Lukose, B.; Mane, M. V.; Heine, T.; Banerjee, R., Construction of crystalline 2D covalent organic frameworks with remarkable chemical (acid/base) stability via a combined reversible and irreversible route. *J. Am. Chem. Soc.* **2012,** *134* (48), 19524-19527.

82. Fang, Q.; Zhuang, Z.; Gu, S.; Kaspar, R. B.; Zheng, J.; Wang, J.; Qiu, S.; Yan, Y., Designed synthesis of large-pore crystalline polyimide covalent organic frameworks. *Nat. Commun.* **2014,** *5* (1), 1-8.

83. Meng, Z.; Aykanat, A.; Mirica, K. A., Proton conduction in 2D aza-fused covalent organic frameworks. *Chem. Mater.* **2018,** *31* (3), 819-825.

84. Wang, P.-L.; Ding, S.-Y.; Zhang, Z.-C.; Wang, Z.-P.; Wang, W., Constructing robust covalent organic frameworks via multicomponent reactions. *J. Am. Chem. Soc.* **2019,** *141* (45), 18004-18008.

85. Kuhn, P.; Antonietti, M.; Thomas, A., Porous, covalent triazine-based frameworks prepared by ionothermal synthesis. *Angew. Chem., Int. Ed.* **2008,** *47* (18), 3450-3453.

86. Liu, M.; Huang, Q.; Wang, S.; Li, Z.; Li, B.; Jin, S.; Tan, B., Crystalline covalent triazine frameworks by in situ oxidation of alcohols to aldehyde monomers. *Angew. Chem., Int. Ed.* **2018,** *57* (37), 11968-11972.

87. Zhang, S.; Cheng, G.; Guo, L.; Wang, N.; Tan, B.; Jin, S., Strong-base-assisted synthesis of a crystalline covalent triazine framework with high hydrophilicity via benzylamine monomer for photocatalytic water splitting. *Angew. Chem., Int. Ed.* **2020,** *59*, 6007-6014.

88. Yu, S. Y.; Mahmood, J.; Noh, H. J.; Seo, J. M.; Jung, S. M.; Shin, S. H.; Im, Y. K.; Jeon, I. Y.; Baek, J. B., Direct synthesis of a covalent triazine-based framework from aromatic amides. *Angew. Chem., Int. Ed.* **2018,** *57* (28), 8438-8442.

89. Li, X. L. Cai, S. L.; Sun, B.; Yang, C. Q.; Zhang, J.; Liu, Y., Chemically Robust Covalent Organic Frameworks: Progress and Perspective. *Matter* **2020,** *3* (5), 1507-1540.

90. Zhuang, X.; Zhao, W.; Zhang, F.; Cao, Y.; Liu, F.; Bi, S.; Feng, X., A two-dimensional conjugated polymer framework with fully sp 2-bonded carbon skeleton. *Polym. Chem* **2016,** *7* (25), 4176-4181.

91. Jin, E. Q.; Asada, M.; Xu, Q.; Dalapati, S.; Addicoat, M. A.; Brady, M. A.; Xu, H.; Nakamura, T.; Heine, T.; Chen, Q. H.; Jiang, D. L., Two-dimensional sp(2) carbon-conjugated covalent organic frameworks. *Science* **2017,** *357* (6352), 673-676.

92. Lyu, H.; Diercks, C. S.; Zhu, C. H.; Yaghi, O. M., Porous Crystalline Olefin-Linked Covalent Organic Frameworks. *J. Am. Chem. Soc.* **2019,** *141* (17), 6848-6852.

93. Bi, S.; Yang, C.; Zhang, W.; Xu, J.; Liu, L.; Wu, D.; Wang, X.; Han, Y.; Liang, Q.; Zhang, F., Two-dimensional semiconducting covalent organic frameworks via condensation at arylmethyl carbon atoms. *Nat. Commun.* **2019,** *10* (1), 1-10.

94. Xu, J.; Yang, C.; Bi, S.; Wang, W.; He, Y.; Wu, D.; Liang, Q.; Wang, X.;Zhang, F., Vinylene-Linked Covalent Organic Frameworks (COFs) with Symmetry-Tuned Polarity and Photocatalytic Activity. *Angew. Chem., Int. Ed.* **2020,** *59* (52), 23845-23853.

95. Meng, F.; Bi, S.; Sun, Z.; Jiang, B.; Wu, D.; Chen, J. S.; Zhang, F., Synthesis of Ionic Vinylene-Linked Covalent Organic Frameworks through Quaternization-Activated Knoevenagel Condensation. *Angew. Chem., Int. Ed.* **2021,** *60,* 13614-13620.

96. Bi, S.; Zhang, Z.; Meng, F.; Wu, D.; Chen, J. S.; Zhang, F., Heteroatom-Embedded Approach to Vinylene-Linked Covalent Organic Frameworks with Isoelectronic Structures for Photoredox Catalysis. *Angew. Chem., Int. Ed.* **2022,** *61,* e202111627.

97. Pastoetter, D. L.; Xu, S.; Borrelli, M.; Addicoat, M.; Biswal, B. P.; Paasch, S.; Dianat, A.; Thomas, H.; Berger, R.; Reineke, S., Synthesis of Vinylene-Linked Two-

Dimensional Conjugated Polymers via the Horner–Wadsworth–Emmons Reaction. *Angew. Chem., Int. Ed.* **2020,** *59* (52), 23620-23625.

98. Han, X. H.; Gong, K.; Huang, X.; Yang, J. W.; Feng, X.; Xie, J.; Wang, B., Syntheses of Covalent Organic Frameworks via a One-Pot Suzuki Coupling and Schiff's Base Reaction for C2H4/C3H6 Separation. *Angew. Chem., Int. Ed.* **2022**, e202202912.

99. Wang, Z.; Yang, Y.; Zhao, Z.; Zhang, P.; Zhang, Y.; Liu, J.; Ma, S.; Cheng, P.; Chen, Y.; Zhang, Z., Green synthesis of olefin-linked covalent organic frameworks for hydrogen fuel cell applications. *Nat. Commun.* **2021,** *12* (1), 1-8.

100. Zhou, Z.-B.; Tian, P.-J.; Yao, J.; Lu, Y.; Qi, Q.-Y.; Zhao, X., Toward azo-linked covalent organic frameworks by developing linkage chemistry via linker exchange. *Nat. Commun.* **2022,** *13* (1), 1-8.

101. Li, Z.; Feng, X.; Zou, Y.; Zhang, Y.; Xia, H.; Liu, X.; Mu, Y., A 2D azine-linked covalent organic framework for gas storage applications. *Chem. Comm.* **2014,** *50* (89), 13825-13828.

102. Nath, B.; Li, W. H.; Huang, J. H.; Wang, G. E.; Fu, Z. H.; Yao, M. S.; Xu, G., A new azodioxy-linked porphyrin-based semiconductive covalent organic framework with I-2 doping-enhanced photoconductivity. *Crystengcomm* **2016,** *18* (23), 4259-4263.

103. Guan, X.; Li, H.; Ma, Y.; Xue, M.; Fang, Q.; Yan, Y.; Valtchev, V.; Qiu, S., Chemically stable polyarylether-based covalent organic frameworks. *Nat. Chem.* **2019,** *11* (6), 587-594.

104. Zhao, C.; Lyu, H.; Ji, Z.; Zhu, C.; Yaghi, O. M., Ester-linked crystalline covalent organic frameworks. *J. Am. Chem. Soc.* **2020,** *142* (34), 14450-14454.

105. Haldar, S.; Wang, M.; Bhauriyal, P.; Hazra, A.; Khan, A. H.; Bon, V.; Isaacs, M. A.; De, A.; Shupletsov, L.; Boenke, T., Porous Dithiine-Linked Covalent Organic Framework as a Dynamic Platform for Covalent Polysulfide Anchoring in Lithium–Sulfur Battery Cathodes. *J. Am. Chem. Soc.* **2022**, *144*, 20, 9101–9112.

106. Ong, W. J.; Swager, T. M., Dynamic self-correcting nucleophilic aromatic substitution. *Nat. Chem.* **2018,** *10* (10), 1023-1030.

107. Evans, A. M.; Parent, L. R.; Flanders, N. C.; Bisbey, R. P.; Vitaku, E.; Kirschner, M. S.; Schaller, R. D.; Chen, L. X.; Gianneschi, N. C.; Dichtel, W. R., Seeded growth of single-crystal two-dimensional covalent organic frameworks. *Science* **2018,** *361* (6397), 52-57.

108. Ma, T. Q.; Kapustin, E. A.; Yin, S. X.; Liang, L.; Zhou, Z. Y.; Niu, J.; Li, L. H.; Wang, Y. Y.; Su, J.; Li, J.; Wang, X. G.; Wang, W. D.; Wang, W.; Sun, J. L.; Yaghi, O. M., Single-crystal x-ray diffraction structures of covalent organic frameworks. *Science* **2018,** *361* (6397), 48-52.

109. Li, X.; Yadav, P.; Loh, K. P., Function-oriented synthesis of two-dimensional (2D) covalent organic frameworks - from 3D solids to 2D sheets. *Chem Soc Rev.* **2020,** *49* (14), 4835-4866.

110. Li, J.; Jing, X. C.; Li, Q. Q.; Li, S. W.; Gao, X.; Feng, X.; Wang, B., Bulk COFs and COF nanosheets for electrochemical energy storage and conversion. *Chem Soc Rev.* **2020,** *49* (11), 3565-3604.

111. Berlanga, I.; Ruiz-González, M. L.; González-Calbet, J. M.; Fierro, J. L. G.; Mas-Ballesté, R.; Zamora, F., Delamination of layered covalent organic frameworks. *Small* **2011,** *7* (9), 1207-1211.

112. Chandra, S.; Kandambeth, S.; Biswal, B. P. Lukose, B.; Kunjir, S. M.; Chaudhary, M.; Babarao, R.; Heine, T.; Banerjee, R., Chemically stable multilayered covalent organic nanosheets from covalent organic frameworks via mechanical delamination. *J. Am. Chem. Soc.* **2013,** *135* (47), 17853-17861.

113. Khayum, M. A.; Kandambeth, S.; Mitra, S.; Nair, S. B.; Das, A.; Nagane, S. S.; Mukherjee, R.; Banerjee, R., Chemically delaminated free-standing ultrathin covalent organic nanosheets. *Angew. Chem., Int. Ed.* **2016,** *55*, 15604-15608.

114. Kahveci, Z.; Islamoglu, T.; Shar, G. A.; Ding, R.; El-Kaderi, H. M., Targeted synthesis of a mesoporous triptycene-derived covalent organic framework. *CrystEngComm* **2013,** *15* (8), 1524-1527.

115. Galek, P.; Mackowiak, A.; Bujewska, P.; Fic, K., Three-Dimensional Architectures in Electrochemical Capacitor Applications–Insights, Opinions, and Perspectives. *Front. Energy Res.* **2020,** *8*, 139.

116. Babu, B.; Simon, P.; Balducci, A., Fast charging materials for high power applications. *Adv. Energy Mater.* **2020,** *10* (29), 2001128.

117. Scherf, U., Ladder-type materials. *J. Mater. Chem.* **1999,** *9* (9), 1853-1864.

118. Lee, J.; Kalin, A. J.; Yuan, T.; Al-Hashimi, M.; Fang, L., Fully conjugated ladder polymers. *Chem. Sci.* **2017,** *8* (4), 2503-2521.

119. Wu, J.; Rui, X.; Long, G.; Chen, W.; Yan, Q.; Zhang, Q., Pushing up lithium storage through nanostructured polyazaacene analogues as anode. *Angew. Chem., Int. Ed.* **2015,** *54* (25), 7354-7358.

120. Kou, Y.; Xu, Y.; Guo, Z.; Jiang, D., Supercapacitive energy storage and electric power supply using an aza-fused π-conjugated microporous framework. *Angew. Chem., Int. Ed.* **2011,** *50*, 8753-8757.

121. Nithya, V., A review on holey graphene electrode for supercapacitor. *J Energy Storage* **2021,** *44*, 103380.

122. Li, M.; Liu, J.; Zhang, T.; Song, X.; Chen, W.; Chen, L., 2D redox-active covalent organic frameworks for supercapacitors: Design, synthesis, and challenges. *Small* **2021,** *17* (22), 2005073.

123. Wang, S.; Wang, Q.; Shao, P.; Han, Y.; Gao, X.; Ma, L.; Yuan, S.; Ma, X.; Zhou, J.; Feng, X., Exfoliation of covalent organic frameworks into few-layer redox-active nanosheets as cathode materials for lithium-ion batteries. *J. Am. Chem. Soc.* **2017,** *139* (12), 4258-4261.

124. DeBlase, C. R.; Silberstein, K. E.; Truong, T.-T.; Abruña, H. D.; Dichtel, W. R., β-Ketoenamine-linked covalent organic frameworks capable of pseudocapacitive energy storage. *J. Am. Chem. Soc.* **2013,** *135* (45), 16821-16824.

125. Halder, A.; Ghosh, M.; Khayum M, A.; Bera, S.; Addicoat, M.; Sasmal, H. S.; Karak, S.; Kurungot, S.; Banerjee, R., Interlayer hydrogen-bonded covalent organic frameworks as high-performance supercapacitors. *J. Am. Chem. Soc.* **2018,** *140* (35), 10941-10945.

126. Zeng, X.-X.; Yin, Y.-X.; Li, N.-W.; Du, W.-C.; Guo, Y.-G.; Wan, L.-J., Reshaping lithium plating/stripping behavior via bifunctional polymer electrolyte for

room-temperature solid Li metal batteries. *J. Am. Chem. Soc.* **2016,** *138* (49), 15825-15828.

127. Khurana, R.; Schaefer, J. L.; Archer, L. A.; Coates, G. W., Suppression of lithium dendrite growth using cross-linked polyethylene/poly (ethylene oxide) electrolytes: a new approach for practical lithium-metal polymer batteries. *J. Am. Chem. Soc.* **2014,** *136* (20), 7395-7402.

128. Shim, J.; Kim, L.; Kim, H. J.; Jeong, D.; Lee, J. H.; Lee, J.-C., All-solid-state lithium metal battery with solid polymer electrolytes based on polysiloxane crosslinked by modified natural gallic acid. *Polymer* **2017,** *122*, 222-231.

129. Garcia-Calvo, O.; Lago, N. Devaraj, S.; Armand, M., Cross-linked solid polymer electrolyte for all-solid-state rechargeable lithium batteries. *Electrochim. Acta* **2016,** *220*, 587-594.

130. Zhao, X.; Chen, Y.; Wang, Z.; Zhang, Z., Design and application of covalent organic frameworks for ionic conduction. *Polym. Chem.* **2021**, *12*, 4874-4894.

131. Zhou, T.; Huang, X.; Ding, N.; Lin, Z.; Yao, Y.; Guo, J., Porous polyelectrolyte frameworks: synthesis, post-ionization and advanced applications. *Chem Soc Rev.* **2022**, *51*, 237-267.

132. Gao, Z.; Liu, Q.; Zhao, G.; Sun, Y.; Guo, H., Covalent organic frameworks for solid-state electrolytes of lithium metal batteries. *J. Mater. Chem. A.* **2022,** *10* (14), 7497-7516.

133. Xu, Q.; Tao, S.; Jiang, Q.; Jiang, D., Ion conduction in polyelectrolyte covalent organic frameworks. *J. Am. Chem. Soc.* **2018,** *140* (24), 7429-7432.

134. Hu, Y.; Dunlap, N. Wan, S.; Lu, S.; Huang, S.; Sellinger, I.; Ortiz, M.; Jin, Y.; Lee, S.-h.; Zhang, W., Crystalline lithium imidazolate covalent organic frameworks with high Li-ion conductivity. *J. Am. Chem. Soc.* **2019,** *141* (18), 7518-7525.

135. Chen, H.; Tu, H.; Hu, C.; Liu, Y.; Dong, D.; Sun, Y.; Dai, Y.; Wang, S.; Qian, H.; Lin, Z., Cationic covalent organic framework nanosheets for fast Li-ion conduction. *J. Am. Chem. Soc.* **2018,** *140* (3), 896-899.

136. Guo, Z.; Zhang, Y.; Dong, Y.; Li, J.; Li, S.; Shao, P.; Feng, X.; Wang, B., Fast ion transport pathway provided by polyethylene glycol confined in covalent organic frameworks. *J. Am. Chem. Soc.* **2019,** *141* (5), 1923-1927.

137. Li, Z., Zhu, R., Zhang, P., Yang, M., Zhao, R., Wang, Y., Dai, X., Liu, W., Functionalized polyarylether-based COFs for rapid and selective extraction of uranium from aqueous solution. *Chem. Eng. J.* **2022**, 434, 134623.

138. Guo, L., Jia, S., Diercks, C., Yang, X., Alshmimri, S., Yaghi, O. M., Amidation, Esterification, and Thioesterification of a Carboxyl-Functionalized Covalent Organic Framework. *Angew. Chem., Int. Ed*. **2020**, 132 (5), 2039-2043.

139. Gendy, E. A.; Ifthikar, J.; Ali, J.; Oyekunle, D. T.; Elkhlifia, Z.; Shahib, I. I.; Khodair, A. I.; Chen, Z., Removal of heavy metals by covalent organic frameworks (COFs): A review on its mechanism and adsorption properties. *J. Environ. Chem. Eng*. **2021**, 9, 105687.

140. Meyers, H. P.; Myers, H. P., Introductory Solid State Physics, Taylor & Francis, London **2014**.

141. Vandenabeele, P., Practical Raman Spectroscopy – An Introduction, John Wiley & Sons, Ltd, **2013**, 1.

142. Brunauer, S.; Emmett, P. H.; Teller, E., Adsorption of gases in multimolecular layers. *J. Am. Chem. Soc.* **1938**, *60*, 309-319.

143. Wang, Y.; Wang, Y., Recent advances in additive-enhanced magnesium hydride for hydrogen storage. *Prog. Nat. Sci. Mater.* **2017**, *27*, 41-49.

144. Torad, N. L.; Salunkhe, R. R.; Li, Y.; Hamoudi, H.; Imura, M.; Sakka, Y.; Hu, C.; Yamauchi, Y., Electric Double-Layer Capacitors Based on Highly Graphitized Nanoporous Carbons Derived from ZIF-67. *Chem. Eur. J.* **2014**, *20*, 7895-7900.

145. Negroiu, R.; Svasta, P.; Pirva, C.; Vasile, A.; Marghescu, C., Electrochemical impedance spectroscopy for different types of supercapacitors. presented at *2017 40th International Spring Seminar on Electronics Technology (ISSE).* **2017**.

Chapter 2

Fluorindine-Linked Covalent Organic Frameworks

2.1 Contributions to this Chapter

HR-TEM images for FL-COF were obtained by Yang Liu. SEM images for FL-COF were obtained by Lunjie Liu. Construction of FL-COF model and simulation calculations were performed by Xue Wang and Linjiang Chen. Optimization of the synthesis condition of FL-COF was synthesised with the help of Haofan Yang. All other work was performed by the thesis author.

2.2 Background and Context

The rational design and implementation of redox-active sites into covalent organic framework (COF) electrode materials is difficult yet one of the most efficient methods to improve supercapacitance and energy density. Generally, these redox-active sites are connected within the framework through single bonds which can limit electron transfer. Here, we report a fluorindine-linked COF (FL-COF) whereby the redox-active sites are connected by two bonds using ladder-like bonding which provides efficient pseudocapacitance and extended π-conjugation throughout the framework improving electron transfer and supercapacitance (**Figure 2.2.1**). FL-COF exhibited a high specific capacitance of 393 F g^{-1} at current density of 0.5 A g^{-1}. The symmetric two-electrode supercapacitor showed a maximum energy density and power density of 50.28 Wh kg^{-1} and 39.79 kW kg^{-1} respectively, which is higher than many state-of-the-art COF-based electrode materials.

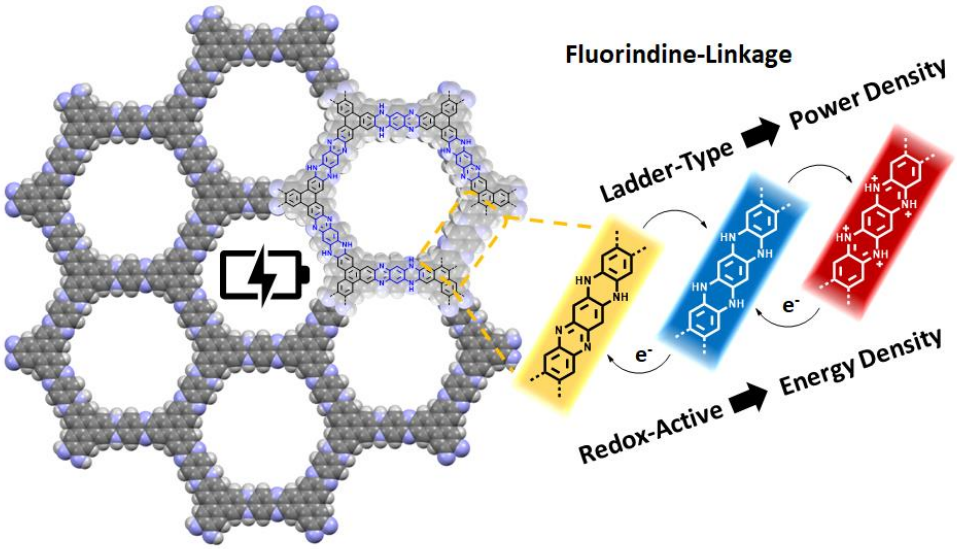

Figure 2.2.1 Fluorindine-linked COF and its redox-contained ladder structure for energy storage.

2.3 Introduction

Supercapacitors are important electrochemical energy storage devices, and unlike ion batteries, do not require chemical reactions during the energy storage process so have good electrochemical reversibility and high charge-discharge rates.[1] Supercapacitors have several advantages compared with ion batteries, including high power density and long cycling lifetimes. From a safety perspective, they also have advantages as they are much more suitable for some emergency uses such as uninterrupted power supplies in air atmosphere.[2, 3] However, the relative low energy density of supercapacitors limits their wider applications.[4] To improve the energy density of supercapacitors, extra pseudocapacitance has been introduced using redox active sites and has attracted significant attention in recent years.[5] Based on the energy storage mechanisms of both electric double layer capacitors (EDLCs) and pseudocapacitor there are several important factors for high performing electrode materials. These include high stability in various electrolytes, large surface areas with pore sizes that support channels for ion

transmission and enrichment, high conductivity for charge transfer, and redox groups for additional active sites.[6]

COFs are a class of crystalline porous polymers that are constructed by reversible covalent bonds.[7] Their structural tunability has enabled the development of COFs with redox-active building blocks and is a promising direction for energy storage materials.[8] However, the major drawbacks of these reported COF electrode materials is that the redox sites are connected to the framework either as side groups[9] or through a single bond[10]. These polarized linkages with limited conjugation result in materials with poor electronic conductivity.[11, 12] One way to increase charge carrier mobility is to have a fully π-conjugated system connecting the redox sites.[13] Conjugated ladder polymers have emerged as highly conductive polymers for energy storage applications with high charge carrier mobility due to their fully π-conjugated 2D aromatized skeletons.[14, 15] Here, we connect redox-active sites with pseudocapacitance properties through ladder-type connectivity for highly π-conjugated COF electrode materials with improved energy density, power density, and high supercapacitance.

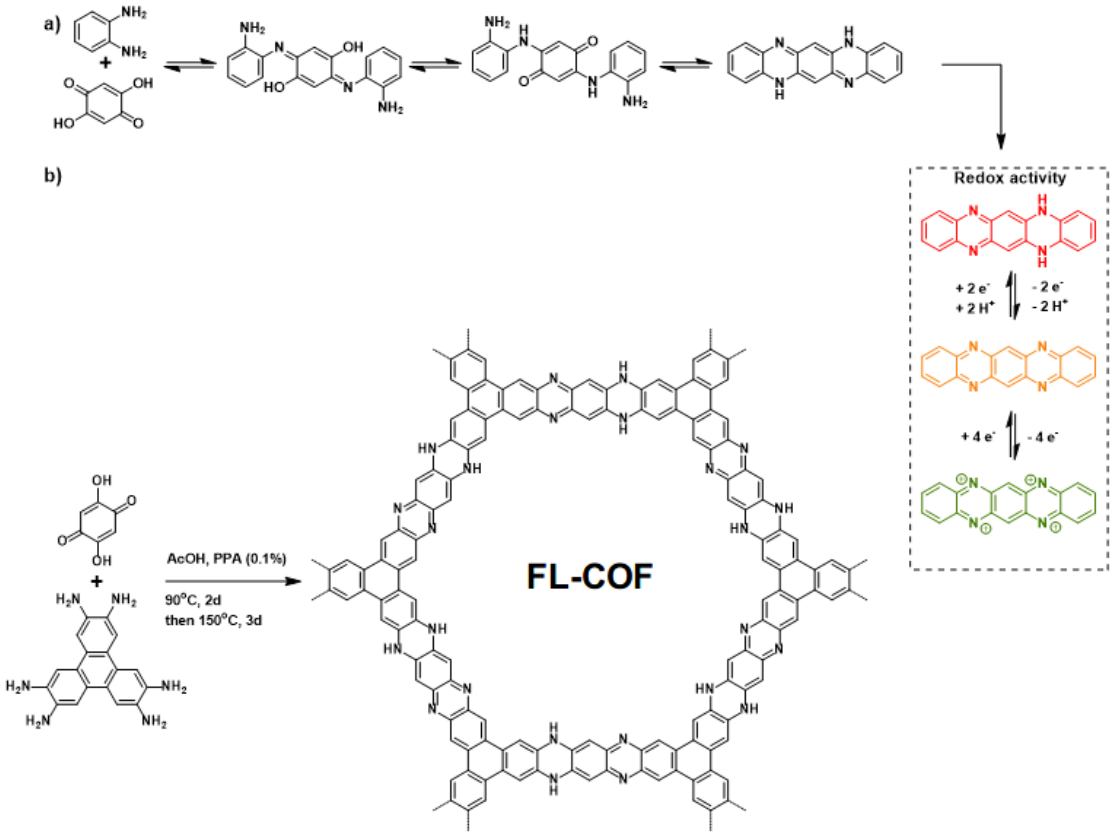

Scheme 2.3.1. (a) Mechanism of fluorindine synthesis and redox activity. (b) Synthesis of FL-COF.

Fluorindine groups are underexplored redox-active groups which can be synthesized by the condensation of aromatic diamines and dihydroxy benzoquinones (**Scheme 2.3.1**). The fluorindine group fulfils several of our design criteria: the formation is reversible and thus allows the error correction processes required for the growth of crystalline frameworks; they can undergo redox reactions to facilitate pseudocapacitance; and they are highly planar and conjugated.[16]

2.4 Experimental

2.4.1 Chemical Reagents

All reagents were obtained from Sigma-Aldrich, TCI Europe or Acros Organics. Anhydrous solvents were purchased from Sigma-Aldrich or Fisher Scientific. All chemicals were used without further purification.

2.4.2 Characterization Methods and Measurements

General methods.

Air sensitive reactions were performed under N_2 using standard Schlenk techniques. Glassware was oven-dried overnight or dried using a heat gun.

1. Nuclear magnetic resonance measurements

Solution ^{1}H and ^{13}C NMR spectra were recorded in deuterated solution at 400 MHz and 100 MHz, respectively, using a Bruker Avance 400 NMR spectrometer.

Solid-state ^{13}C magic-angle spinning measurements were carried out at 100.63 MHz using a Bruker Avance III HD spectrometer (Durham University solid-state NMR service) and 4 mm (rotor o.d.) probe. Spectra were acquired at a spin rate of 10 kHz. Cross-polarisation (CP) spectra were recorded with TOSS spinning sideband suppression, 1 ms contact time and with a recycle delay of 1 s. Carbon spectral referencing is relative to neat tetramethylsilane, carried out by setting the high-

frequency signal from an external sample of adamantane to 38.5 ppm. 50 Hz of line broadening was added to improve the signal to noise.

2. High resolution mass spectrometry

High resolution mass spectrometry (HR-MS) as performed on an Agilent Technologies 6530B accuratemass QTOF mixed ESI/APCI mass spectrometer (capillary voltage 4000 V, fragmentor 225 V) in positiveion detection mode.

3. Powder X-ray diffraction

Powder X-ray diffraction (PXRD) measurements were carried out on a Panalytical Empyrean diffractometer, equipped with a Cu X-ray source (λ = 1.5418 Å, Cu Kα), PIXcel3D detector and X-ray focusing mirror. The loose powdered sample was held on Mylar film in aluminium well plates and screened in high throughput transmission mode. For HT screening, PXRD patterns were measured over the 2θ range 1-56° in 0.013° steps over 30 minutes.

4. Thermogravimetric analysis

Thermogravimetric analysis (TGA) was measured on an EXSTAR6000 with an automated vertical overhead thermobalance under nitrogen flow, ramping heating at 10 °C min^{-1} from 25 °C to 800 °C.

5. Gas sorption analysis

Nitrogen adsorption and desorption were measured at 77 K using a Micromeritics ASAP 2420 volumetric adsorption analyzer. Powder samples were degassed ocffline at 393 K for 12 hours under dynamic vacuum (10-5 bar) before analysis. BET surface areas were fitted over relative pressure (p/p_0) from 0.05 to 0.3. Pore size distributions of COFs were obtained from the adsorption data by fitting a nonlocal density functional theory (NL-DFT) model with method of N_2-cylindrical pores-oxide surface.

6. Fourier-transform infrared spectroscopy

FT-IR spectra were collected with an attenuated total reflectance (ATR) method on a Bruker Tensor 27 FT-IR spectrometer.

7. X-ray photoelectron spectroscopy (XPS) measurements

X-ray photoelectron spectroscopy (XPS) was carried out on a Kratos ASAM 800, performing at 12 kV and 15 mA with a monochromatic Al Kα source ($h\nu$ = 1486.6 eV).

8. Scanning electron microscopy (SEM).

SEM images were carried out on Super Octane cold field emission scanning electron microscope. Samples were prepared by depositing the dry powders on 15 mm Hitachi M4 aluminum stubs using an adhesive high-purity carbon tab before coating with a 2 nm layer of gold using an Emitech K550X automated sputter coater. Imaging was conducted at a working voltage of 3 kV and a working distance of 8 mm using a combination of upper and lower secondary electron detectors.

9. Transmission electron microscopy (TEM).

TEM images were obtained on a Talos F200S microscope (FEI Corporation, Hillsboro, OR, USA) operated at an accelerating voltage of 200 kV.

10. Raman spectroscopy.

The Raman measurements were performed on an inVia Reflex Qontor Confocal Raman microscope upon excitation of 532 nm laser.

11. Electrochemical measurements.[17]

The electrochemical experiments were carried out using aqueous three-electrode system or symmetric two-electrode device employing 1 M H_2SO_4 as electrolyte at ambient temperature. The three-electrode system incorporates Ag/AgCl electrode (Argenthal, 3 M KCl, 0.207 V vs. standard hydrogen electrode at room temperature) as reference electrode, Pt as counter electrode and FL-COF as working electrode. The working electrode was prepared by grinding active materials (FL-COF, 70 wt.%), conductive additive (acetylene black, 20 wt.%), and binder (polyvinylidene fluoride,

10 wt.%) with N-methylpyrrolidinone (NMP) in a mortar. The graphite substrate (10 ×10 × 5 mm) current collector was coated with the slurry, dried under vacuum at 80 °C for 12 hours and weighted before using. The two-electrode device was assembled by two as-mentioned working electrodes with same mass loading of active material. The following cyclic voltammetry (CV), galvanostatic charge/discharge (GCD) measurements and electrochemical impedance spectroscopy (EIS) were performed by EC-Lab SP-200 electrochemical workstation.

12. Calculation Methods.

The specific capacitance C (F g^{-1}) of three-electrode system was calculated from the discharge part of GCD curves by the following equations:

$$C = I\Delta t/m\Delta V$$

where C (F g^{-1}) is the experimentally determined specific capacitance, I (mA) is the discharge current, and Δt (s), m (mg), and ΔV (V) are the total discharge time, the mass of active material, and the potential drop during discharge, respectively.

The specific capacitance C_s (F g^{-1}) of the two-electrode device was calculated by the following equation:

$$C_s = 2\times C_{cell} = 4\times I\Delta t/m\Delta V$$

where C_{cell} (F g^{-1}) is the experimentally determined specific capacitance, I (mA), Δt (s), m (mg), and ΔV (V) are the discharge current, the total discharge time, the mass of active material, and the potential drop during discharge, respectively.

The energy density (E) was calculated from the discharge profiles of the two-electrode system by using the following equation:

$$E = 0.5\times C_{cell}\times(\Delta V)^2/3.6$$

where E (Wh kg^{-1}) is the energy density, C_{cell} (F g^{-1}) the specific capacitance of the active material and ΔV (V) the discharge voltage range.

The power density (P) was calculated as follows:

$$P = E \times 3600/\Delta t$$

where P (W kg^{-1}) is the power density, and E (Wh kg^{-1}) and Δt (s) are energy density and discharge time, respectively.

2.4.3 Synthetic Route and Preparation Procedure

2.4.3.1 Synthesis of Monomers

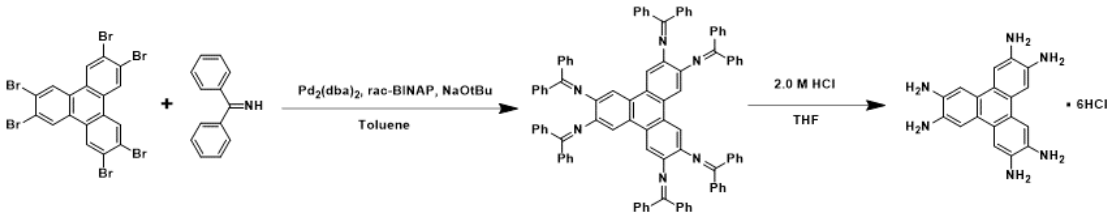

Scheme 2.4.1. Synthesis route of 2, 3, 6, 7, 10, 11-Hexaaminetriphenylene·6HCl.

Hexakis(diphenylmethylene)triphenylene-2, 3, 6, 7, 14, 15-hexaamine: The synthesis is followed by the procedure of the literature before.[18] A toluene solution (50 mL) of tris(dibenzylideneacetone)dipalladium (0) (0.448 g, 0.49 mmol) and rac-BINAP (0.607 g, 0.98 mmol) was degassed by three freeze-pump-thaw cycles, purged with N_2, and stirred at 110 °C for 0.5 h. After cooling to room temperature, the mixture was added with benzophenone imine (2.65 mL, 15.77 mmol), 2,3,6,7,10,11-hexabromo-triphenylene (1.419 g, 2.02 mmol), and sodium tert-butoxide (1.516 g, 15.77 mmol), and the mixture was stirred at 110 °C overnight. The mixture was cooled to room temperature, diluted with DCM, filtered through a pad of Celite, and evaporated to dryness. The residue was subjected to column chromatography on silica gel with hexane /EA (4:1) as eluent. The last fraction was collected and evaporated to dryness, to give 1.92 g Hexakis(diphenylmethylene)triphenylene-2, 3, 6, 7, 14, 15-hexaamine as yellow solid in 73% yield. ^{1}H NMR (400 MHz, $CDCl_3$) (**Figure 2.4.1.)**: δ (ppm) 7.68-7.70 (m, 12 H), 7.39-7.42 (m, 6 H), 7.32-7.36 (m, 12 H), 7.20-7.24 (m, 12 H), 7.18 (s, 6 H), 7.12-7.16 (m, 12 H), 6.87-6.89 (m, 12 H). ^{13}C NMR (100 MHz, $CDCl_3$) (**Figure 2.4.2.)**: δ (ppm) 167.6, 141.0, 140.1, 136.9, 130.3, 129.5, 129.3, 128.6, 127.9, 125.8, 115.0.

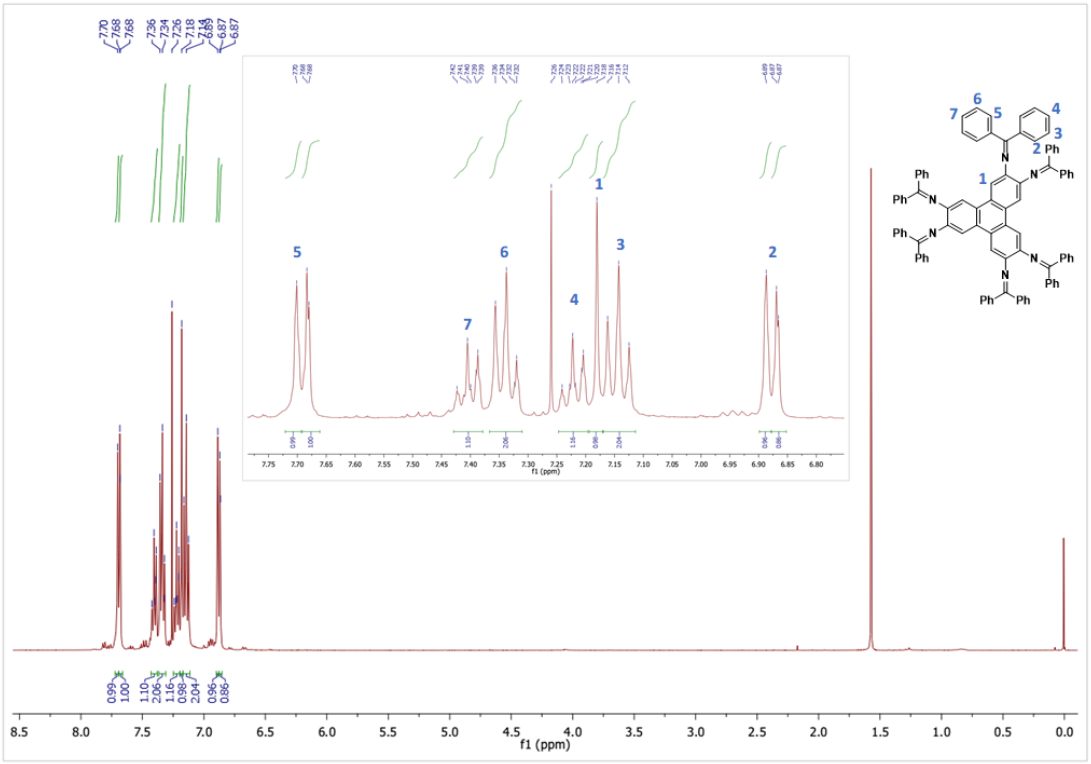

Figure 2.4.1. ^{1}H NMR of Hexakis(diphenylmethylene)triphenylene-2, 3, 6, 7, 14, 15-hexaamine (400 MHz, $CDCl_3$).

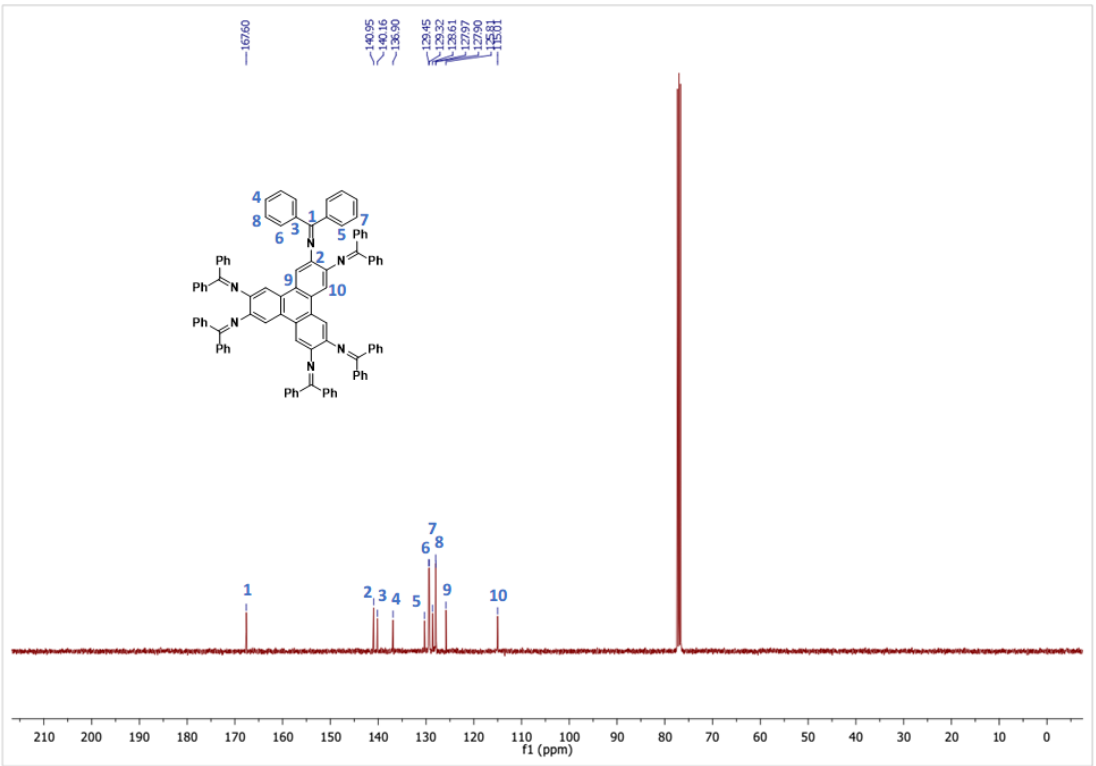

Figure 2.4.2. ^{13}C NMR of Hexakis(diphenylmethylene)triphenylene-2, 3, 6, 7, 14, 15-hexaamine (100 MHz, $CDCl_3$).

2, 3, 6, 7, 10, 11-Hexaaminetriphenylene (**HAT·6HCl**): To a THF solution (5 mL) of Hexakis(diphenylmethylene)triphenylene-2,3,6,7,14,15-hexaamine (0.11 g, 0.85 mmol) added a 2.0 M HCl aqueous solution (0.25 mL, 0.50 mmol) and the mixture was stirred at r.t. for 0.5 h. The precipitate was isolated by centrifugation, washed with hexane (15.0 mL), and dried under vacuum, to give 82 mg **HAT·6HCl** as light grey powder in 88% yield. ^1H NMR (400 MHz, DMSO-d_6) (**Figure 2.4.3.)**: δ (ppm) 7.92 (s, 6 H), 6.54 (brs, about 12 H). ^{13}C NMR (100 MHz, DMSO-d_6) (**Figure 2.4.4.)**: δ (ppm) 133.4, 124.6, 114.0.

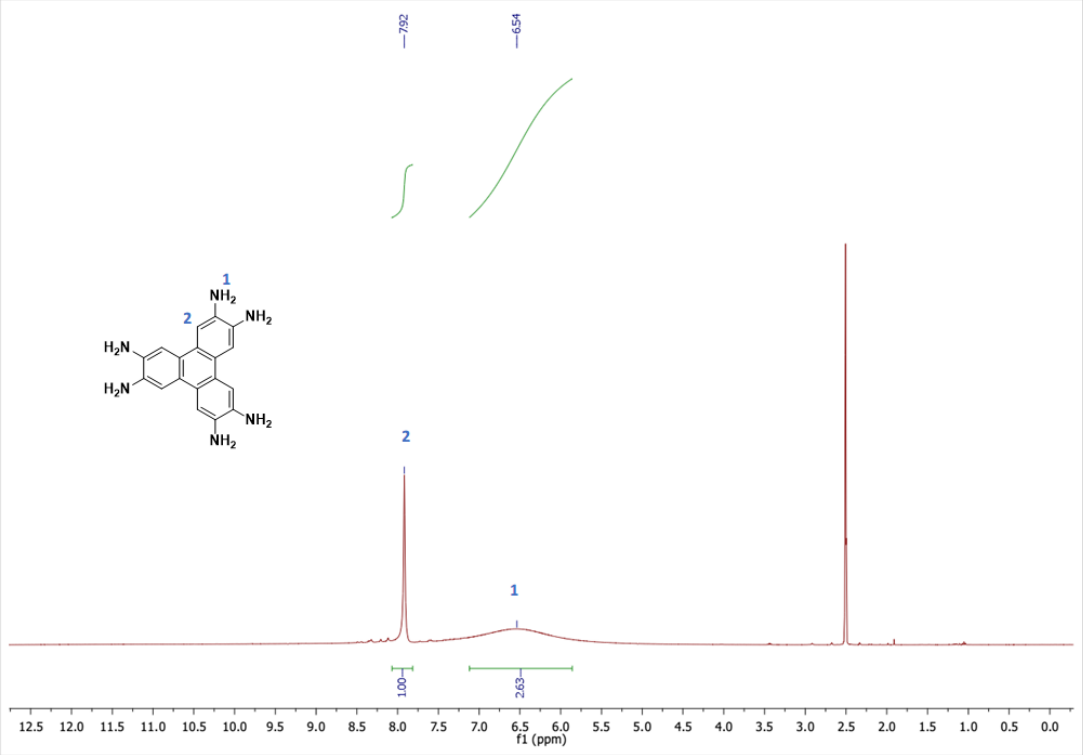

Figure 2.4.3. ^1H NMR of 2, 3, 6, 7, 10, 11-Hexaaminetriphenylene·6HCl (400 MHz, DMSO-d_6).

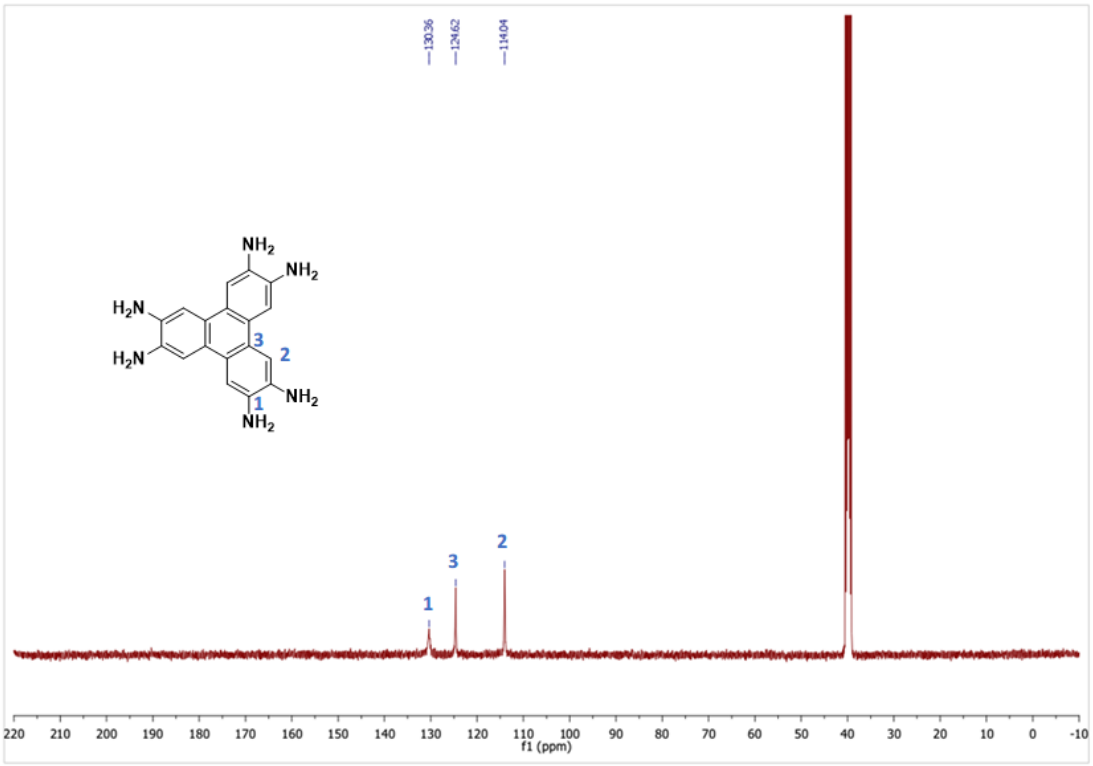

Figure 2.4.4. ^{13}C NMR of 2, 3, 6, 7, 10, 11-Hexaaminetriphenylene·6HCl (100 MHz, DMSO-d_6).

2.4.3.2 Synthesis of Model compound

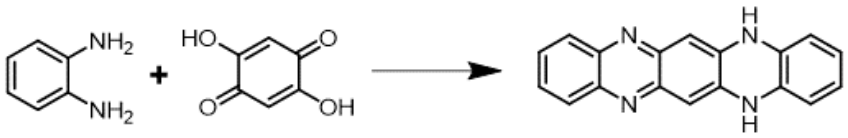

Scheme 2.4.2. Synthesis route of model compound (fluorindine).

Fluorindine: The synthesis is followed by precedure of the literature before.[19] 2,5-dihydroxy-1,4-benzoquinone (0.42 g, 3 mmol) and 1,2-phenylediamine (1.62 g, 15 mmol) were mixed well and ground together with a mortar and pestle. The resulted mixture was heated to 150 ℃ for 24 hours under N_2 atmosphere. The crude product was cooled to room temperature and ground with acetone. The resulting slurry was filtered, washed with acetone for several times, and dried under vacuum. 0.67 g of fluorindine was obtained as dark purple powder in a yield of 78%. ^{1}H-NMR (DMSO-d_6) δ(ppm) (**Figure 2.4.5.)**: 9.70 (s, 2 H), 7.67 (dd, 2 H), 7.43 (dd, 2 H), 6.61 (dd, 2 H),

6.49 (dd, 2 H), 6.34 (s, 2 H); ^{13}C-NMR was tested by ss-NMR (CP/ MAS) due to the low solubility (**Figure 2.4.6.**). MALDI-TOF MS for $C_{18}H_{12}N_4$: cald. for ($[M]^+$): 284.11, found: 284.108.

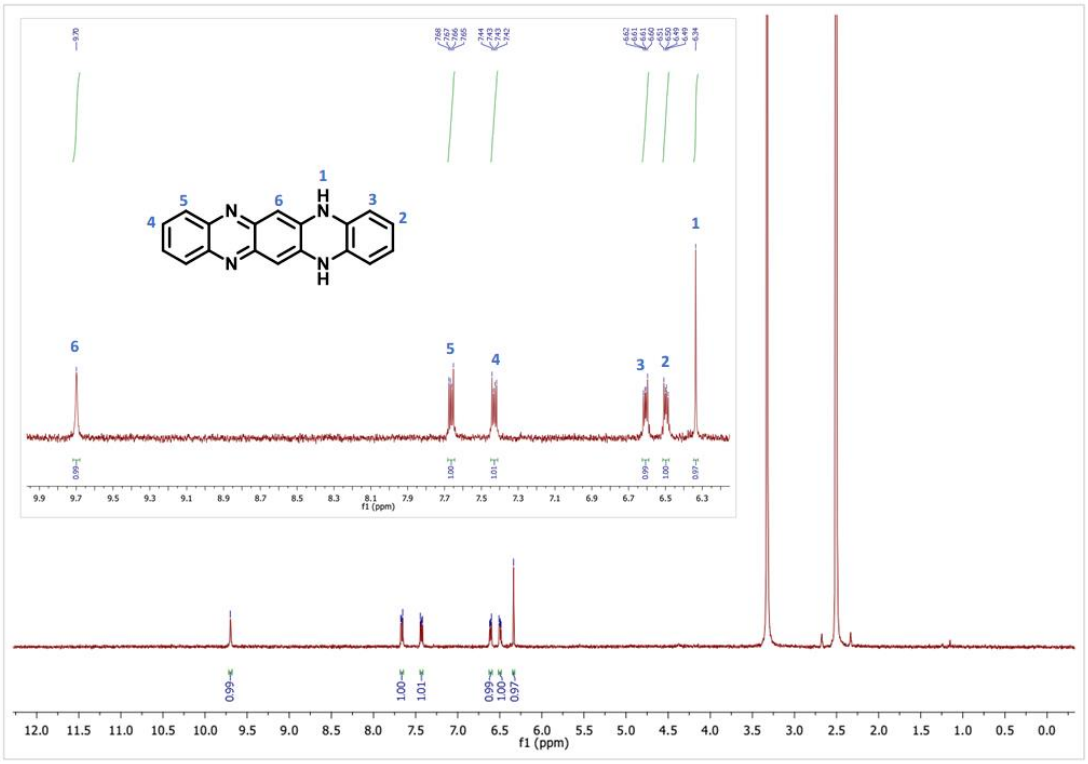

Figure 2.4.5. ^{1}H NMR of fluorindine (400 MHz, DMSO-d_6).

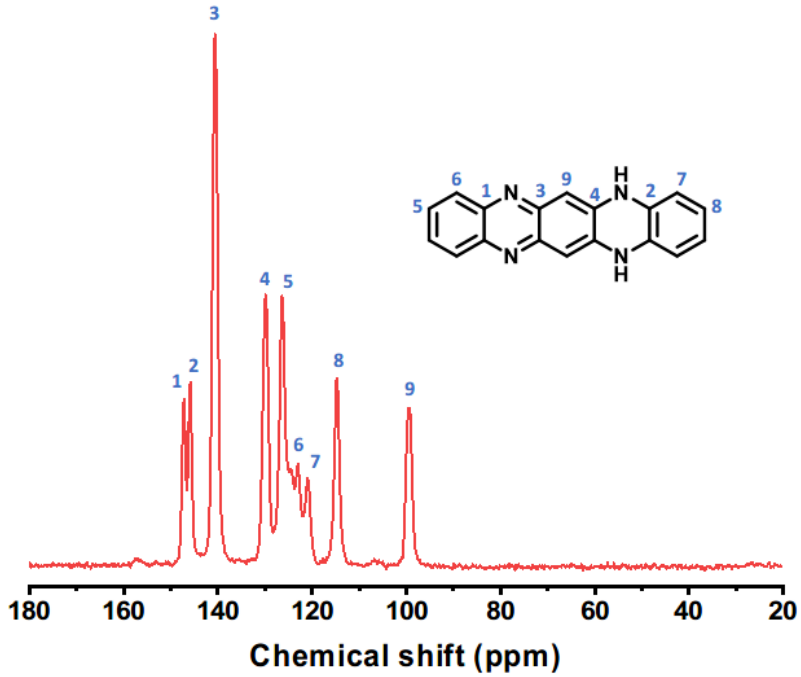

Figure 2.4.6. Solid-state ^{13}C cross-polarization magic angle spinning (CP/ MAS) NMR of fluorindine.

2.4.3.3 Synthesis of Fluorindine-Linked Covalent Organic Framework

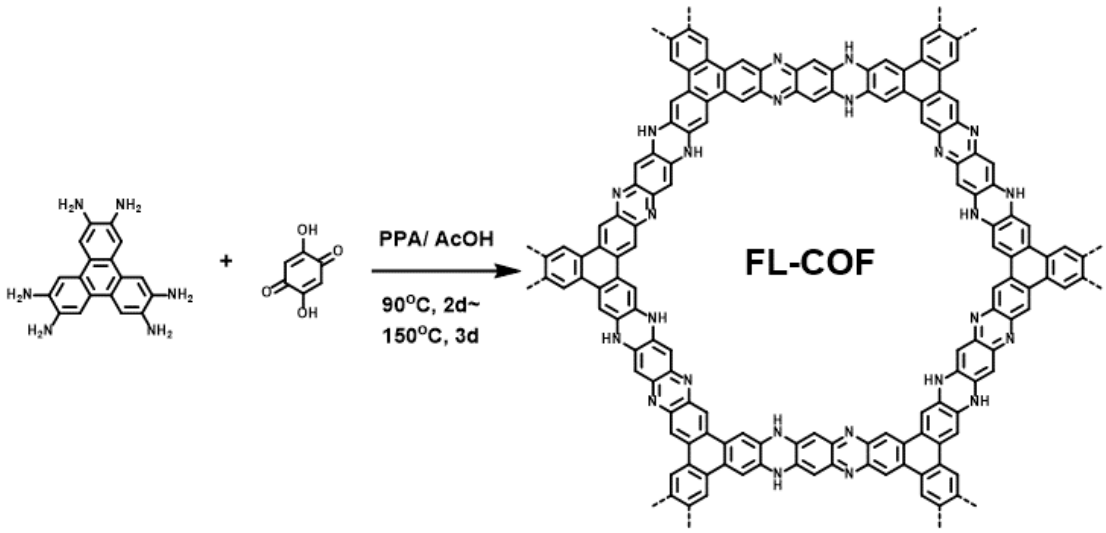

Scheme 2.4.3. Synthesis route of FL-COF.

To a dried Pyrex tube, HAT·6HCl (26.87 mg, 0.05 mmol), 2,5-dihydroxy-1,4-benzoquinone (10.51 mg, 0.075 mmol, 1.5 eq.), glacial acetic acid (1.0 mL) and 1 drop

of degassed polyphosphoric acid were charged in sequence. After sonication for 5 min, the tube was flash frozen at 77 K (liquid N_2 bath). After three freeze-pump-thaw cycles, the tube was placed in an oven of 90 °C for 3 days, and then 150 °C for 2 days. The resulting solid was collected *via* filtration, briefly washed with acetone, ethanol and water. The wet solid was transferred to a Soxhlet extractor and thoroughly washed with THF and methanol for 24 h, respectively. Following that, the sample was evacuated at 80 °C for 12 h in vacuum oven to yield product as black powder (18.1 mg, 86%).

2.4.4 Preparation of Electrode and Assembly of Supercapacitor Device

The electrochemical experiments were carried out using aqueous three-electrode system or symmetric two-electrode device employing 1 M H_2SO_4 as electrolyte at ambient temperature. The three-electrode system incorporates Ag/AgCl electrode (Argenthal, 3 M KCl, 0.207 V vs. standard hydrogen electrode at room temperature) as reference electrode, Pt as counter electrode and FL-COF as working electrode. The working electrode was prepared by grinding active materials (FL-COF, 70 wt.%), conductive additive (acetylene black, 20 wt.%), and binder (polyvinylidene fluoride, 10 wt.%) with N-methylpyrrolidinone (NMP) in a mortar. The graphite substrate (10 ×10 × 5 mm) current collector was coated with the slurry, dried under vacuum at 80 °C for 12 hours and weighted before using. The two-electrode device was assembled by two as-mentioned working electrodes with same mass loading of active material.

2.5 Results and Discussion

2.5.1 The optimization of Synthesis of FL-COF

A fluorindine COF (**FL-COF)** was prepared by the condensation of hexaminetriphenelne (HAT) and 2, 5-dihydroxy-1, 4-benzoquinone (DHQ) using catalytic polyphosphoric acid in acetic acid in 86% yield (**Scheme 2.4.3**). After screening several different solvents and reaction temperatures, we found that applying a temperature gradient (90 ℃ for 72 hours and then 150 ℃ for 48 hours) gave the highest crystallinity (**Table 2.5.1 and Figure 2.5.1**). A model compound was prepared

by the condensation of 1, 4 diaminobenzene and 2, 5-dihydroxy-1, 4-benzoquinone under the same reaction condition in 78% yield (**Scheme 2.4.2**).

Table 2.5.1. Synthetic conditions screened for the synthesis of FL-COF.

Sample	Temperature and Time	Solvents	Catalyst	Crystallinity[a]
FL-COF-a	150 °C, 96 h	AcOH	None	46%
FL-COF-b	120 °C, 72 h	AcOH	None	34%
FL-COF-c	120 °C, 72 h	Mesitylene: Ethylene glycol = 1:1	AcOH	56%
FL-COF-d	90 °C, 72 h	AcOH	None	53%
FL-COF-e	150 °C, 72 h	AcOH	None	35%
FL-COF-f	120 °C, 72 h + 150 °C, 48 h	AcOH	None	54%
FL-COF-g	90 °C, 72 h + 120 °C, 48 h	AcOH	None	39%
FL-COF-h	90 °C, 72 h + 150 °C, 48 h	AcOH	None	100%
FL-COF-i	90 °C, 72 h + 150 °C, 48 h	AcOH	PPA	98%
FL-COF-j	120 °C, 72 h	AcOH	H_2SO_4	94%

Crystallinity[a]: The crystallinity is evaluated based on the intensity of (1, 1, 0) peak in FL-COF-h.

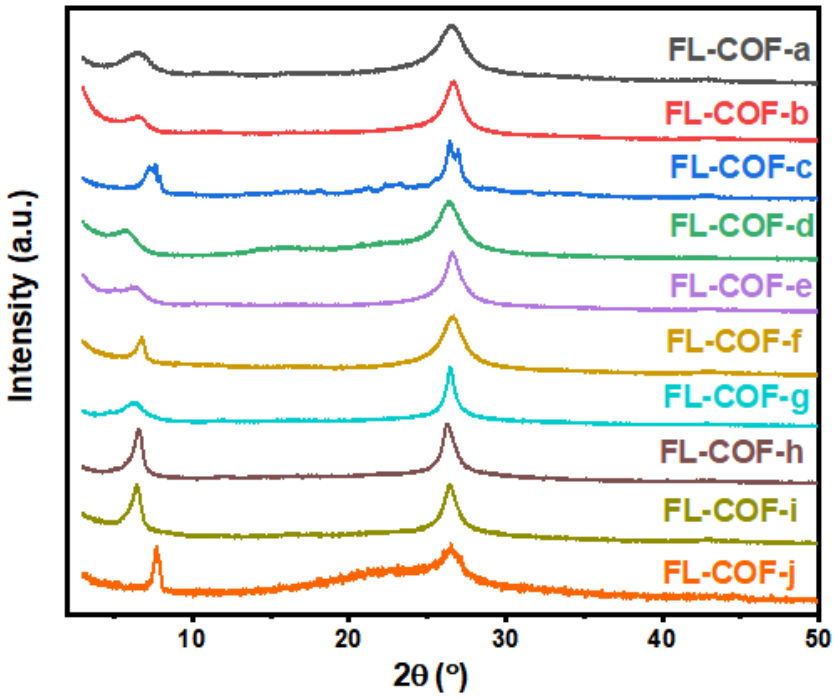

Figure 2.5.1. PXRD patterns of FL-COFs synthesized with indicated conditions.

2.5.2 Characterization of Chemical Structures

The formation of the fluorindine linkages was confirmed by Fourier transform infrared (FT-IR) spectroscopy (**Figure 2.5.2a**). Strong absorption peaks at around 1624 cm^{-1}, 1520 cm^{-1}, 1150 cm^{-1} and 850 cm^{-1} correspond to -C=N-, -C-NH- and aromatic phenazine ring stretching vibrations, respectively. This coincides with the disappearance of the C=O (~1710 cm^{-1}) and O-H (~ 3295 cm^{-1}) stretching bands from the DHQ monomer and the NH_2 (~ 3219 cm^{-1} and 3340 cm^{-1}) from the HAT monomer.

^{13}C cross-polarization magic angle spinning (CP-MAS) solid-state NMR spectroscopy confirms the presence of C=N (155 ppm) and C-N (130 ppm) carbons of the fluorindine group (**Figure 2.5.2b**).

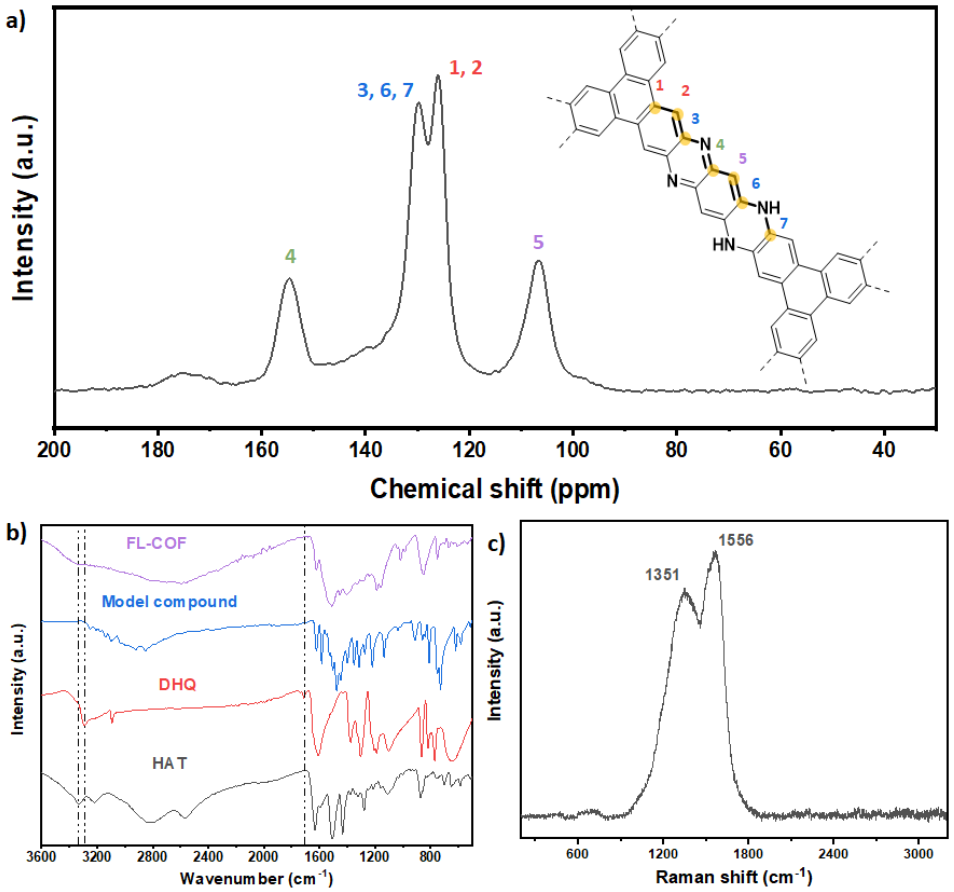

Figure 2.5.2. (a) Solid-state ^{13}C cross-polarization magic angle spinning (CP/MAS) NMR of FL-COF. Insert shows the chemical structure of FL-COF with the assignments for the ^{13}C chemical shifts. (b) FT-IR spectra of FL-COF (purple), model compound (blue), DHQ (red) and HAT (black). (c) Raman spectra of FL-COF. (d) C 1s binding energy profiles of FL-COF. (e) N 1s binding energy profiles of FL-COF.

The Raman spectra further confirms the presence of C=N and C-N stretching at 1351 cm^{-1} and 1556 cm^{-1}, respectively, which belong to the different N species in fluorindine linkages (**Figure 2.5.2c**).

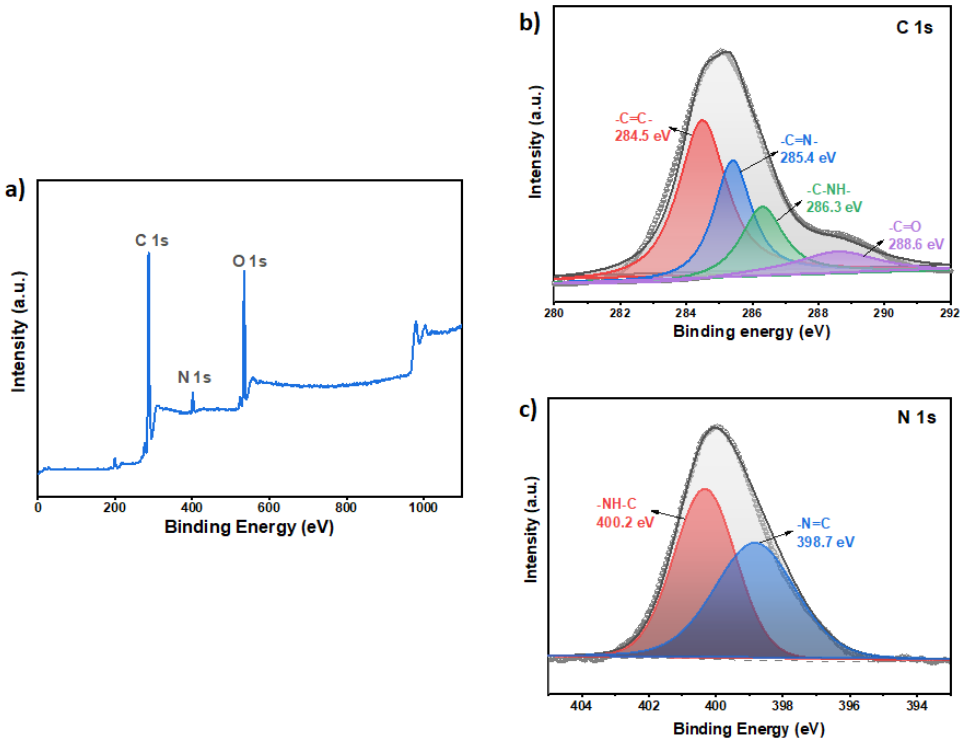

Figure 2.5.3. (a) Overall XPS spectra of FL-COF. (b) C 1s binding energy profiles of FL-COF. (c) N 1s binding energy profiles of FL-COF.

X-ray photoelectron spectrometry (XPS) revealed C 1s, N 1s, and O 1s peaks with binding energies of 284.8 eV, 400.0 eV and 532.0 eV, respectively (**Figure 2.5.3a**). The small amount of O 1s observed can be ascribed to remaining oxygen-containing groups at the edges of the material and potentially absorbed atmospheric air/moisture.[24] The C 1s curve-fit spectra of **FL-COF** shows four sub-peaks at 284.5 eV, 285.4 eV, 286.3 eV and 288.6 eV (**Figure 2.5.3b**), which can be attributed to C=C (sp^2), C=N (sp^2), C-N (sp^3) and C=O groups, respectively. In addition, the N 1s curve-fit spectra also exhibited two different nitrogen configurations N=C (398.7 eV) and N-C (400.2 eV) (**Figure 2.5.3c**). The representative integral peak area ratio of N=C and N-C is close to 1:1, which is in good agreement with the theoretical calculation.

2.5.3 Characterization of Crystallinity and Morphologies

Powder X-ray diffraction (PXRD) measurements indicated that **FL-COF** is crystalline and adopts an ABC staggered structure (**Figure 2.5.4a**). The experimental PXRD pattern displayed intense Bragg peaks at 6.6° and 26.2°, corresponding to (1,1,0), and (1,0,-2) planes with a weaker signal at 12.1° corresponding to the (3,0,0) plane according to the simulated PXRD pattern (**Figure 2.5.4b**). The Pawley refined pattern is close to the experimental data with R_{wp}= 3.32% and R_p= 2.66%, which confirms the structure modelled in the trigonal space group *R-3* with the unit cell values $a = b =$ 27.125 Å, $c =$ 5.716 Å, $\alpha = \beta = 90^{o}$, $\gamma = 120^{o}$. Calculating from the *d*-spacing of (001) plane, the interlayer distance of π-π stacking of **FL-COF** is 0.34 nm, which correlates well with interlayer distances observed in the lattice by transmission electron microscopy (TEM) microscopy (**Figure 2.5.5d**).

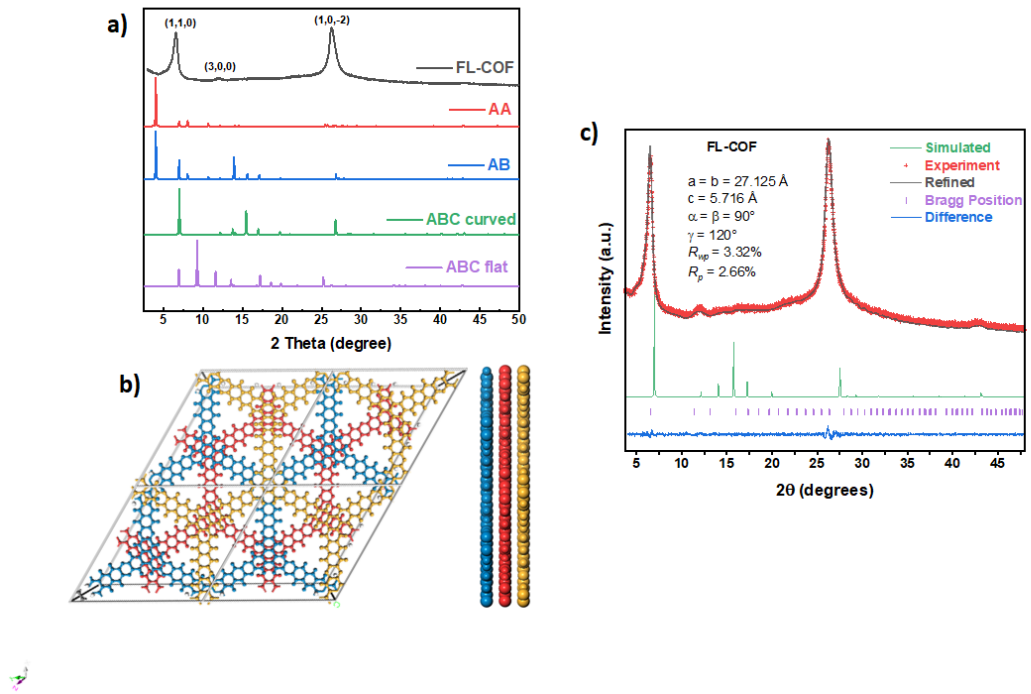

Figure 2.5.4. (a) Experimental PXRD patterns of FL-COF (black) and the simulated PXRD pattern with different stacking modes: AA (red), AB (blue), ABC (green). (b) Top and side views of simulated structure (ABC stacking mode) of FL-COF. (c) Crystal structure of FL-COF. Experimental diffraction patterns (red), profiles calculated from Pawley fitting (black) showing

the residual (blue), and pattern simulated from the structural model with ABC stacking (green). Reflection positions are shown by tick marks (purple).

The morphology of **FL-COF** was investigated by scanning electron microscopy (SEM) and TEM. SEM images revealed a cubic-like polyhedron morphology with the average particle sizes around 2 μm (**Figure 2.5.5a-b**). To avoid the interference of bulk structure from irregular stacking, we selected the area of thinner layer for taking TEM images. The TEM images clearly show the long-range ordered lattice of self-assembled nanosheets. Lattice fringes with a distance of 0.34 nm, could also be visualised, and are attributed to the (001) plane of **FL-COF** (**Figure 2.5.5c-d**). It is worth noting that COF materials including FL-COF are a kind of organic materials which are not stable under a strong electron beam, thus a short irradiation time should be controlled to get clear lattice stripes.

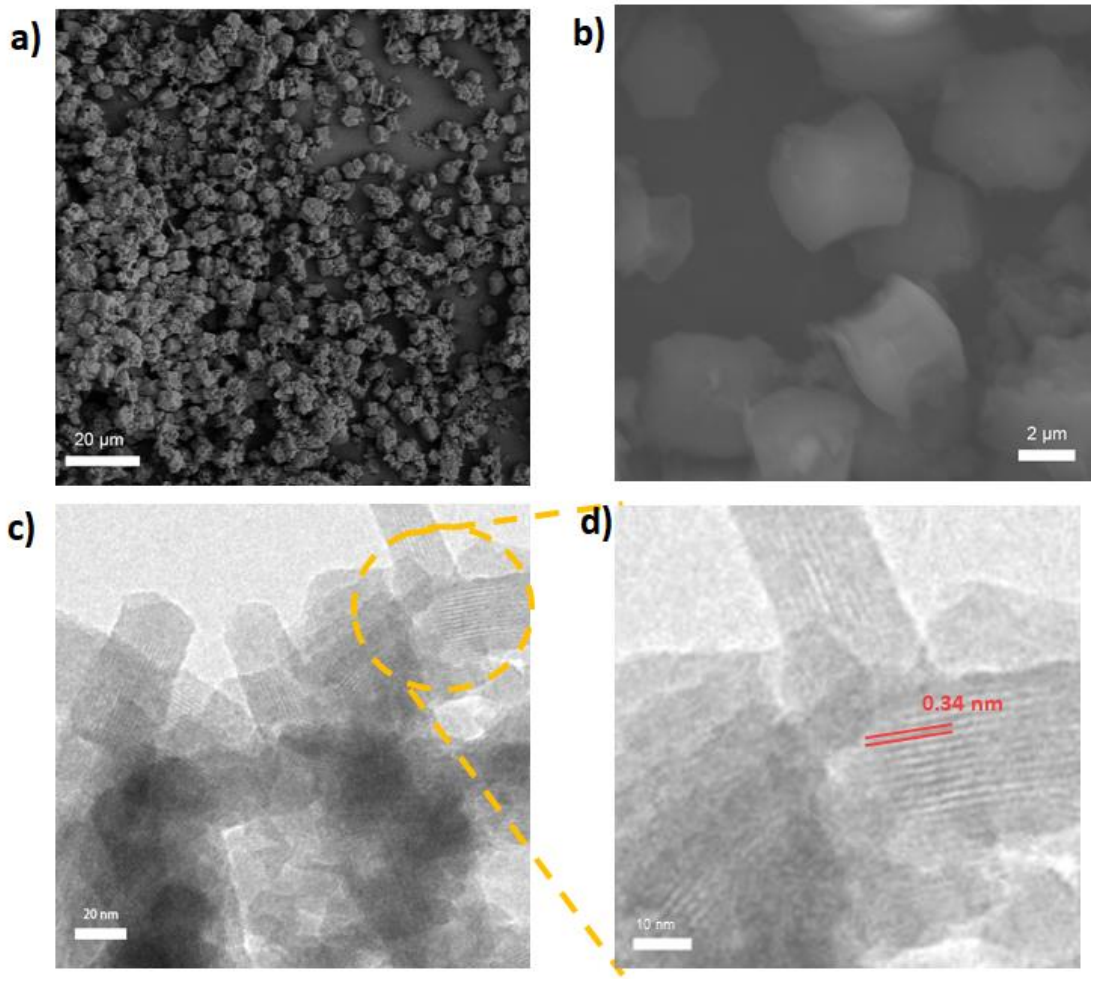

Figure 2.5.5. (a-b) SEM images of FL-COF. (c-d) TEM images of FL-COF.

2.5.4 Characterization of Porous Properties and Stability

The N_2 adsorption measured at 77 K exhibits an isotherm with type II shape (**Figure 2.5.6a**). Similar to other π-conjugated COFs with ABC stacking, **FL-COF** shows a low Brunauer-Emmett-Teller specific surface area (SA_{BET}) of 19 $m^2\ g^{-1}$ (from the pressure region of p/p_0 = 0.05-0.35), which is presumably due to the slipped π-π stacking caused by the interlayer repulsion between polarized fluorindine linkages.[13, 15]

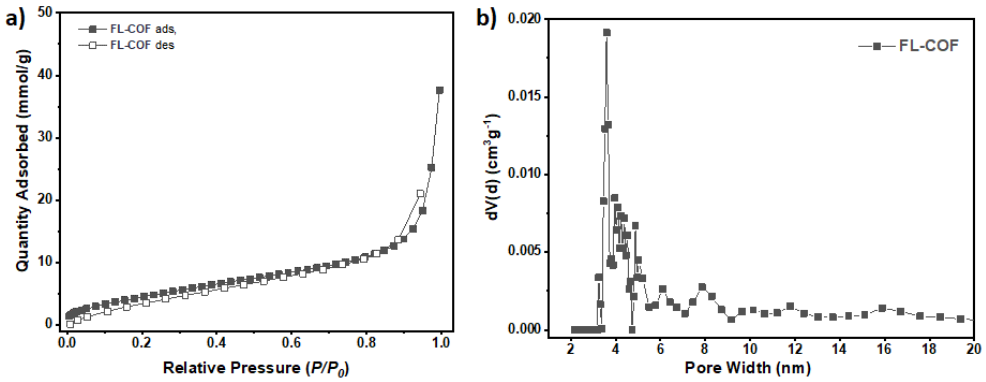

Figure 2.5.6. (a) Nitrogen adsorption and desorption isotherms for FL-COF recorded at 77 K (filled symbols= adsorption; open symbols= desorption). (b) Pore size distribution of FL-COF calculated by NLDFT method.

Thermo-gravimetric analysis (TGA) under nitrogen atmosphere shows that the weight of sample can still remain at 75% up to 400°C, indicating good thermal stability (**Figure 2.5.7**).

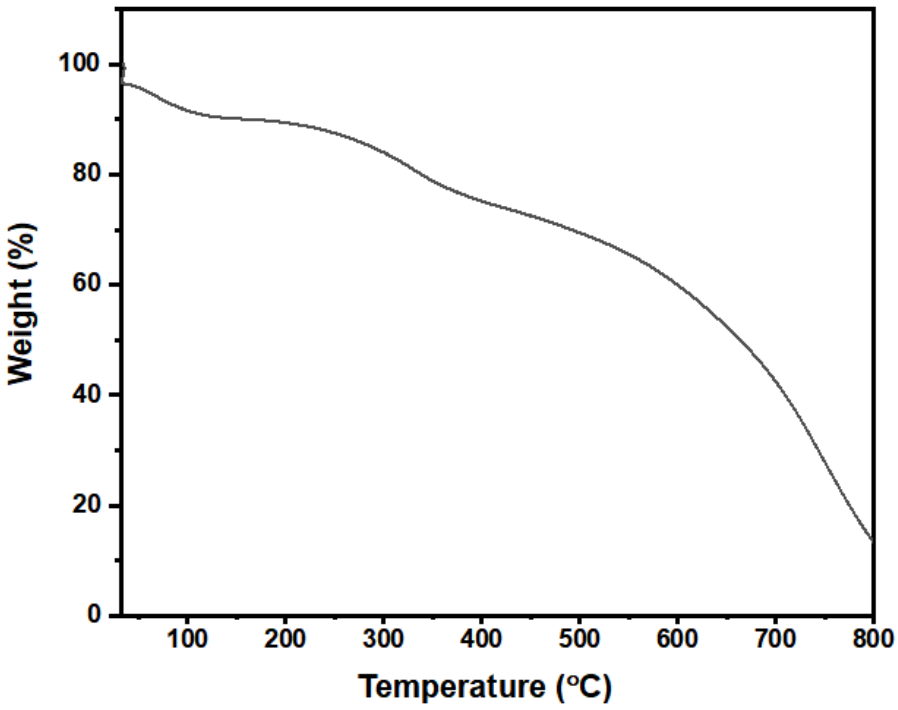

Figure 2.5.7. TGA curves of FL-COF.

We also investigated the chemical stability by immersing FL-COF into solvents (boiling water, THF and DMF) and traditional electrolytes (1 M H_2SO_4 aqueous solution and 6 M KOH aqueous solution) for 48 hours. Benefited from the ladder-type fluorindine linkages, FL-COF showed a good stability in all the conditions, indicating a rational usage as the electrode material in acid or base electrolytes (**Figure 2.5.8**).

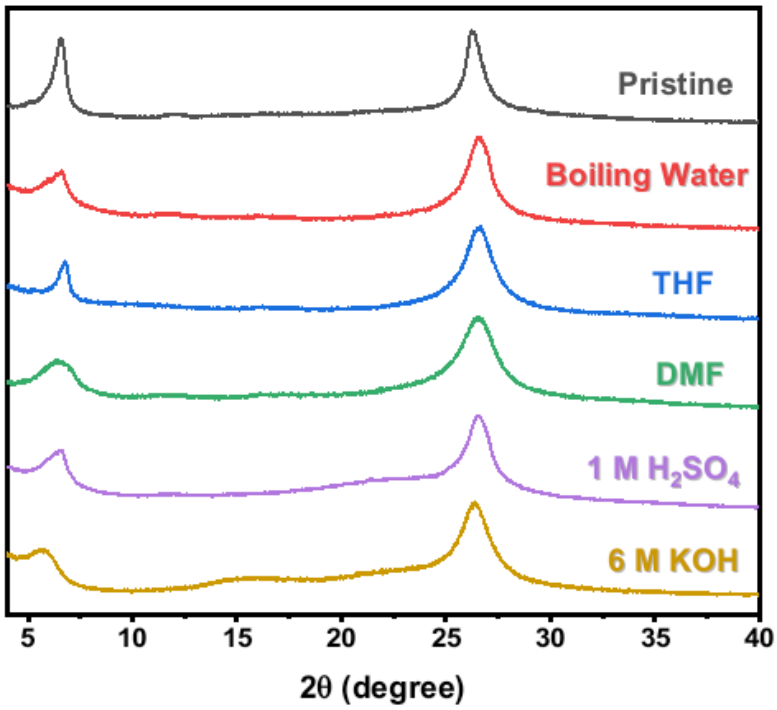

Figure 2.5.8. PXRD patterns of FL-COF after stability test by various solvents (Boiling water: 100 ℃ for 48 h; THF and DMF: 25 ℃ for 48 h) and electrolyes (1 M H_2SO_4 aqueous solution and 6 M KOH aqueous solution: 25 ℃ for 48 h).

2.5.5 Electrochemical Properties and Supercapacitive Performance

2.5.5.1 Elctrochemical Properties from Three-electrodes System

To evaluate the electrochemical performance of **FL-COF**, a three-electrode system was initially setup with 1 M H_2SO_4 aqueous solution as the electrolyte. Cyclic voltammetry (CV) curves were measured at different scan rates (10 to 1000 mV s^{-1}) within the potential window of -0.2 to 0.8 V. From the CV curves at the scan rates of 10 mV s^{-1}, two pairs of redox peaks can be observed at 0.39/ 0.28 V and 0.23/ -0.03 V (vs. Ag/ AgCl), respectively, indicating a multiple state reversible conversion of four electrons redox process based on the fluorindine linkages (**Figure 2.5.9**).

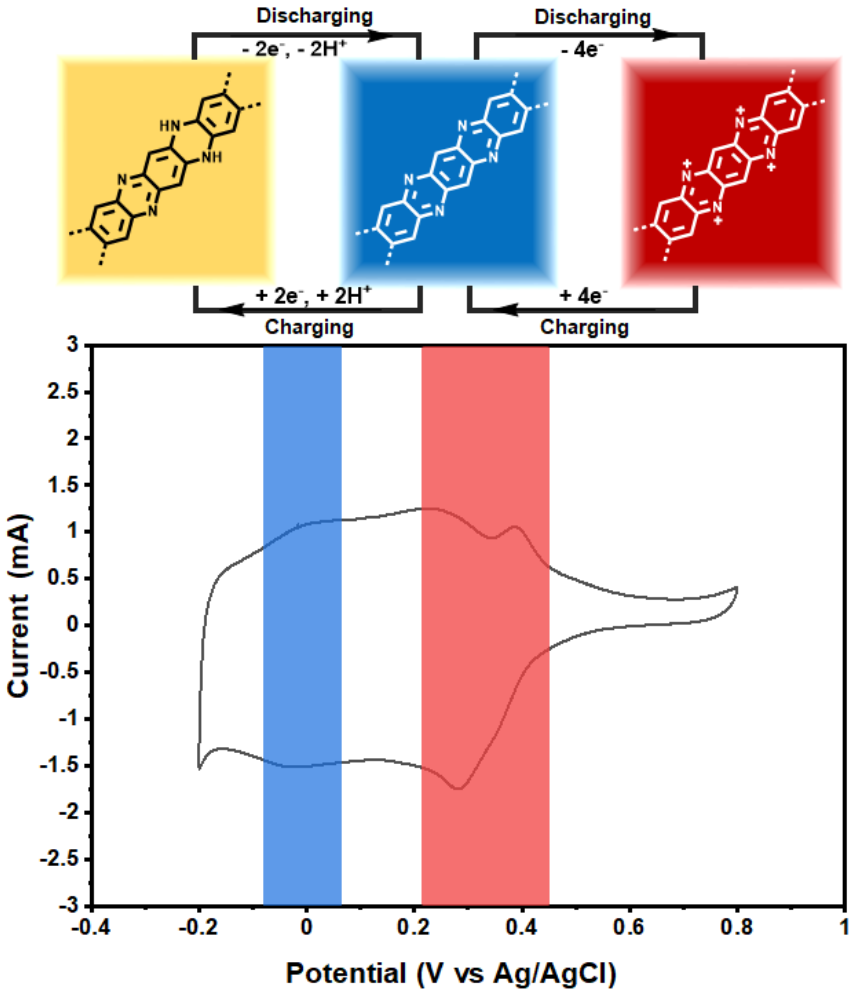

Figure 2.5.9. The proposed mechanism of redox process based on fluorindine unit and the cyclic voltammograms curves of FL-COF at the scan rate of 10 mV s^{-1} (In standard three electode supercapacitor system: FL-COF, platinum flakes, Ag/AgCl electrode and 1 M H_2SO_4 aqueous solution were used as working electrode, counter electrode, reference electrode and electrolyte, respectively).

These redox processes contribute to Faradic pseudocapacitance during scanning and therefore the integral area of the CV curve is much larger compared with carbon black, for example, indicating the capacitance of the working electrode is almost entirely from **FL-COF** (**Figure 2.5.10)**.

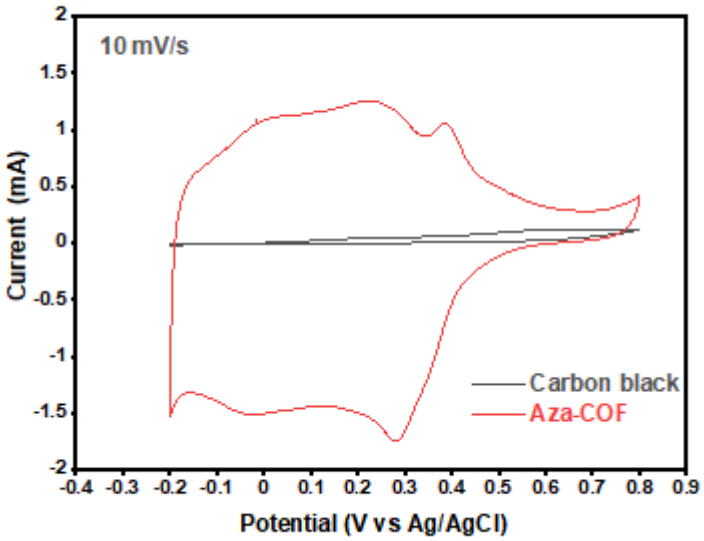

Figure 2.5.10. Cyclic voltammograms curves of FL-COF (red) and carbon black (black) at the scan rate of 10 mV s^{-1} (In standard three electode supercapacitor system: FL-COF, platinum flakes, Ag/AgCl electrode and 1 M H_2SO_4 aqueous solution were used as working electrode, counter electrode, reference electrode and electrolyte, respectively).

The separation between reductive and oxidative peaks is small, demonstrating a fast electron transfer during the redox process. The CV curves from 10 to 1000 mV s^{-1} also show clear redox peaks, denoting a good electrochemical behaviour even at high scan rates (**Figure 2.5.11a**).

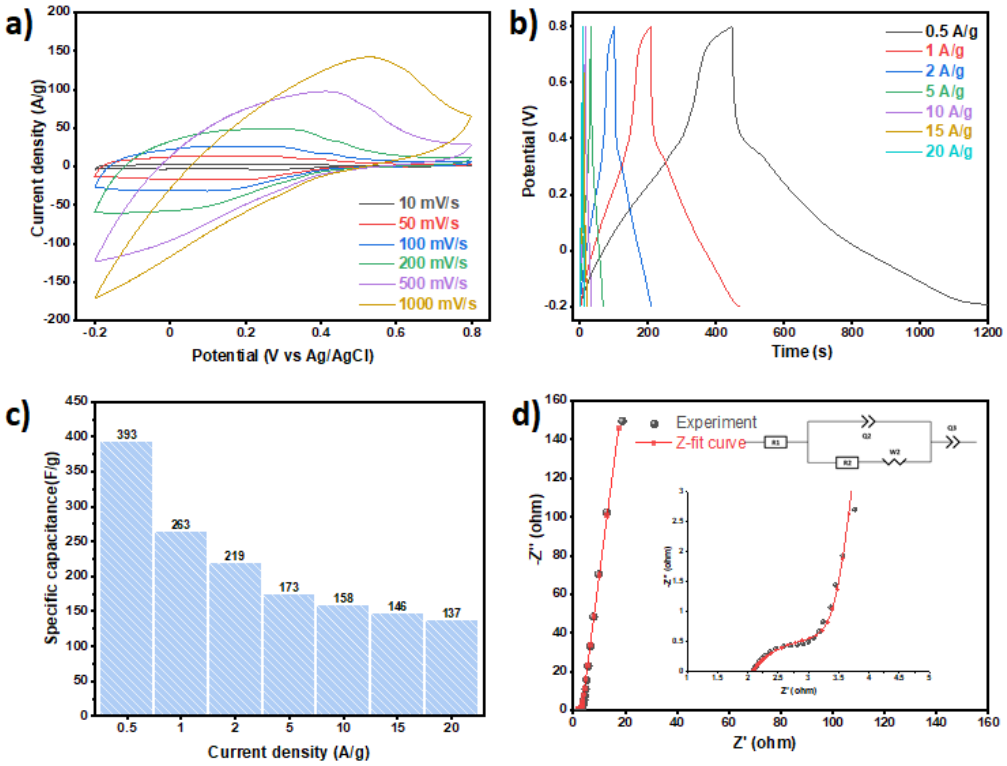

Figure 2.5.11. Electrochemical performance of three-electode supercapacitor system: FL-COF, platinum flakes, Ag/AgCl electrode and 1 M H_2SO_4 aqueous solution were used as working electrode, counter electrode, reference electrode and electrolyte, respectively (a) Cyclic voltammograms curves of FL-COF at the scan rates from 10 mV s^{-1} to 1000 mV s^{-1}. (b) Galvanostatic charge–discharge curves of FL-COF at the current densities from 0.5 A g^{-1} to 20 A g^{-1}. (c) Specific capacitance at various current densities. (d) Nyquist plots (black) with the *Z*-fit curve (red). Inset shows the enlarged part of the high-frequency region and equivalent circuit.

Galvanostatic charge-discharge (GCD) tests with current densities from 0.1 A g^{-1} to 10 A g^{-1} were carried out to further verify this observation. All the GCD profiles of **FL-COF** exhibit a triangular shape with two plateaus at around 0.4 V and 0.2 V, which can be attributed to the two redox peaks observed in the CV curves and indicate the pseudocapacitive characteristics of **FL-COF** (**Figure 2.5.11b**). This phenomenon is seen in other COF materials with redox-active sites. The charge storage capacity of **FL-COF** is likely a combination of both pseudocapacitive and EDLCs capacitance. The specific capacitance calculated using the slope of the discharge curve at current density of 0.5 A g^{-1} is approximately 378 F g^{-1}, which is higher than many state-of-the-art COF-based materials (**Table 2.5.1**). At high current density, the curves still show nearly symmetrical triangular shapes, suggesting fast ion and electron transport within the **FL-**

COF electrodes. The specific capacitance remains high when the current density is increased to 10 A g^{-1} (158 F g^{-1}) and 20 A g^{-1} (137 F g^{-1}) indicating a good rate performance (**Figure 2.5.11c**).

Table 2.5.1. Comparison of gravimetric capacitances of various COF-based electrode materials reported in the literature.

Materials	Gravimetric capacitance (F g^{-1})	Current density (A g^{-1})	Electrolytes	Refer.
Aza-CMP@350	508	0.5	6 M KOH	[25]
TPT-DAHQ COF	256	0.5	1 M KOH	[26]
PDC-MA COF	355	1	6 M KOH	[27]
DAB-TFP COF	15	0.1	1 M H_2SO_4	[28]
[TEMPO]100%-NiP-COF	167	0.1	0.1 M $(C_4H_9)_4NClO_4$	[29]
[TEMPO]50%-NiP-COF	124	0.1	0.1 M $(C_4H_9)_4NClO_4$	
TPA-COF-1	51.3	0.2	0.5 M H_2SO_4	[30]
TaPa-Py COF	209	0.5	1 M H_2SO_4	[31]
TPPDA-TPPyr COF	188.7	2	1 M KOH	[32]
TpPa-$(OH)_2$	416	0.5	1 M phosphate buffer	[33]
FL-COF	398	0.5	1 M H_2SO_4	This work

The kinetic behaviour of **FL-COF** was studied by electrochemical impedance spectroscopy (EIS) measurement in the frequency range 100 kHz to 0.01 Hz. Nyquist plots show a small quasi-semicircle in the high-frequency range, followed by a straight sloped line in the low-frequency region (**Figure 2.5.11d**). The curve was fitted with a suitable equivalent circuit by using the *Z*-fit method. The intercept with the Z' axis is around 2.1 Ω, representing internal resistance that derives from the resistance of the electrolyte. The diameter of the high-frequency semi-circle corresponds to the charge transfer resistance (R_{CT}) of the electrode kinetics. **FL-COF** possesses a R_{CT} of 1.43 Ω, which is significantly lower than that of other 2D porous materials (**Table 2.5.2**).

Table 2.5.2. Comparison of charge transfer resistance (R_{ct}) of various COF-based electrode materials reported in the literature.

Materials	Charge transfer resistance (Ω)	Electrolytes	Refer.
DAAQ-COF	199	1 M LiTFSI	[34]
DAAQ-ECOF	149		
(C60)0.025-COF	7.84	1 M Na_2SO_4	[35]
(C60)0.025-COF	1.38	1 M Na_2SO_4	
(C60)0.025-COF	6.72	1 M Na_2SO_4	
(C60)0.025-COF	12.63	1 M Na_2SO_4	
PI-COF	120	1 M LiTFSI	[36]
PANI@TCOF-1	10.5	1 M H_2SO_4	[37]
PANI@TCOF-2	1.60	1 M H_2SO_4	
Aza-CMP@350	1.40	6 M KOH	[25]
FL-COF	1.43	1 M H_2SO_4	This work

In the low-frequency region, **FL-COF** displays linear plots with a relatively large slope, indicating a low diffusive resistance of electrolyte ion within the hierarchical pores. Lower diffusion resistance can lead to easier permeation of electrolyte ions in the pore channels, which can further improve the rate of the electrode. This performance can be attributed to the good charge mobility improved by the ladder-like conjugated skeleton of **FL-COF**.

2.5.5.2 Supercapacitive Performance from Two-electrodes Device

Based on the excellent electrochemical properties of **FL-COF**, we further investigated the particle performance of a two-electrode symmetric supercapacitor device with **FL-COF** as the electrode. We assembled 5 supercapacitor devices for each electrochemical test to make sure the results are reproducible. The basic electrochemical performance of the supercapacitor device was tested with the potential window retained at 1 V. As shown in **Figure 2.5.12a-b**, the CV and GCD curves of the **FL-COF**-based supercapacitor device shows similar results with those tested by the three-electrode system. The specific capacitances of the device at different current density (0.1-20 A g^{-1}) calculated from discharge part of GCD curves are listed in the **Table 2.5.3**.

Table 2.5.3. Gravimetric capacitances, energy density and power density of the FL-COF based supercapacitor device.

Sample	Current density (A g^{-1})	Gravimetric capacitance (F g^{-1})	Energy density (Wh kg^{-1})	Power density (kW kg^{-1})
FL-COF	0.1	362	50.28	0.2
	0.25	230	31.94	0.5
	0.5	182	25.28	1
	1	152	25.11	2.37
	2.5	118	16.39	5

5	92	12.78	10
10	66	9.17	20
20	59	8.19	39.79

Notably, the Ragone plots (energy vs. power density) are shown in **Figure 2.5.12c**. The maximum energy density of the supercapacitor device based on **FL-COF** is 50.28 Wh kg^{-1} at the power density of 200 W kg^{-1}, which is higher than many other COF or nitrogen-doped porous carbon materials. The excellent energy density can be attributed to the added pseudocapacitance from the redox-active sites of the fluorindine linkage. Meanwhile, the fully conjugated fluorindine linkage also improves the electron transfer ability and hence in addition, the supercapacitor device exhibits almost no loss in Coulombic efficiency with 77% capacitance retention even after 10000 cycles under a large current density of 20 A g^{-1} (**Figure 2.5.12d**). There is no significant change to the CV curves, GCD curves and Nyquist plots after long-term cycling experiments (**Figure 2.5.12e-f**). These results indicate the device has an outstanding cycle life.

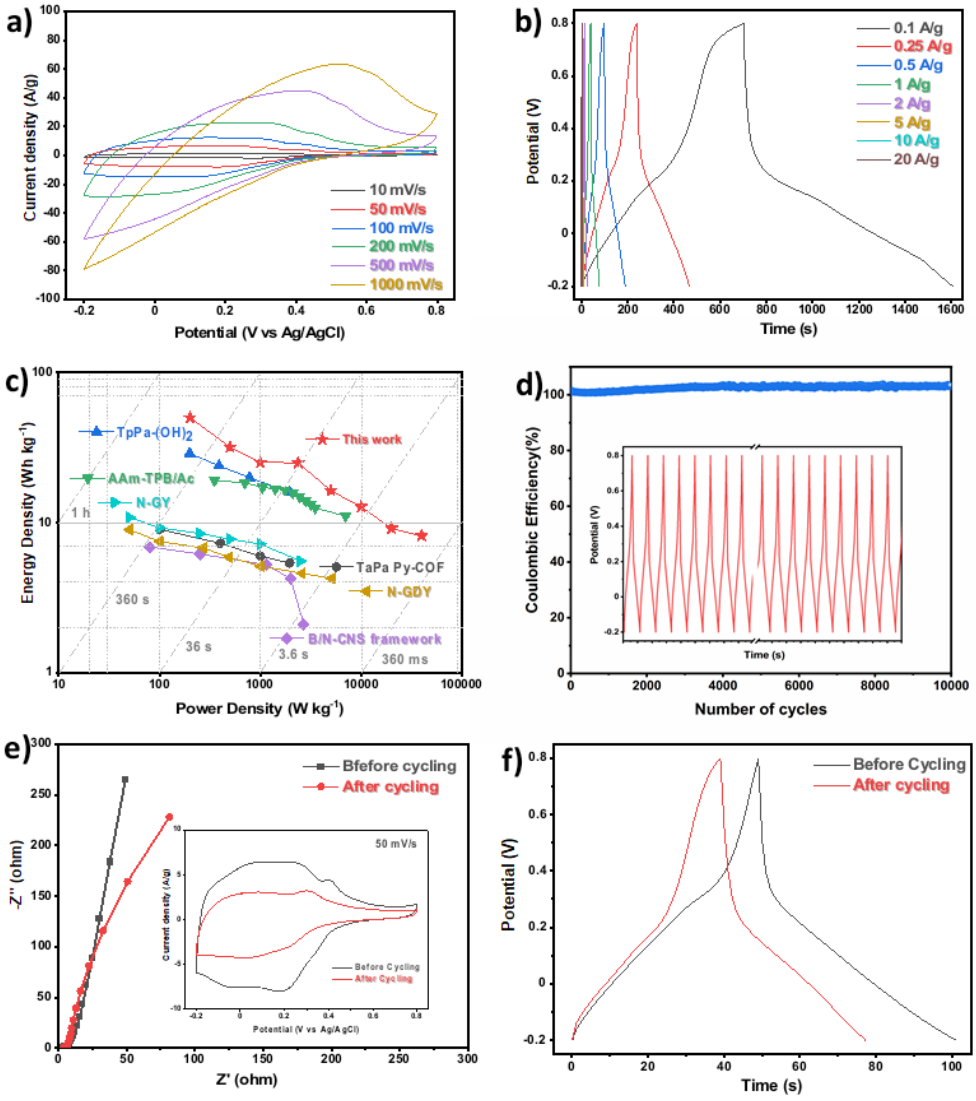

Figure 2.5.12. Electrochemical performance of two-electrode supercapacitor device (FL-COF and 1 M H_2SO_4 were used as electrode and electrolyte, respectively): (a) Cyclic voltammograms curves of FL-COF based supercapacitor device at the scan rates from 10 mV s^{-1} to 1000 mV s^{-1}. (b) Galvanostatic charge-discharge curves of FL-COF based supercapacitor device at the current densities from 0.5 A g^{-1} to 20 A g^{-1}. (c) Ragone plots of gravimetric energy density versus power density. (d) Capacitance for a 10000-cycle charge-discharge stability tested at a current density of 20 A g^{-1}. Inset shows the charge-discharge curve during a test of 10000 cycles. (e) Nyquist plots of FL-COF based supercapacitor device. Inset shows the CV curves comparison of FL-COF based supercapacitor device before and after 10000-cyclic performance at the scan rates of 50 mV s^{-1}. (e) GCD curves comparison of FL-COF based supercapacitor device before and after 10000-cyclic performance at the current densities from 20 A g^{-1}.

2.6 Conclusions

In summary, we report a new fluorindine-based COF (**FL-COF**) with excellent capacitance of 393 F g^{-1} at 0.5 A g^{-1} and high energy and power densities reaching 50.28 Wh kg^{-1} and 39.79 kW kg^{-1} respectively. The high performance can be attributed to the redox-active fluorindine groups connected through planar highly conjugated building blocks allowing reversible four electron redox processes and fast inter- and intra-layer charge transfer. We expect these design principles will be adopted by other research groups and accelerate the development of high performance redox-active ladder COF materials for energy storage.

2.7 References

1. Winter, M.; Brodd, R. J., What are batteries, fuel cells, and supercapacitors? *Chem. Rev.* **2004**, 104 (10), 4245-4270.

2. Simon, P.; Gogotsi, Y.; Dunn, B., Where do batteries end and supercapacitors begin? *Science* **2014**, 343 (6176), 1210-1211.

3. Raza, W.; Ali, F.; Raza, N.; Luo, Y.; Kim, K.-H.; Yang, J.; Kumar, S.; Mehmood, A.; Kwon, E. E., Recent advancements in supercapacitor technology. *Nano Energy* **2018**, 52, 441-473.

4. Wang, G.; Zhang, L.; Zhang, J., A review of electrode materials for electrochemical supercapacitors. *Chem Soc Rev.* **2012**, 41 (2), 797-828.

5. Yu, L.; Chen, G. Z., Redox electrode materials for supercapatteries. *J. Power Sources* **2016**, 326, 604-612

6. Najib, S.; Erdem, E., Current progress achieved in novel materials for supercapacitor electrodes: mini review. *Nanoscale Adv.* **2019**, 1 (8), 2817-2827.

7. Ding, S.-Y.; Wang, W., Covalent organic frameworks (COFs): from design to applications. *Chem Soc Rev.* **2013**, 42 (2), 548-568.

8. Wang, S.; Wang, Q.; Shao, P.; Han, Y.; Gao, X.; Ma, L.; Yuan, S.; Ma, X.; Zhou, J.; Feng, X., Exfoliation of covalent organic frameworks into few-layer redox-active

nanosheets as cathode materials for lithium-ion batteries. *J. Am. Chem. Soc.* **2017**, 139 (12), 4258-4261.

9. Xu, F.; Xu, H.; Chen, X.; Wu, D.; Wu, Y.; Liu, H.; Gu, C.; Fu, R.; Jiang, D., Radical covalent organic frameworks: a general strategy to immobilize open-accessible polyradicals for high-performance capacitive energy storage. *Angew. Chem. Int. Ed*. **2015**, 54, 6814-6818.

10. DeBlase, C. R.; Silberstein, K. E.; Truong, T.-T.; Abruña, H. D.; Dichtel, W. R., β-Ketoenamine-linked covalent organic frameworks capable of pseudocapacitive energy storage. *J. Am. Chem. Soc.* **2013**, 135 (45), 16821-16824.

11. Xie, J.; Rui, X.; Gu, P.; Wu, J.; Xu, Z. J.; Yan, Q.; Zhang, Q., Novel conjugated ladder-structured oligomer anode with high lithium storage and long cycling capability. *ACS Appl. Mater. Interfaces* **2016**, 8 (26), 16932-16938.

12. Lee, J.; Kalin, A. J.; Yuan, T.; Al-Hashimi, M.; Fang, L., Fully conjugated ladder polymers. *Chem. Sci.* **2017**, 8 (4), 2503-2521.

13. Mahmood, J.; Lee, E. K.; Noh, H. J.; Ahmad, I.; Seo, J. M.; Im, Y. K.; Jeon, J. P.; Kim, S. J.; Oh, J. H.; Baek, J. B., Fused Aromatic Network with Exceptionally High Carrier Mobility. *Adv. Mater.* **2021**, 33 (9), 2004707.

14. Kandambeth, S.; Jia, J.; Wu, H.; Kale, V. S.; Parvatkar, P. T.; Czaban-Jóźwiak, J.; Zhou, S.; Xu, X.; Ameur, Z. O.; Abou-Hamad, E., Covalent Organic Frameworks as Negative Electrodes for High-Performance Asymmetric Supercapacitors. *Adv. Energy Mater*. **2020**, 10 (38), 2001673.

15. Wang, W.; Kale, V. S.; Cao, Z.; Lei, Y.; Kandambeth, S.; Zou, G.; Zhu, Y.; Abouhamad, E.; Shekhah, O.; Cavallo, L., Molecular Engineering of Covalent Organic Framework Cathodes for Enhanced Zinc-Ion Batteries. *Adv. Mater.* **2021**, 33 (39), 2103617.

16. Wu, J.; Rui, X.; Long, G.; Chen, W.; Yan, Q.; Zhang, Q., Pushing up lithium storage through nanostructured polyazaacene analogues as anode. *Angew. Chem. Int. Ed*. **2015**, 54 (25), 7354-7358.

17. Lee, J.-S. M.; Briggs, M. E.; Hu, C.-C.; Cooper, A. I., Controlling electric double-layer capacitance and pseudocapacitance in heteroatom-doped carbons derived from hypercrosslinked microporous polymers. *Nano Energy* **2018**, 46, 277-289.

18. Chen, L.; Kim, J.; Ishizuka, T.; Honsho, Y.; Saeki, A.; Seki, S.; Ihee, H.; Jiang, D., Noncovalently netted, photoconductive sheets with extremely high carrier mobility and conduction anisotropy from triphenylene-fused metal trigon conjugates. *J. Am. Chem. Soc*. **2009**, 131 (21), 7287-7292.

19. Seillan, C.; Brisset, H.; Siri, O., Efficient synthesis of substituted dihydrotetraazapentacenes. Org. Lett. 2008, 10 (18), 4013-4016.

20. Xu, Y.; Sprick, R. S.; Brownbill, N. J.; Blanc, F.; Li, Q.; Ward, J. W.; Ren, S.; Cooper, A. I., Bottom-up wet-chemical synthesis of a two-dimensional porous carbon material with high supercapacitance using a cascade coupling/ cyclization route. *J. Mater. Chem. A* **2021**, 9 (6), 3303-3308.

21. Kou, Y.; Xu, Y.; Guo, Z.; Jiang, D., Supercapacitive energy storage and electric power supply using an Aza-fused π-conjugated microporous framework. *Angew. Chem. Int. Ed*. **2011**, 50, 8753-8757.

22. El-Mahdy, A. F. M.; Hung, Y. H.; Mansoure, T. H.; Yu, H. H.; Chen, T.; Kuo, S. W., A Hollow Microtubular Triazine-and Benzobisoxazole-Based Covalent Organic Framework Presenting Sponge-Like Shells That Functions as a High-Performance Supercapacitor. *Chem Asian. J*. **2019**, 14 (9), 1429-1435.

23. Li, L.; Lu, F.; Xue, R.; Ma, B.; Li, Q.; Wu, N.; Liu, H.; Yao, W.; Guo, H.; Yang, W., Ultrastable triazine-based covalent organic framework with an interlayer hydrogen bonding for supercapacitor applications. *ACS Appl. Mater. Interfaces* **2019**, 11 (29), 26355-26363.

24. DeBlase, C. R.; Silberstein, K. E.; Truong, T.-T.; Abruña, H. D.; Dichtel, W. R., β-Ketoenamine-linked covalent organic frameworks capable of pseudocapacitive energy storage. *J. Am. Chem. Soc*. **2013**, 135 (45), 16821-16824.

25. Xu, F.; Xu, H.; Chen, X.; Wu, D.; Wu, Y.; Liu, H.; Gu, C.; Fu, R.; Jiang, D., Radical covalent organic frameworks: a general strategy to immobilize open-accessible

polyradicals for high-performance capacitive energy storage. *Angew. Chem. Int. Ed*. **2015**, 54, 6814-6818.

26. El-Mahdy, A. F. M.; Kuo, C.-H.; Alshehri, A.; Young, C.; Yamauchi, Y.; Kim, J.; Kuo, S.-W., Strategic design of triphenylamine-and triphenyltriazine-based two-dimensional covalent organic frameworks for CO2 uptake and energy storage. *J. Mater. Chem. A* **2018**, 6 (40), 19532-19541.

27. Khattak, A. M.; Ghazi, Z. A.; Liang, B.; Khan, N. A.; Iqbal, A.; Li, L.; Tang, Z., A redox-active 2D covalent organic framework with pyridine moieties capable of faradaic energy storage. *J. Mater. Chem. A* **2016**, 4 (42), 16312-16317.

28. El-Mahdy, A. F. M.; Mohamed, M. G.; Mansoure, T. H.; Yu, H.-H.; Chen, T.; Kuo, S.-W., Ultrastable tetraphenyl-p-phenylenediamine-based covalent organic frameworks as platforms for high-performance electrochemical supercapacitors. *Chem. Comm.* **2019**, 55 (99), 14890-14893.

29. Chandra, S.; Roy Chowdhury, D.; Addicoat, M.; Heine, T.; Paul, A.; Banerjee, R., Molecular level control of the capacitance of two-dimensional covalent organic frameworks: role of hydrogen bonding in energy storage materials. *Chem. Mater*. **2017**, 29 (5), 2074-2080.

30. Wang, S.; Wang, Q.; Shao, P.; Han, Y.; Gao, X.; Ma, L.; Yuan, S.; Ma, X.; Zhou, J.; Feng, X., Exfoliation of covalent organic frameworks into few-layer redox-active nanosheets as cathode materials for lithium-ion batteries. *J. Am. Chem. Soc*. **2017**, 139 (12), 4258-4261.

35. Zhao, X.; Sajjad, M.; Zheng, Y.; Zhao, M.; Li, Z.; Wu, Z.; Kang, K.; Qiu, L., Covalent Organic Framework Templated Ordered Nanoporous C60 as Stable Energy Efficient Supercapacitor Electrode Material. *Carbon* **2021**, 182, 144-154.

31. Iqbal, R.; Badshah, A.; Ma, Y.-J.; Zhi, L.-J., An electrochemically stable 2D covalent organic framework for high-performance organic supercapacitors. *Chin. J. Polym. Sci.* **2020**, 38 (5), 558-564.

32. Dutta, T. K.; Patra, A., Post-synthetic Modification of Covalent Organic Frameworks through in situ Polymerization of Aniline for Enhanced Capacitive Energy Storage. *Chem Asian J.* **2021**, 16 (2), 158-164.

Chapter 3

Quinoline-Linked Covalent Organic Frameworks

3.1 Contributions to this Chapter

HR-TEM and AFM images for Qu-COFs were obtained by Yang Liu and Dr. Marco Zanella. Construction of Qu-COF models and simulation calculations were performed by Xue Wang. UV-Vis absorption spectra and DLS data was obtained by Haofan Yang. Water contact angle measurements were carried out by Lunjie Liu. Exfoliation experiments get the suggestions from Haiyan Duan and Kai Wu. Metal ions uptake experiments was carried out with the help from Peiying Wang. The analysis of metal ions uptake was gotten the help from Aiting Kai. Optimization of the synthesize condition of Qu-COFs was synthesised under the discussion with Kewei Wang. All other work was performed by the thesis author.

3.2 Background and Context

Due to the poor reversibility of the reaction combined cyclization in one step, the as-obtained fluorindine-linked COF (FL-COF) in the **Chapter 2** shows a good stability with a poor crystallinity, leading us to think about a new method for making COFs with both good stability and crystallinity. Multicomponent reactions that comprise reversible and irreversible bond forming reactions are efficient methods for the synthesis of robust covalent organic frameworks (COFs) with high crystallinity and stability.

The large two-dimensional property of crystalline 2D covalent organic frameworks (COFs) is one of the most unique properties compared with other porous materials, leading widely applying in many fields from fundamental research to specific applications like energy storage, photocatalysis and sensors. However, most reported COFs are obtained in the form of insoluble bulk powder, which has a poor processability to limit the further usage in many practical applications to a certain extent. Accordingly, the efficient exfoliation of bulk COFs to prepare COF nanosheets is an effective way to solve this problem.

Among all of the COF exfoliation cases reported before, the most common using imine-linked COFs are not chemically stable enough in the exfoliation conditions, leading to an unavoidable break-up of imine bonds during the exfoliation. While the COF

materials linked by quinoline other than imine bonds have resulted in significantly enhanced chemical stability.

Here we have developed the strategy for prepare stable quinolone-linked COFs (Qu-COFs) based on a multicomponent Doebner reaction in both one-pot and post-modification methods with mild synthetic conditions. Following this strategy, a series of robust Qu-COFs can be obtained with high crystallinity and porosity. Furthermore, by using pyruvic acid, we combine the stability of quinolone linkages with the unique 4-carboxylic acid groups to increase wettability and ion intercalation sites. In doing so we obtain a hydrophilic Qu-COF-2a which has twisted layer structure with large d-spacing and weak interlayer interaction. This results in a simple exfoliation of Qu-COFs into 2D nanosheets (Qu-CONs) in a mild condition with high efficiency. This provides a new mild and efficient method for synthesizing stable, functionally diverse 2D nanosheets and further expands the potential applications, such as the heavy metal ions uptake from industrial waste water.

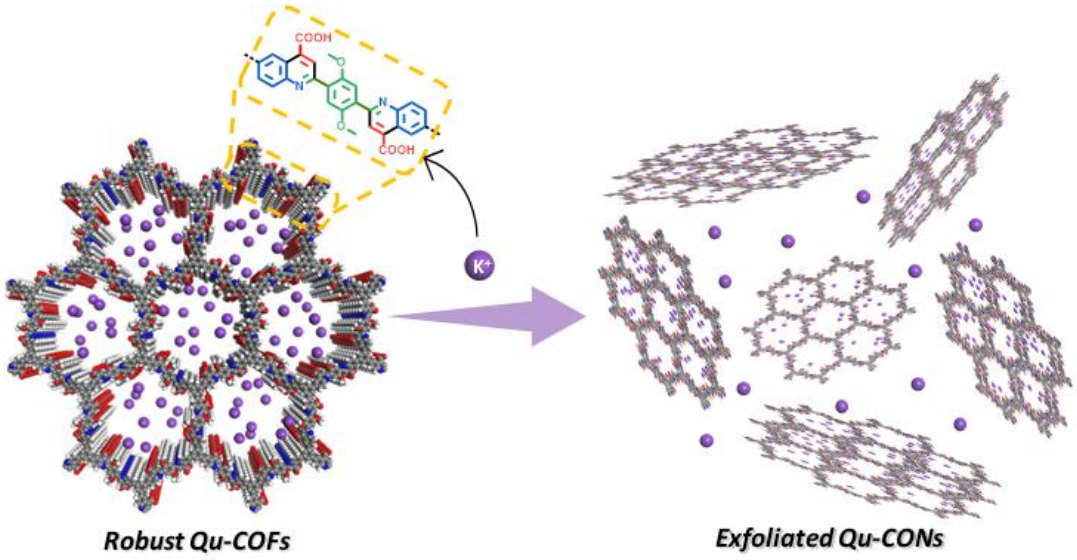

Figure 3.2.1 Exfoilated 2D quinoline-linked covalent organic nanosheets (Qu-CONs) from the robust quinoline-linked covalent organic frameworks (Qu-COFs) using a multicomponent Doebner reaction.

3.3 Introduction

Reversible covalent linkages that allow for error-correction processes and interlayer π–π interactions between 2D layers are key for the successful construction of crystalline

2D COFs.[1-9] However, the low chemical stability resulting from reversibility and the poor processibility of bulk powders can limit the practical applications of 2D COFs.[10, 11] By increasing dispersibility, it is possible to form COF nanosheets.[12-14] Several methods have been investigated for the preparation of nanosheets by exfoliation of bulk 2D COFs. Exfoliated nanosheets have benefits that include exposed surface functionalities and more accessible active sites. They have therefore been used for applications such as separation and energy storage applications.[15-18] Because of the weak chemical stability and strong interlayer interactions of most reported COFs, it is still challenging to find a general strategy to achieve exfoliation.[19, 20] Several research groups have reported in-depth studies of how the stacking structure and interlayer interaction influence exfoliation of 2D COFs, but no general rules apply. [21-23] Hence, development of robust 2D COF nanosheets will have significant implications for the practical applications of COFs.

Multicomponent reactions (MCRs) are efficient and atom economical reactions involving three or more reactants to give a single product in a one-pot process. MCRs are ideal candidates for the synthesis of stable, crystalline COFs because they can combine reversible covalent bond-forming reactions to confer crystallinity with irreversible steps that confers stability.[25] Furthermore, due to the introduction of a third component, MCRs can be an efficient method for the structural diversification and functionalization of COFs. The first reported COF synthesis using a multicomponent reaction was by Wang and co-workers using the Debus reaction.[26] Subsequently, several groups, including our own, [27] have reported COF syntheses using multicomponent reactions, but challenges still remain. Quinoline and tetrahydroquinoline-linked COFs have been synthesised using both multicomponent and post-synthetic Povarov reactions, which require strong Lewis acids or high temperatures. [28-30] The Doebner reaction is an alternative multicomponent reaction for the synthesis of quinolines which uses a combination of amine, aldehyde and an α-ketoacid or α-ketoester functionality under mild reaction conditions. [31]

Here, we report the synthesis of stable quinoline-linked COFs using a three-component Doebner reaction. The synthetic flexibility of the Doebner reaction enabled access to quinoline-linked COFs (Qu-COFs) from both one-pot synthetic and post-synthetic methods (**Scheme 3.3.1**). The quinoline-4-carboxylic acid linking groups in the framework, which are unique to the Doebner reaction, allows efficient exfoliation of the bulk material to 2D nanosheets (Qu-CONs) under mild conditions. The heavy metal ions uptake ability of the nanosheets was also investigated due to the much more exposed active sites through exfoliation.

3.4 Experimental

3.4.1 Chemical Reagents

All reagents were obtained from Sigma-Aldrich, TCI Europe or Carbosynth Ltd. Anhydrous solvents were purchased from Acros Organics or Fisher Scientific. All chemicals were used without further purification.

3.4.2 Characterization Methods and Measurements

1. Basic characterizations

The measurements of NMR, PXRD, TGA, Nitrogen adsorption and desorption, FT-IR spectra, XPS, SEM, TEM were similar and described in the experimental part in **Chapter 2**.

2. UV-Visible absorption spectra

UV-Visible absorption spectra were measured on a Shimadzu UV-2550 UV-vis spectrometer by measuring the reflectance of powders in the solid-state.

3. Atomic Force Microscopy (AFM).

All the AFM images were obtained on a Smart SPM atomic force microscope (AIST-NT, Novato, CA, USA). The samples were mounted on Si wafer substrates. Images were processed using Gwyddion 2.38.

4. Inductively coupled plasma optical emission spectrometry (ICP-OES).

Inductively coupled plasma optical emission spectrometry (ICP-OES) analysis was performed on an ICP-OES Agilent 5110. The solutions were diluted with water before

the measurement and the instrument was calibrated with Pd standards in aqueous solution and Y-89 as the internal standard.

3.4.3 Synthetic Route and Preparation Procedure

3.4.3.1 Synthesis of Model Compound

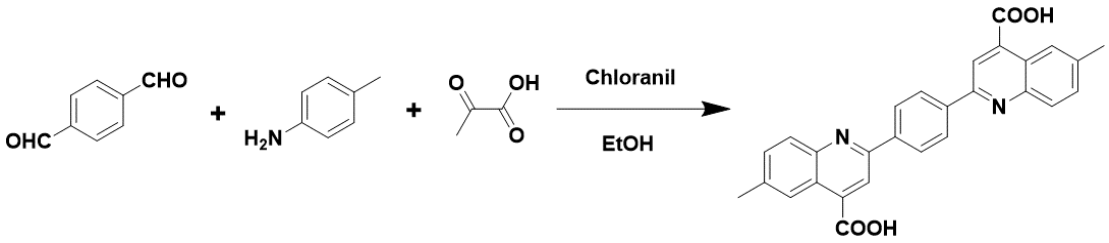

Scheme 3.4.1 Synthesis of model compound **M_1**.

Synthesis of M_1. A mixture of EtOH (1.5 mL), terephthalaldehyde (56 mg, 0.16 mmol), *p*-toluidine (46 mg, 0.24 mmol, 2 eq.), pyruvic acid (78.0 μL, 0.560 mmol, 4.0 eq.) and chloranil (46 mg, 0.24 mmol, 2.4 eq.) was degassed in a Pyrex tube (10 mL) by three freeze-pump-thaw cycles. The tube was sealed and heated at 120 °C for 3 days. The precipitate was collected by centrifugation, washed with methanol, and dried at 60 °C under vacuum overnight to give **M_1** in 83% yield.

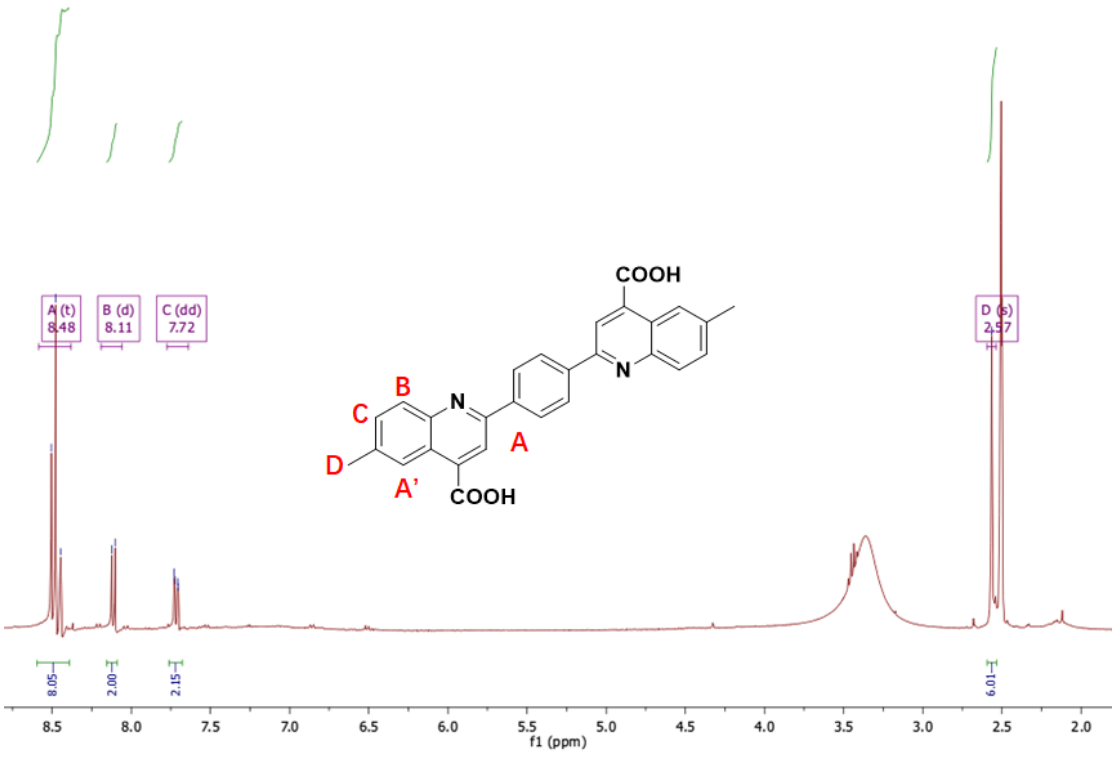

Figure 3.4.1 ^{1}H NMR spectrum of **M_1** in DMSO-d_6.

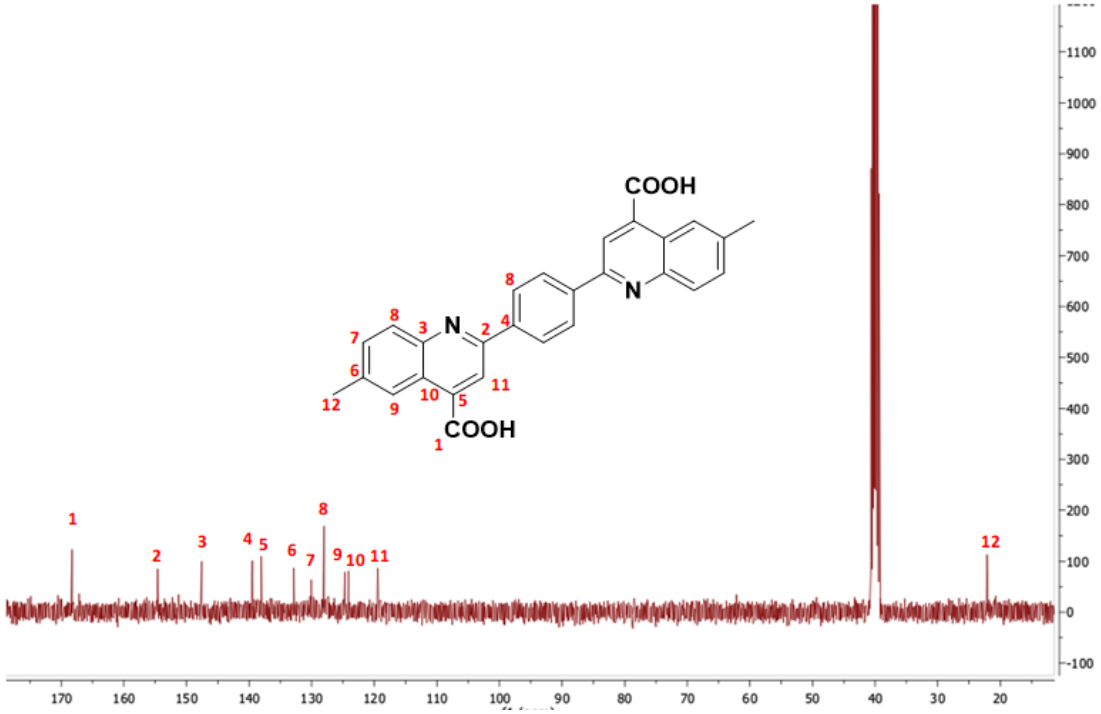

Figure 3.4.2 $^{13}C\{1H\}$ NMR spectrum of $\mathbf{M_1}$ in DMSO-d_6.

3.4.3.2 Synthesis of Quinoline-Linked Covalent Organic Frameworks

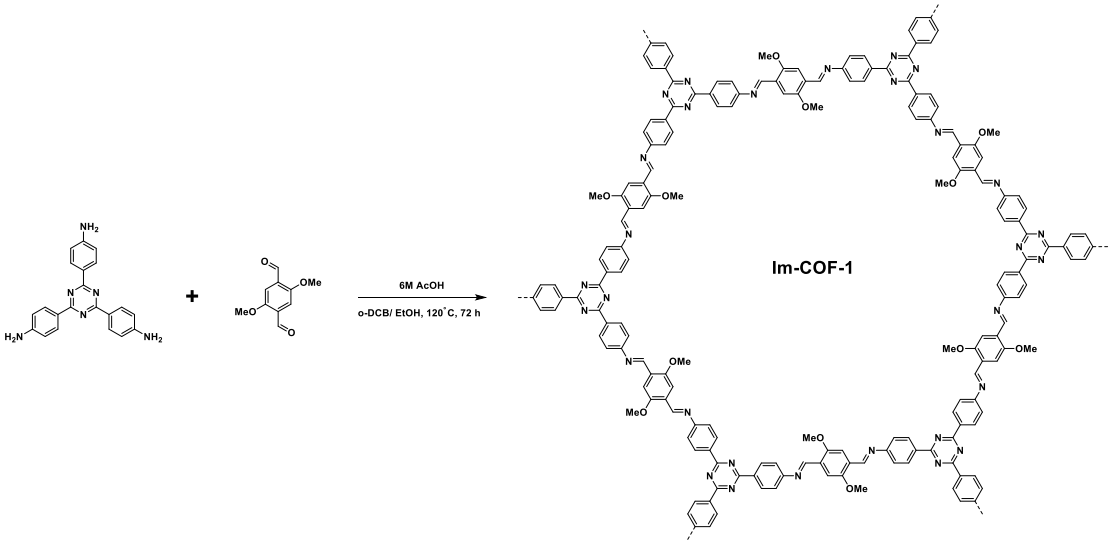

Scheme 3.4.2 Synthesis of Im-COF-1.

Synthesis of Im-COF-1.[32] A mixture of *o*-DCB/ EtOH (1 mL/ 1 mL), 2,4,6-Tris(4-aminophenyl)-s-triazine (40 mg, 0.112mmol) and 2,5-dimethoxy terephthalaldehyde (33 mg, 0.169 mmol, 1.5 eq.), and an aqueous acetic acid solution (6 M, 0.2 mL) was degassed in a Pyrex tube (10 mL) by three freeze-pump-thaw cycles. The tube was sealed and heated at 120 °C for 3 days. The precipitate was collected by centrifugation,

washed with acetone, ethanol and THF, and dried at 100 °C under vacuum overnight to give Im-COF-1 as bright yellow powder in 82% yield.

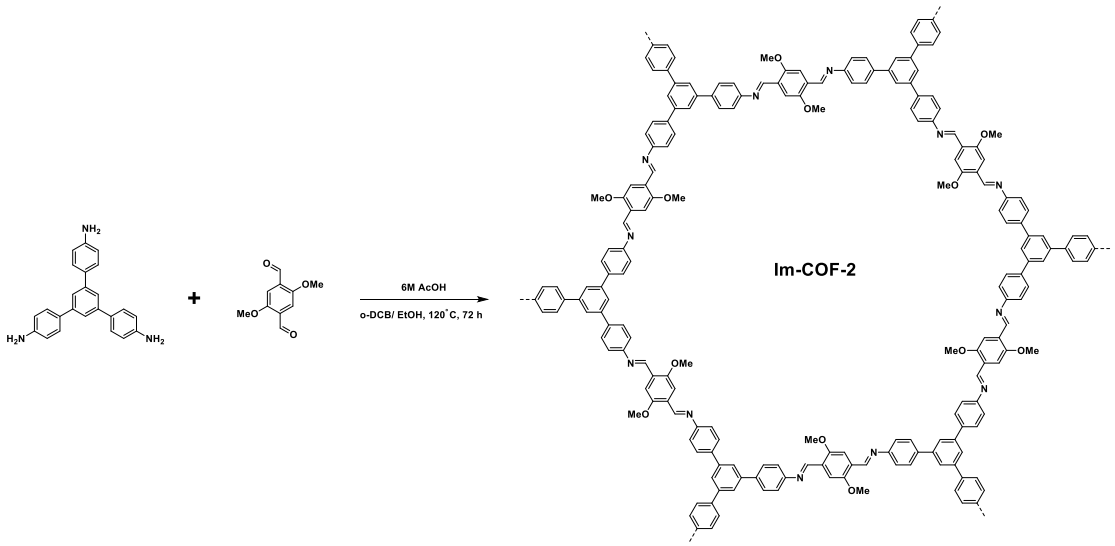

Scheme 3.4.3 Synthesis of Im-COF-2.

Synthesis of Im-COF-2.[33] A mixture of *o*-DCB/ EtOH (0.5 mL/ 1 mL), 1,3,5-tri-(4-aminophenyl) benzene (56 mg, 0.16 mmol), 2,5-dimethoxy terephthalaldehyde (46 mg, 0.24 mmol, 1.5 eq.), and an aqueous acetic acid solution (6 M, 0.15 mL) was degassed in a Pyrex tube (10 mL) by three freeze-pump-thaw cycles. The tube was sealed and heated at 120 °C for 3 days. The precipitate was collected by centrifugation, washed with acetone, ethanol and THF, and dried at 100 °C under vacuum overnight to give Im-COF-2 as yellow powder in 88% yield.

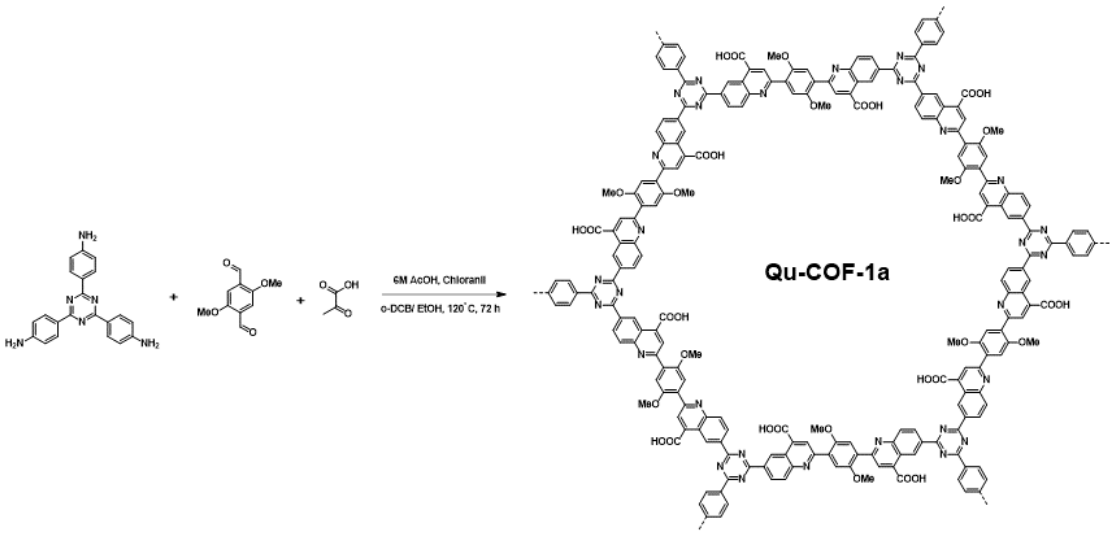

Scheme 3.4.4. Synthesis of Qu-COF-1a via one-pot synthesis.

Synthesis of Qu-COF-1a. The reaction is followed the conventional solvothermal reaction conditions, i.e., to an oven dried Pyrex tube (10 mL), A mixture of *o*-DCB/ EtOH (1 mL/ 1 mL), 2,4,6-tris(4-aminophenyl)-s-triazine (40 mg, 0.112mmol) and 2,5-dimethoxy terephthalaldehyde (33 mg, 0.169 mmol, 1.5 eq.) was sonicated for 5 min, then pyruvic acid (24.6 μL, 0.35 mmol, 3.1 eq.), chloranil (7 mg, 0.03 mmol, 0.25 eq.) and an aqueous acetic acid solution (6 M, 0.2 mL) were charged in sequence. After sonicating for 5 min, the tube was flash frozen at 77 K (liquid N_2 bath). After three freeze-pump-thaw cycles, the tube was placed in an oven of 120 °C for 3 days. The resulting solid was collected via filtration, briefly washed with acetone and ethanol. The wet solid was transferred to acetone, then extracted and activated with CO_2 under the supercritical conditions for 5 h to yield product Qu-COF-2 as orange powder (78.7 mg, 87%).

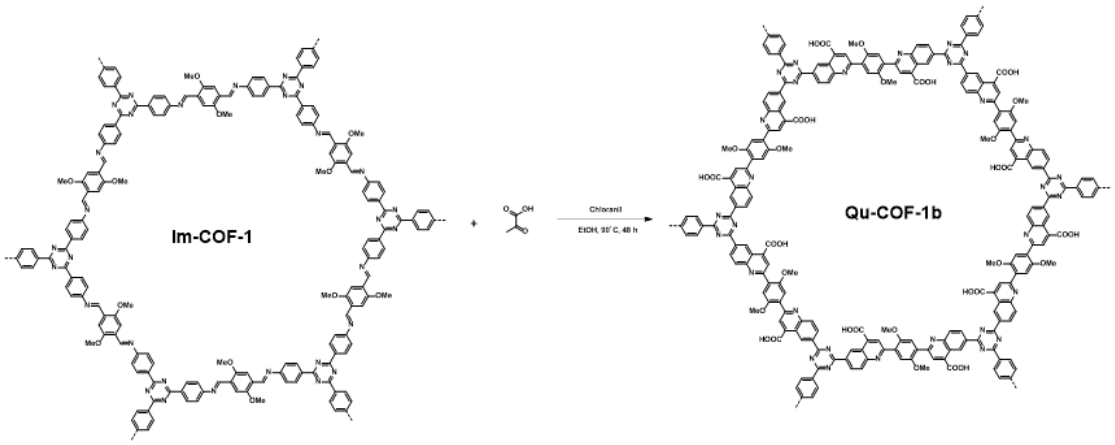

Scheme 3.4.5 Synthesis of Qu-COF-1b via post-modification method.

Synthesis of Qu-COF-1b. To an oven dried Pyrex tube (10 mL), a mixture of EtOH (1.5 mL), Im-COF-1 (33 mg), pyruvic acid (12.7 μL, 0.18 mmol), chloranil (7 mg, 0.03 mmol) and an aqueous acetic acid solution (6 M, 0.1 mL) were charged in sequence. After sonicating for 5 min, the tube was flash frozen at 77 K (liquid N_2 bath). After three freeze-pump-thaw cycles, the tube was placed in an oven of 120 °C for 3 days. The resulting solid was collected via filtration, briefly washed with acetone and ethanol. The wet solid was transferred to acetone, then extracted and activated with CO_2 under the supercritical conditions for 5 h to yield product Qu-COF-1b as dark red powder (41.4 mg, 91%).

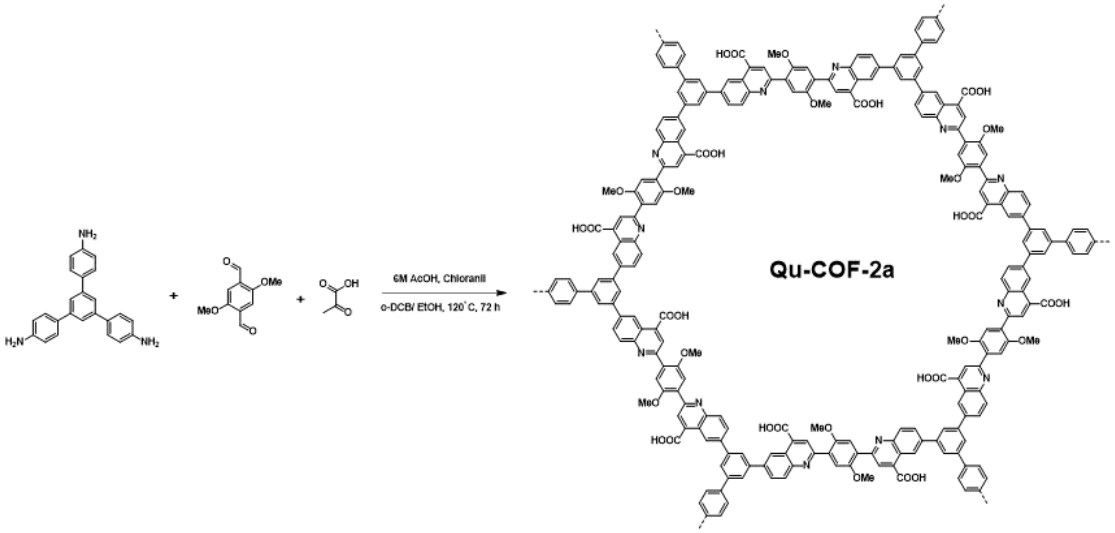

Scheme 3.4.6 Synthesis of Qu-COF-2a via one-pot synthesis.

Synthesis of Qu-COF-2a. This reaction followed conventional solvothermal reaction conditions; that is, to an oven-dried Pyrex tube (10 mL), a mixture of o-DCB/ EtOH (0.5 mL/ 1 mL), 1,3,5-tri-(4-aminophenyl) benzene (56 mg, 0.16 mmol), 2,5-dimethoxy terephthalaldehyde (46 mg, 0.24 mmol, 1.5 eq.) was added and sonicated for 5 min, then pyruvic acid (35.0 μL, 0.50 mmol, 3.1 eq.), chloranil (8 mg, 0.04 mmol, 0.25 eq.) and an aqueous acetic acid solution (6 M, 0.15 mL) were charged in sequence. After sonicating for a further 5 min, the tube was flash frozen at 77 K (liquid N_2 bath). After three freeze-pump-thaw cycles, the tube was placed in an oven of 120 °C for 3 days. The resulting solid was collected via filtration, briefly washed with acetone and ethanol. The wet solid was transferred to acetone, then extracted and activated with CO_2 under the supercritical conditions for 5 h to yield product Qu-COF-2a as brown powder (107.8 mg, 85%).

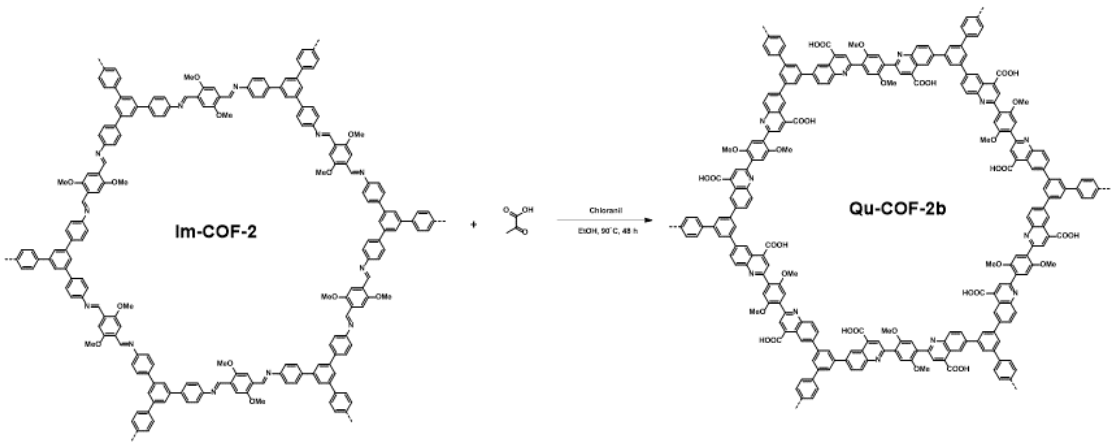

Scheme 3.4.7 Synthesis of Qu-COF-2b via post-modification method.

Synthesis of Qu-COF-2b. To an oven-dried Pyrex tube (10 mL), a mixture of EtOH (1.5 mL), Im-COF-2 (45 mg), pyruvic acid (17.5 μL, 0.25 mmol), chloranil (8 mg, 0.04 mmol) and an aqueous acetic acid solution (6 M, 0.1 mL) were charged in sequence. After sonicating for 5 min, the tube was flash frozen at 77 K (liquid N_2 bath). After three freeze-pump-thaw cycles, the tube was placed in an oven of 120 °C for 3 days. The resulting solid was collected via filtration, briefly washed with acetone and ethanol. The wet solid was transferred to acetone, then extracted and activated with CO_2 under

the supercritical conditions for 5 h to yield product Qu-COF-2b as dark red powder (56.9 mg, 92%).

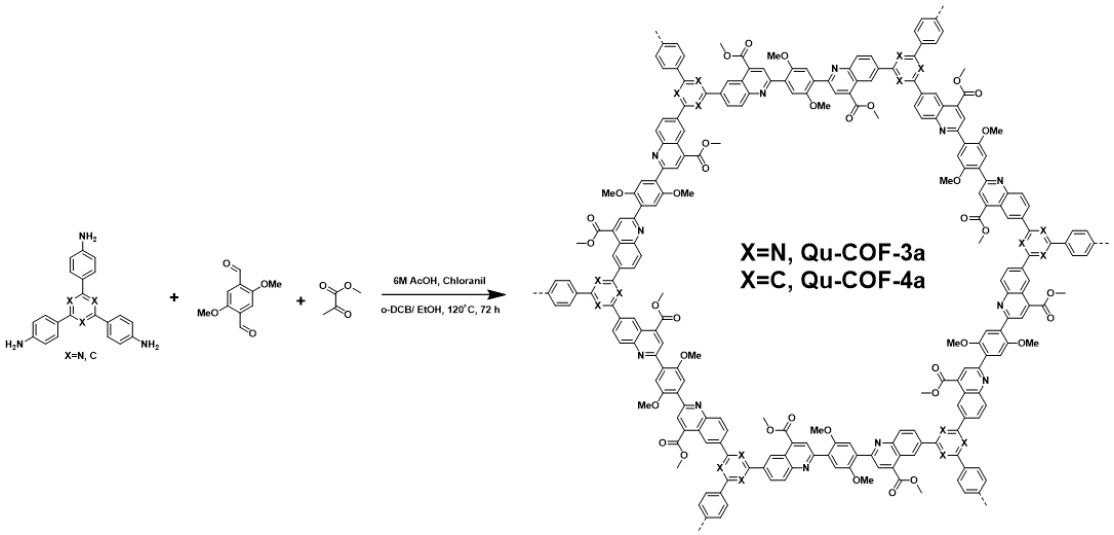

Scheme 3.4.8. Synthesis of Qu-COF-3a& 4a via one-pot synthesis.

Synthesis of Qu-COF-3a. The procedure is similar to that of Qu-COF-1a but using methyl pyruvate instead of pyruvic acid. A mixture of o-DCB/ EtOH (1 mL/ 1 mL), 2,4,6-tris(4-aminophenyl)-s-triazine (40 mg, 0.112mmol) and 2,5-dimethoxy terephthalaldehyde (33 mg, 0.169 mmol, 1.5 eq.) was sonicated for 5 min, then methyl pyruvate (31.6 μL, 0.35 mmol, 3.1 eq.), chloranil (6 mg, 0.03 mmol, 0.25 eq.) and an aqueous acetic acid solution (6 M, 0.2 mL) were charged in sequence. After sonicating for 5 min, the tube was flash frozen at 77 K (liquid N_2 bath). After three freeze-pump-thaw cycles, the tube was placed in an oven of 120 °C for 3 days. The resulting solid was collected via filtration, briefly washed with acetone and ethanol. The wet solid was transferred to acetone, then extracted and activated with CO_2 under the supercritical conditions for 5 h to yield product Qu-COF-3a as dark orange powder (77.1 mg, 81%).

Synthesis of Qu-COF-4a. The procedure is similar to that of Qu-COF-2a but using methyl pyruvate instead of pyruvic acid. A mixture of o-DCB/ EtOH (0.5 mL/1 mL), 1,3,5-tri-(4-aminophenyl) benzene (56 mg, 0.16 mmol), 2,5-dimethoxy terephthalaldehyde (46 mg, 0.24 mmol, 1.5 eq.) was sonicated for 5 min, then methyl pyruvate (45.1 μL, 0.50 mmol, 3.1 eq.), chloranil (8 mg, 0.04 mmol, 0.25 eq.) and an

aqueous acetic acid solution (6 M, 0.15 mL) were charged in sequence. After sonicating for 5 min, the tube was flash frozen at 77 K (liquid N_2 bath). After three freeze-pump-thaw cycles, the tube was placed in an oven of 120 °C for 3 days. The resulting solid was collected via filtration, briefly washed with acetone and ethanol. The wet solid was transferred to acetone, then extracted and activated with CO2 under the supercritical conditions for 5 h to yield product Qu-COF-4a as brown powder (113.6 mg, 85%).

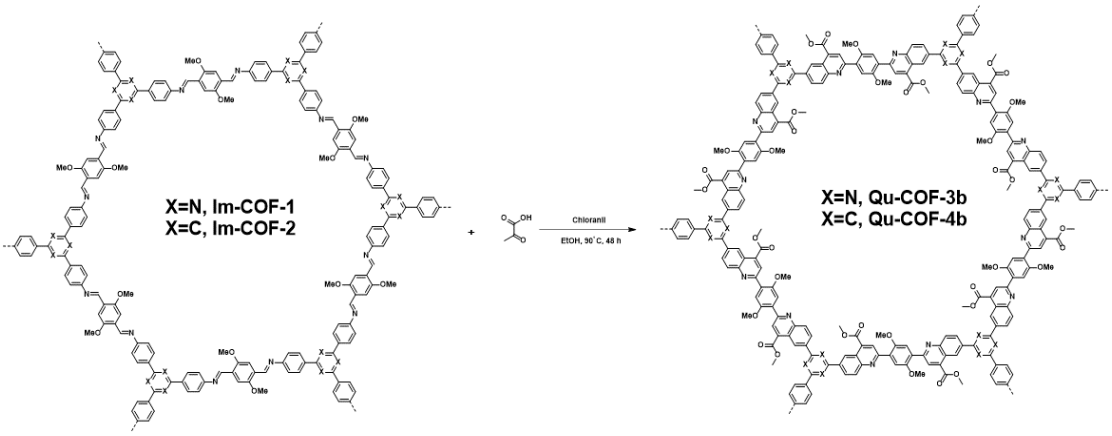

Scheme 3.4.9 Synthesis of Qu-COF-3b& 4b via post-modification method.

Synthesis of Qu-COF-3b. The procedure is similar to that of Qu-COF-1b but using methyl pyruvate instead of pyruvic acid. To an oven-dried Pyrex tube (10 mL), a mixture of EtOH (1.5 mL), Im-COF-1 (33 mg), methyl pyruvate (16.3 μL, 0.18 mmol), chloranil (7 mg, 0.03 mmol) and an aqueous acetic acid solution (6 M, 0.1 mL) were charged in sequence. After sonicating for 5 min, the tube was flash frozen at 77 K (liquid N_2 bath). After three freeze-pump-thaw cycles, the tube was placed in an oven of 90 °C for 2 days. The resulting solid was collected via filtration, briefly washed with acetone and ethanol. The wet solid was transferred to acetone, then extracted and activated with CO_2 under the supercritical conditions for 5 h to yield product Qu-COF-3b as dark red powder (38.9 mg, 81%).

Synthesis of Qu-COF-4b. The procedure to similar with that of Qu-COF-2b but using methyl pyruvate instead of pyruvic acid. To an oven-dried Pyrex tube (10 mL), a mixture of EtOH (1.5 mL), Im-COF-2 (45 mg), methyl pyruvate (22.6 μL, 0.250 mmol),

chloranil (8 mg, 0.04 mmol) and an aqueous acetic acid solution (6 M, 0.1 mL) were charged in sequence. After sonicating for 5 min, the tube was flash frozen at 77 K (liquid N_2 bath). After three freeze-pump-thaw cycles, the tube was placed in an oven of 90 °C for 2 days. The resulting solid was collected via filtration, then briefly washed with acetone and ethanol. The wet solid was transferred to acetone, then extracted and activated with CO_2 under the supercritical conditions for 5 h to yield product Qu-COF-4b as dark red powder (55.4 mg, 84%).

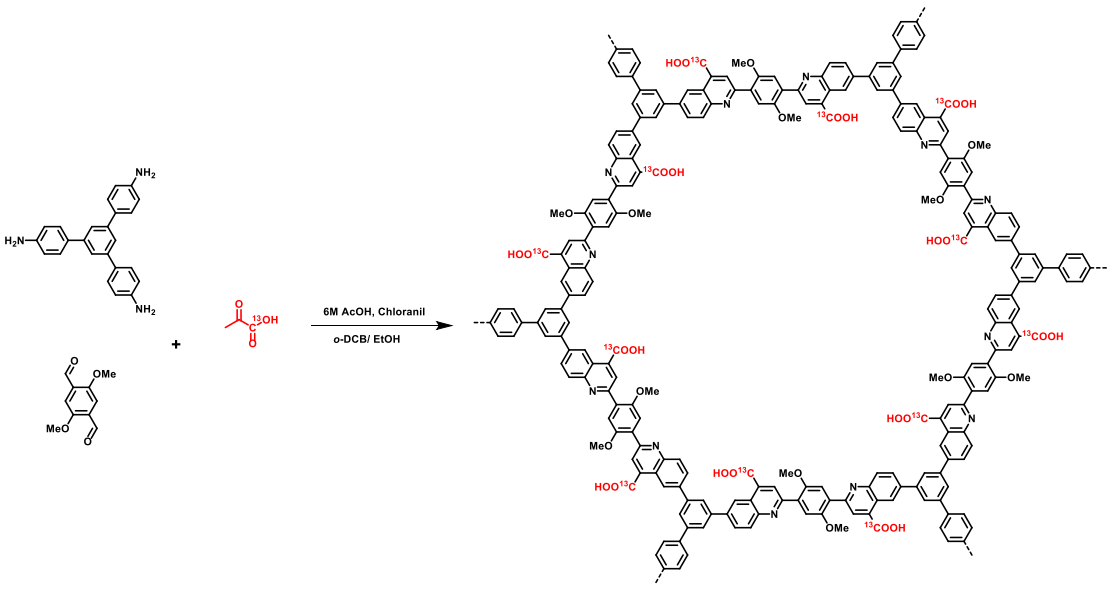

Scheme 3.4.10 Synthesis of ^{13}C labelled Qu-COF-2a via one-pot synthesis.

Synthesis of ^{13}C labelled Qu-COF-2a. The procedure is similar to that of Qu-COF-2a but using ^{13}C labelled pyruvic acid instead. The reaction followed conventional solvothermal reaction conditions: to an oven-dried Pyrex tube (10 mL), a mixture of o-DCB/ EtOH (0.3 mL/ 0.6 mL), 1,3,5-tri-(4-aminophenyl) benzene (28 mg, 0.08 mmol), 2,5-dimethoxy terephthalaldehyde (23 mg, 0.12 mmol, 1.5 eq.) was sonicated for 5 min, then pyruvic acid (17.5 μL, 0.25 mmol, 3.1 eq.), chloranil (4 mg, 0.02 mmol, 0.25 eq.) and an aqueous acetic acid solution (6 M, 0.1mL) were charged in sequence. After sonicating for 5 min, the tube was flash frozen at 77 K (liquid N_2 bath). After three freeze-pump-thaw cycles, the tube was placed in an oven of 120 °C for 3 days. The resulting solid was collected via filtration, briefly washed with acetone and ethanol. The wet solid was transferred to acetone, then extracted and activated with CO_2 under

the supercritical conditions for 5 h to yield product ^{13}C labelled Qu-COF-2a as brown powder (55.8 mg, 88%).

3.4.4 Exfoliation of Quinoline-Linked Covalent Organic Frameworks

To a 20 mL vial was added COF powder (10 mg) and then a mixture of 6 M KOH aqueous solution and EtOH (1:1 v/v, 10 mL). The vial was capped and the mixture was sonicated for 45 minutes and then stirred at 600 rpm overnight at room temperature to provide the COF suspension. The COF suspension was filtered through a 5 μm filter before further tests.

3.4.5 Procedure of Metal Ions Uptake

Aqueous solutions of metal ions with different concentration were prepared by diluting the respective metal stock solutions (100 ppm) with the proper amount of Milli-Q water unless otherwise indicated. The concentration of metal ions was detected by inductively coupled plasma-optical emission spectroscopy (ICP-OES). All the adsorption experiments were performed at ambient conditions.

Heavy metal ions uptake capacity tests for COF samples

2 mg of COF samples were added into 10 mL of a 10 ppm aqueous Cu^{2+}, Co^{2+}, Ni^{2+}, Ag^{+}, Zn^{2+}, Cd^{2+}, Eu^{2+}, Mg^{2+}, Mn^{2+} and Pb^{2+} solution. The mixtures were shaken on a tube rotator overnight to reach the adsorption equilibrium. The treated solution was then filtered through a 0.45 μm filter paper and the filtrate was analysed using ICP.

Cd^{2+} sorption isotherm

2 mg of activated COF sample was added into 10 mL aqueous solutions with different concentration of Cd^{2+}. The mixtures were shaken overnight to reach the adsorption equilibrium. The treated solution was then filtered through a 0.45 μm filter paper and the filtrate was analysed using ICP.

Q_e, the amount of metal ions was calculated using the following equation:

$$Q_e = (C_i - C_e) \times V/m$$

where V is the volume of the solution (mL), m is the amount of COF sorbent (g), and C_i and C_e are the initial concentration and the final equilibrium concentration of Cd^{2+}, respectively.

Distribution coefficient

The distribution coefficient K_d used for the determination of the affinity of sorbents for Cd^{2+} is given by the equation:

$$K_d = (C_i\text{-}C_e)/C_e \times V/m$$

where V is the volume of the Cd^{2+} solution (mL), m is the amount of COF sorbent (g), C_i and C_e are the initial concentration and the final equilibrium concentration of Cd^{2+}, respectively. K_d was determined by immersing 2 mg COF sample in 10 mL Cd^{2+} solution with the concentration of 10 ppm. The mixture was shaken overnight to reach the adsorption equilibrium. The treated solution was then filtered through a 0.45-μm filter paper and the filtrate was analysed using ICP.

Adsorption kinetics for cadmium removal

20 mg of activated COF sample was added into 100 mL aqueous solutions with 10 ppm of Cd^{2+}. The mixtures were stirred at room temperature for 3 h. During the stirring period, the mixture was filtered at intervals through a 0.45-μm membrane filter for all samples. The filtrates were analysed using ICP to determine the remaining Cd^{2+} concentration. The experimental data were fitted with a pseudo-second-order kinetic model using the following equation:

$$t/q_t = 1/(k_2 \times q_e^2) + t/q_e$$

where k_2 is the pseudo-second-order rate constant of adsorption (g/ mg·min) and q_e is the amount of Cd^{2+} adsorbed at equilibrium (mg/g). The slope and intercept of the linear plot t/q_t vs. t yielded the values of q_e and k_2, respectively.

Metal ions selectivity tests

2 mg of COF samples were added into 10 mL of aqueous solution with a concentration of 10 ppm of Cu^{2+}, Co^{2+}, Ni^{2+}, Ag^{+}, Zn^{2+}, Cd^{2+}, Eu^{2+}, Mg^{2+}, Mn^{2+} and Pb^{2+}. The mixtures were placed on a tube revolver overnight to reach the adsorption equilibrium. The treated solution was then filtered through a 0.45-µm membrane filter and the filtrate was analysed using ICP.

3.5 Results and Discussion

3.5.1 Synthesis of Qu-COFs

The Doebner reaction is an efficient, operationally simple multicomponent reaction for the synthesis of quinoline-4-carboxylic acids. The proposed mechanism begins with the condensation of an amine and an aldehyde to form an imine-based compound **(1)** followed by nucleophilic attack of pyruvic acid and Pictet-Spengler-like cyclisation to afford hydroquinone **(3)** after aromatization and dehydration steps. Oxidation then irreversibly forms the desired quinoline-4-carboxylic acid **(4)** (**Scheme 3.5.1**). The multicomponent Doebner reaction was used to construct quinoline-linked covalent organic frameworks (Qu-COFs) by both one-pot and two-step post-synthetic methods, respectively.

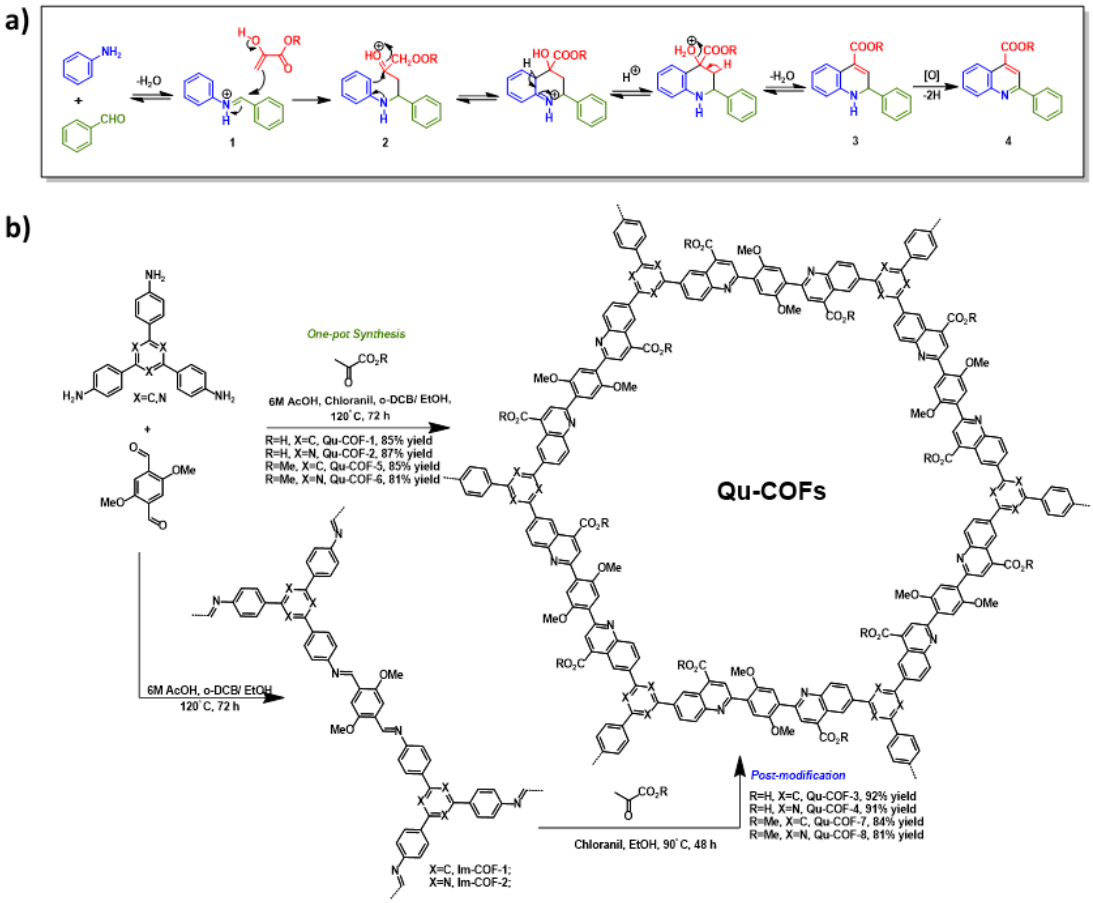

Scheme 3.5.1 Synthesis of quinoline-linked covalent organic frameworks (**Qu-COFs**) by a multicomponent Doebner reaction. (a) Proposed mechanism of quinoline formation; (b) Synthesis of **Qu-COFs** *via* one-pot synthesis route and two-step post-modification route.

For the one-pot method, we selected 4,4',4''-(1,3,5-triazine-2,4,6-triyl)tribenzaldehyde (**TAPT**) and 2,5-dimethoxy terephthalaldehyde (**DMTPA**), and 1,3,5-tri(4-aminophenyl)benzene (**TAPB**) monomers to react with pyruvic acid in the presence of 6 M AcOH and chloranil as oxidant to give **Qu-COF-1a& 2a**. After investigating these initial reaction conditions, we found **Qu-COF-2** was less crystalline so decided to optimize on this COF. After screening solvents, co-solvents, oxidants, concentration, stoichiometry, and temperature (**Scheme 3.5.2** and **Table 3.5.1**), the optimal reaction conditions afforded **Qu-COF-2a** in 85% yield (**Scheme 3.4.6**) and **Qu-COF-2b** in 85% yield (**Scheme 3.4.7**). This yield is comparable with the model compound **M1** prepared under the same reaction conditions (**Scheme 3.4.1**).

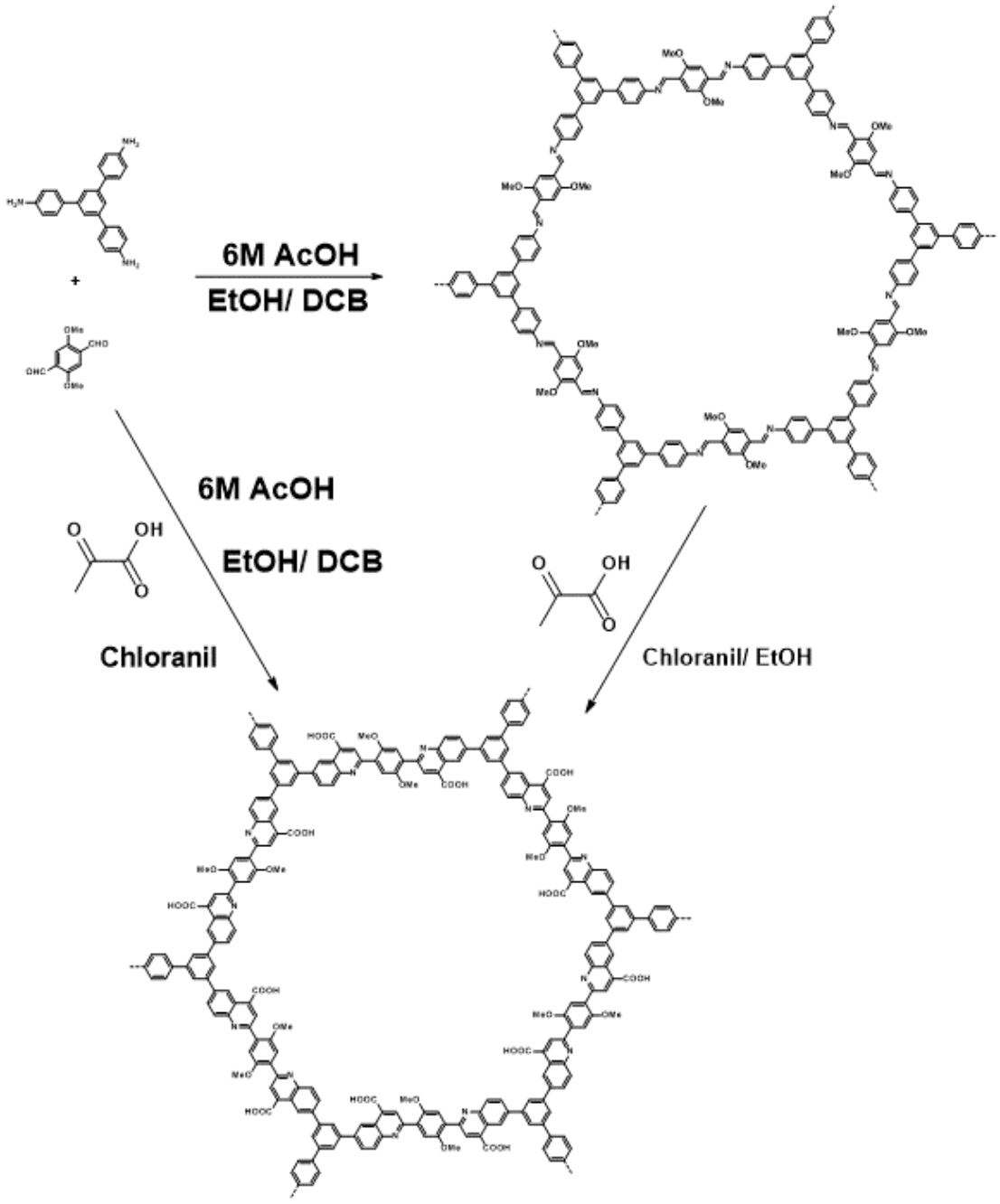

Scheme 3.5.2 Screen the reaction conditions of Qu-COF-2a&b *via* one-pot synthesis and post-modification method.

Table 3.5.1 Experimental details of Qu-COF-2a&b

Sample	Method	Start materials	Oxidant	Acid	Status
Qu-COF-2a-a	In-situ	Monomers	NH_4SO_3H	None	Amorphous
Qu-COF-2a-b	In-situ	Monomers	None	None	Amorphous

Qu-COF-2a-c	In-situ	Monomers	None	6 M AcOH	Amorphous
Qu-COF-2a-d	In-situ	Monomers	Chloranil	6 M AcOH	Crystalline
Qu-COF-2a-e	In-situ	Monomers	DDQ	6 M AcOH	Crystalline
Qu-COF-2b-f	Post-modification	Im-COF-2	NH_4SO_3H	None	Amorphous
Qu-COF-2b-g	Post-modification	Im-COF-2	None	None	Amorphous
Qu-COF-2b-h	Post-modification	Im-COF-2	None	6 M AcOH	Amorphous
Qu-COF-2b-i	Post-modification	Im-COF-2	Air	None	Semi-crystalline
Qu-COF-2b-j	Post-modification	Im-COF-2	Chloranil	6 M AcOH	Crystalline
Qu-COF-2b-k	Post-modification	Qu-COF-2a-a	Chloranil	6 M AcOH	Amorphous
Qu-COF-2b-l	Post-modification	Im-COF-2	DDQ	6 M AcOH	Semi-crystalline

We found that the choice of oxidant affected the crystallinity, with chloranil giving the highest crystallinity (**Figure 3.5.1** and **Figure 3.5.2**). The two-step post-synthetic method was initially investigated with **Im-COF-2** (**Scheme 3.5.1**). After screening reaction conditions, we found that 3 equivalents of pyruvic acid in the presence of 6 M AcOH and chloranil in neat ethanol at 90 ºC afforded **Qu-COF-2b** in 92% yield (**Scheme 3.4.7**).

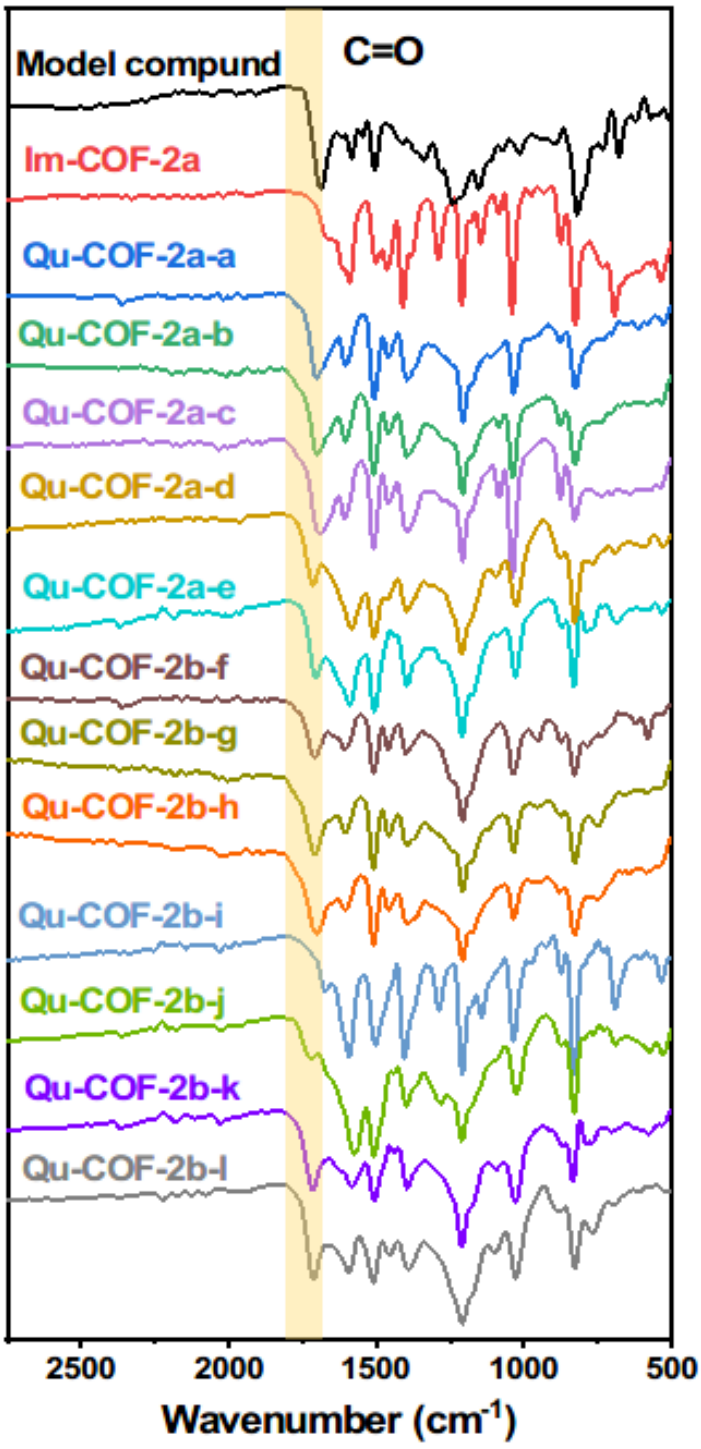

Figure 3.5.1 FT-IR spectra of Qu-COF-2a& 2b synthesized with indicated conditions.

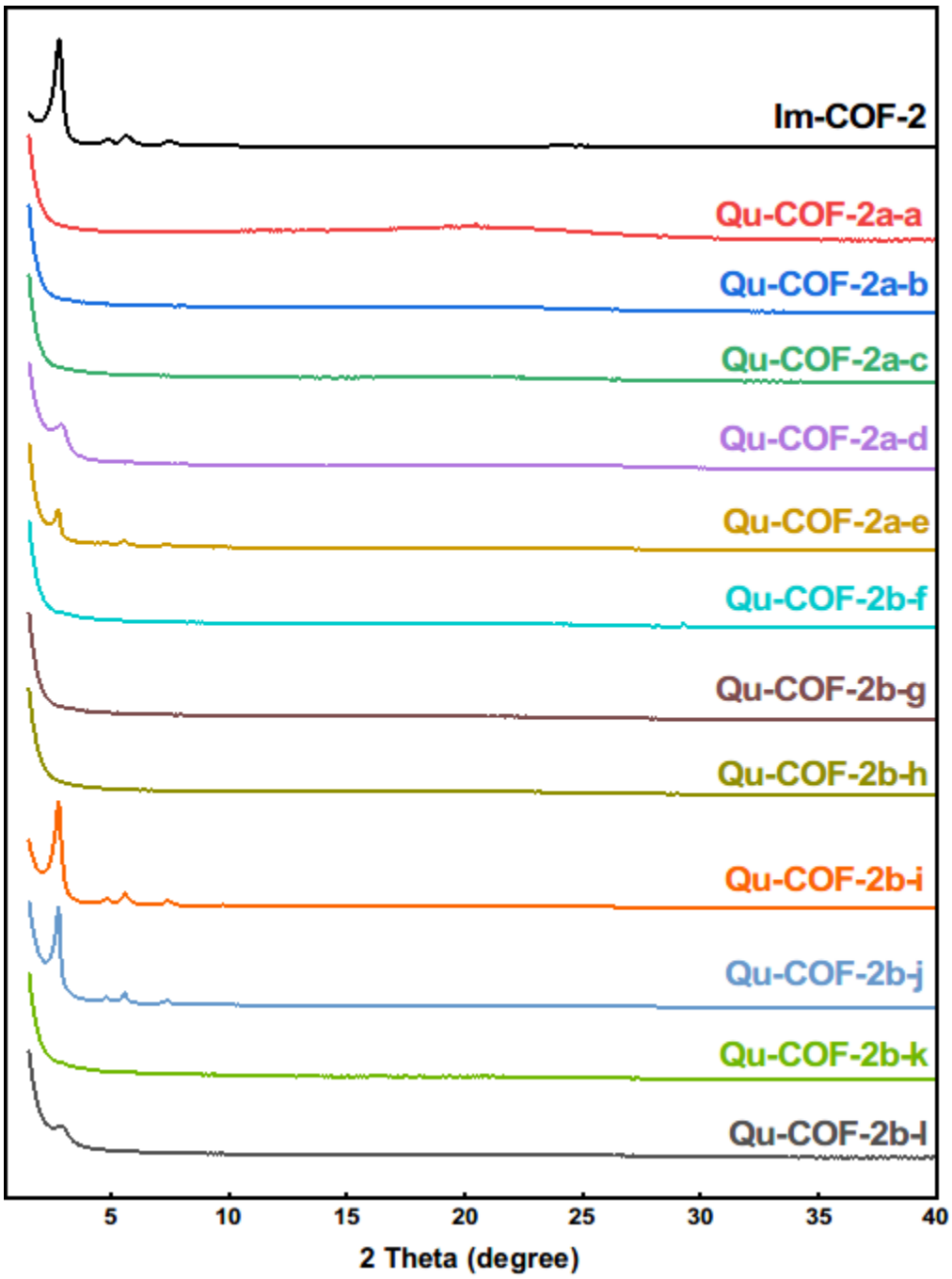

Figure 3.5.2 PXRD patterns of Qu-COF-2a& 2b synthesized with indicated conditions.

From the comparison of **Qu-COF-1a** and **Qu-COF-1b**, the crystallinity and surface areas obtained from both methods are comparable (**Figure 3.5.3**). To investigate the scope of the pyruvate component in both methods we also used methyl pyruvate to produce **Qu-COF-3a&b** and **Qu-COF-4a&b** respectively (**Scheme 3.4.8** and **Scheme 3.4.9**). Qu-COFs 1-4 were all synthesized under mild conditions in high yields and exhibited good crystallinity.

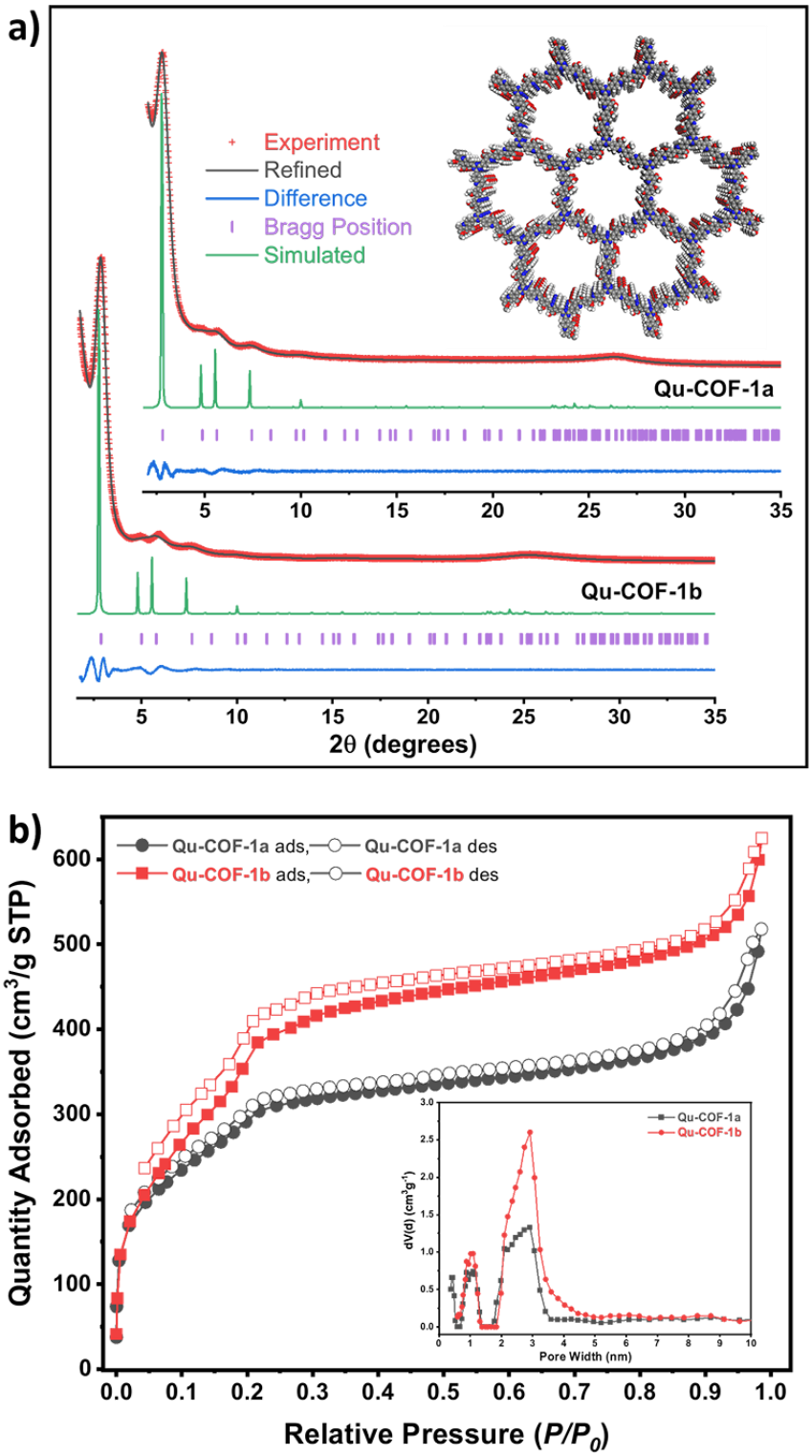

Figure 3.5.3 (a) Structural models for **Qu-COF-1a&b** with eclipsed AA stacking patterns, shown parallel to the pore channel along the crystallographic c axis (inset). Experimental diffraction patterns (red), profiles calculated from Pawley fitting (black) showing the residual (blue), and pattern simulated from the structural model (green). Reflection positions are shown

by tick marks (purple). (b) Nitrogen adsorption and desorption isotherms for **Qu-COF-1a** (black) and **Qu-COF-1b** (red) recorded at 77 K (filled symbols = adsorption; open symbols = desorption). Insert is the pore size distribution calculated by NL-DFT method.

3.5.2 Characterization of Crystallinity

Powder X-ray diffraction (PXRD) was used to characterize the frameworks, based on comparison with optimized, idealized structural models of the expected networks (**Figure 3.5.3a** and **Figure 3.5.4**). The diffraction patterns of all frameworks exhibited characteristic reflections that indicated ordered layers within the structure. In all Qu-COFs cases, the diffraction patterns were more consistent with the eclipsed AA-stacking arrangement, rather than a staggered AB stacking. An intense low angle peak is present in all Qu-COFs which correspond to the (100) reflection plane. The diffraction peaks were relatively broad, as is common for COFs of this type that feature stable, irreversible bonds. The diffraction patterns of **Qu-COF-1a&b** and **Qu-COF-3a&b** show a series of peaks at 2.89°, 4.93°, 5.94° and 7.66°, corresponding to (100), (110), (200) and (210) reflection planes, respectively. Similarly, the PXRD patterns of **Qu-COF-2a&b** and **Qu-COF-4a&b** exhibit four peaks at 2.78°, 4.84°, 5.60° and 7.42°, belonging to the (100), (110), (200) and (210) facets, respectively.

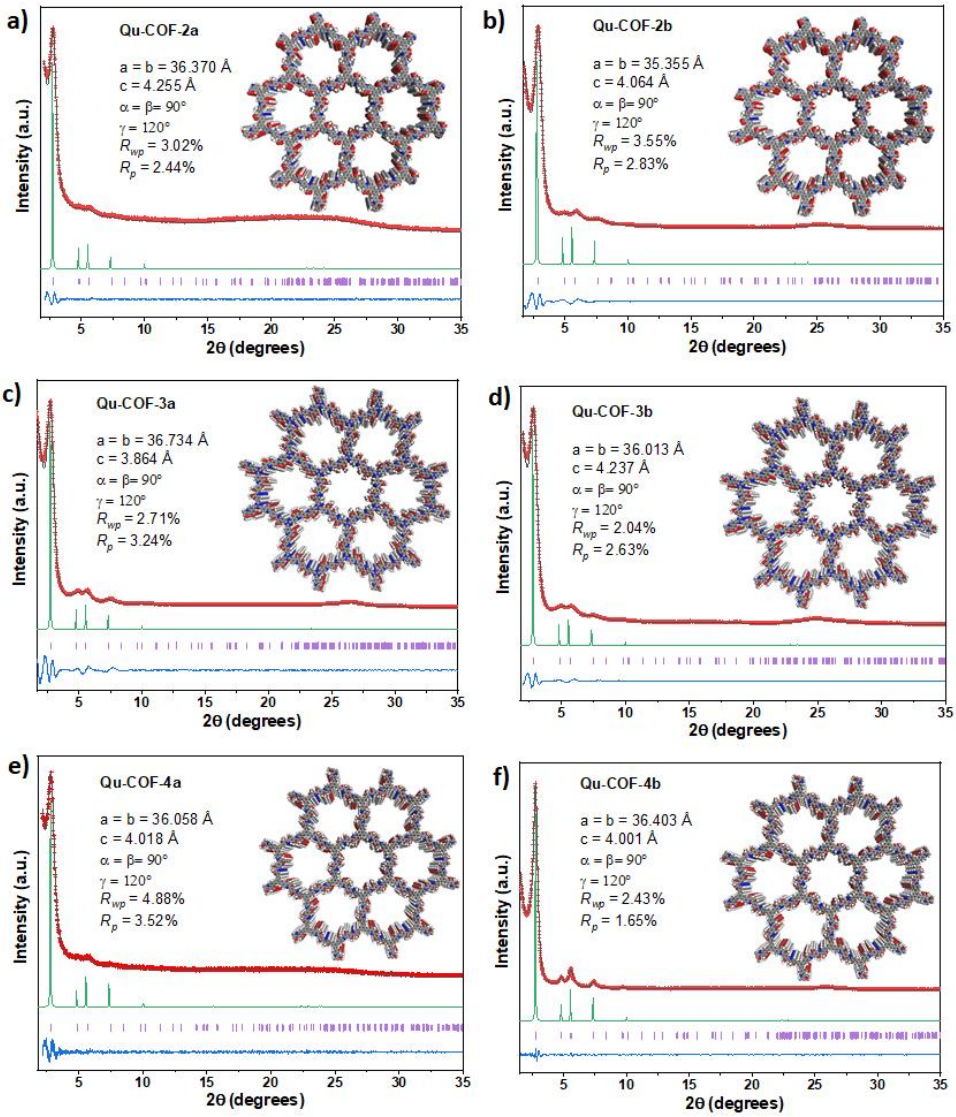

Figure 3.5.4 Crystal structures of **Qu-COF-2a&b~4a&b** (a−f). Structural models for all the **Qu-COFs** with eclipsed AA stacking patterns, shown parallel to the pore channel along the crystallographic c axis (inset). Experimental diffraction patterns (red), profiles calculated from Pawley fitting (black) showing the residual (blue), and pattern simulated from the structural model (green). Reflection positions are shown by tick marks (purple).

Compared with calculated structural models of eclipsed AA-stacking, all the experimental PXRD curves of Qu-COFs are in good agreement with simulation patterns. The unit cell parameters were determined by Pawley refinements with respect to the experimental diffraction patterns. The differences between the experimental and the simulated PXRD patterns were small and the refined curves show close matching

for all reflection positions with reasonable converged *R* factors (R_{wp} and R_p), indicating good agreement of experimental data and simulation models.

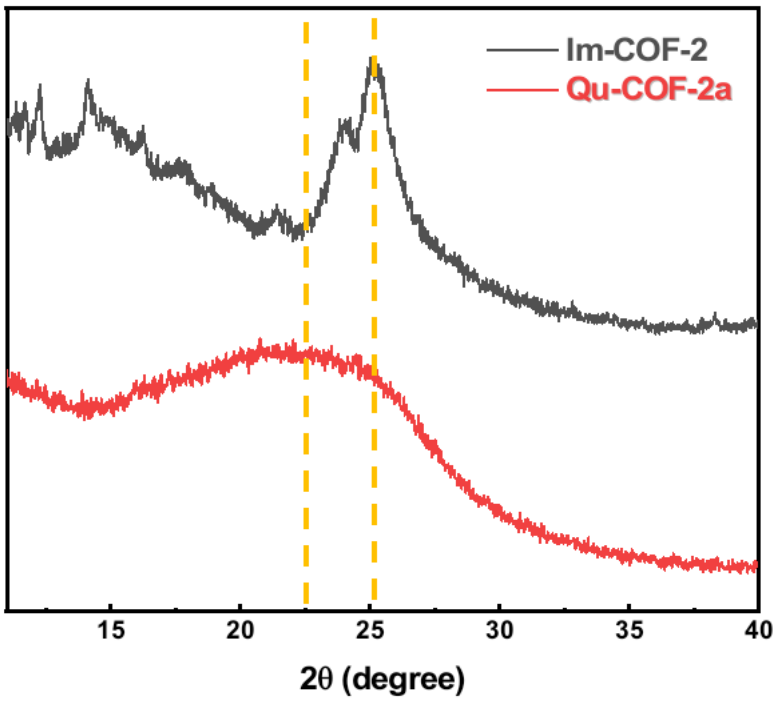

Figure 3.5.5 PXRD patterns of Im-COF-2 (black) and Qu-COF-2a (red).

During the modelling of the Qu-COFs, we compared the *c* values with their parent Im-COFs and found that Qu-COFs have a (001) peak with larger 2θ degree (**Figure 3.5.5**) which illustrates a bigger interlayer stacking distance (3.8-4.2 Å) and are slightly twisted out of the plane (larger dihedral angle) causing much larger *d*-spacing (**Figure 3.5.6**).

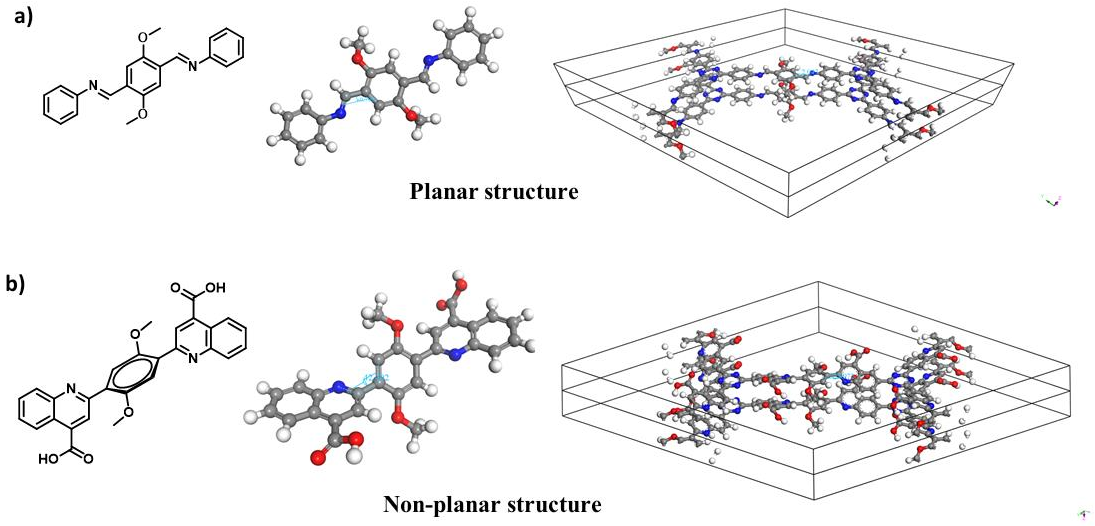

Figure 3.5.6 a) Structure and modelling of Im-COF-1 and its imine fragment. b) Structure and modelling of Qu-COF-1 and its quinoline fragment. After Forcite Calculation in Materials Studio, Im-COF-1 and its imine fragment show the dihedral angle around 2.05º and 0.71º, respectively, indicating a good planarity. But Qu-COF-1 and its quinoline fragment show the dihedral angle around 23.97º and 42.49º, respectively, indicating a twisted structure of quinoline linkage. The dihedral angle in Qu-COF-1 is smaller than the quinoline fragment due to the π-π stacking interaction between each plane of 2D-COF.

3.5.3 Characterization of Chemical Structures

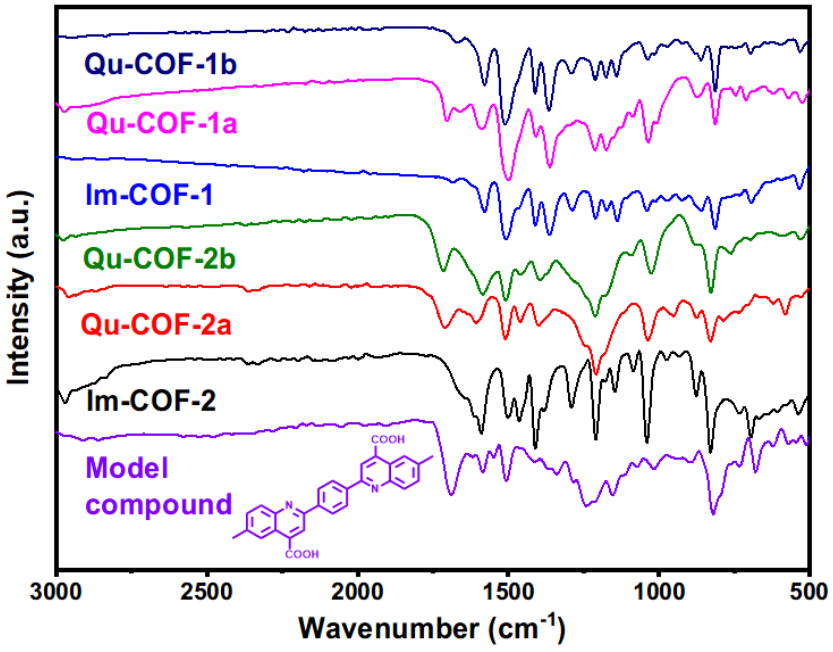

Figure 3.5.7 FT-IR spectra of Qu-COFs, Im-COFs and the model compound (M_1).

The formation of the quinoline linkages was confirmed by Fourier-transformed infrared (FT-IR) spectroscopy (**Figure 3.5.7**). One salient feature of the quinoline-4-carboxylic acid or ester is the carbonyl (C=O) stretch at 1700 cm^{-1} which appears in all Qu-COFs. The appearance of a C=O stretch coincides with the disappearance of C=N stretch from the imine bond at 1614 cm^{-1}. The same was observed for the model compound $\mathbf{M_1}$.

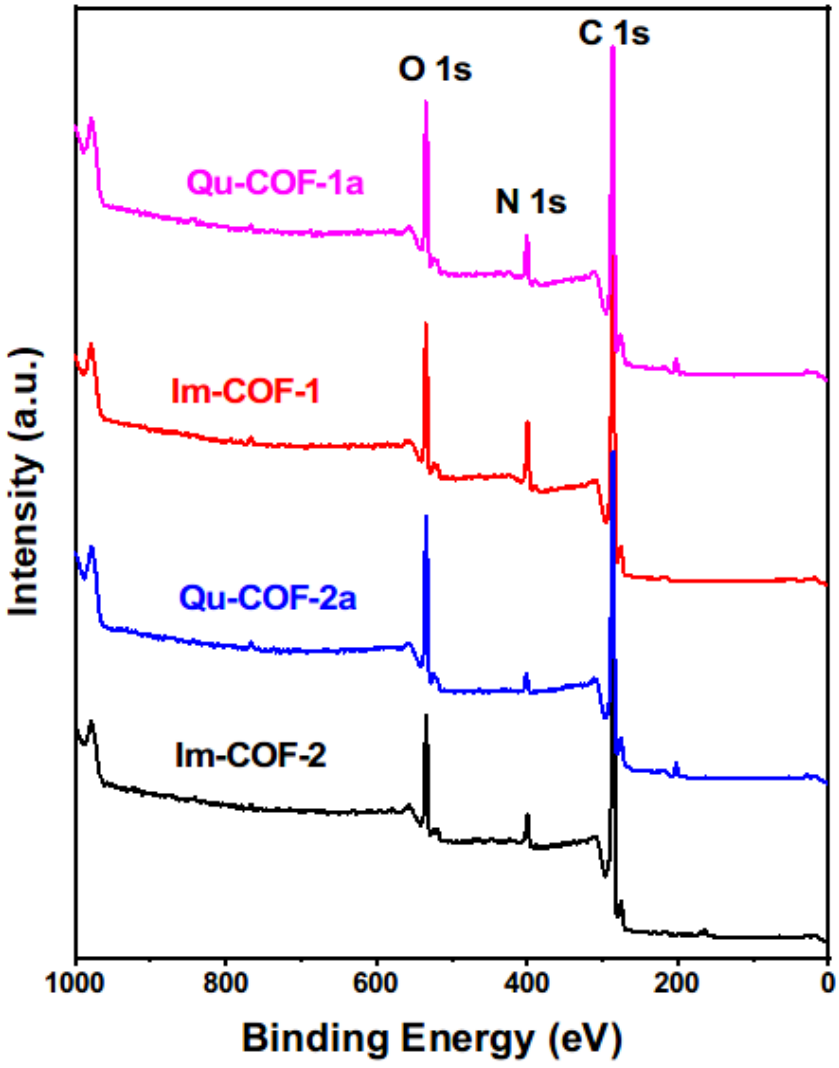

Figure 3.5.8 XPS spectra of Im-COF-1 (red), Im-COF-2 (black), Qu-COF-1a (purple) and Qu-COF-2a (blue).

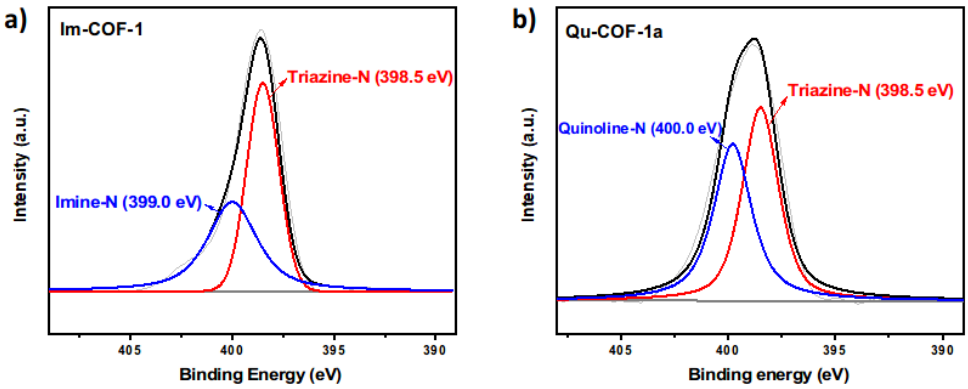

Figure 3.5.9 (a) N 1s spectra of Im-COF-1. (b) N 1s spectra of Qu-COF-1a.

X-Ray photoelectron spectrometry (XPS) measurements confirmed the elemental configurations of Qu-COFs, showing the presence of C 1s, N 1s, and O 1s (**Figure S8**). Compared with the N 1s peak (399.0 eV) from the imine bond of Im-COFs, the N 1s peak of Qu-COFs is red-shift to 400.0 eV, which corresponds to quinoline-N (**Figure 3.5.9 and Figure 3.5.12b**), indicating the formation of quinoline rings.

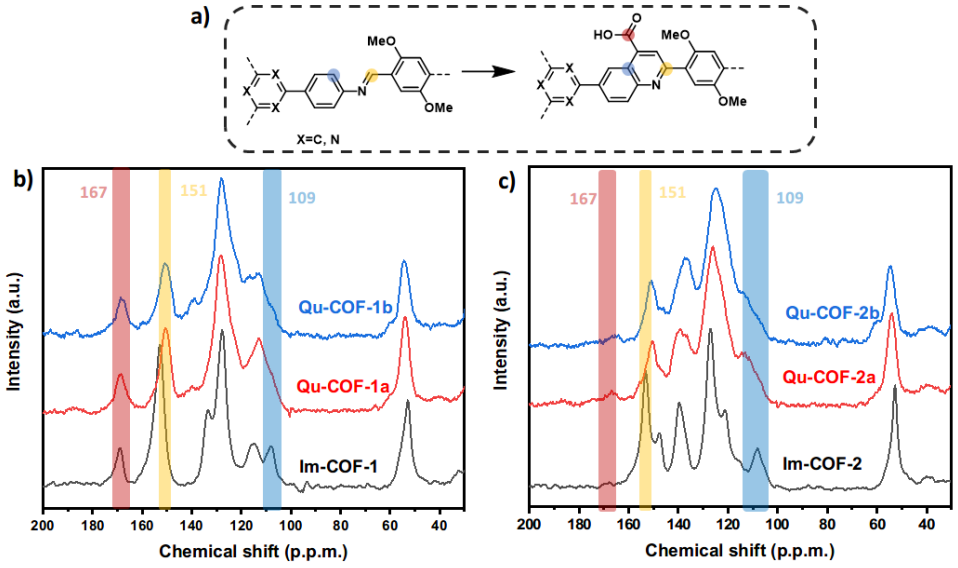

Figure 3.5.10 (a) Assignment of the ^{13}C ss-NMR signals to the respective ^{13}C in the structures of **Im-COFs** and **Qu-COFs.** (b) Solid-state ^{13}C cross-polarization magic angle spinning (CP/MAS) NMR of **Im-COF-1** (black), **Qu-COF-1a** (red), **Qu-COF-1b** (blue). (c) Solid-state ^{13}C cross-polarization magic angle spinning (CP/MAS) NMR of **Im-COF-2** (black), **Qu-COF-2a** (red), **Qu-COF-2b** (blue).

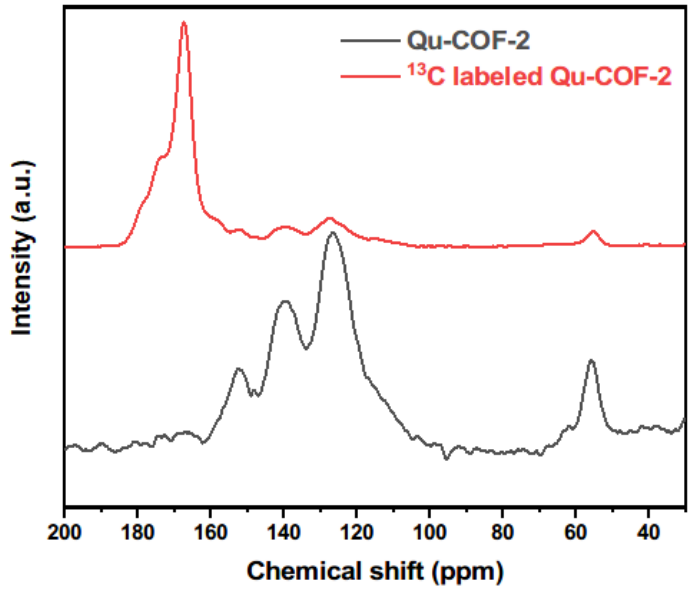

Figure 3.5.11 Solid-state ^{13}C cross-polarization magic angle spinning (CP/MAS) NMR of **Qu-COF-2** (black), ^{13}C labeled **Qu-COF-2** (red).

Solid-state ^{13}C cross polarization magic angle spinning (CP/MAS) NMR spectroscopy shows a shift of the sp^3-hybridised carbon from the methoxy group of Qu-COFs from 52 ppm to 56 ppm of the corresponding Im-COFs (**Figure 3.5.10**). Such shift might come from the high electron density on the quinoline rings. Compared with Im-COFs, the shift peak at 151 ppm of Qu-COFs can be assigned to the 2-quinolyl carbon and the peak at around 167 ppm can be assigned to the carbon from the carboxylic acid. This signal can be enhanced dramatically by using ^{13}C-labelling **Qu-COF-2a** using ^{13}C-labelled pyruvic acid (**Scheme 3.4.10 and Figure 3.5.11**).

These observations are consistent in all of Qu-COFs (Qu-COF-2, 3, 4-a&b) synthesized (**Figure 3.5.12- Figure 3.5.16**), and provide evidence of successful quinoline linkage formation.

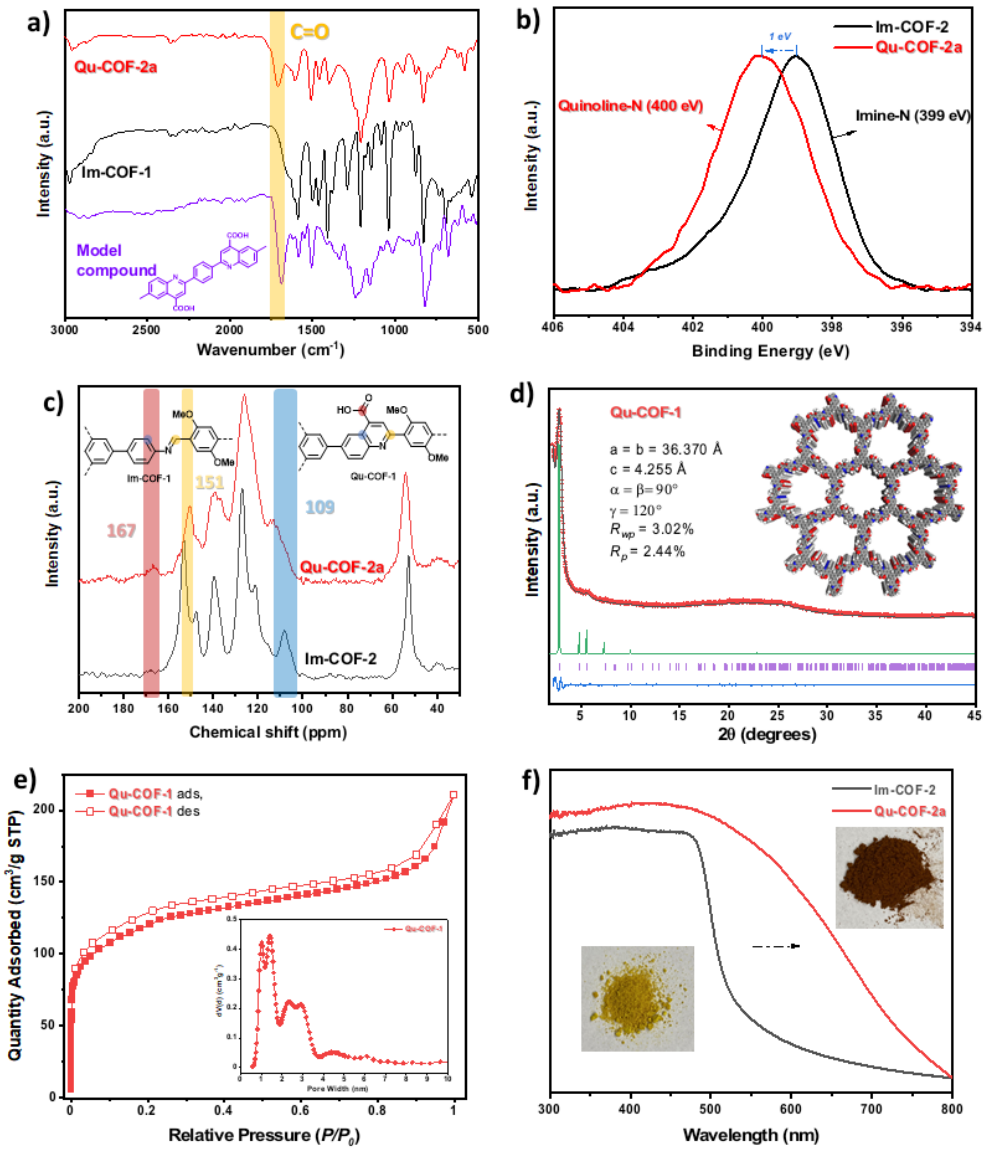

Figure 3.5.12. FT-IR spectra of **Qu-COF-1**, **Im-COF-1** and model compound. (b) N 1s binding energy profiles of **Qu-COF-1** and **Im-COF-1**. **Qu-COF-1** (red) and **Im-COF-1** (black). (c) Solid-state ^{13}C cross-polarization magic angle spinning (CP/MAS) NMR of **Im-COF-1** (black), **Qu-COF-1** (red). (d) Crystal structure of **Qu-COF-1**. Experimental PXRD patterns (red), profiles calculated from Pawley fitting (black) showing the residual (blue), and pattern simulated from the structural model (green). Reflection positions are shown by tick marks (purple). (e) Nitrogen adsorption and desorption isotherms for **Qu-COF-1** recorded at 77 K (filled symbols = adsorption; open symbols = desorption). Insert shows the pore size distribution of Qu-COF-1 calculated by NLDFT method. (f) Solid-state UV-Vis absorption spectra of **Im-COF-1** (black) and **Qu-COF-1** (red). Insert shows the photographs of **Im-COF-1** and **Qu-COF-1** after filter from reaction.

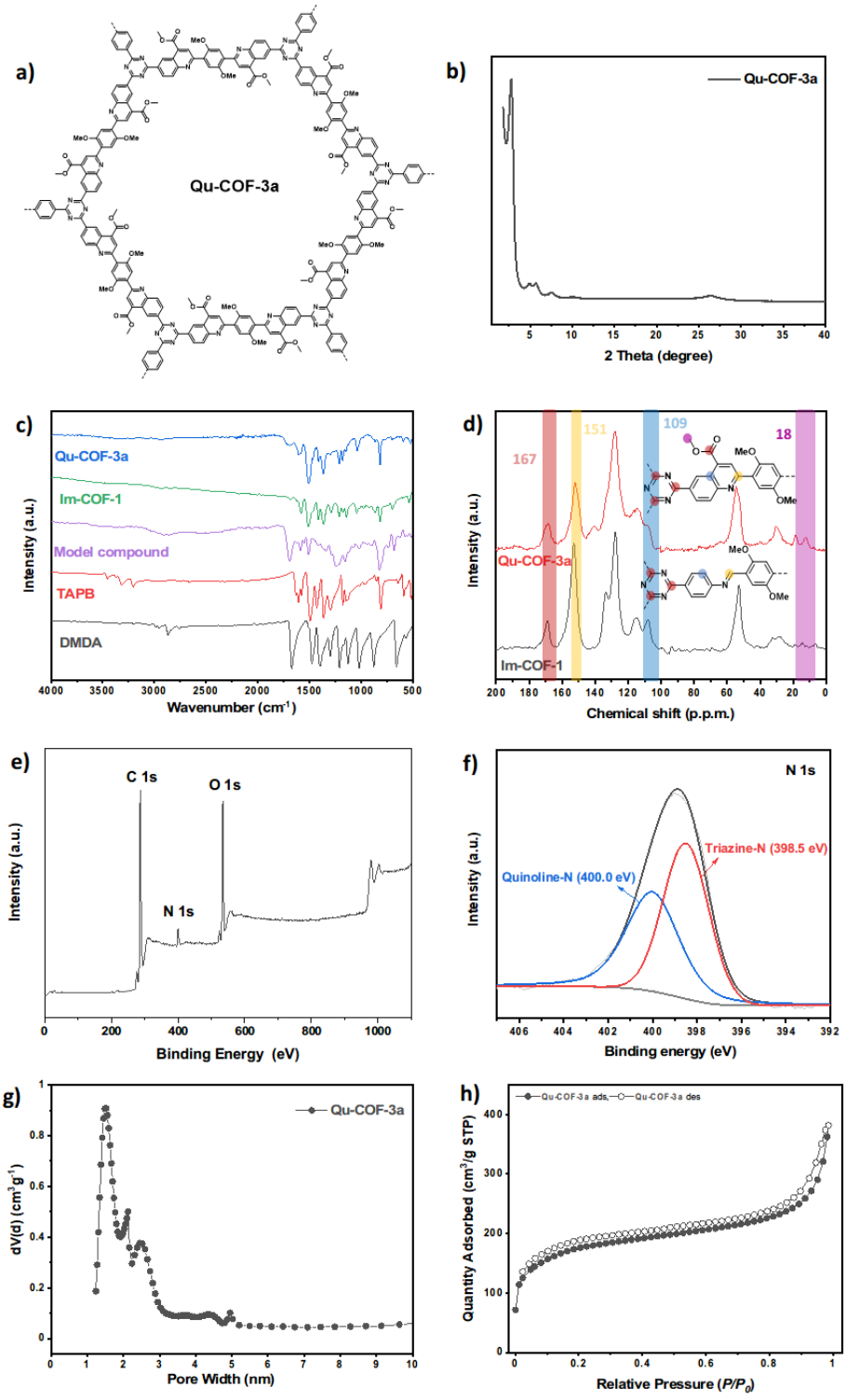

Figure 3.5.13 (a) Chemical structure of **Qu-COF-3a**. (b) PXRD patterns of **Qu-COF-3a**. (c) FT-IR spectra of **Qu-COF-3a** (blue), Im-COF-1 (green), model compound (purple), TAPT (red), DMDA (black). (d) Solid-state ^{13}C cross-polarization magic angle spinning (CP/MAS) NMR of Im-COF-1 (black), **Qu-COF-3a** (red). (e) Full XPS spectrum of **Qu-COF-3a** shown from 0 up to 1100 eV. (f) N 1s XPS spectra of **Qu-COF-3a** with fit. (g) Nitrogen adsorption

and desorption isotherms for **Qu-COF-3a** recorded at 77 K (filled symbols = adsorption; open symbols = desorption). (h) Pore size distribution of **Qu-COF-3a** calculated by NLDFT method.

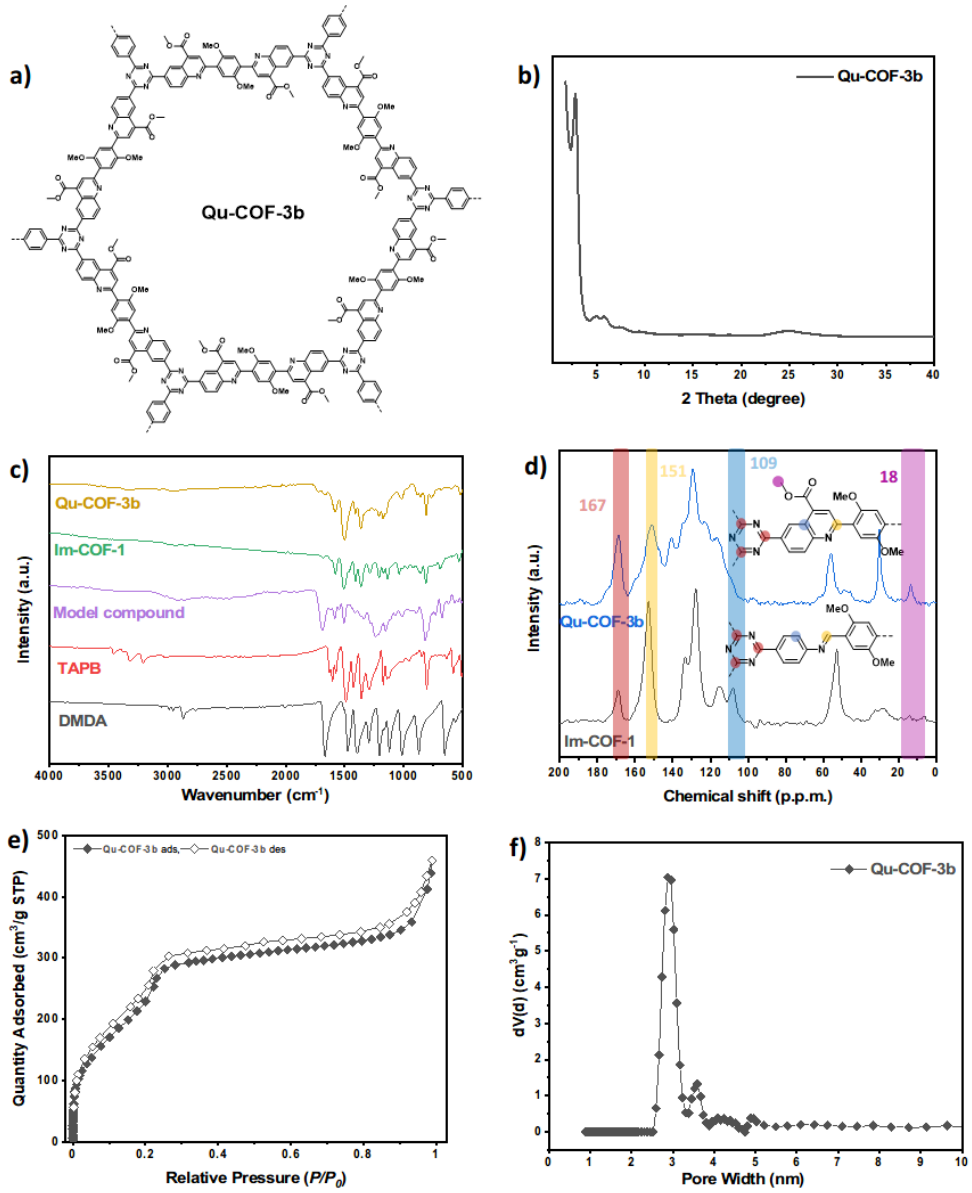

Figure 3.5.14 (a) Chemical structure of **Qu-COF-3b**. (b) PXRD patterns of **Qu-COF-3b**. (c) FT-IR spectra of **Qu-COF-3b** (yellow), Im-COF-1 (green), model compound (purple), TAPT (red), DMDA (black). (d) Solid-state ^{13}C cross-polarization magic angle spinning (CP/MAS) NMR of Im-COF-1 (black), **Qu-COF-3b** (blue). (e) Nitrogen adsorption and desorption isotherms for **Qu-COF-3b** recorded at 77 K (filled symbols = adsorption; open symbols = desorption). (f) Pore size distribution of **Qu-COF-3b** calculated by NLDFT method.

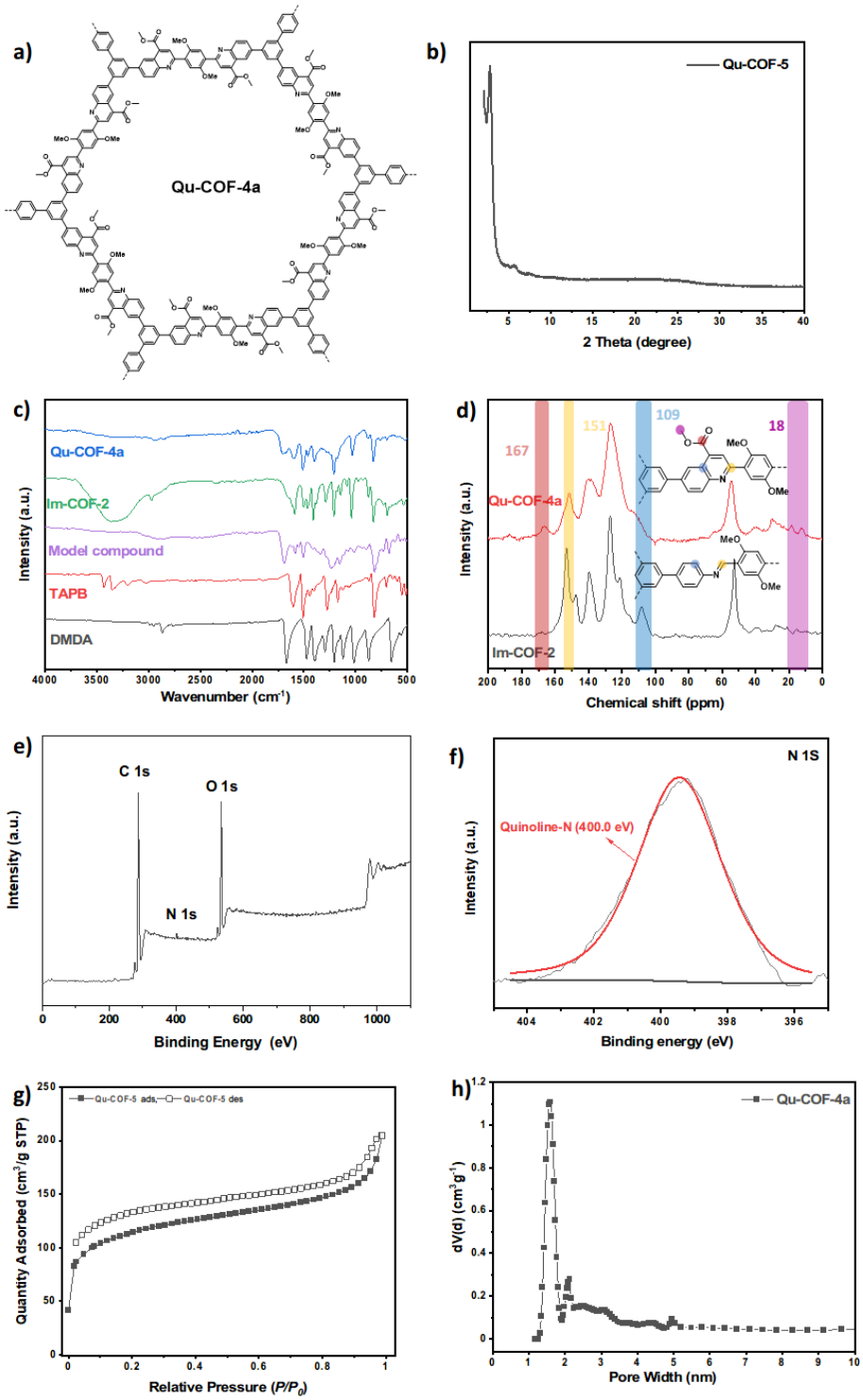

Figure 3.5.15 (a) Chemical structure of **Qu-COF-4a**. (b) PXRD patterns of **Qu-COF-4a**. (c) FT-IR spectra of **Qu-COF-4a** (blue), Im-COF-2 (green), model compound (purple), TAPB (red), DMDA (black). (d) Solid-state ^{13}C cross-polarization magic angle spinning (CP/MAS) NMR of Im-COF-2 (black), **Qu-COF-4a** (red). (e) Full XPS spectrum of **Qu-COF-4a** shown from 0 up to 1100 eV. (f) N 1s XPS spectra of **Qu-COF-4a** with fit. (g) Nitrogen adsorption

and desorption isotherms for **Qu-COF-4a** recorded at 77 K (filled symbols = adsorption; open symbols = desorption). (h) Pore size distribution of **Qu-COF-4a** calculated by NLDFT method.

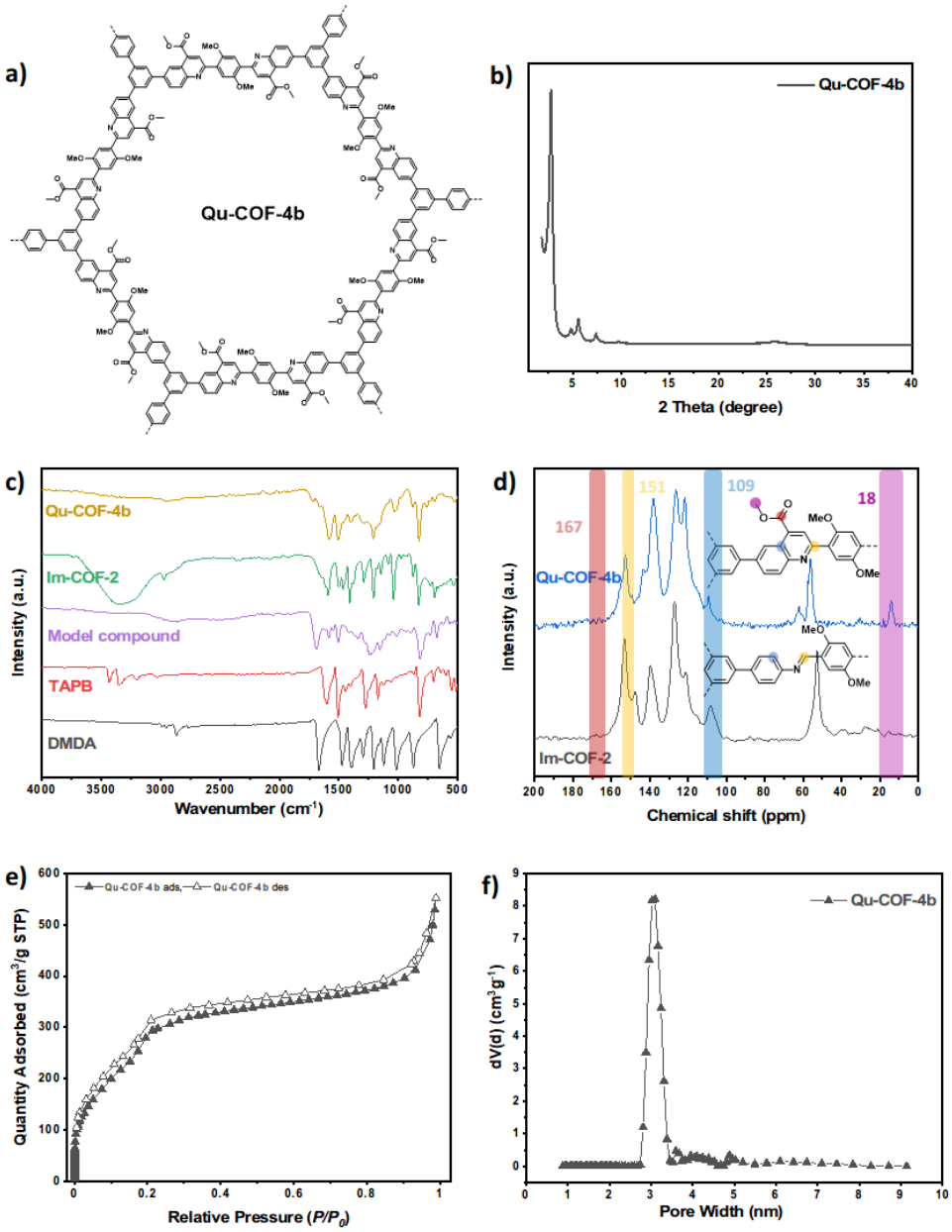

Figure 3.5.16 (a) Chemical structure of **Qu-COF-4b**. (b) PXRD patterns of **Qu-COF-4b**. (c) FT-IR spectra of **Qu-COF-4b** (yellow), Im-COF-2 (green), model compound (purple), TAPB (red), DMDA (black). (d) Solid-state ^{13}C cross-polarization magic angle spinning (CP/MAS) NMR of Im-COF-2 (black), **Qu-COF-4b** (blue). (e) Nitrogen adsorption and desorption isotherms for **Qu-COF-4b** recorded at 77 K (filled symbols = adsorption; open symbols = desorption). (f) Pore size distribution of **Qu-COF-4b** calculated by NLDFT method.

3.5.4 Characterization of Porous Properties and Morphologies

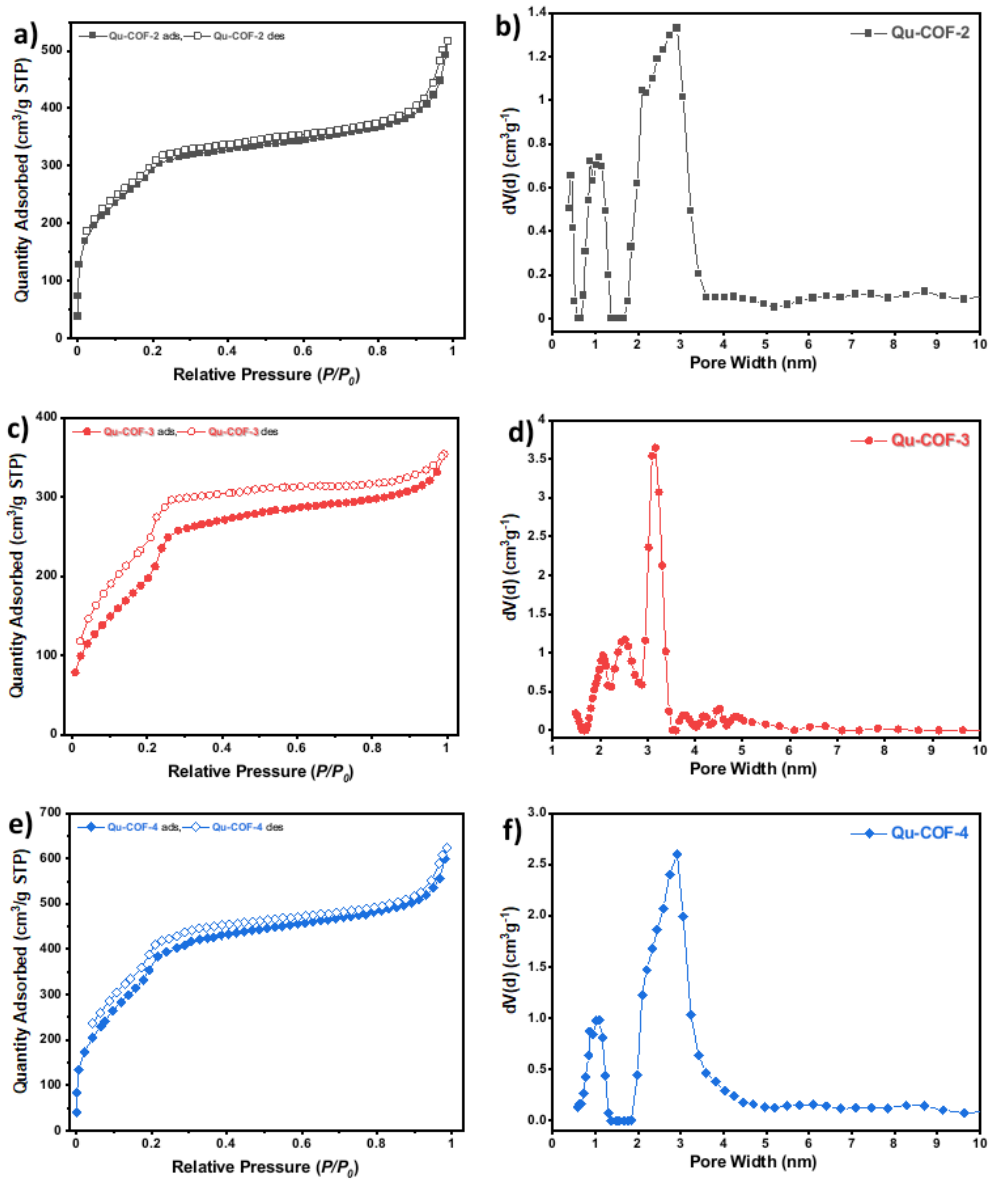

Figure 3.5.17 (a) Nitrogen adsorption and desorption isotherms for **Qu-COF-1a** recorded at 77 K (filled symbols = adsorption; open symbols = desorption). (b) Nitrogen adsorption and desorption isotherms for **Qu-COF-1b** recorded at 77 K (filled symbols = adsorption; open symbols = desorption). (c) Nitrogen adsorption and desorption isotherms for **Qu-COF-2b** recorded at 77 K (filled symbols = adsorption; open symbols = desorption). (d) Pore size distribution of **Qu-COF-1a** calculated by NLDFT. (e) Pore size distribution of **Qu-COF-1b** calculated by NLDFT. (f) Pore size distribution of **Qu-COF-2b** calculated by NLDFT.

The surface area and porosity of Qu-COFs were measured by nitrogen adsorption-desorption analysis at 77 K (**Figure 3.5.17**). The Brunauer-Emmett-Teller (BET) surface areas of Qu-COFs made by the one-pot method (**Qu-COF-1-4a**) are 1047, 436,

888 and 415 $m^2 g^{-1}$ respectively. The BET surface areas of Qu-COFs made by post-modification methods (**Qu-COF-1-4b**) are 1316, 912, 998 and 643 $m^2 g^{-1}$, respectively. The pore size distributions were calculated using nonlocal density functional theory (NL-DFT), showing pore size distributions for Qu-COFs centred at around 2.6 nm, which is consistent with the PXRD results. The pore size distributions of Qu-COFs are close to their corresponding Im-COFs, indicating the topology of Qu-COFs is similar.

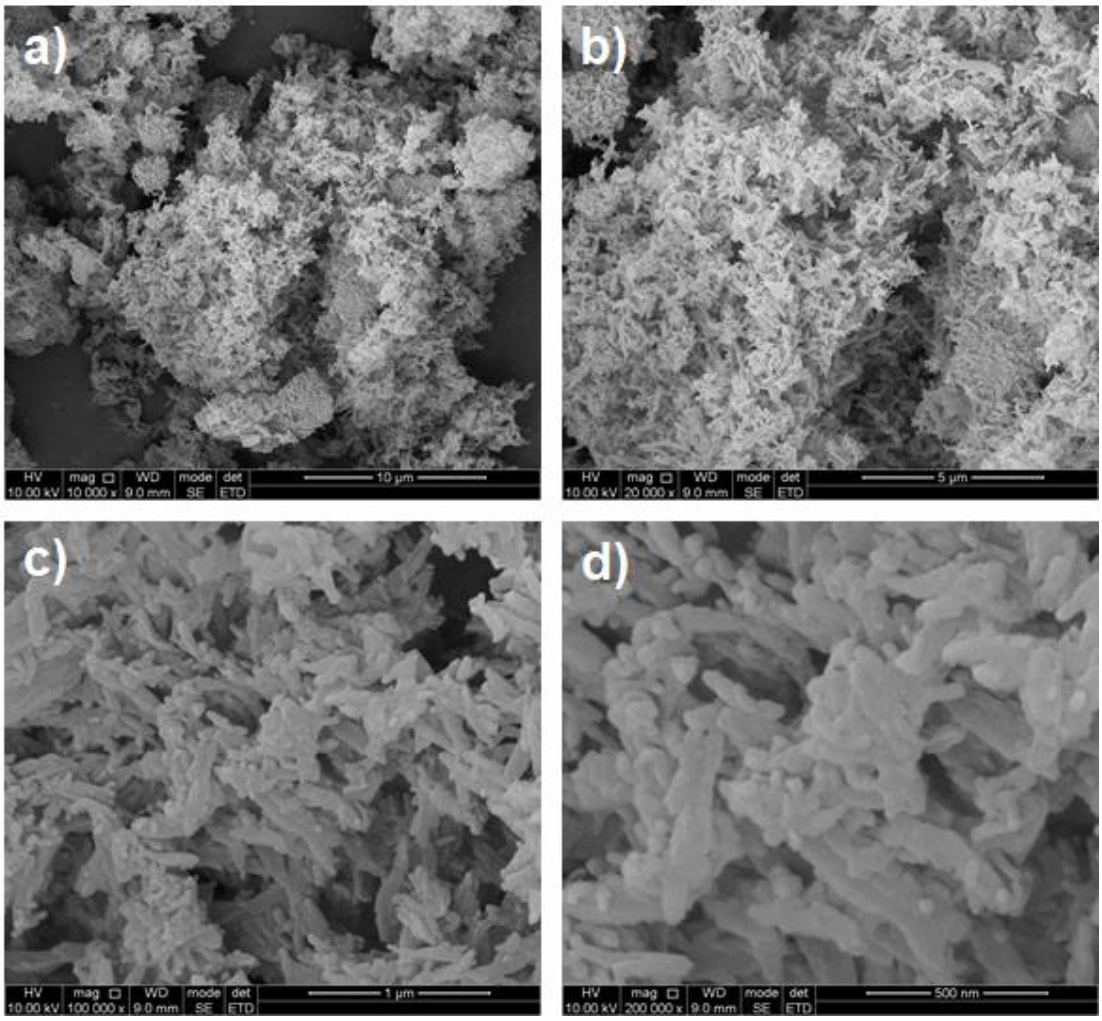

Figure 3.5.18 Scanning electron microscope images of Im-COF-1 at different magnifications.

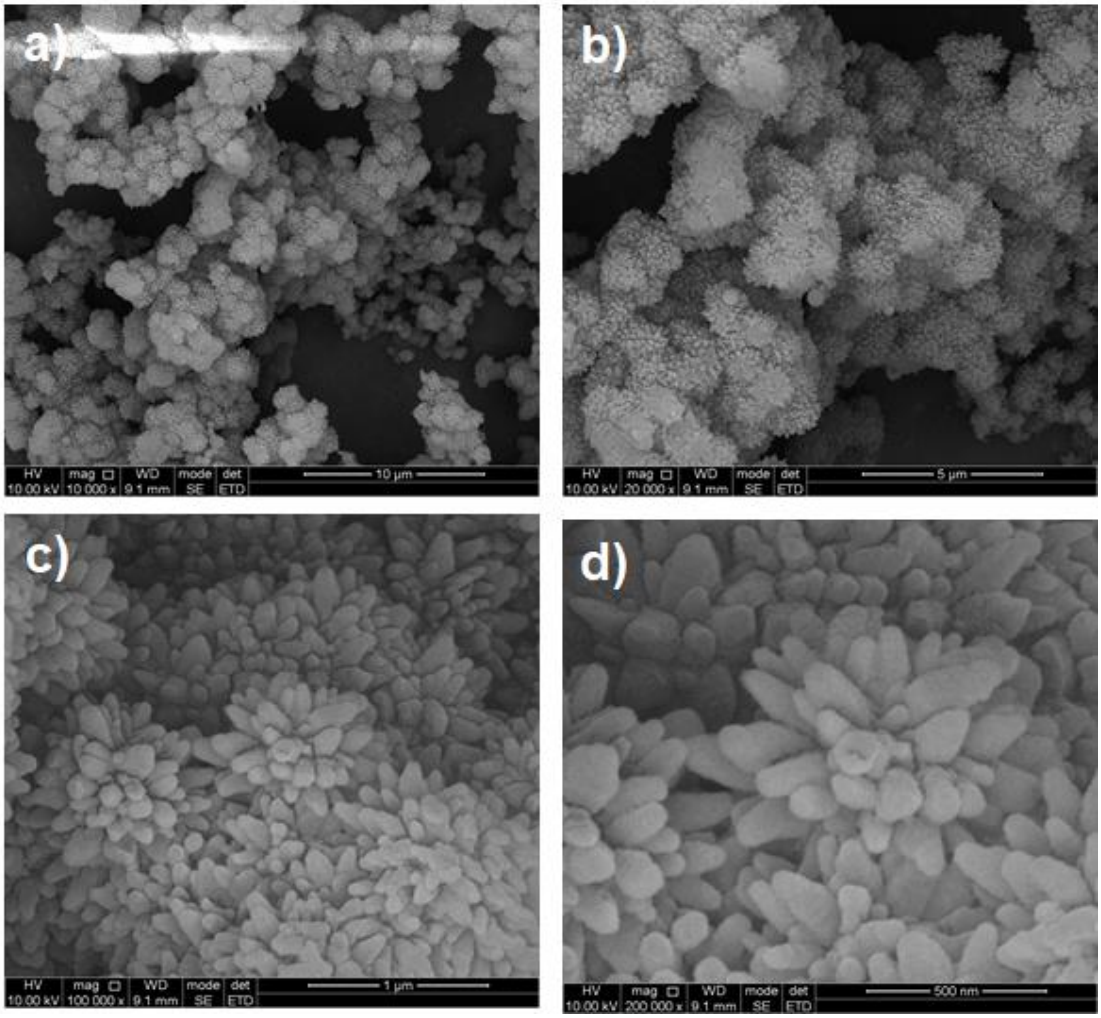

Figure 3.5.19 Scanning electron microscope images of Im-COF-2 at different magnifications.

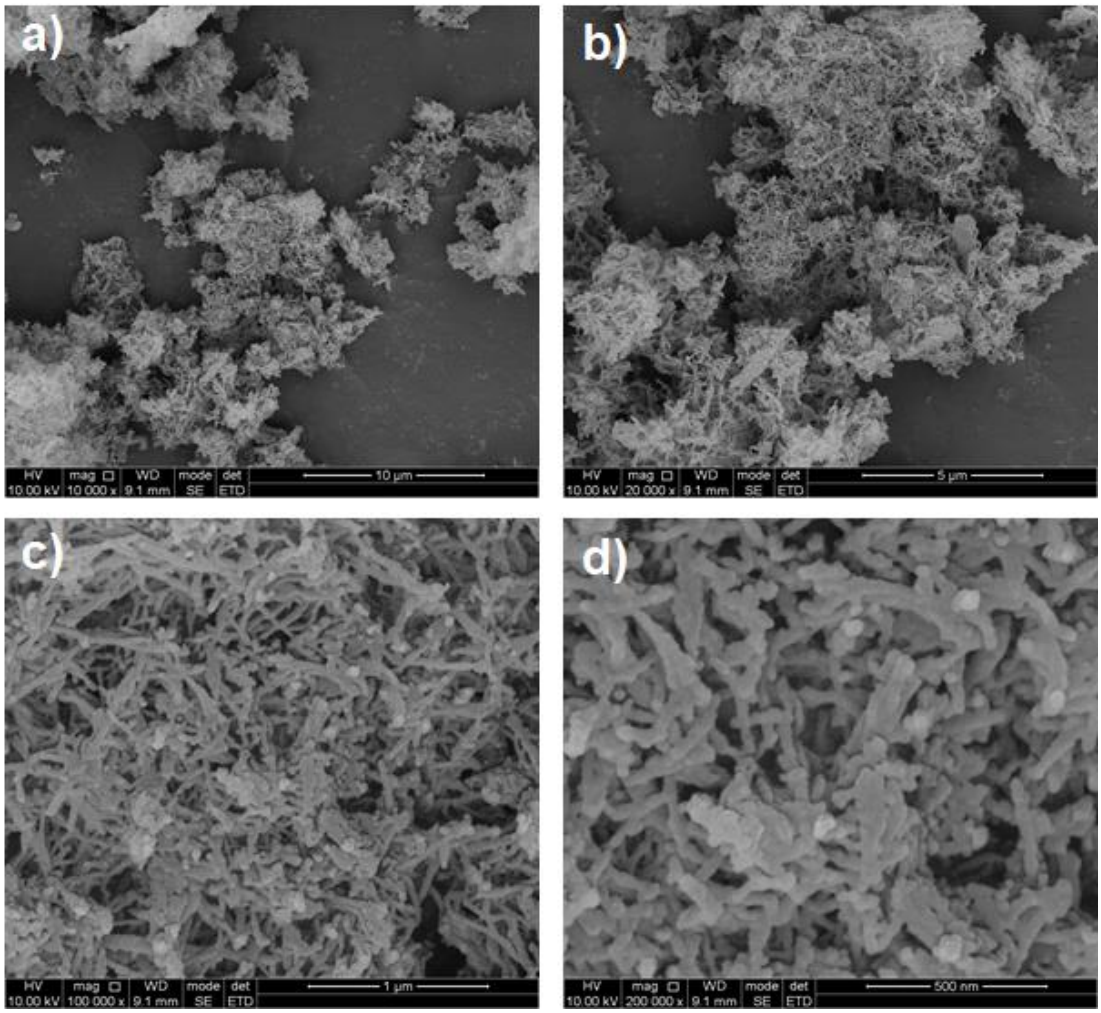

Figure 3.5.20 Scanning electron microscope images of Qu-COF-1a at different magnifications.

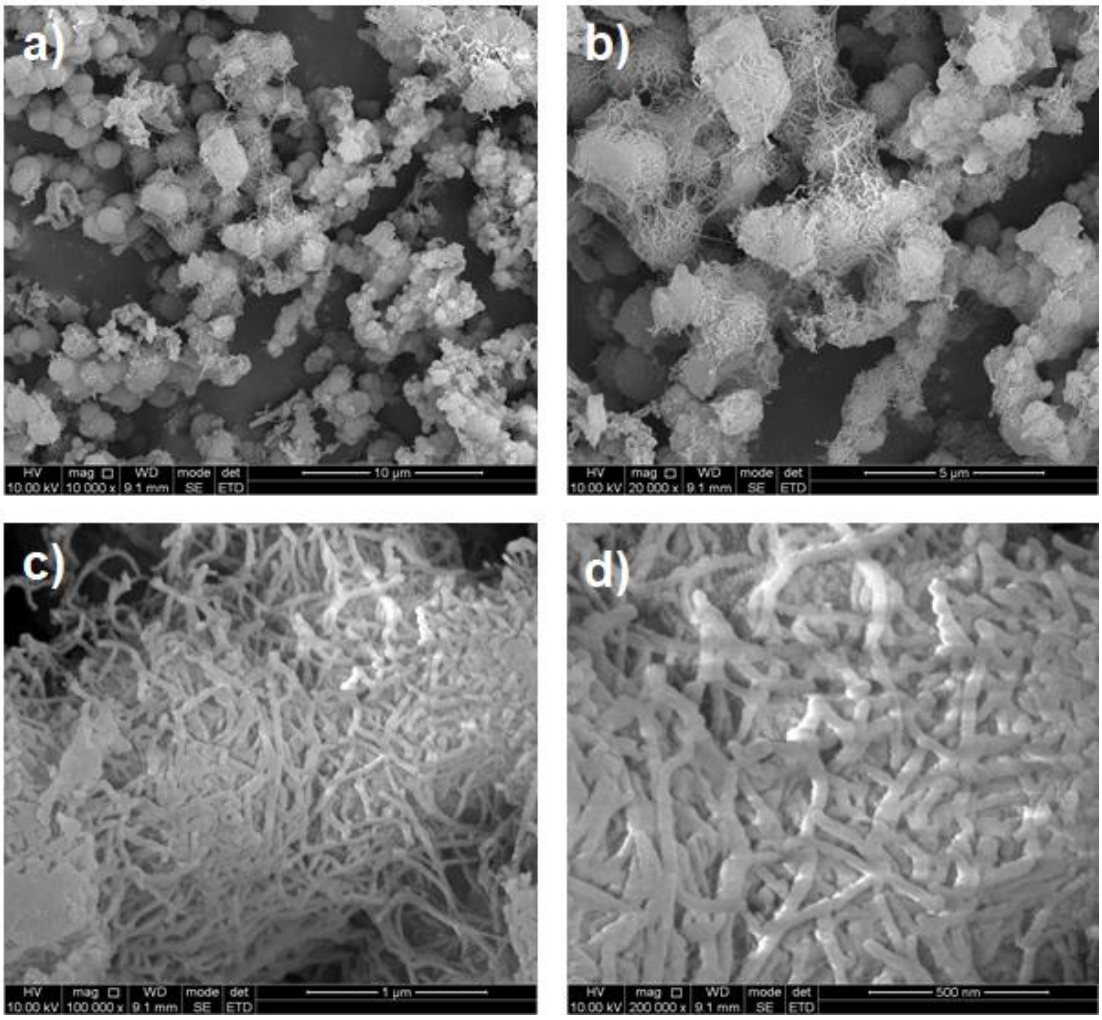

Figure 3.5.21 Scanning electron microscope images of Qu-COF-2a at different magnifications.

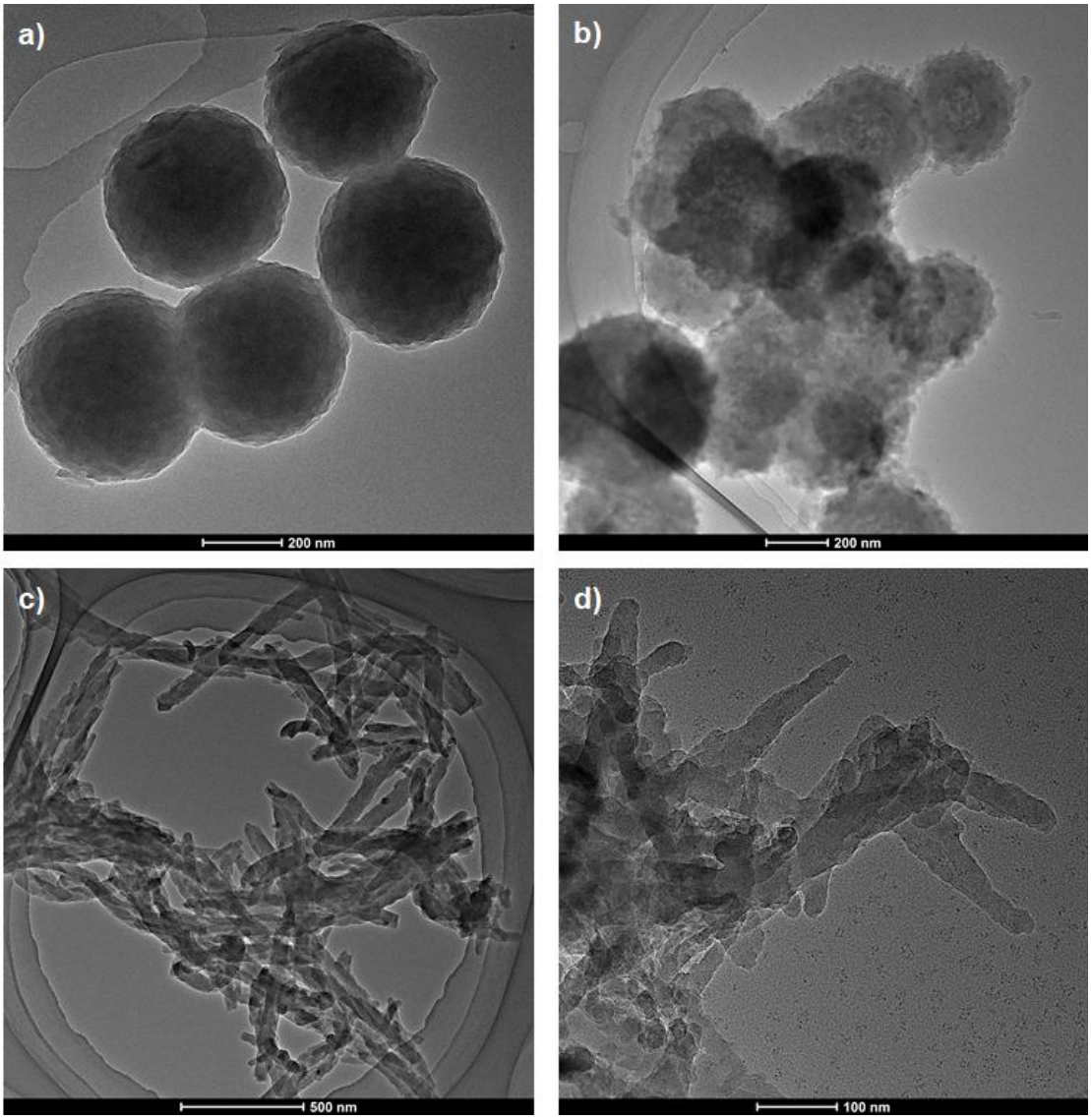

Figure 3.5.22 TEM images of (a) Im-COF-2; (b) Qu-COF-2a; (c) Im-COF-1 and (d) Qu-COF-1a.

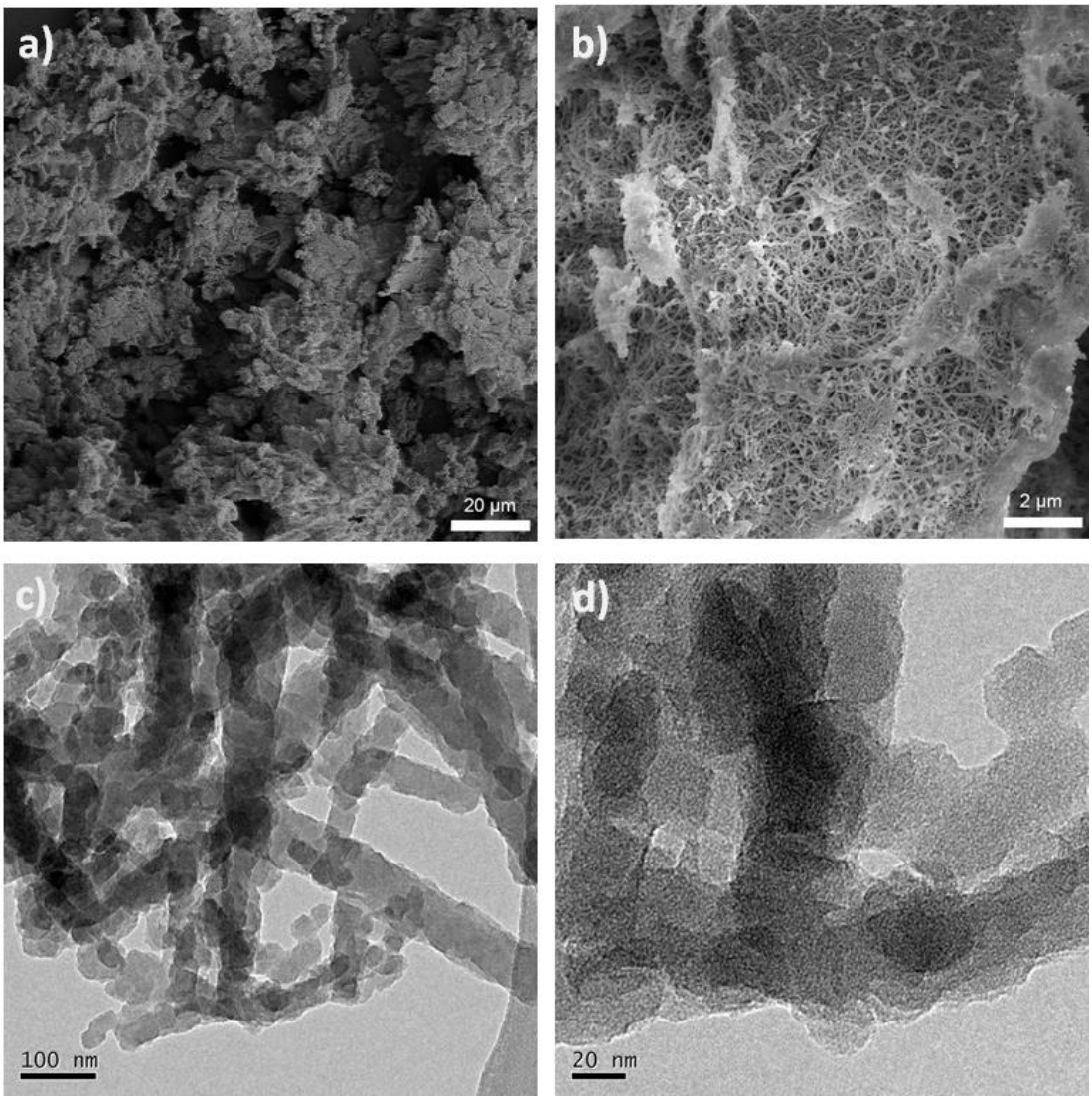

Figure 3.5.23 (a-b) SEM images of Qu-COF-1b; (c) (c-d) TEM images of Qu-COF-1b.

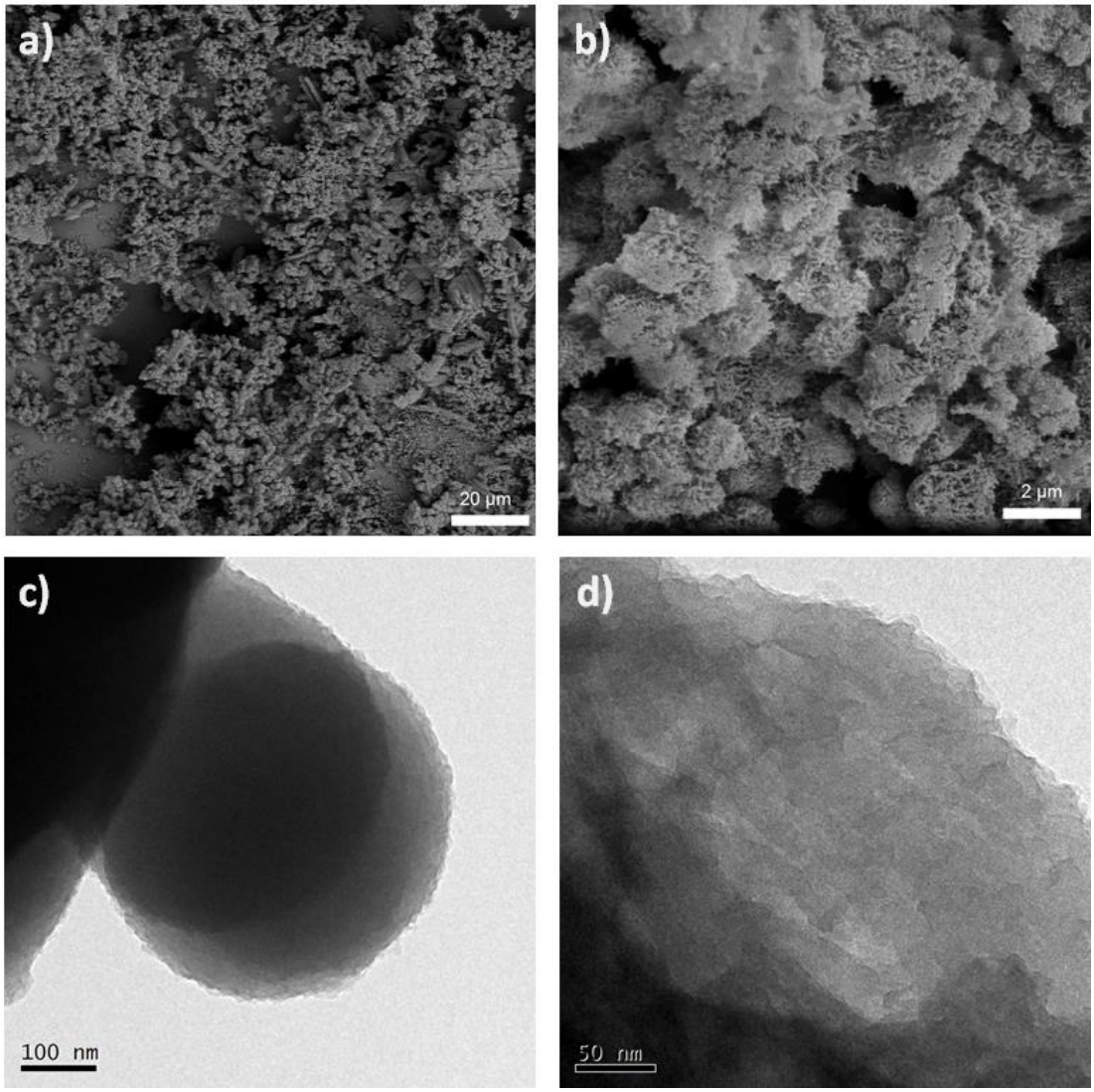

Figure 3.5.24 (a-b) SEM images of Qu-COF-2b; (c) (c-d) TEM images of Qu-COF-2b.

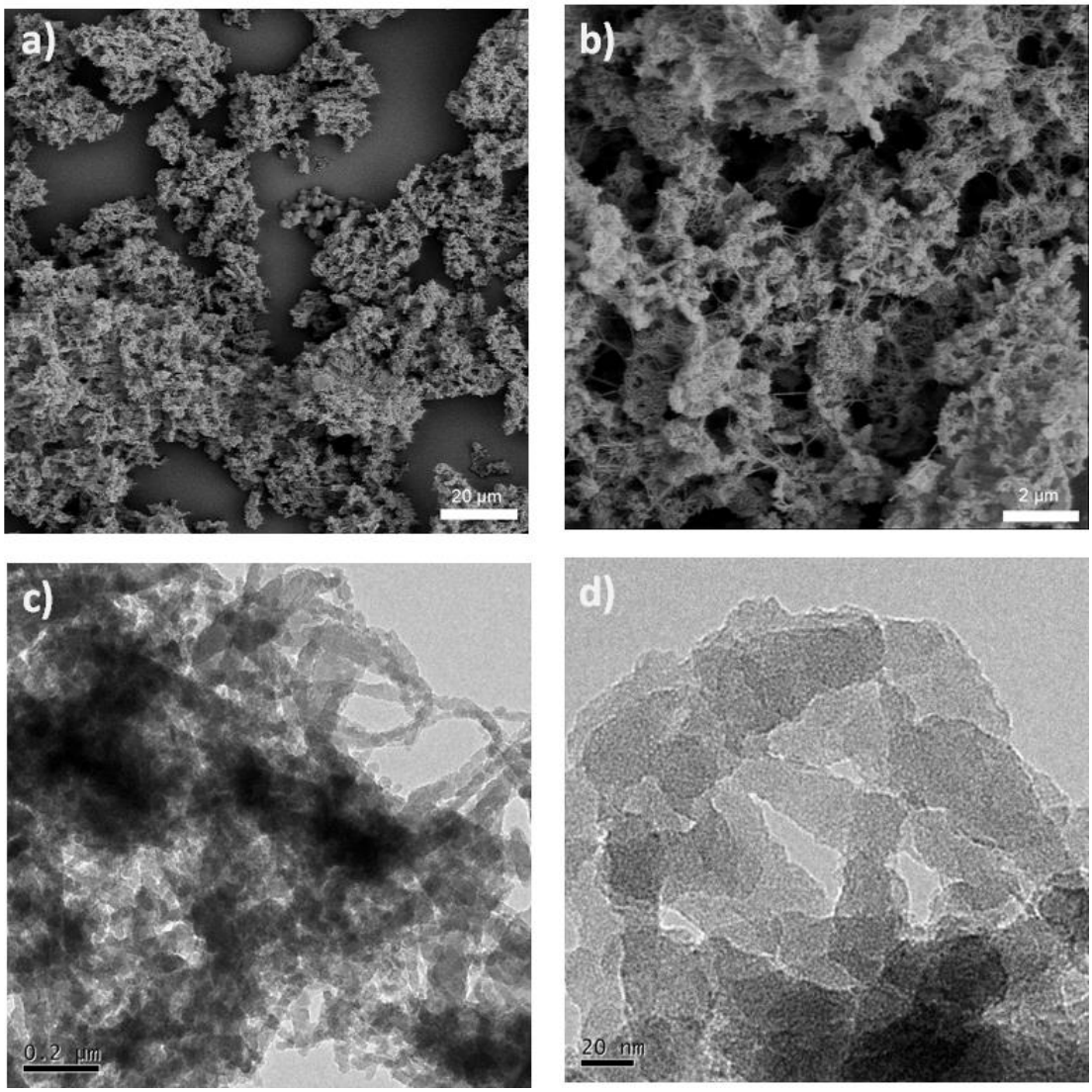

Figure 3.5.25 (a-b) SEM images of Qu-COF-3a; (c) (c-d) TEM images of Qu-COF-3a.

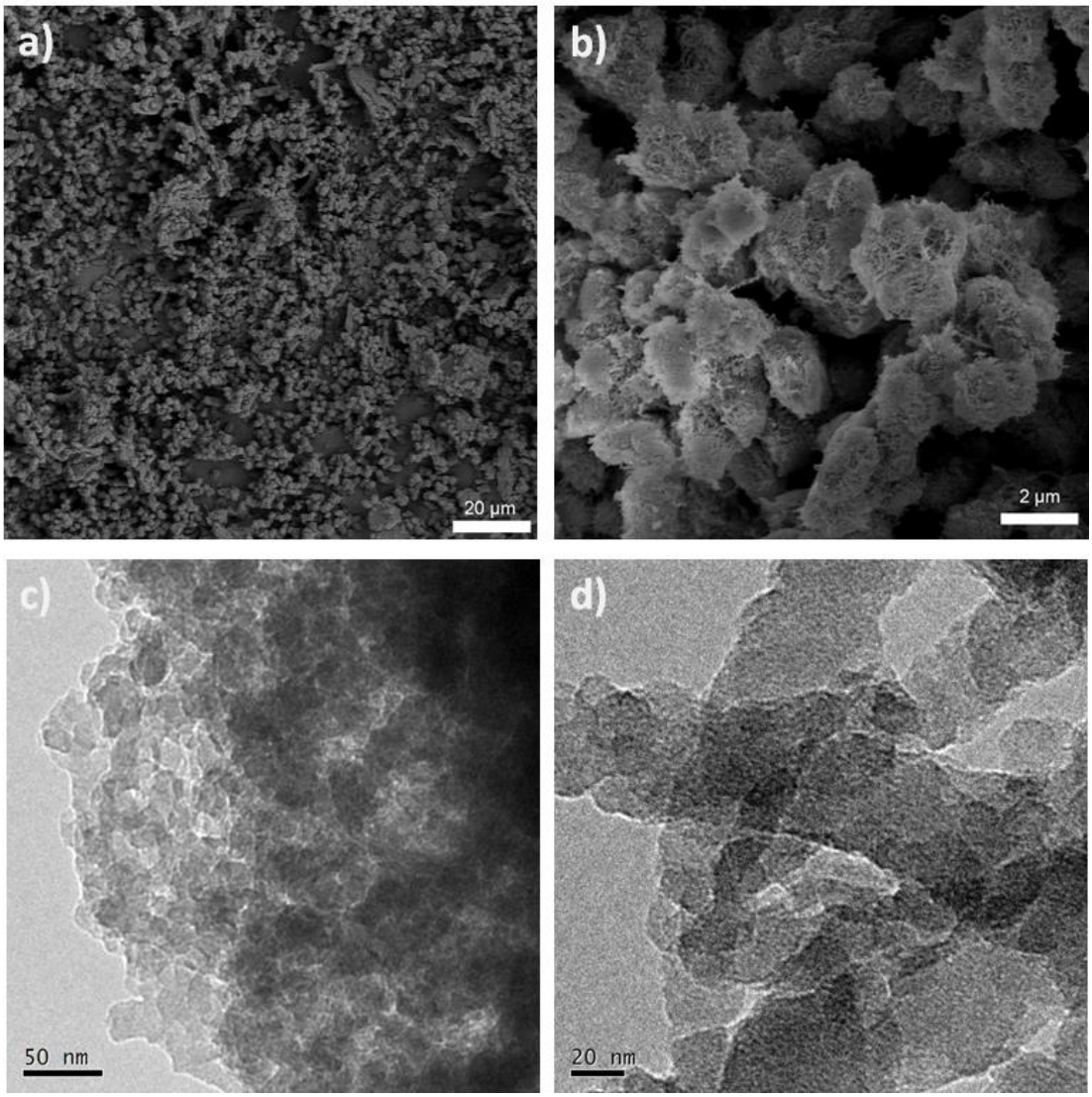

Figure 3.5.26 (a-b) SEM images of Qu-COF-4a; (c) (c-d) TEM images of Qu-COF-4a.

From the images of field-emission scanning electron microscopy (FE-SEM) and high-resolution transmission electron microscopy (HR-TEM), both **Qu-COF-1&3** and **Im-COF-1** show a rod-like structures while **Qu-COF-2&4** and **Im-COF-2** show a microsphere-like structure (**Figure 3.5.18-Figure 3.5.26**), also indicating the topologies and morphologies of Qu-COFs is similar.

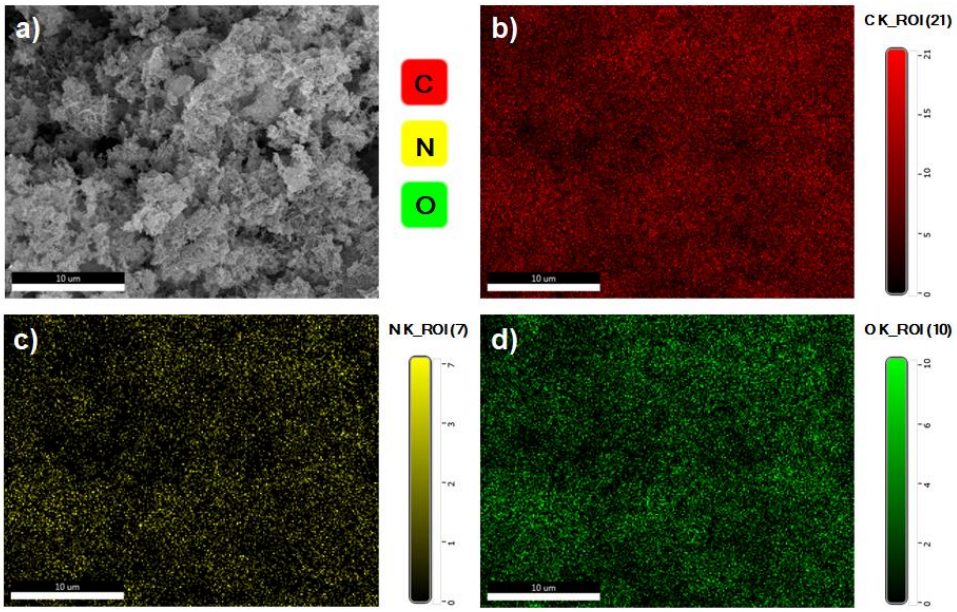

Figure 3.5.27 SEM image of (a) Qu-COF-1a; corresponding EDS elemental mapping of (b) carbon, (c) nitrogen and (d) oxygen.

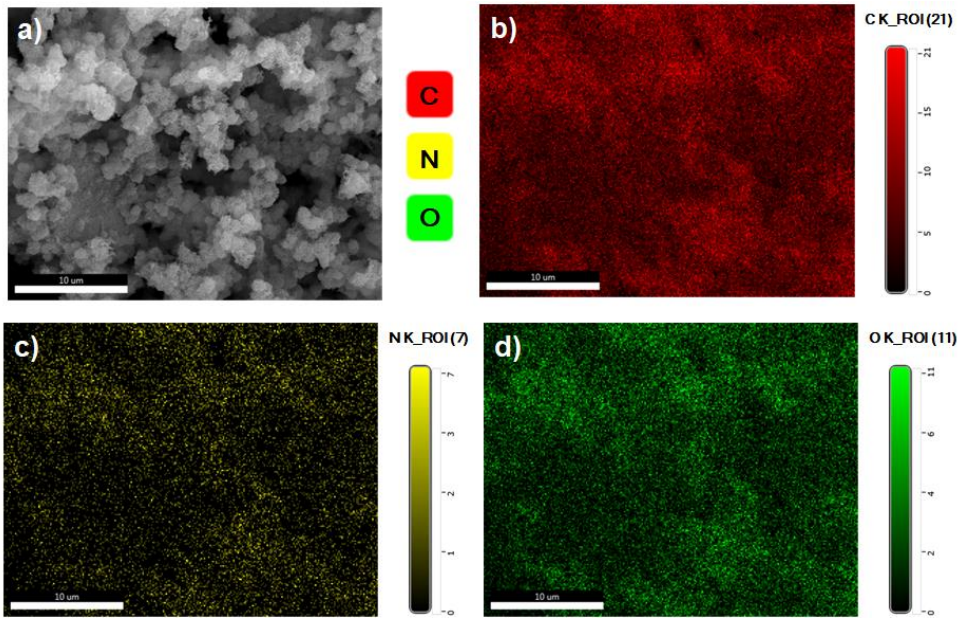

Figure 3.5.28 SEM image of (a) Qu-COF-2a; corresponding EDS elemental mapping of (b) carbon, (c) nitrogen and (d) oxygen.

Energy dispersive X-ray spectrum (EDS) elemental mapping of Qu-COFs show a homogenous elemental distribution of carbon, nitrogen and oxygen within the skeleton structures, indicating the successful introduction of quinoline functionality from the Doebner reaction (**Figure 3.5.27** and **Figure 3.5.28**).

3.5.5 Characterization of Optical Properties

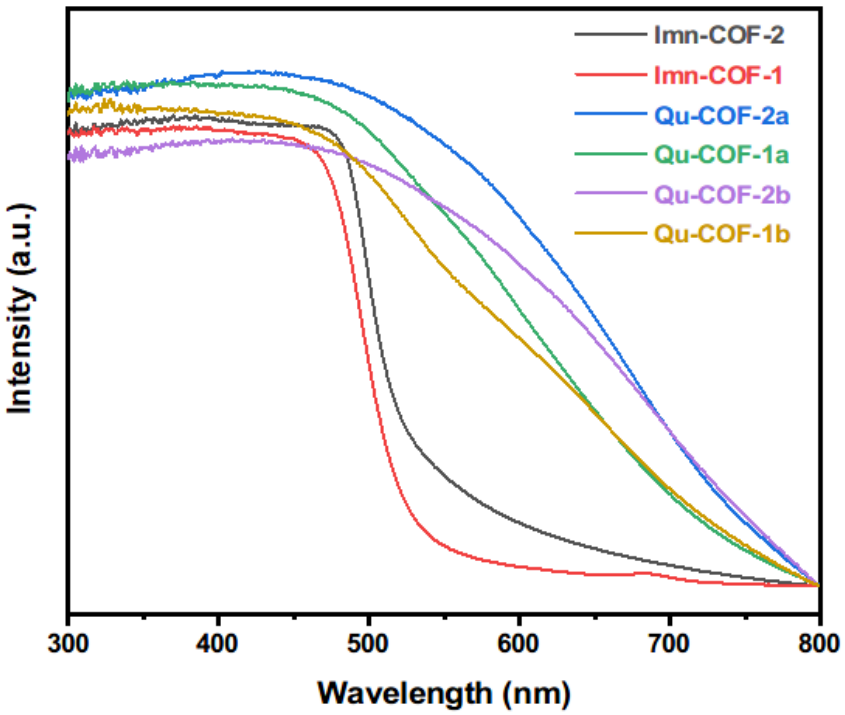

Figure 3.5.29 UV-Vis absorption spectra of Im-COFs and Qu-COFs measured in the solid-state.

Solid-state UV/visible adsorption spectra was used to assess the optical properties of Qu-COFs (**Figure 3.5.29**). The spectra show that all the COFs can absorb light in the UV and visible regions. In comparison with Im-COFs, these Qu-COFs exhibit a red shift of their absorption edge to longer wavelength and enhanced intensity of visible-light absorption. The optical band gaps of **Qu-COFs 1a&b-2a&b** were calculated to be 1.58, 1.62, 1.75 and 1.69 eV, respectively. These are narrower than their respective **Im-COF-1** and **Im-COF-2** (2.35 and 2.31 eV) (**Figure 3.5.30**).

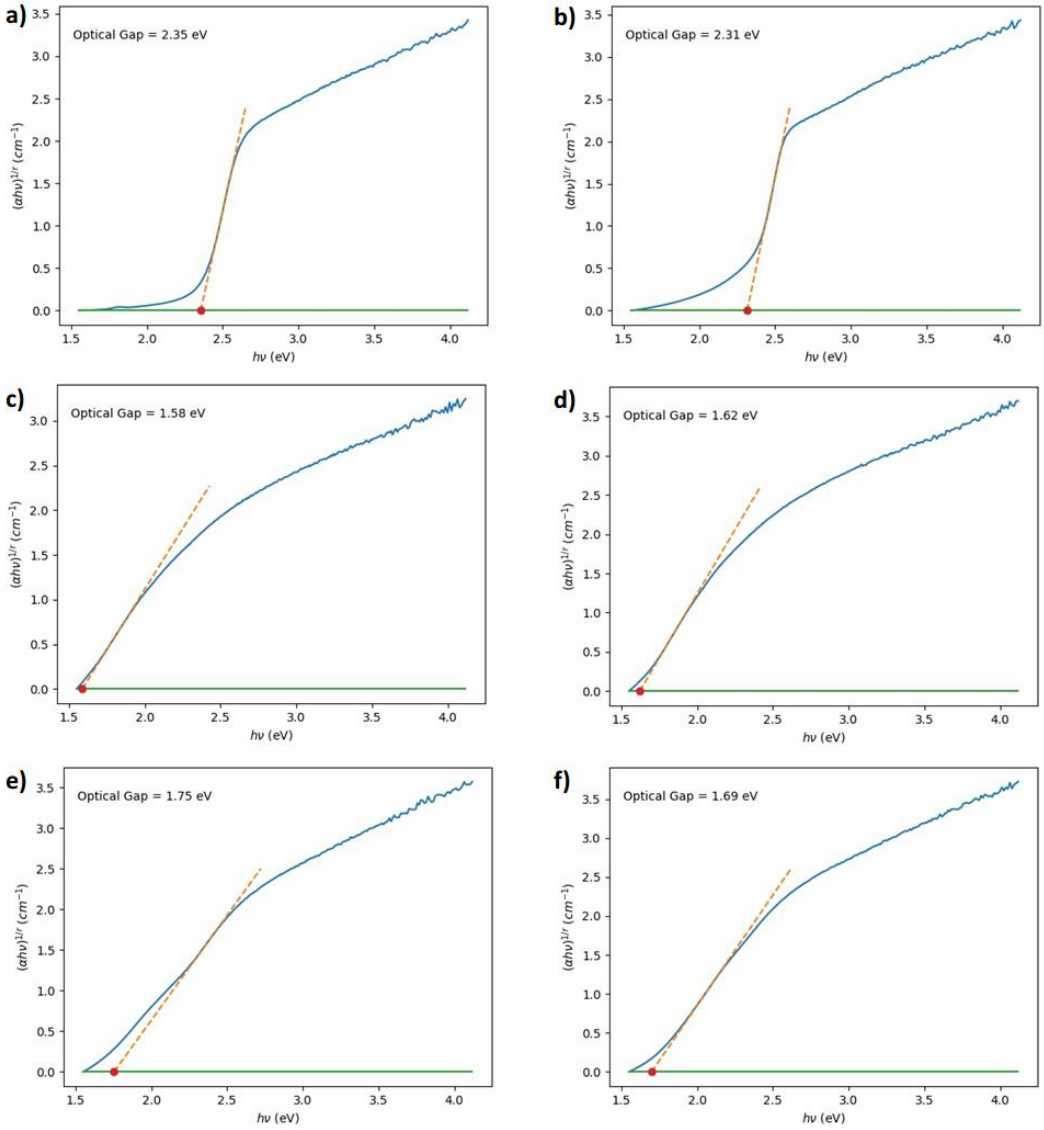

Figure 3.5.30 UV-Vis absorption spectra and band-gap calculation of (a) Im-COF-1; (b) Im-COF-2; (c) Qu-COF-1a; (d) Qu-COF-2a; (e) Qu-COF-1b; (f) Qu-COF-2b.

Encouraged by the high stability and conjugation of Qu-COFs from quinoline-linkages, we investigated the optical property of Qu-COFs in aqueous solutions with different pH values. Interestingly, we found the colour of Qu-COF-2a dispersed in the solution turned from dark red to orange and finally bright yellow ((**Figure 3.5.31a**) when the of pH value was changed from 1.0 to 14.0. This phenomenon could be observed by the naked eye, showing the Qu-COFs with a potential for pH-dependent colorimetric sensors. The pH-dependent luminescent property could come from a protonation and

deprotonation processes between the quinoline and the carboxylic acid groups *via* an excited-state intermolecular proton transfer (ESIPT) effect.

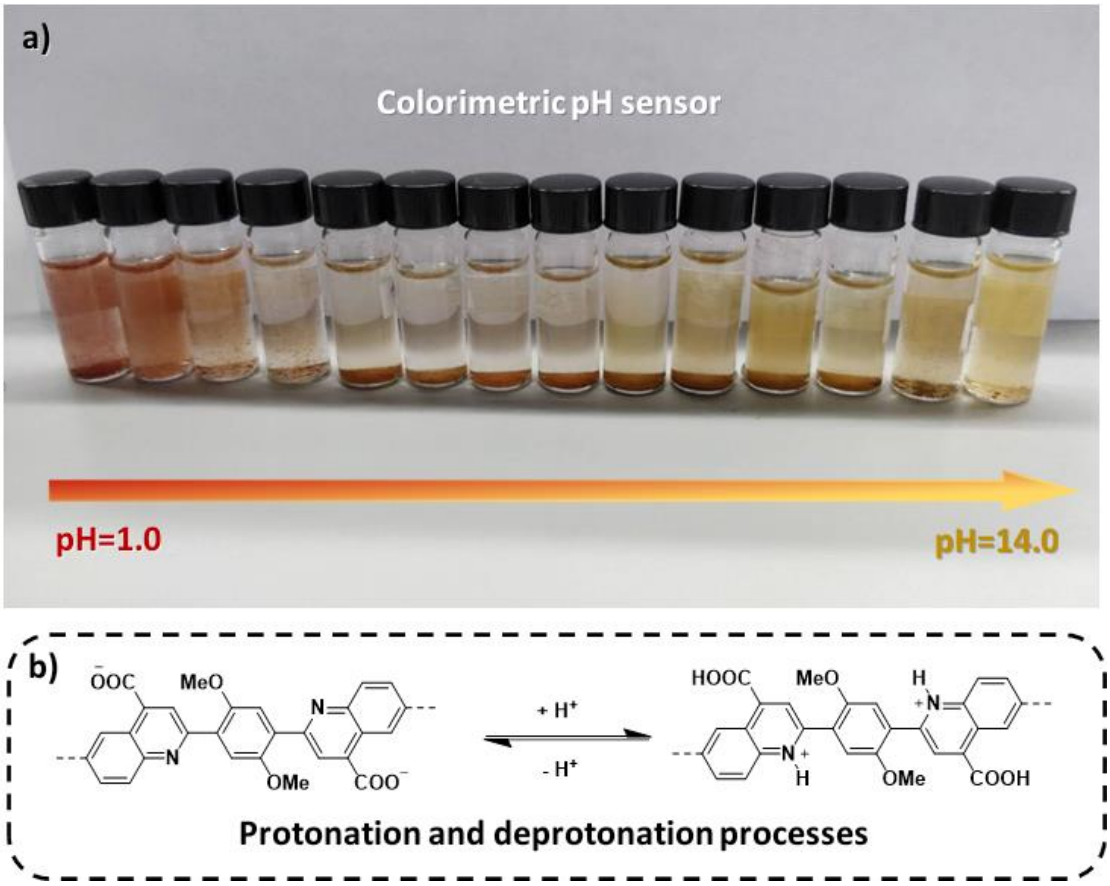

Figure 3.5.31 (a) Eye-naked colour changes of Qu-COF-2a after immersion in varieties of aqueous solutions from pH=1.0 to pH=14.0.; (b) Protonation and deprotonation process of quinoline-4-carboxylic acid linkage within the Qu-COFs in acidic and basic media.

3.5.6 Characterization of Quinoline-Linked Covalent Organic Nanosheets

3.5.6.1 Stability of Quinoline-Linked Covalent Organic Frameworks

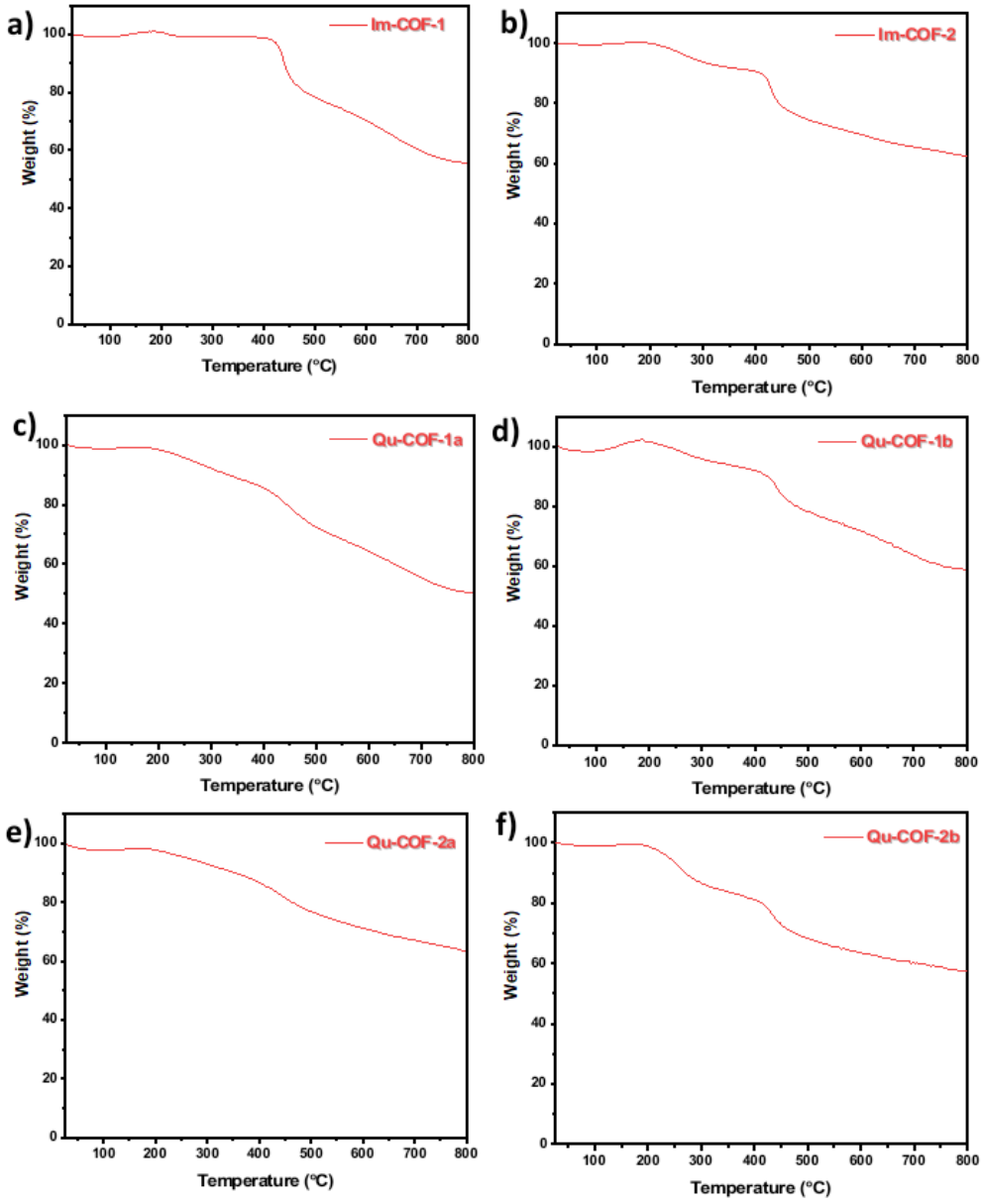

Figure 3.5.32 TGA curves of Im-COF-1&2, Qu-COF-1a&b~2a&b measured in N_2.

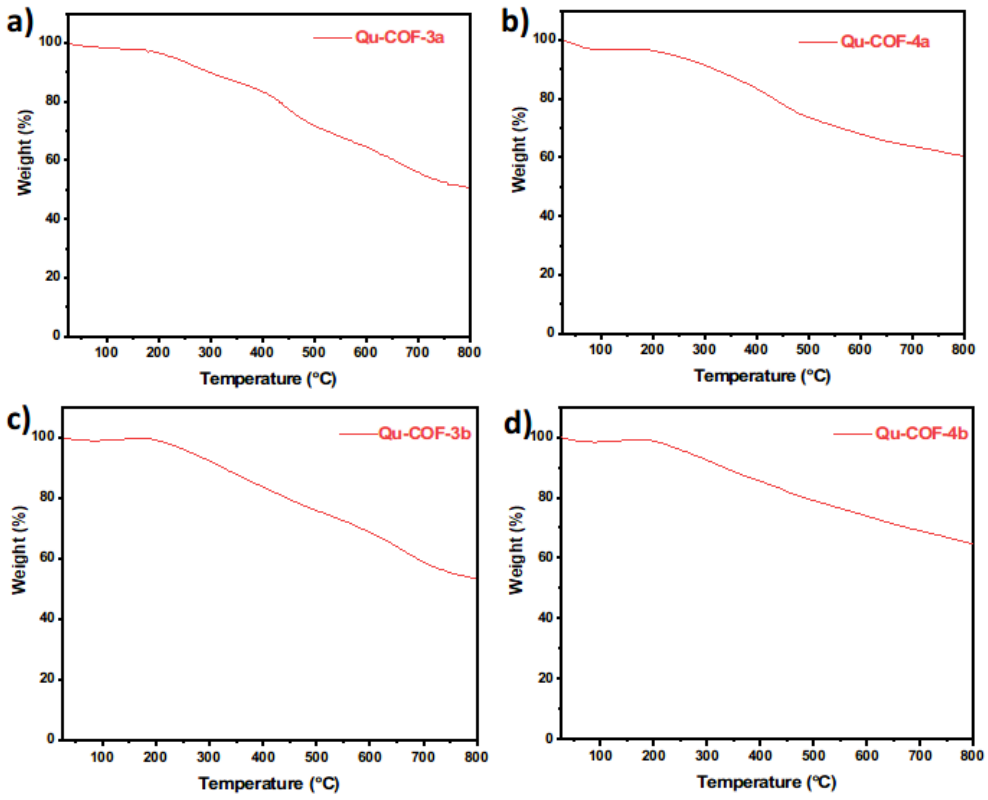

Figure 3.5.33 TGA curves of Qu-COF-3a&b~4a&b measured in N_2.

Thermogravimetric analysis (TGA) revealed Qu-COFs are thermally stable up to approximately 300 °C. We propose the weight loss at 300 °C is due to decarboxylation of the carboxylic acids (**Figure 3.5.32** and **Figure 3.5.33**).

The stability of Qu-COFs was examined in common solvents, such as water, acetone, tetrahydrofuran (THF), N, N-dimethylformamide (DMF), trichloromethane, aqueous KOH (6 M), and HCl (6 M). The original Im-COF show a good chemical stability in all the organic solvents and only loss the crystallinity in 6 M HCl aqueous solution. However, Qu-COF-2a show amorphous even in mild conditions, such as acetone and ethanol (**Figure 3.5.34**).

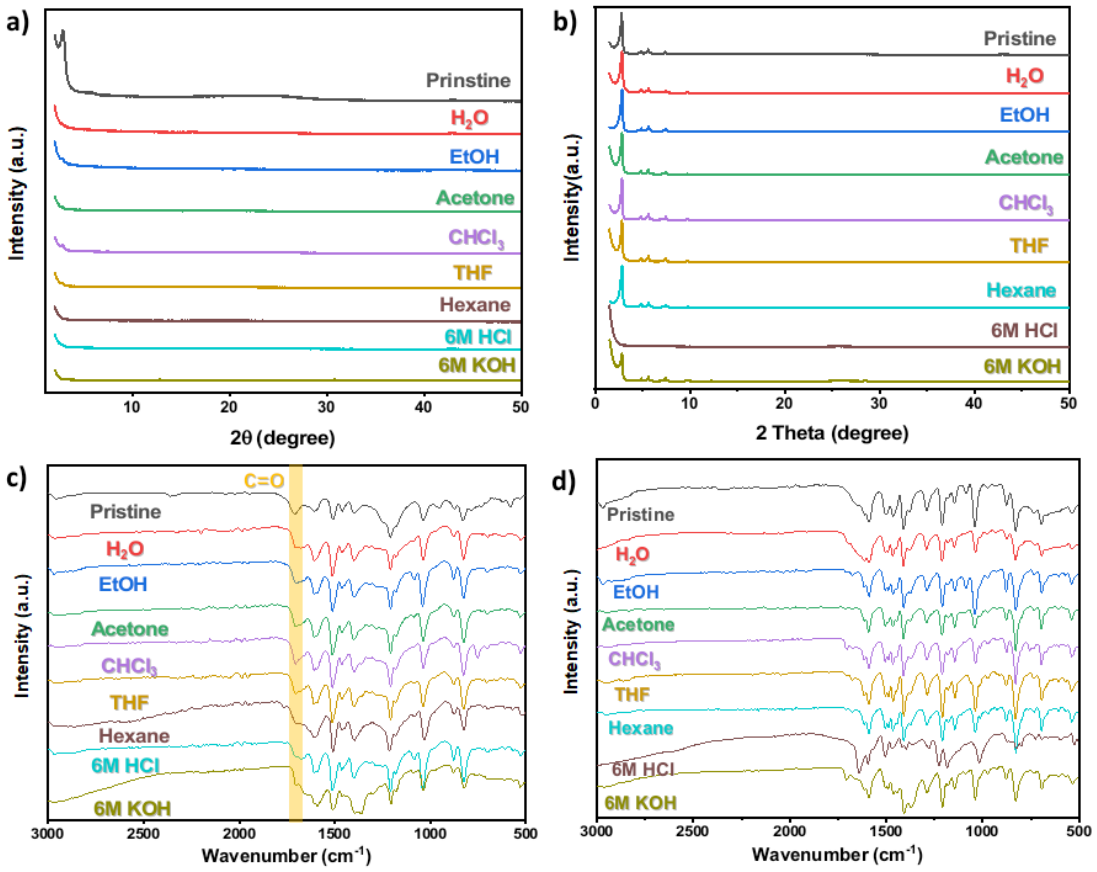

Figure 3.5.34 (a-b) PXRD patterns of **Qu-COF-2a** and **Im-COF-2** after stability test by various solvents. (c-d) FT-IR spectra of **Qu-COF-2a** and **Im-COF-2** after stability test by various solvents.

To investigate the reason, we tried same stability tests for all the Qu-COFs and test PXRD and FT-IR after filter. The loss of crystallinity was observed in each case, but the FT-IR spectra remain unchanged indicating retention of the atomic-level connectivity (**Figure 3 and Figure S33**). Considering the quinoline linkage should be stable under these conditions, we hypothesized that this loss of crystallinity could be due to the unique structural features of the twisted quinoline-4-carboxylic acid group resulting from the Doebner reaction disrupting the interlayer interaction.

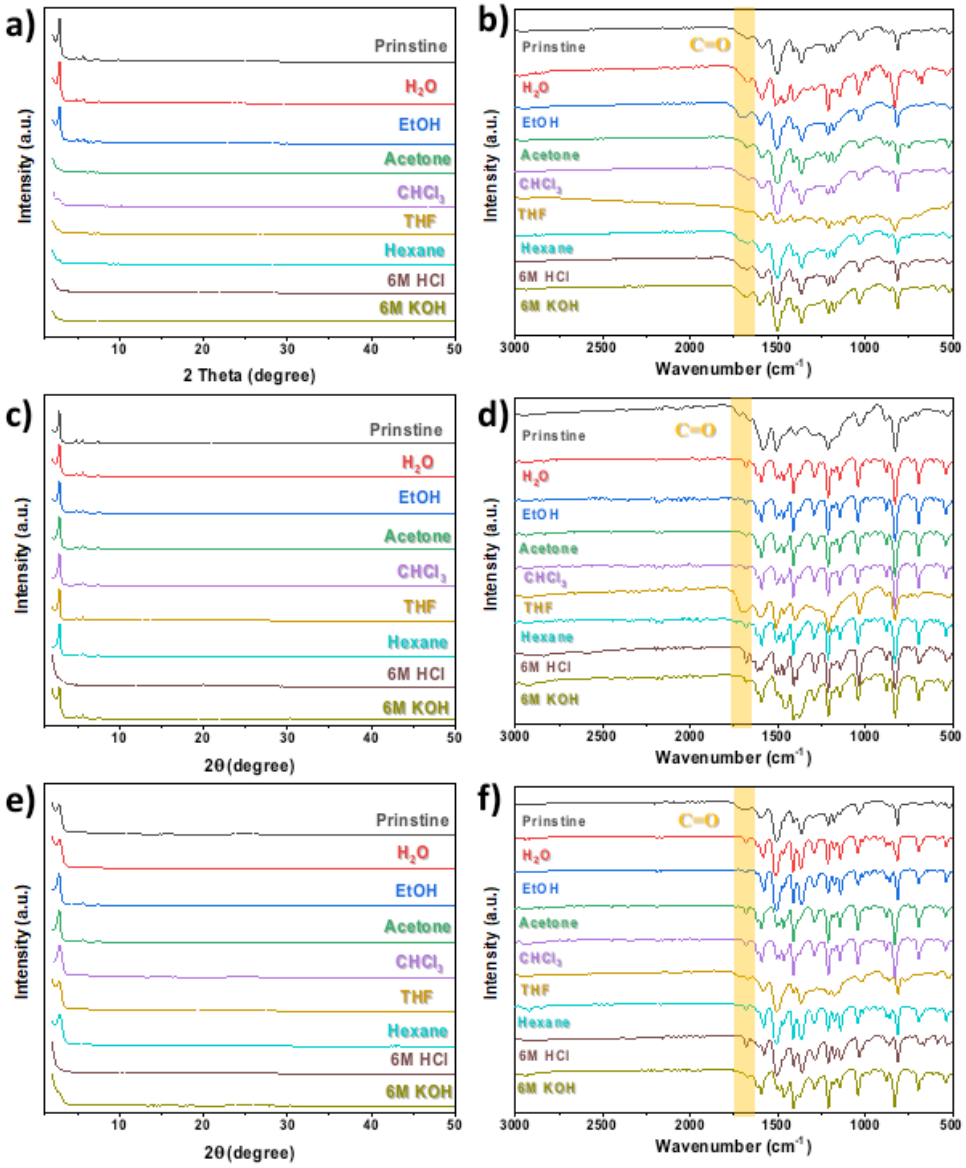

Figure 3.5.35 (a-b) PXRD patterns and FT-IR spectra of Qu-COF-1a after stability test by various solvents. (c-d) PXRD patterns and FT-IR spectra of Qu-COF-3a after stability test by various solvents. (e-f) PXRD patterns and FT-IR spectra of Qu-COF-4a after stability test by various solvents.

3.5.6.2 Morphologies of Quinoline-Linked Covalent Organic Nanosheets

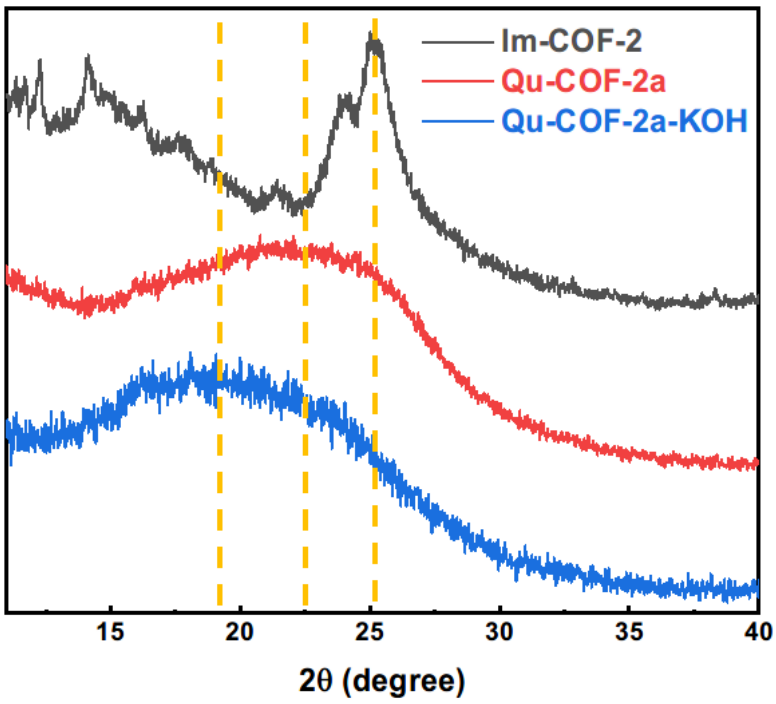

Figure 3.5.36 PXRD patterns of Im-COF-2 (black), Qu-COF-2a (red) and Qu-COF-2a after immersing in 6 M KOH solution for 24 h (blue).

Immersion of **Qu-COF-2a** in 6 M KOH solution for 24 h resulted in a boarder (001) peak from 15° to 25° with maximum at around 20° in the PXRD. This indicates larger *d*-spacing of interlayers and exfoliation of layers in the basic solution[34] (**Figure 3.5.36**).

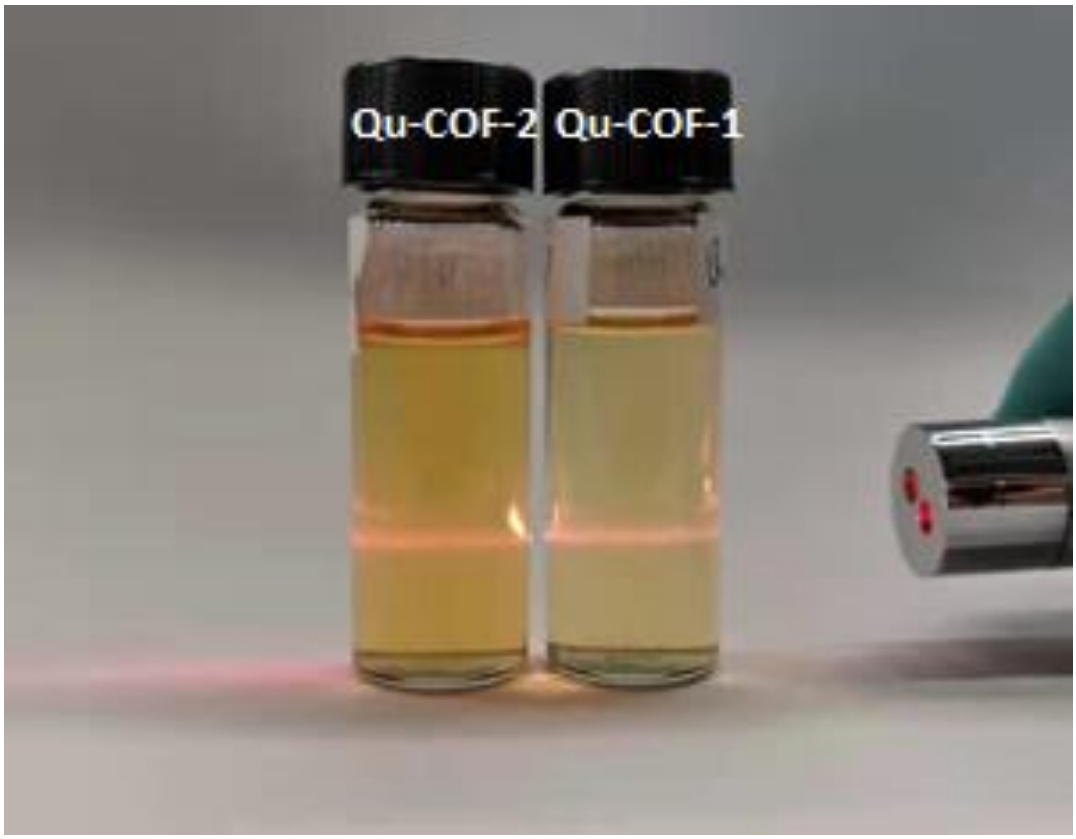

Figure 3.5.37 Tyndall effect of the exfoliated Qu-COF-1 (right) and Qu-COF-2 (left) in aqueous suspensions. (The picture shows a red laser point being shone through both samples.)

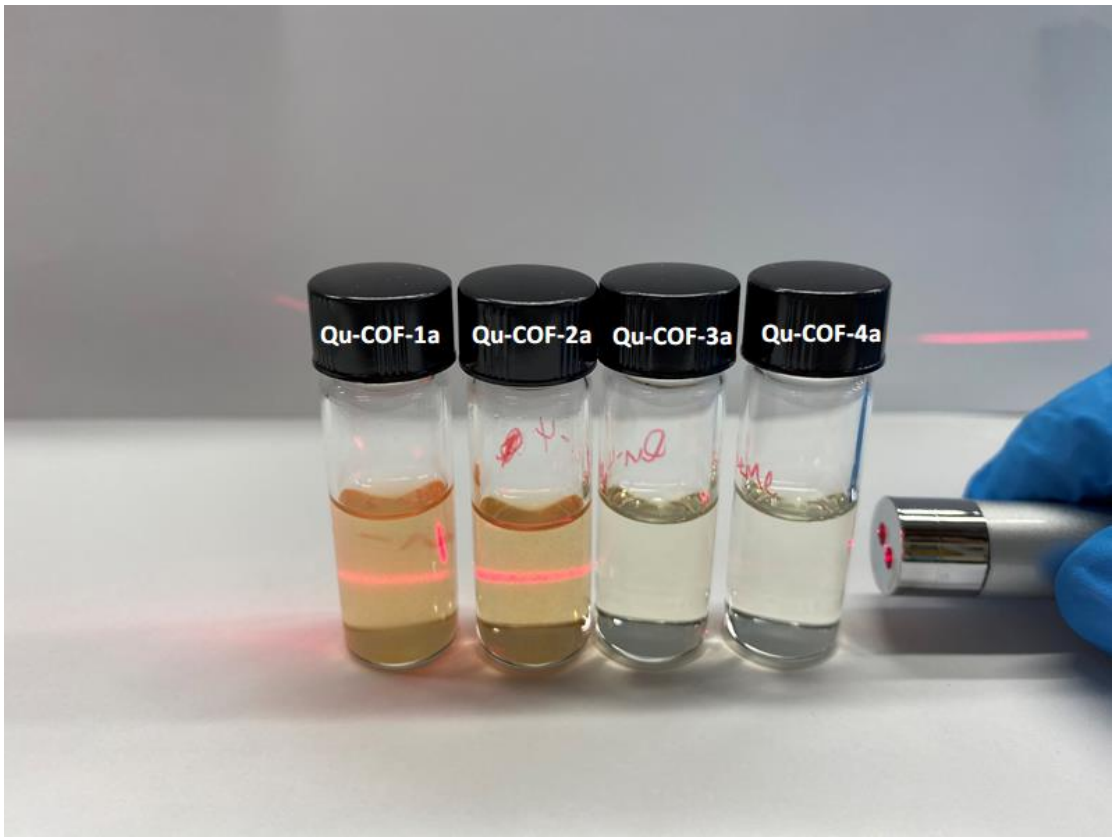

Figure 3.5.38 Tyndall effect of the exfoliated Qu-COFs in aqueous suspensions.

Then the quinoline-linked covalent organic nanosheets, Qu-CONs, were prepared under mild conditions by immersing the Qu-COFs in a mixture of aqueous 6 M KOH and ethanol (1:1) and sonicated for 45 minutes at room temperature. Samples of the representative Im-COFs were prepared in the same way. Suspensions of **Qu-CON-1a** and **Qu-CON-2a** exhibited a pronounced Tyndall effect and retained their colloidal stability for up to one week (**Figure 3.5.37** and **Figure 3.5.38**) while both Im-COFs and Qu-COFs made by pyruvic ether (Qu-COF-3&4) didn't show the Tyndall effect, indicating the exfoliation has the relationship with the unique quinoline-4-carboxylic acid groups.

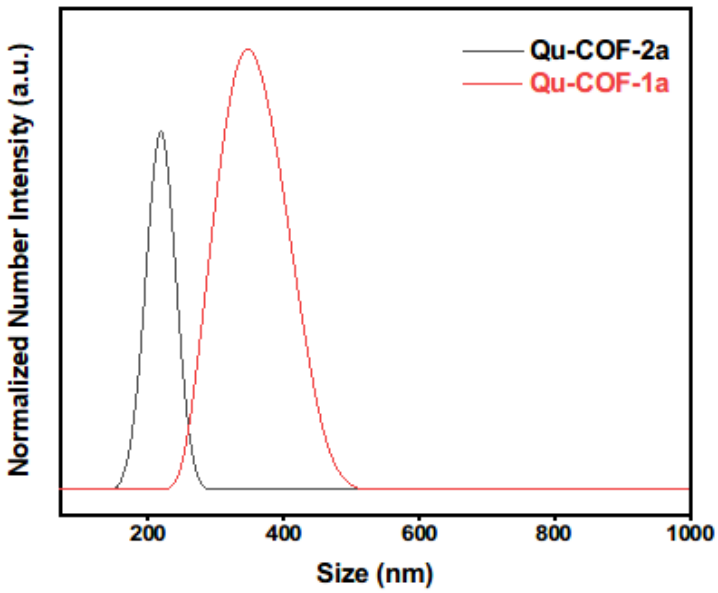

Figure 3.5.39 DLS trace of exfoliated Qu-COFs suspension.

The size of the dispersed nanosheets in solution were characterized using dynamic light scattering (DLS). **Qu-CON-2a** has an average particle size of around 200 nm, which is smaller than that of **Qu-CON-1a** (around 350 nm) (**Figure 3.5.39**). Such sizes are much smaller than the original sizes of Qu-COF-1a and Qu-COF-2a, indicating a successful exfoliation.

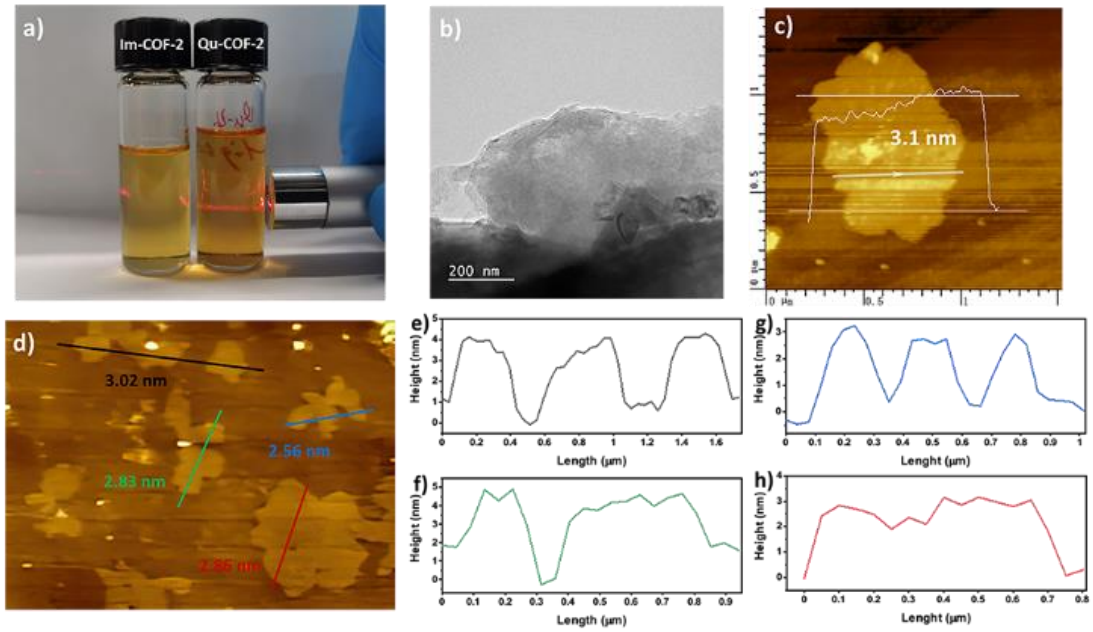

Figure 3.5.40 (a) Images of bulk **Im-COF-2** and exfoliated **Qu-CON-2a** suspension showing Tyndall effect for the latter. (b) HR-TEM image of **Qu-CON-2a**. (c) AFM image of **Qu-CON-2a**. Insert is the height of the nanosheet. (d) AFM image of **Qu-CON-2a** nanosheets with different sizes. (e-h) Corresponding height curves for the selective areas in (**d**).

To investigate the morphological properties of the **Qu-CON-2a** nanosheets, high resolution transmission electron microscopy (HR-TEM) and atomic force microscopy (AFM) were used to probe the layered structure. **Qu-CON-2a** exhibits a 2D-layered morphology which are thinner than un-exfoliated **Qu-COF-2a** (**Figure 3.5.40b**). AFM revealed the 2D sheets have an area of 1-3 μm^2 and thickness of less than 3 nm (**Figure 3.5.40c-h**), which show larger area and thinner thickness than many other reported covalent organic nanosheets.

3.5.6.3 Mechanism of the Exfoliation

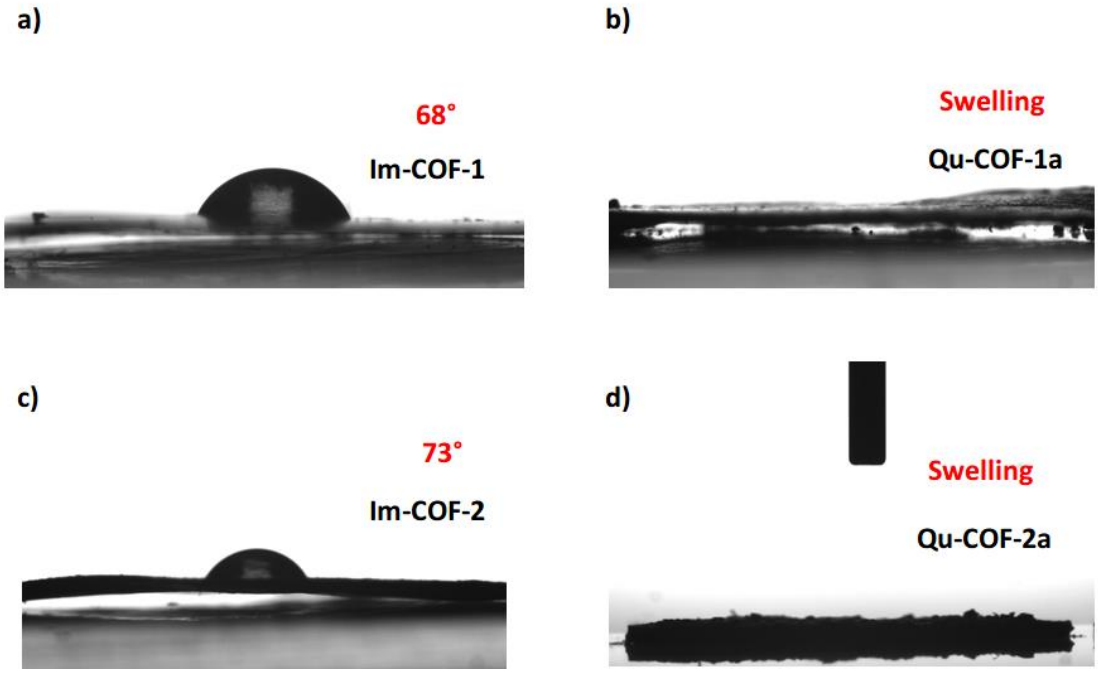

Figure 3.5.41. Water contact angle measurements for (a) Im-COF-1; (b) Qu-COF-1a; (c) Im-COF-2; (d) Qu-COF-2a. No contact angle can be obtained for the Qu-COF materials because they simply absorb the water since they are highly hydrophilic.

To further probe the effects of the unique quinoline-4-carboxylic acid motif, we performed water contact angles to access wettability. The hydrophilic carboxylic acid groups greatly enhanced the wettability of **Qu-COF-1a** and **Qu-COF-2a**, which is advantageous for exfoliation. By contrast, **Im-COF-1** and **Im-COF-2** showed water contact angles of ~68° and ~73°, respectively (**Figure 3.5.41**).

Based on the results showed above, we propose that the carboxylic acid groups contained in the quinoline-4-carboxylic acid motif are active sites for ion insertion and result in ionic repulsive groups facilitating exfoliation. This mechanism is similar to that proposed for the exfoliation of graphene oxide and has rarely been used for the exfoliation of 2D COF materials[35] (**Figure 3.5.42**).

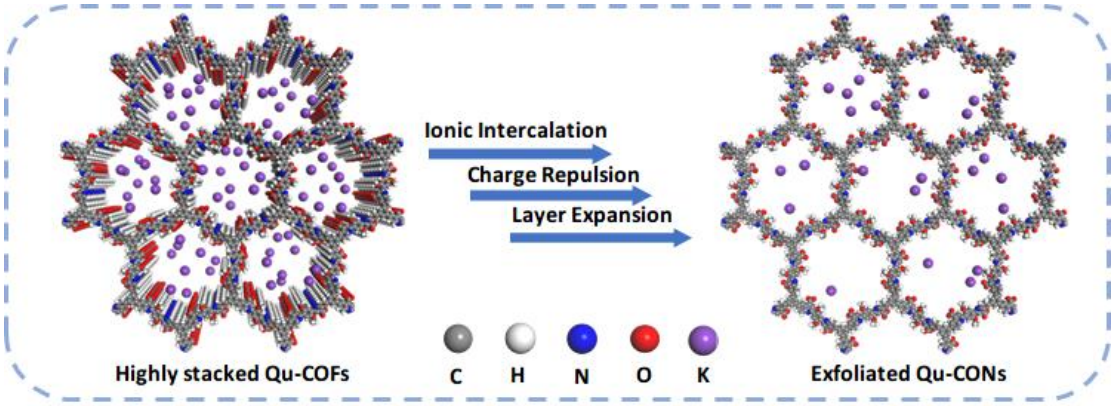

Figure 3.5.42 Proposed mechanism of generating Qu-CONs from the exfoliation of Qu-COFs.

3.5.7 Performance and Selectivity of Metal Ion Uptake

As discussed, we have found that exfoliated Qu-CONs with unique quinoline-4-carboxylic acid linkages have high wettability in aqueous solutions which we propose is due to the carboxylic acid groups anchored in the pores. With a high concentration of easily accessible carboxylic groups, we decided to Qu-CONs for metal ion adsorbents for water purification.

The performance of exfoliated Qu-CON-2a, as well as the controlled experimental samples (Im-COF-2, Qu-COF-2b and Qu-COF-4a) were assayed for the uptake of metal ions (Cu^{2+}, Co^{2+}, Ni^{2+}, Zn^{2+}, Cd^{2+}, Eu^{3+}, Pb^{2+}, Mn^{2+} and Mg^{2+}) from water (**Figure 3.5.43a**). All the COFs showed high values of metal ion uptake except for Mn^{2+} and Mg^{2+}. Im-COF-2 shows a much lower uptake of all these heavy metal ions, especially for Co^{2+}, Ni^{2+}, Zn^{2+} and Cd^{2+}, indicating that the quinoline motif results in an enhanced adsorption. Similarly, Qu-COF-2b showed better performance than Qu-COF-4a due to the adsorption coming from the carboxylic acid groups, indicating both the carboxylic acid and quinoline-N in the linkages make a dual contribution on the removal of metal ions from water because of the strong electrostatic interaction. Qu-CON-2a showed the best performance among all of the tested samples – which we believe is due to the more exposed active sites (quinoline-4-carboxylic acid) after exfoliation. Cadmium has the chronic potential to cause kidney, liver, bone and blood damage from long-term exposure at levels above the maximum contaminant level

(MCL) and so was further investigation as it is widely used in various industries but causes the pollution of the environment and has health risks for all creatures.

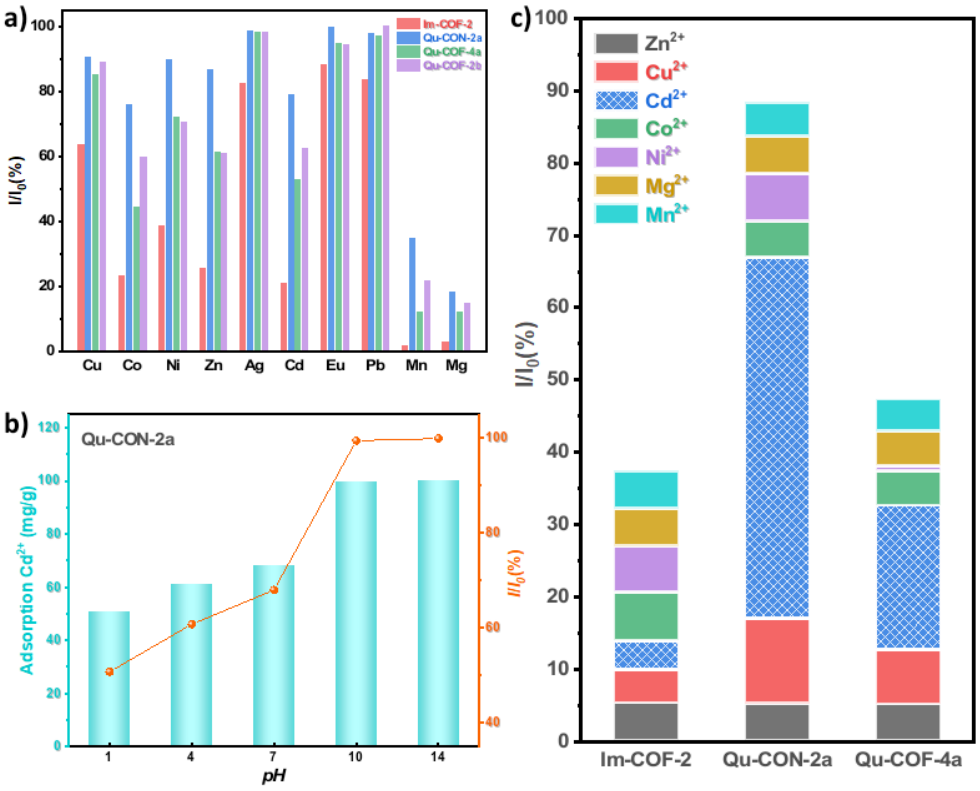

Figure 3.5.43 (a) Different metal ions adsorption measurement of Im-COF-2 (red), Qu-CON-2a (blue), Qu-COF-4a (green) and Qu-COF-2b (purple). (b) Adsorption of Cd^{2+} by Qu-CON-2a at different pH (initial concentration of Cd^{2+} is 20 ppm). (c) Adsorption selectivity test of Im-COF-2, Qu-CON-2a and Qu-COF-4a.

We investigated the adsorption of Cd^{2+} in aqueous solutions at different pH values. We varied the pH due to the protonation and deprotonation properties of quinoline-linkages that might affect the adsorption behaviour of metals. The pH effect tests were carried out from pH of 1.0 to 13.0 where Cd^{2+} is the main form (**Figure 3.5.43b**). The adsorption of Cd^{2+} on Qu-CON-2a significantly increased from 50.78 mg g^{-1} at pH = 1.0 to 99.95 mg g^{-1} at pH = 13.0 when the initial concentration of Cd^{2+} is 100 ppm. We believe this is because the quinoline-N atoms are easily protonated in the acid solution with a high concentration of H^{+}, and thus results in a reduction of Cd^{2+} adsorption. The selectivity test[36] of Qu-CON-2a was carried out with the neutral aqueous solution

containing 10 ppm Cu^{2+}, Co^{2+}, Ni^{2+}, Zn^{2+}, Cd^{2+}, Mn^{2+} and Mg^{2+} (**Figure 3.5.43c**). Im-COF-2, Qu-CON-2a show an extraction efficiency of Cd^{2+} around 50% while the extraction efficiencies of other metal ions are all less than 11%, which illustrated Qu-CON-2a with a good selectivity of Cd^{2+}.

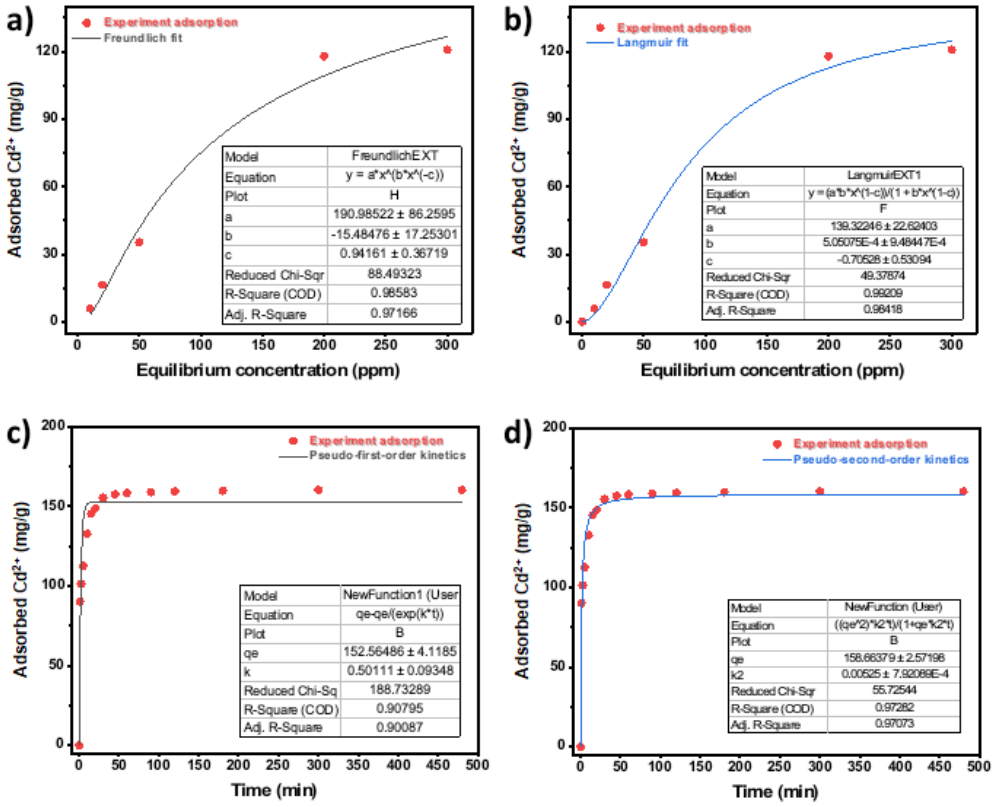

Figure 3.5.44 (a) Cd^{2+} adsorption isotherm for Qu-CON-2a fitted using the Freundlich model. (b) Cd^{2+} adsorption isotherm for Qu-CON-2a fitted using the Langmuir model. (c) Cd^{2+} adsorption kinetic curves of Qu-CON-2a fitted using pseudo-first-order kinetic plot. (d) Cd^{2+} adsorption kinetics curves of Qu-CON-2a fitted using pseudo-second-order kinetic plot.

To further investigate the adsorption behaviour and mechanism of Cd^{2+} on the Qu-CON-2a, thermodynamic and kinetic experiments of Cd^{2+} adsorption were performed on Qu-CON-2a in neutral aqueous solution. The adsorption isotherm of Cd^{2+} on Qu-CON-2a revealed the thermodynamic process, exhibiting the mechanism and the capacity of the adsorption. The adsorption isotherm fits better with Langmuir model (R^2 of 0.992) than Freundlich model (R^2 of 0.986), indicating the monolayer sorption mechanism (**Figure 3.5.44a-b**). The saturate adsorption capacity (Q_m) calculated by the

Langmuir equation is 139± 22 mg g^{-1}, which is competitive with previously reported COFs, showing the advantage of COFs with the exposed active sites from the exfoliation. From the kinetics data, it can be observed that the Cd^{2+} in the solution can be captured quickly by Qu-CON-2a and reach up to about 96% of the adsorption equilibrium within 30 minutes. The adsorption behaviour of Qu-CON-2a matches well with the pseudo-second-order kinetics model in a high coefficient of association (R^2) of 0.973, while the R^2 of the pseudo-first-order kinetics fitting is only 0.908 (**Figure 3.5.44c-d**), indicating a main driving force of Cd^{2+} adsorption on Qu-CON-2a comes from the chemical interaction by the quinoline-4-carboxylic acid.[37]

3.6 Conclusions

In conclusion, we have developed a simple and efficient multicomponent Doebner reaction route to stable, porous and crystalline quinoline-linked covalent organic frameworks (**Qu-COFs**). Post-synthetic modification of imine-based COFs with pyruvic acid were also successful. These Qu-COFs can be easily exfoliated under mild basic conditions owing to the unique quinoline-4-carboxylic acid motif installed using this approach. The quinoline-4-carboxylic acid group has two roles to play in the disruption of interlayer interactions and exfoliation to quinoline-linked covalent organic nanosheets (**Qu-CONs**): (i) modelling suggests the layers are slightly twisted out of the plane causing larger *d*-spacing and (ii) ion insertion at the carboxylic group leads to repulsion of the layers. Our approach provides an efficient way to access robust functional 2D COFs and exfoliated nanosheets. Due to the much more exposed active sites through exfoliation, Qu-CONs exhibit an excellent performance on cadmium capture from water, including the high capacity, high adsorbed rate and good selectivity.

3.7 References

1. Diercks, C. S.; Yaghi, O. M., The atom, the molecule, and the covalent organic framework. *Science* **2017**, 355 (6328), eaal1585.

2. Furukawa, H.; Yaghi, O. M., Storage of hydrogen, methane, and carbon dioxide in highly porous covalent organic frameworks for clean energy applications. *J. Am. Chem. Soc.* **2009**, 131 (25), 8875-8883.

3. Oh, H.; Kalidindi, S. B.; Um, Y.; Bureekaew, S.; Schmid, R.; Fischer, R. A.; Hirscher, M., A cryogenically flexible covalent organic framework for efficient hydrogen isotope separation by quantum sieving. *Angew. Chem., Int. Ed*. **2013**, 52 (50), 13219-13222.

4. Lu, S.; Hu, Y.; Wan, S.; McCaffrey, R.; Jin, Y.; Gu, H.; Zhang, W., Synthesis of ultrafine and highly dispersed metal nanoparticles confined in a thioether-containing covalent organic framework and their catalytic applications. *J. Am. Chem. Soc*. **2017**, 139 (47), 17082-17088.

5. Bhadra, M.; Kandambeth, S.; Sahoo, M. K.; Addicoat, M.; Balaraman, E.; Banerjee, R., Triazine Functionalized Porous Covalent Organic Framework for Photo-organocatalytic E–Z Isomerization of Olefins. *J. Am. Chem. Soc*. **2019**, 141 (15), 6152-6156.

6. Wang, X.; Chen, L.; Chong, S. Y.; Little, M. A.; Wu, Y.; Zhu, W.-H.; Clowes, R.; Yan, Y.; Zwijnenburg, M. A.; Sprick, R. S., Sulfone-containing covalent organic frameworks for photocatalytic hydrogen evolution from water. *Nat. Chem*. **2018**, 10 (12), 1180-1189.

7. DeBlase, C. R.; Silberstein, K. E.; Truong, T.-T.; Abruña, H. C. D.; Dichtel, W. R., β-Ketoenamine-linked covalent organic frameworks capable of pseudocapacitive energy storage. *J. Am. Chem. Soc*. **2013**, 135 (45), 16821-16824.

8. Vitaku, E.; Gannett, C. N.; Carpenter, K. L.; Shen, L.; Abruña, H. D.; Dichtel, W. R., Phenazine–Based Covalent Organic Framework Cathode Materials with High Energy and Power Densities. *J. Am. Chem. Soc*. **2020**, 142, 1, 16–20.

9. Haase, F.; Gottschling, K.; Stegbauer, L.; Germann, L. S.; Gutzler, R.; Duppel, V.; Vyas, V. S.; Kern, K.; Dinnebier, R. E.; Lotsch, B. V., Tuning the stacking behaviour of a 2D covalent organic framework through non-covalent interactions. *Mater. Chem. Front*. **2017**, 1 (7), 1354-1361.

10. Lyu, H.; Diercks, C. S.; Zhu, C.; Yaghi, O. M., Porous crystalline olefin-linked covalent organic frameworks. *J. Am. Chem. Soc*. **2019**, 141 (17), 6848-6852.

11. Jin, E.; Asada, M.; Xu, Q.; Dalapati, S.; Addicoat, M. A.; Brady, M. A.; Xu, H.; Nakamura, T.; Heine, T.; Chen, Q., Two-dimensional sp^2 carbon–conjugated covalent organic frameworks. *Science* **2017**, 357 (6352), 673-676.

12. Wang, K.; Yang, L. M.; Wang, X.; Guo, L.; Cheng, G.; Zhang, C.; Jin, S.; Tan, B.; Cooper, A., Covalent Triazine Frameworks via a Low-Temperature Polycondensation Approach. *Angew. Chem., Int. Ed*. **2017**, 56 (45), 14149-14153.

13. Guo, J.; Xu, Y.; Jin, S.; Chen, L.; Kaji, T.; Honsho, Y.; Addicoat, M. A.; Kim, J.; Saeki, A.; Ihee, H., Conjugated organic framework with three-dimensionally ordered stable structure and delocalized π clouds. *Nat. Commun*. **2013**, 4 (1), 1-8.

14. Wei, P.-F.; Qi, M.-Z.; Wang, Z.-P.; Ding, S.-Y.; Yu, W.; Liu, Q.; Wang, L.-K.; Wang, H.-Z.; An, W.-K.; Wang, W., Benzoxazole-linked ultrastable covalent organic frameworks for photocatalysis. *J. Am. Chem. Soc*. **2018**, 140 (13), 4623-4631.

15. Pyles, D. A.; Coldren, W. H.; Eder, G. M.; Hadad, C. M.; McGrier, P. L., Mechanistic investigations into the cyclization and crystallization of benzobisoxazole-linked two-dimensional covalent organic frameworks. *Chem. Sci*. **2018**, 9 (30), 6417-6423.

16. Zhang, B.; Wei, M.; Mao, H.; Pei, X.; Alshmimri, S. A.; Reimer, J. A.; Yaghi, O. M., Crystalline dioxin-linked covalent organic frameworks from irreversible reactions. *J. Am. Chem. Soc*. **2018**, 140 (40), 12715-12719.

17. Guan, X; Li, H.; Ma, Y.; Xue, M.; Fang, Q.; Yan, Y.; Valtchev, V.; Qiu, S., Chemically stable polyarylether-based covalent organic frameworks. *Nat. Chem*. **2019**, 11 (6), 587-594.

18. Dalapati, S.; Jin, S.; Gao, J.; Xu, Y.; Nagai, A.; Jiang, D., An azine-linked covalent organic framework. *J. Am. Chem. Soc*. **2013**, 135 (46), 17310-17313.

19. Kandambeth, S.; Mallick, A; Lukose, B.; Mane, M. V.; Heine, T.; Banerjee, R., Construction of crystalline 2D covalent organic frameworks with remarkable chemical (acid/ base) stability via a combined reversible and irreversible route. *J. Am. Chem. Soc*. **2012**, 134 (48), 19524-19527.

20. Liu, H.; Chu, J.; Yin, Z.; Cai, X.; Zhuang, L.; Deng, H., Covalent organic frameworks linked by amine bonding for concerted electrochemical reduction of CO_2. *Chem*. **2018**, 4 (7), 1696-1709.

21. Waller, P. J.; Lyle, S. J.; Osborn Popp, T. M.; Diercks, C. S.; Reimer, J. A.; Yaghi, O. M., Chemical conversion of linkages in covalent organic frameworks. *J. Am. Chem. Soc*. **2016**, 138 (48), 15519-15522.

22. Waller, P. J.; AlFaraj, Y. S.; Diercks, C. S.; Jarenwattananon, N. N.; Yaghi, O. M., Conversion of imine to oxazole and thiazole linkages in covalent organic frameworks. *J. Am. Chem. Soc*. **2018**, 140 (29), 9099-9103.

23. Li, X.; Zhang, C.; Cai, S.; Lei, X.; Altoe, V.; Hong, F.; Urban, J. J.; Ciston, J.; Chan, E. M.; Liu, Y., Facile transformation of imine covalent organic frameworks into ultrastable crystalline porous aromatic frameworks. *Nat. Commun*. **2018**, 9 (1), 1-8.

24. Lyle, S. J.; Osborn Popp, T. M.; Waller, P. J.; Pei, X.; Reimer, J. A.; Yaghi, O. M., Multistep Solid-State Organic Synthesis of Carbamate-Linked Covalent Organic Frameworks. *J. Am. Chem. Soc*. **2019**, 141 (28), 11253-11258.

25. Toure, B. B.; Hall, D. G., Natural product synthesis using multicomponent reaction strategies. *Chem. Rev*. **2009**, 109 (9), 4439-4486.

26. Wang, P.-L.; Ding, S.-Y.; Zhang, Z.-C.; Wang, Z.-P.; Wang, W., Constructing Robust Covalent Organic Frameworks via Multicomponent Reactions. *J. Am. Chem. Soc*. **2019**, 141 (45), 18004-18008.

27. Wang, K.; Jia, Z.; Bai, Y.; Wang, X.; Hodgkiss, S. E.; Chen, L.; Chong, S.; Yang, H.; Xu, Y.; Feng, F.; Ward, J. W.; Cooper, A. I., Synthesis of Stable Thiazole-Linked Covalent Organic Frameworks via a Multicomponent Reaction. *J. Am. Chem. Soc*. **2020**, 142 (45), 11131-11138.

28. Li, X.-T.; Zou, J.; Wang, T. H.; Ma, H.-C.; Chen, G.-J.; Dong, Y.-B., Construction of Covalent Organic Frameworks via Three-Component One-Pot Strecker and Povarov Reactions. *J. Am. Chem. Soc*. **2020**, 142, 14, 6521–6526.

29. Haase, F.; Troschke, E.; Savasci, G.; Banerjee, T.; Duppel, V.; Dörfler, S.; Grundei, M. M. J.; Burow, A. M.; Ochsenfeld, C.; Kaskel, S., Topochemical conversion of an

imine-into a thiazole-linked covalent organic framework enabling real structure analysis. *Nat. Commun*. **2018**, 9 (1), 1-10.

30. Li, C.; Ma, Y.; Liu, H.; Tao, L.; Ren, Y.; Chen, X.; Li, H.; Yang, Q., Asymmetric photocatalysis over robust covalent organic frameworks with tetrahydroquinoline linkage. *Chinese J. Catal*. **2020**, 41 (8), 1288-1297.

31. Yamashkin, S.; Oreshkina, E., Traditional and modern approaches to the synthesis of quinoline systems by the Skraup and Doebner-Miller methods. *Chem Heterocycl Compd*. **2006**, 42.

32. Mullangi D, Chakraborty D, Pradeep A, Koshti V, Vinod CP, Panja S, Nair S, Vaidhyanathan R. Highly Stable COF-Supported Co/Co (OH) 2 Nanoparticles Heterogeneous Catalyst for Reduction of Nitrile/Nitro Compounds under Mild Conditions. *Small*. **2018**, 14 (37), 1801233.

33. Xu H, Gao J, Jiang D., Stable, crystalline, porous, covalent organic frameworks as a platform for chiral organocatalysts. *Nat. Chem*. **2018**, 7 (11), 905.

34. Sui, X.; Wang, Y.; Liu, F.; Yuan, Z.; Wang, C.; Yu, Y.; Zhou, K.; Goh, K.; Chen, Y., The tripartite role of 2D covalent organic frameworks in graphene-based organicsolvent nanofiltration membranes. *Matter*. **2021**, 4, 2953-2969.

35. Tao, Y.; Ji, W.; Ding, X.; Han, B., Exfoliated covalent organic framework nanosheets. *J. Mater. Chem. A.* **2021**, 9, 7336-7365.

36. Guo, L., Jia, S., Diercks, C., Yang, X., Alshmimri, S., Yaghi, O. M., Amidation, Esterification, and Thioesterification of a Carboxyl-Functionalized Covalent Organic Framework. *Angew. Chem., Int. Ed*. **2020**, 132 (5), 2039-2043.

37. Li, Z., Zhu, R., Zhang, P., Yang, M., Zhao, R., Wang, Y., Dai, X., Liu, W., Functionalized polyarylether-based COFs for rapid and selective extraction of uranium from aqueous solution. *Chem. Eng. J.* **2022**, 434, 134623.

Chapter 4

Imidazole-Linked Covalent Organic Frameworks

4.1 Contributions to this Chapter

SEM and HR-TEM images for IMD-COFs were obtained by Haofan Yang and Lunjie Liu. Raman spectra was obtained by Peiying Wang. XPS spectra was obtained by Yang Liu. Haiyan Duan helped with the assembly of all the cells. Dr. Alex R. Neale, Haiyan Duan and Hui Gao helped with the electrochemical cells. Dr. Tom Fellowes helped with the measurement of single crystal structure of the model compound and the corresponding data analysis Solid-state NMR spectra was obtained by Dr. Samuel Page. DSC data was obtained by Aiting Kai. Rob Clowes helped with gas adsorption measurements. Xue Wang constructed IMD-COF models and simulation calculations. All other work was performed by the thesis author.

4.2 Background and Context

Polymer-based solid-state electrolytes (SSEs) with good performance are a potential solution for the safety issues associated with next-generation lithium-ion batteries (LIBs). However, the low Li^+ conductivity of polymer SSEs at room temperature restricts their use. Here, we present a series of oligoethylene glycol-anchored imidazole-linked covalent organic framework (IMD-COF-OEG-x) as SSEs for Li^+ conductor. The post-modification reaction was used for grafting OEG chains into the imidazole-sites in the pore wall of IMD-COF. By combining the mechanism of Li ions transference from linear polymers and COFs, the OEG chains can increase the concentration and accelerate the movement of Li^+ in the COFs nanochannels while the COF can offer the oriented lithium ion hopping paths and inhibit the phase-change of OEG chains. This gives IMD-COF-OEG-3 SSE with the highest Li^+ conductivity by 1900 times improvement and a lithium transference number of 0.83 is achieved at room temperature. Moreover, the IMD-COF-OEG-3 SSE exhibits a low activation energy and high stability during a Li plating-stripping cycling over 560 h. Our study provides an approach towards a novel class of highly efficient Li^+ conducting COFs which could be used in solid-state electrolytic devices.

4.3 Introduction

SSEs are generally used to keep lithium-ion batteries within a broad potential window with lower activation energies, higher flexibility, and non-volatilization for environmentally friendly and higher safety.[1-4] Poly (ethylene glycol) (PEG) is one of the most prospective organic solid-state electrolytes because for its good processability and simple fabrication with a large amount of industrial production. The ethylene glycol chains form Li-O bonds,[5] which has a good compatibility with lithium salts as ion hopping sites to help the intermolecular transport of lithium ions.[6, 7] However, PEG-based electrolytes have an insufficient ionic conductivity, especially under the glass-transition temperature, due to the restriction of ion motion from the limited free volume in numerous crystalline phases.[8] To address these issues, a series of methods have been developed, including cross-linking, which is an efficient strategy for preventing the crystallisation of the ethylene glycol chains.[9] Nevertheless, these amorphous cross-linked PEG networks still lack an oriented pathway for the diffusion of lithium ions, leading to unstable ion conductivity performance during the long-term cycling.[10] Moreover, the heterogeneous state of amorphous electrolytes is difficult to characterise at an atomic level and therefore the mechanism of ion transport is poorly understood.[11, 12]

2D-COFs possess abundant one-dimensional (1D) nanochannels for inducing and promoting ion transport due to the extended skeleton within the ordered pore structure.[13-15] Based on the various building blocks and linkages used in COF chemistry, such 1D open nanochannels can be designed with a satisfying pore shape and size, uniform distribution and tuneable interface environment of the pore wall. This leads to good compatibility with electrodes, low interface impedance and further high ion-conductivity.[16-18] Also, COFs can be post-modified with various functional groups, thus endowing them with specific functions for ionic conduction.[19-26] Nevertheless, there are still challenges in the application of COFs for ion conduction.[27, 28] First of all, ion conductivity, especially at room temperature is low because of the limited ordered pathway for ion transport within the pore walls.[29] Also, ion transport in COF

electrolytes often requires extra driving force when the nanochannel is narrow and designed for reducing the cation transference number.[30] Finally, most of the reported COF electrolyte materials are connected by imine or borate bonds, which are unstable during either diaphragm preparation or electrochemical testing, partly destroying the oriented pathway of ion transport.[31-33]

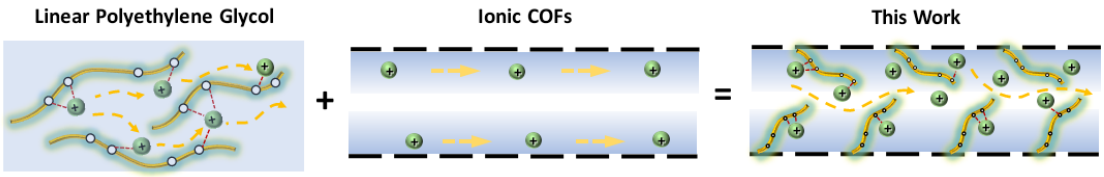

Figure 4.3.1 Illustration of different Li^+ transport models in linear polyethylene glycol, ionic COFs and oligoethylene glycol-anchored IMD-COFs in this work.

Herein, we design and synthesized a series of stable imidazole-linked COFs (IMD-COF-OEG-1~3) for SSE via two steps. Imidazole-linked COFs (IMD-COF) with good stability and crystallinity were synthesized from a multi-component Debus-Radziszewski reaction.[34] Then the as-obtained IMD-COF was reacted with different oligo-ethylene glycol (OEG) length chain bromides to form IMD-COF-OEG-x (x= 1, 2, 3). The OEG chains induce and accelerate the movement of lithium-ions in the 1D nanochannel in these COFs, leading to a high ionic mobility (Figure 1a).[35, 36] Among all the samples, IMD-COF-OEG-3 SSE had the best ionic conductivity of 3.36×10^{-4} S cm^{-1} at room temperature and 4.55×10^{-3} S cm^{-1} at 70 °C. A low activation energy of 0.45 eV and a high lithium transfer number of 0.83 was also observed, which is among the highest of all the reported COF-based SSEs. Moreover, Li-metal battery based on IMD-COF-OEG-3 SSE is stable with reversible Li plating and stripping over 560 h of cycling. These findings demonstrate that chemically functionalized, oligoethylene glycol-anchored imidazole-linked COFs can serve as a promising platform for solid-state electrolytes.

4.4 Experimental

4.4.1 Chemical Reagents

All reagents were obtained from Sigma-Aldrich, TCI Europe or Carbosynth Ltd. Anhydrous solvents were purchased from Acros Organics or Fisher Scientific. All chemicals were used without further purification.

4.4.2 Characterization Methods and Measurements

General methods.

Air sensitive reactions were performed under argon using standard Schlenk techniques. Glassware was oven-dried overnight or dried using a heat gun.

Basic characterizations.

The measurements of NMR, PXRD, TGA, Nitrogen adsorption and desorption, UV-Visible absorption spectra, FT-IR spectra, Raman spectra, XPS, SEM, TEM were similar and described in the experimental part in **Chapter 2**.

Electrochemical measurements.

Before using, all samples were dried under vacuum for at least 12 h to eliminate the possibility of the trapped water molecules assisting the Li-ions mobility. All procedures were conducted inside of an Ar glovebox (H_2O and O_2 levels < 10 ppm).

Typical procedure for pelletization. Around 30 mg of the sample was loaded into a 10 mm die and pressed into a pellet. Propylene carbonate (PC, 6 μL) was added to plasticize the pellet. The thickness ca. 500 μm of the pellets was measured by a thickness gauge. The pellets were stored in a 50 °C chamber for 24 h before the testing.

Assembly of different cells

Stainless-steel | SSEs | Stainless-steel symmetric cell. The as-obtained SSE pellets were sandwiched between two stainless steel electrodes to get swagelok-type cells for EIS measurement.

Li | SSEs | stainless-steel asymmetric cell. The as-obtained SSE pellets were sandwiched between stainless steel electrode and lithium metal electrode to get asymmetric swagelok-type cells.

Li | SSEs | Li symmetric cell. The as-obtained SSE pellets were sandwiched between two lithium metal electrodes to get symmetric coin-type cells.

Electrochemical Impedance Spectroscopy (EIS)

The EIS measurement was carried out on a Biologic SP-300 electrochemical workstation with the frequency range 1000 kHz to 0.1 Hz with an oscillating voltage of 10 mV by the using of Stainless-steel | SSEs | Stainless-steel symmetric cell.

Ionic conductivity σ (S cm^{-1}) was calculated by the following equation:

$$\sigma = L/(R*S)$$

where L is thickness of the pellet (cm), R is the impedance of the pellet (Ω), and S is electrode area (cm^2). R was calculated from the equivalent circuit simulation using *Z*-fit by sum of all the resistance components.

The material's activation energy (E_a) was determined by taking EIS measurements in an oven with temperature range of 20 to 70 ℃. Between each measurement, the sample was allowed to equilibrate for at least 60 minutes. The activation energy could be directly determined by measuring the slope of the Arrhenius plot of the resulting conductivity values.

The Bruce-Vincent-Evans (BVE) technique was used to calculate the lithium-ion transference number (t_+) by using Li | SSEs | Li symmetric cell. Typically, the initial and steady state current values can be measured when adding a constant DC polarization. The steady state was defined as a < 1% change in current measured over a 30 min interval. Initial and steady-state resistance values were measured with EIS directly before and after the application of the DC polarization.

The Li-ion transference number (t_+) was calculated by following equation:

$$t_+ = I_s\,(\Delta V - I_0 R_0)/[I_0\,(\Delta V - I_s R_s)]$$

Where ΔV is the polarization voltage (10 mV), I_0 and R_0 are initial current and resistance value before polarization, and I_s and R_s represent the steady current and resistance value after polarization.

Cyclic voltammetry (CV) and linear Sweep Voltammetry (LSV). Cyclic voltammetry (CV) and linear Sweep Voltammetry (LSV) was conducted using a Biologic SP-300 electrochemical workstation to evaluate their oxidation and reduction stability. The CV and LSV measurements were performed under the scan rate of 1 mV s^{-1} on Li | SSEs | Stainless-steel asymmetric cells at room temperature and 50 °C. To collect the CV curves, a cyclic potential sweep (1 mV s^{-1}) was executed between -1 and 6 V. The linear sweep voltammograms were collected by first sweeping the voltage (1 mV s^{-1}) from the cell's open circuit potential (OCP) down to -1 V, followed by a secondary sweep from the OCP up to 6 V.

Potentiostatic holds test. Potentiostatic holds experiments were measured on a Biologic SP-300 electrochemical workstation using chromoamperometry (CA) techniques.

Li Plating-Stripping tests. Li plating-stripping tests were conducted using multichannel battery cycling equipment (Maccor Series 4000 battery cycler) to demonstrate the reversible Li deposition and dissolution. The test was operated on Li | SSEs | Li symmetric cells at 35 °C with a constant current density of 0.01 mA cm^{-2}. Each plating and stripping step were held for 2 h.

Rate ability tests. Rate ability tests were conducted using multichannel battery cycling equipment (Maccor Series 4000 battery cycler) to demonstrate the reversible Li deposition and dissolution. The test was operated on Li | SSEs | Li symmetric cells at 35 °C with a varying current density from 0.01 mA cm^{-2} to 0.1 mA cm^{-2}. Each charge and discharge step were held for 1 h.

4.4.3 Synthetic Route and Preparation Procedure

4.4.3.1 Synthesis of Monomers

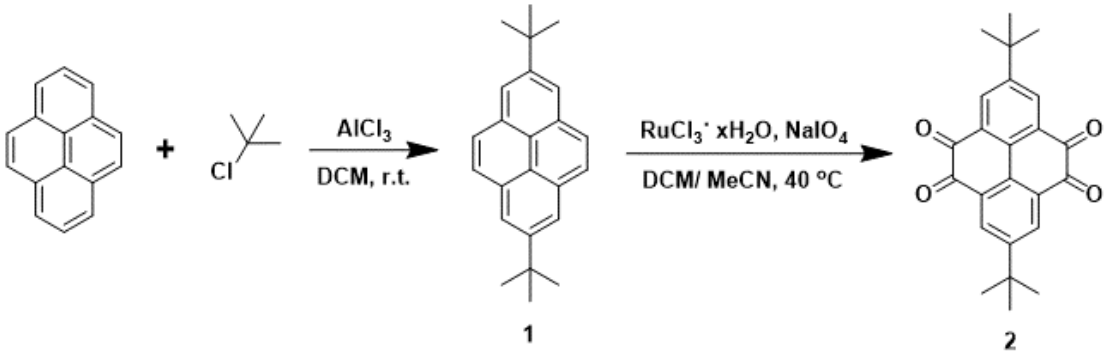

Scheme 4.4.1. Synthesis of 2, 7-di-tert-butylpyrene-4, 5, 9, 10-tetraone.

2, 7-ditert-butylpyrene (**1**). Pyrene (5 g, 24.72 mmol) was dissolved in 50 mL CH_2Cl_2. Then $AlCl_3$ (665 mg, 4.99 mmol) was added into the solution at 0 °C under N_2 atmosphere. *Tert*-butyl chloride (5.88 mL, 5.41 mmol) was added dropwise and stirred overnight at room temperature. The solution was quenched with water, then filter the aluminum salt with celite, extracted with CH_2Cl_2 and dried with anhydrous Na_2SO_4. The solids were further purified by recrystallization with the solvent of EtOH. 2, 7-ditert-butylpyrene (**1**) was obtained as a white crystal (6.53 g, yield: 84 %).

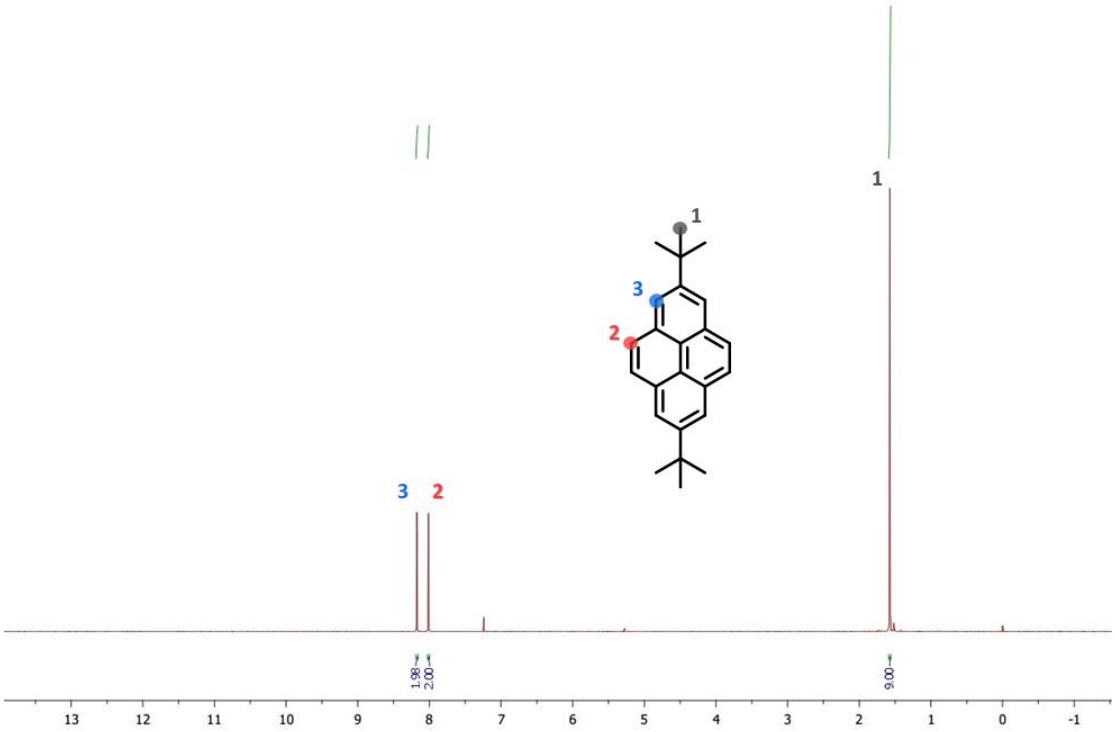

Figure 4.4.1. ^{1}H NMR spectrum of 2, 7-ditert-butylpyrene in $CDCl_3$.

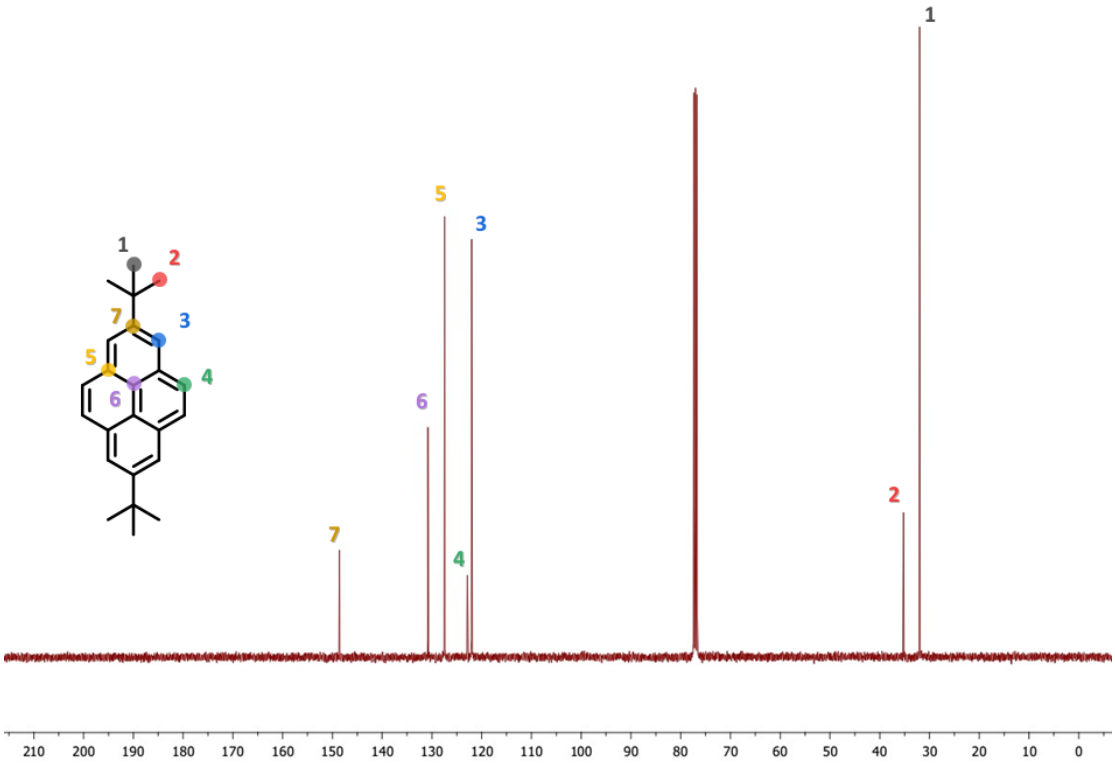

Figure 4.4.2. $^{13}C\{1H\}$ NMR spectrum of 2, 7-ditert-butylpyrene in $CDCl_3$.

2, 7-di-*tert*-butylpyrene-4, 5, 9, 10-tetraone (**2**). In a 500 mL round-bottom flask, 2,7-ditert-butylpyrene (5 g, 15.90 mmol) and $RuCl_3 \cdot xH_2O$ (331.24 mg, 1.59 mmol) were dissolved in 60 mL CH_2Cl_2, then 60 mL MeCN and 70 mL H_2O were added in the solution. $NaIO_4$ (27.21 g, 127.20 mmol) was added in batches. The dark brown suspension was stirred at 40 °C for 5 h. The reaction mixture was poured into H_2O and the organic phase was separated after filtering out the salt. The aqueous phase was extracted with CH_2Cl_2 to give a dark orange solution. Column chromatography (Hexane/ DCM = 1:2) giving pure products as bright an orange crystal (4.17 g, yield: 70 %).

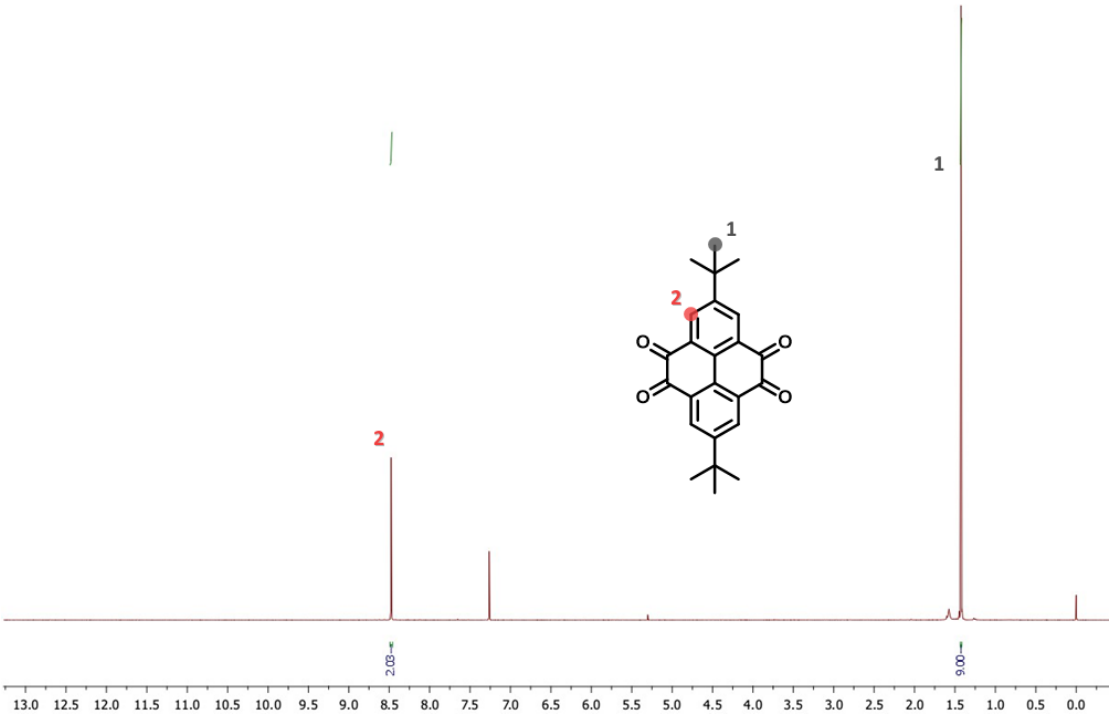

Figure 4.4.3. ^1H NMR spectrum of 2, 7-di-tert-butylpyrene-4, 5, 9, 10-tetraone in $CDCl_3$.

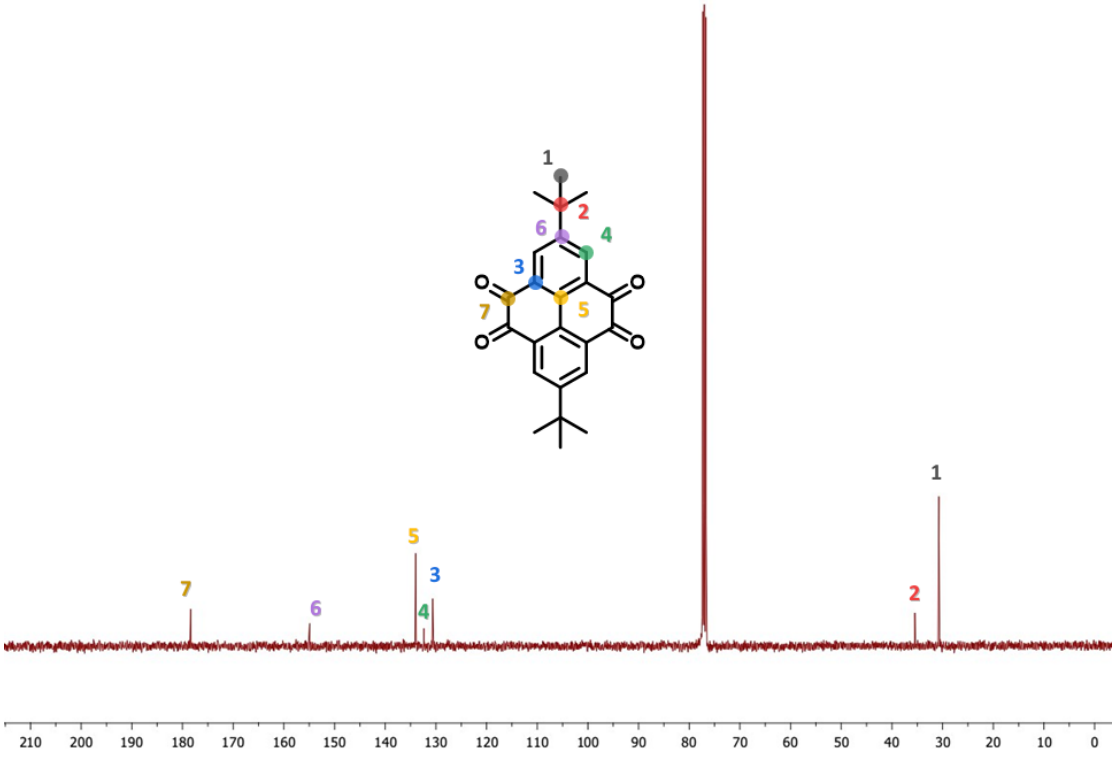

Figure 4.4.4. $^{13}C\{1H\}$ NMR spectrum of 2, 7-di-tert-butylpyrene-4, 5, 9, 10-tetraone in $CDCl_3$.

4.4.3.2 Synthesis of Model Compound

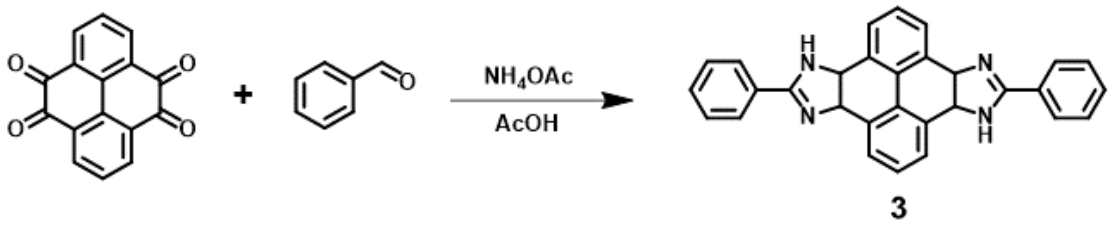

3

Scheme 4.4.2. Synthesis of model compound (**3**).

To a dried Pyrex tube, benzaldehyde (9.5 µL, 0.090 mmol, 3 eq), pyrene-4, 5, 9, 10-tetraone (7.87 mg, 0.03 mmol), ammonium acetate (20.8 mg, 0.270 mmol, 9 eq.) and acetic acid (1 mL) charged in sequence. After sonication for 5 min, the tube was flash frozen in a liquid nitrogen bath. After three freeze-pump-thaw cycles and warming to room temperature, the sealed tube was placed in an oven of 120 °C for 3 days. The resulting product was collected *via* filtration, briefly washed with DI water, DCM and ethanol. The yellow crystal was collected and dried at 80 °C for 12 h.

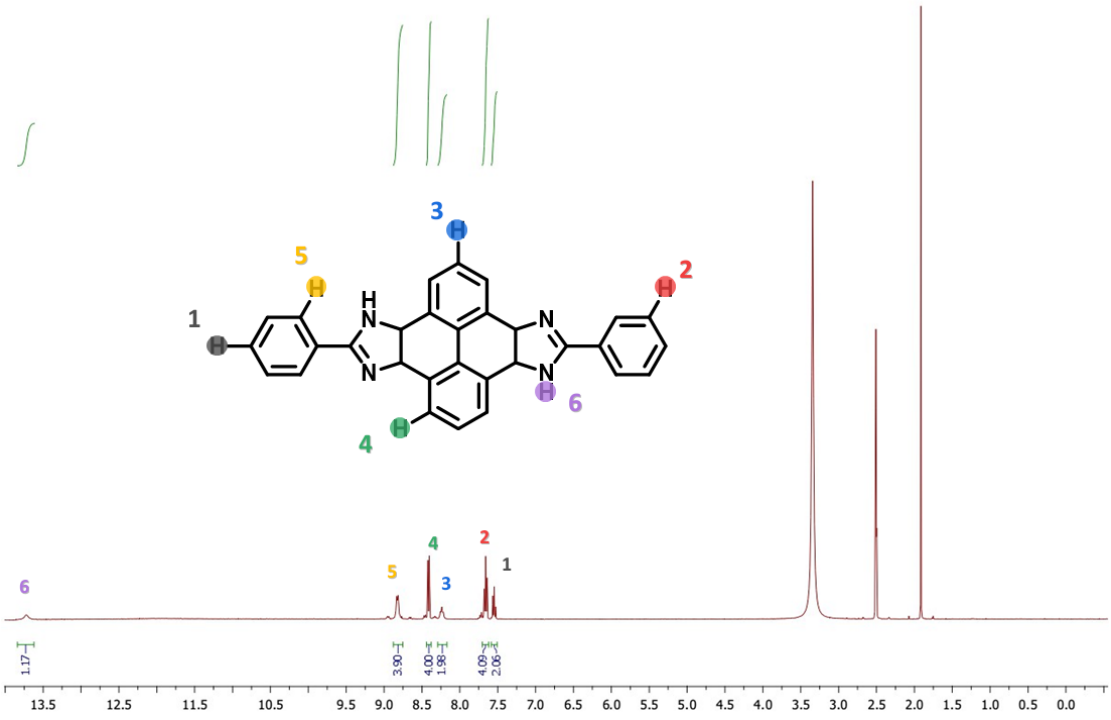

Figure 4.4.5. ^{1}H NMR spectrum of model compound (**3**) in DMSO-d_6.

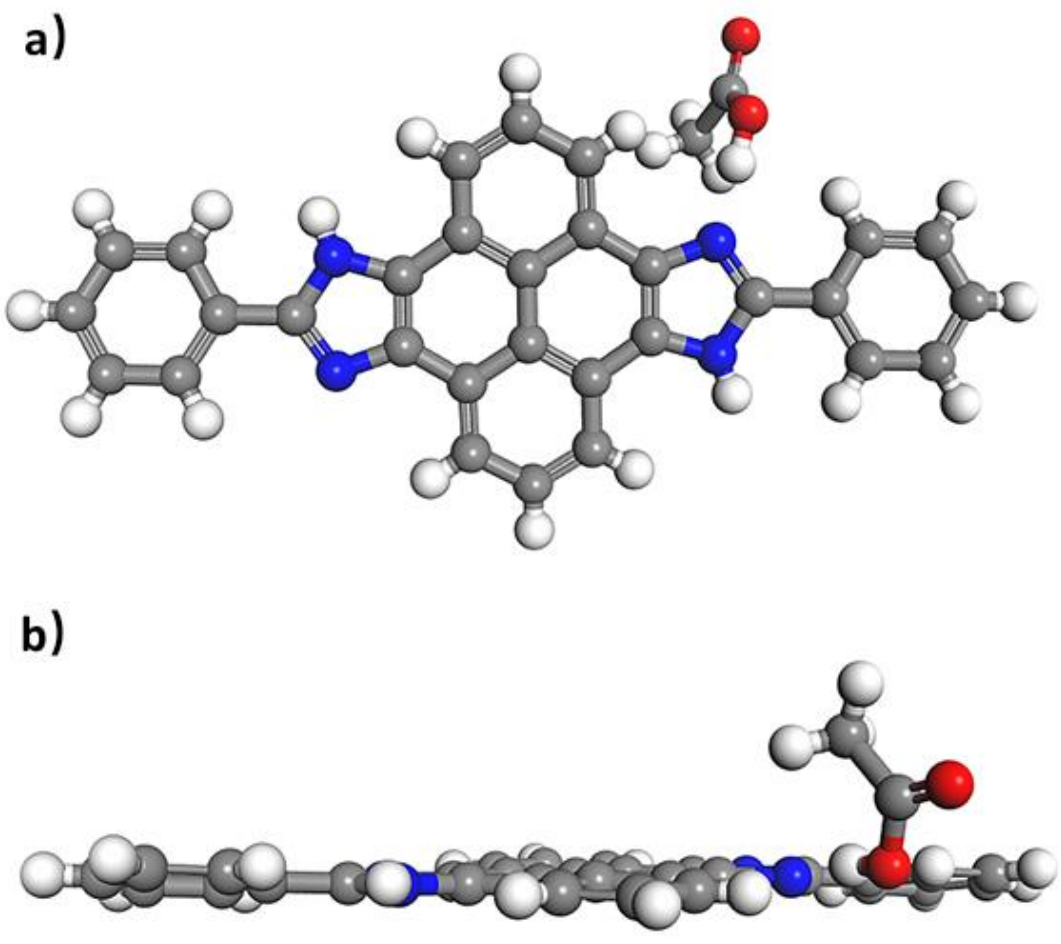

Figure 4.4.6. Single crystal structure of model compound **(3)**: (a) Front view and (b) Side view.

Table 4.4.1. Single crystal refinement details for model compound **(3)**.

Name	Model Compound
Crystallization solvent	Acetic acid
Empirical formula[a]	$C_{34}H_{26}N_4O_4$
Formula weight	554.59
Temperature (K)	100.01(10)
Crystal system	Monoclinic
Space group	$P2_1/n$
a (Å)	5.1076(2)
b (Å)	26.0974(8)
c (Å)	9.4086(3)
α (°)	90
β (°)	97.393(3)
γ (°)	90
Volume (Å^3)	1243.69(7)
Z	2
P_{calc} (g/cm^3)	1.481
M (mm^{-1})	0.099
F (000)	580.0
Crystal size (mm^3)	0.596 × 0.049 × 0.04
Radiation	Mo Kα (λ = 0.71073)
2q range for data collection (°)	3.122 to 56.564
Index ranges	$-6 \leq h \leq 6, -34 \leq k \leq 28, -12 \leq l \leq 12$
Reflections collected	21878

Independent reflections	3087 [R_{int} = 0.0432, R_{sigma} = 0.0264]
Data/ restraints/ parameters	3087/ 1/ 199
Goodness-of-fit on F^2	1.050
Final R indexes [I>= 2σ (I)]	R_1 = 0.0472, wR_2 = 0.1221
Final R indexes [all data]	R_1 = 0.0569, wR_2 = 0.1278

Empirical formula[a], containing an acetic acid molecule with an interaction.

4.4.3.3 Synthesis of Imidazole-Linked Covalent Organic Framework

Synthesis of IMD-COF

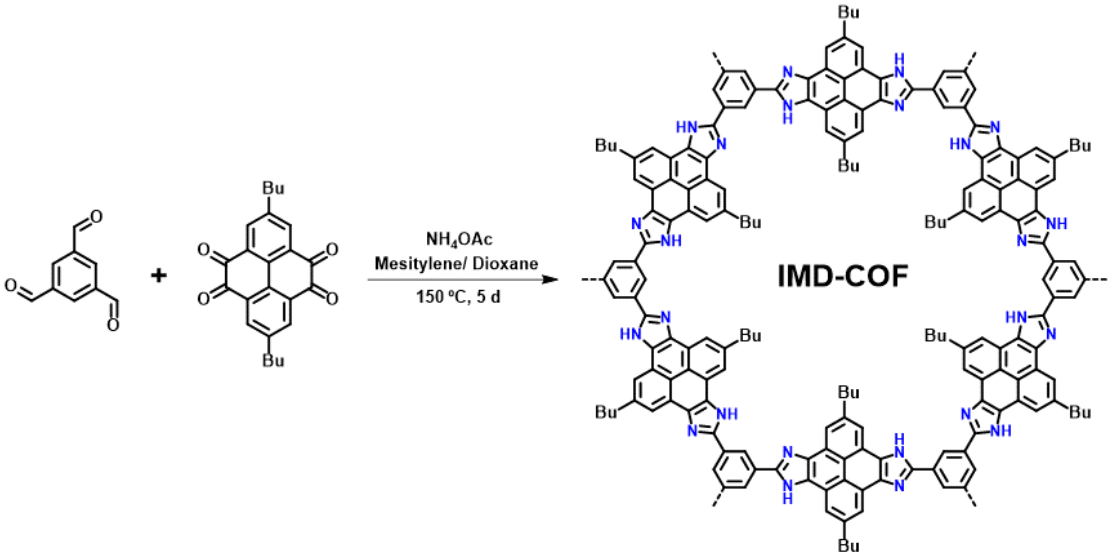

Scheme 4.4.3. Synthesis of IMD-COF.

To a dried Pyrex tube, triformylbenzene (4.9 mg, 0.030 mmol), 2, 7-di-tert-butylpyrene-4, 5, 9, 10-tetraone (16.8 mg, 0.045 mmol, 1.5 eq.), ammonium acetate (20.8 mg, 0.270 mmol, 9 eq.), mesitylene (0.8 mL) and 1, 4-dioxane (0.2 mL) charged in sequence. After sonication for 5 min, the tube was flash frozen in a liquid nitrogen bath. After three freeze-pump-thaw cycles and warming to room temperature, the sealed tube was placed in an oven of 150 °C for 5 days. The resulting light brown solid was collected *via* filtration, briefly washed with acetone, THF, ethanol and DI water. The wet solid was transferred to a Soxhlet extractor and thoroughly washed with THF and methanol for 24 h, respectively.

The powder was collected and dried at 80 °C for 12 h to afford IMD-COF as a yellow powder (26 mg, 97% yield).

4.4.3.4 Post-modification of Polyethylene Glycol-Anchored Imidazole-Linked Covalent Organic Frameworks

Synthesis of IMD-COF-OEG-1

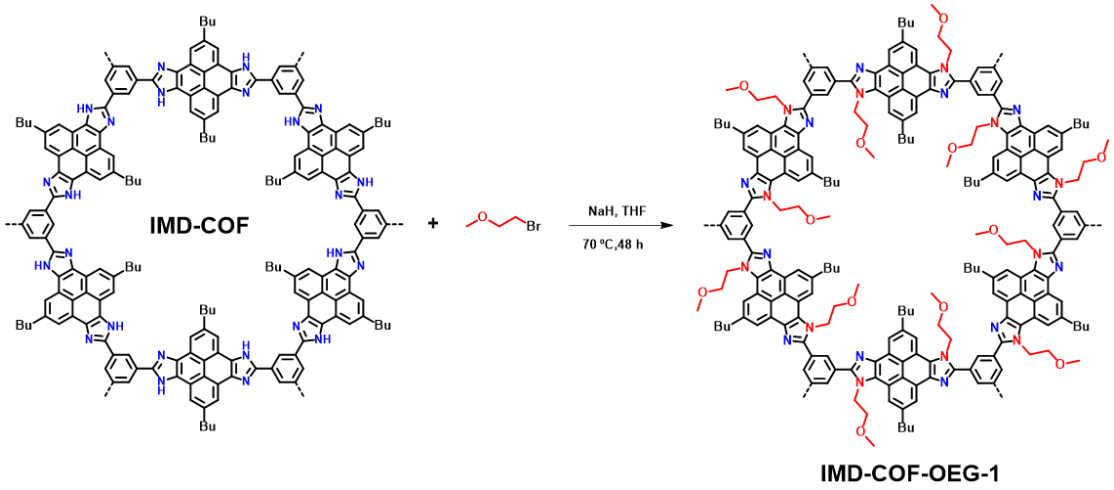

Scheme 4.4.4. Synthesis of IMD-COF-OEG-1.

IMD-COF (30 mg, 0.10 mmol), bromoethyl methyl ether (208.5 mg, 1.50 mmol, 15.0 eq.), and NaH (60% dispersion in mineral oil, 20 mg, 0.50 mmol, 5.0 eq.) were weighed into a round flask. To the mixture was added anhydrous THF (2.0 mL). The mixture was stirring at 70 °C for 48 hours under N_2. After cooling down to room temperature, water (2.0 mL) was added to the mixture. The mixture was filtered, and the residue was washed with DI water, THF and EtOH to afford IMD-COF-OEG-1 as a yellow powder (26 mg, 97% yield).

Synthesis of IMD-COF-OEG-2

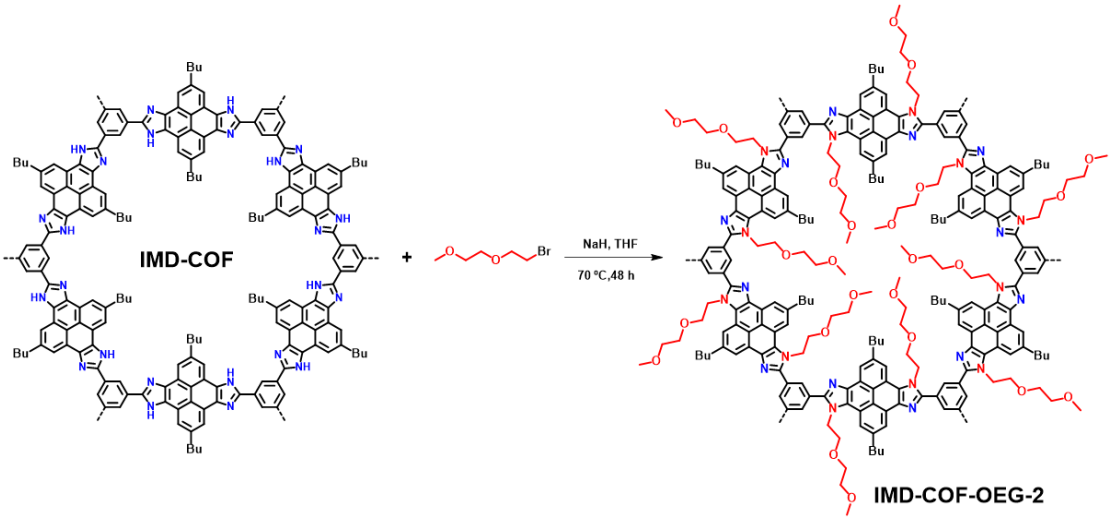

Scheme 4.4.5. Synthesis of IMD-COF-OEG-2.

The synthetic conditions of IMD-COF-OEG-2 were similar to that of IMD-COF-OEG-1, only using 1-Bromo-2-(2-methoxyethoxy) ethane as the corresponding brominated reactants. IMD-COF (30 mg, 0.10 mmol), 1-Bromo-2-(2-methoxyethoxy) ethane (274.5 mg, 1.50 mmol, 15.0 eq.), and NaH (60% dispersion in mineral oil, 20 mg, 0.50 mmol, 5.0 eq.) were weighed into a round flask. To the mixture was added anhydrous THF (2.0 mL). The mixture was stirring at 70 °C for 48 hours under N_2. After cooling down to room temperature, water (2.0 mL) was added to the mixture. The mixture was filtered, and the residue was washed with DI water, THF and EtOH to afford IMD-COF-OEG-2 as a yellow powder (26 mg, 97% yield).

Synthesis of IMD-COF-OEG-3

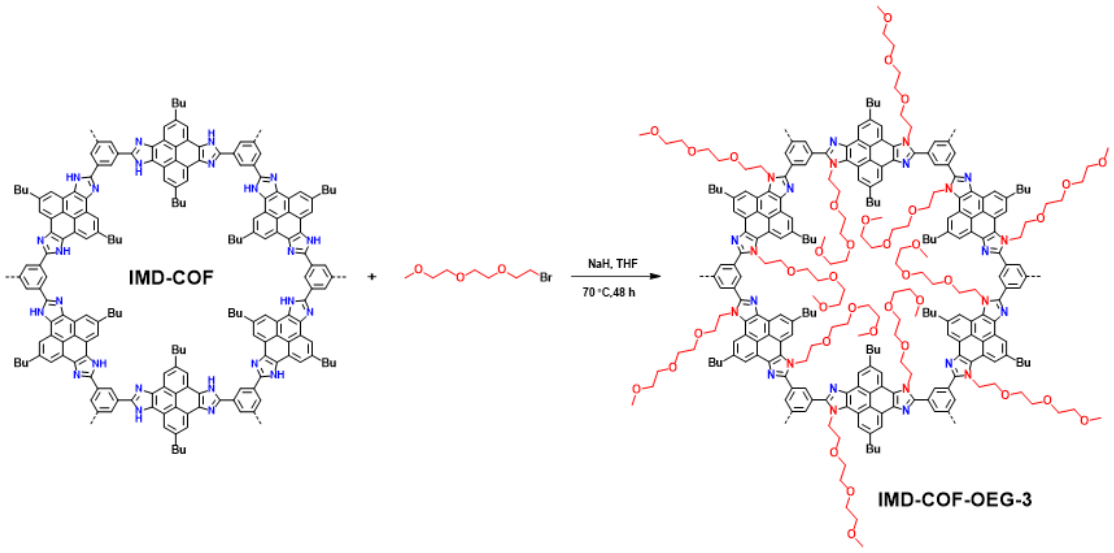

Scheme 4.4.6. Synthesis of IMD-COF-OEG-3.

The synthetic conditions of IMD-COF-OEG-3 were similar to that of IMD-COF-OEG-1 and IMD-COF-OEG-2, only using 1-Bromo-2-[2-(2-methoxyethoxy) ethoxy] ethane as the corresponding brominated reactants. IMD-COF (30 mg, 0.10 mmol), 1-Bromo-2-[2-(2-methoxyethoxy) ethoxy] ethane (340.5 mg, 1.50 mmol, 15.0 eq.), and NaH (60% dispersion in mineral oil, 20 mg, 0.50 mmol, 5.0 eq.) were weighed into a round flask. To the mixture was added anhydrous THF (2.0 mL). The mixture was stirring at 70 °C for 48 hours under N_2. After cooling down to room temperature, water (2.0 mL) was added to the mixture. The mixture was filtered, and the residue was washed with DI water, THF and EtOH to afford IMD-COF-OEG-3 as a yellow powder (26 mg, 97% yield).

4.4.3.5 Preparation of IMD-COF/ PEG composite

Synthesis of IMD-COF-PEG-8000

The infiltration of PEG chains into the COF channels was carried out by the low pressure-driven method. Typically, IMD-COF (30 mg) was suspended in anhydrous THF. The corresponding amount of THF solution of PEG-8000 was then added. After stirring for 12 hours, the mixture was evacuated progressively under reduced pressure. After solvent elimination, thermal annealing was allowed to proceed at 90 °C for 12 hours under reduced pressure to afford IMD-COF-PEG-8000 as a yellow powder.

4.4.4 Preparation of Solid-State Electrolytes

Synthesis of Li@Imidazole-linked COFs solid-state electrolytes

All samples were first dried overnight in a vacuum at 90 °C in a vacuum oven. 30 mg imidazole-linked COFs (IMD-COF, IMD-COF-PEG-8000 and IMD-COF-OEG-x (x= 1, 2, 3)) were immersed into the corresponding amount of MeOH solution of 1 M $LiClO_4$ under N_2 for 24 h. Powders were collected by vacuum filtration and rinsed with MeOH. The as-obtained Li@Imidazole-linked COFs powders were dried at 80 °C overnight under vacuum.

4.5 Results and Discussion

4.5.1 Design Principle and Post-Modification

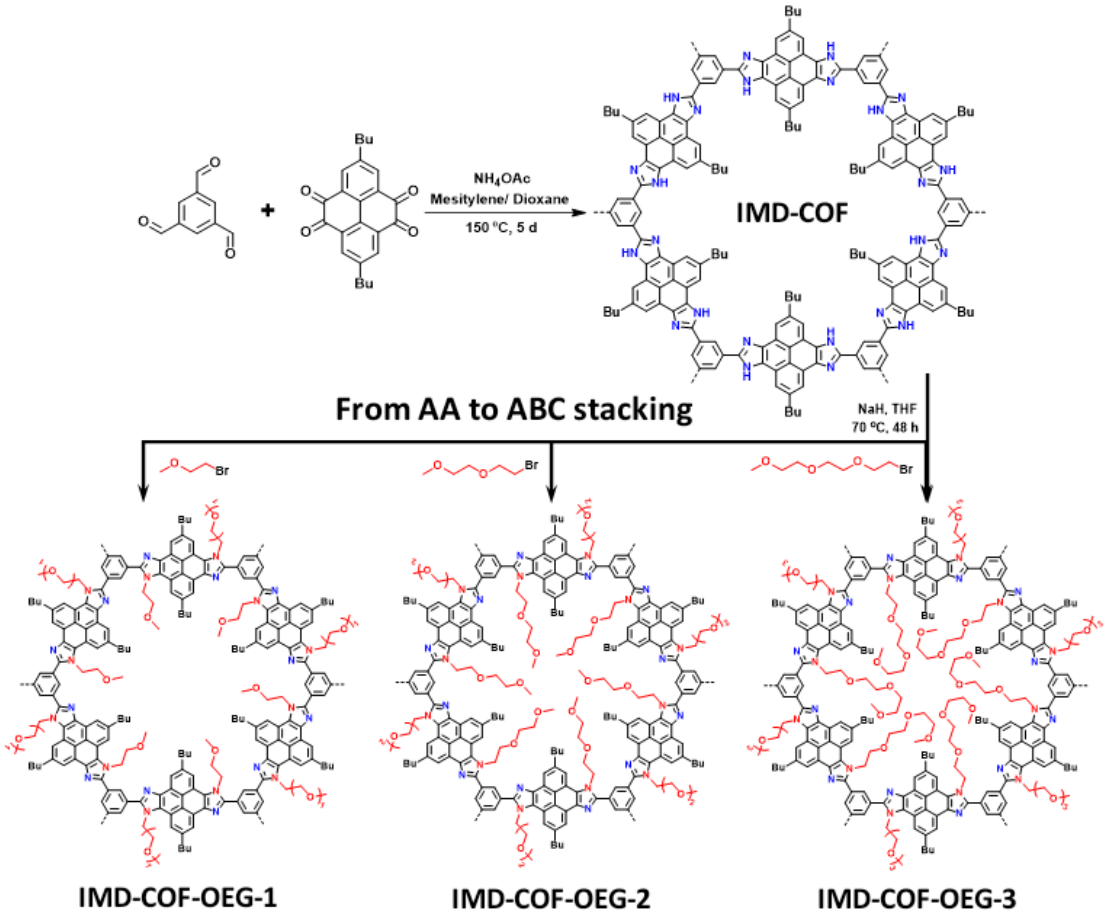

Figure 4.5.1 Synthetic route of IMD-COF and IMD-COF-OEG-x (x=1, 2, 3).

The robust IMD-COF was synthesised by the similar procedure from literature, in which 1, 3, 5-triformylbenzene (TFB), 2, 7-di-*tert*-butylpyrene-4, 5, 9, 10-tetraone

(DBPT) and ammonium acetate (NH_4OAc) was dissolved in the mesitylene and 1, 4-dioxane, and then heated at 150 ℃ for 5 days without stirring. The model compound can be obtained by the same method. The as-obtained yellow solid (IMD-COF) after filtration, washing and drying was collected and suspended in the THF solution of different bromide compounds of oligoethylene glycols (OEG-x-Br, x=1, 2, 3). The mixture was heated at 70 ℃ for 48 hours and purified by washing with THF, ethanol and acetone. Then three oligoethylene glycol-anchored imidazole-linked COFs, IMD-COF-OEG-x, with different length of OEG chains substituted in the imidazole-rings, was obtained as the yellow solids with high yields of over 88% (**Figure 4.5.1**).

4.5.2 Characterization of Crystallinity and Morphologies

The crystallinities of synthesized IMD-COF and IMD-COF-OEG-x were evaluated by powder X-ray diffraction (PXRD) measurement. From the PXRD pattern shown in **Figure 4.5.3**, IMD-COF adopts a fully eclipsed AA stacking mode with the main peak at around 3.8°, which is attributed to the (100) plane reflection according to the simulation pattern. The Pawley refined pattern is close to the experimental data with R_{wp}= 4.51% and R_{wp}= 3.26%, which confirms the structure modelled in the hexagonal space group *P6* with the unit cell values a= b= 25.439 Å, c= 5.778 Å, $\alpha=\beta=90^{o}$, $\gamma=$

120º (**Figure 4.5.2-4.5.3** and **Table 4.5.1**).

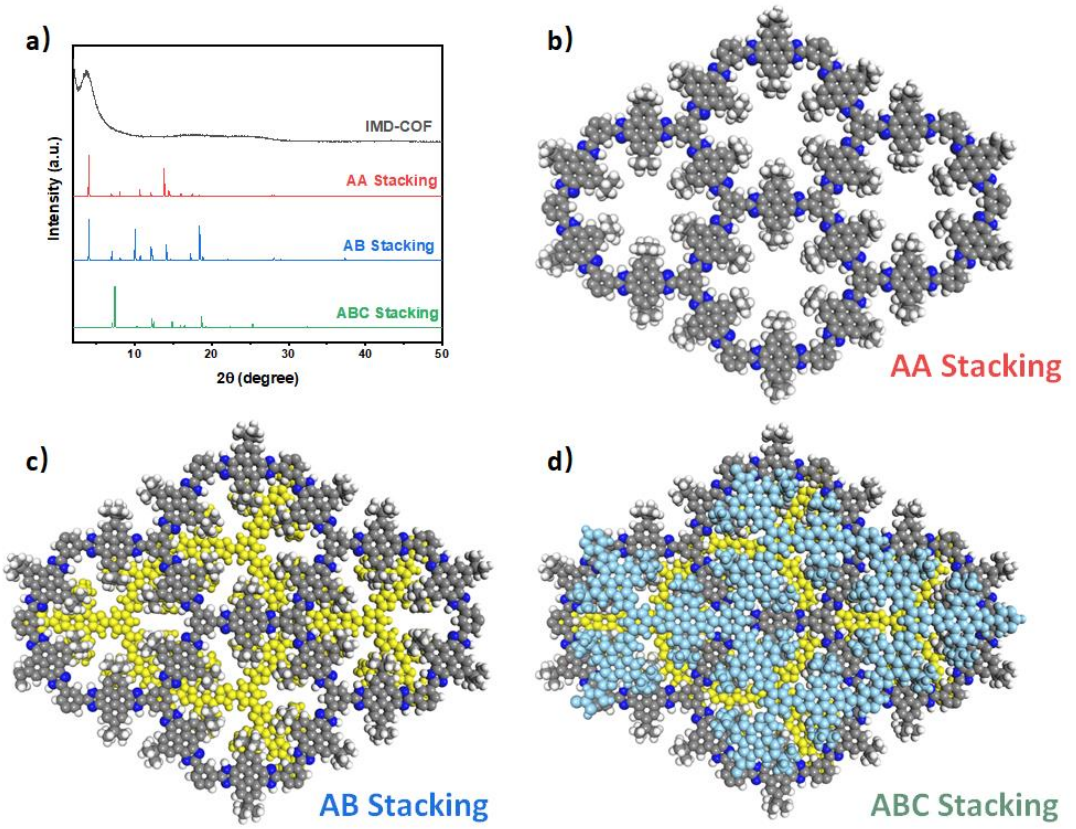

Figure 4.5.2. PXRD patterns of IMD-COF: observed (black) and calculated with the AA stacking mode (red), AB stacking mode (blue) and ABC stacking mode (green). Comparison of the observed and the simulated PXRD patterns suggest s that the preferable structure of IMD-COF is the AA stacking mode.

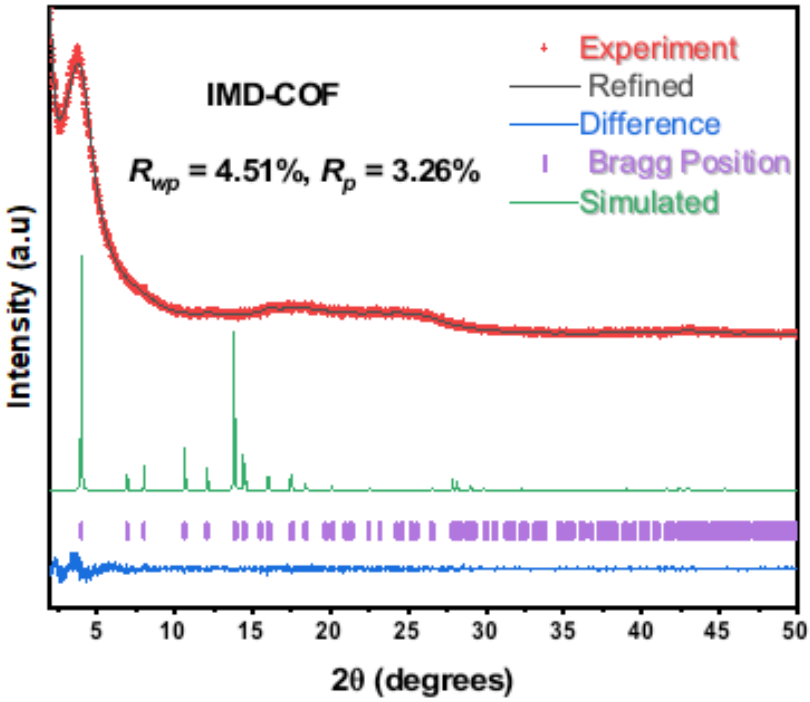

Figure 4.5.3. Crystal structures of IMD-COF. Experimental diffraction patterns (red), profiles calculated from Pawley fitting (black) showing the residual (blue), and pattern simulated from the structural model with AA stacking (green). Reflection positions are shown by tick marks (purple).

Table 4.5.1. Fractional atomic coordinates for the unit cell of IMD-COF.

Space group: P6 a= b= 25.439 Å, c= 5.778 Å α= β= 90°, γ= 120°							
Atom	**X**	**Y**	**Z**	**Atom**	**X**	**Y**	**Z**
C1	0.397	0.69885	-7.5029	C16	0.04842	0.74596	-7.69012
C2	0.36545	0.73164	-7.50299	C17	-0.05862	0.70002	-7.56585
H3	0.44354	0.72248	-7.50289	C18	0.02525	0.7357	-7.3044
C4	0.05574	0.63975	-7.5029	H19	0.09661	0.67918	-7.49589
C5	0.05605	0.58434	-7.50385	H20	-0.09486	0.58426	-7.51782

C6	0.00019	0.52834	-7.50645	H21	0.18173	0.51125	-7.50866
C7	-0.05523	0.52938	-7.50896	H22	0.04653	0.78775	-7.70812
C8	-0.05414	0.58551	-7.514	H23	0.03733	0.72244	-7.83958
C9	0.00109	0.64221	-7.51278	H24	0.09547	0.75967	-7.65342
C10	0.11032	0.58197	-7.5033	H25	-0.07702	0.67716	-7.71455
C11	0.10981	0.52699	-7.50655	H26	-0.05388	0.74516	-7.57466
N12	0.16851	0.6271	-7.50146	H27	-0.09186	0.6752	-7.44366
C13	0.20407	0.60151	-7.50353	H28	-0.00676	0.708	-7.18283
N14	0.16797	0.54055	-7.50664	H29	0.02831	0.78017	-7.30456
C15	0.00351	0.70351	-7.51897	H30	0.06998	0.74256	-7.2634

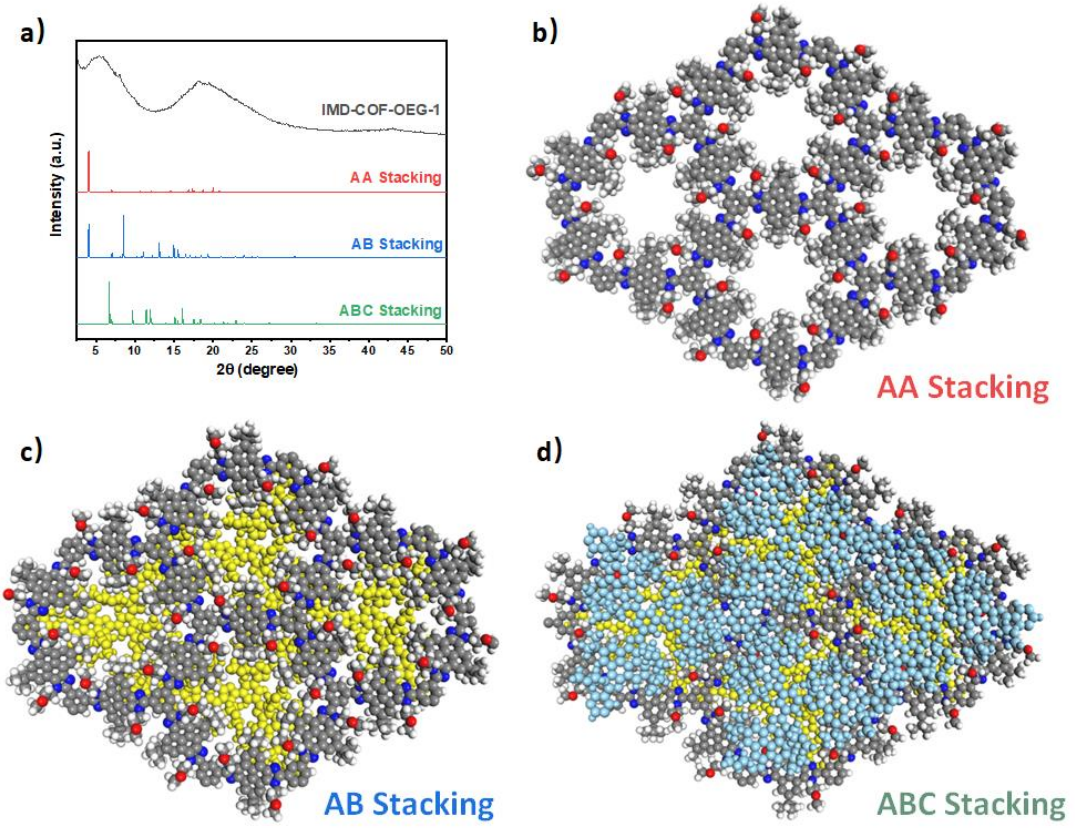

Figure 4.5.4. PXRD patterns of IMD-COF-OEG-1: observed (black) and calculated with the AA stacking mode (red), AB stacking mode (blue) and ABC stacking mode (green). Comparison of the observed and the simulated PXRD patterns suggest s that the preferable structure of IMD-COF-OEG-1 is the ABC stacking mode.

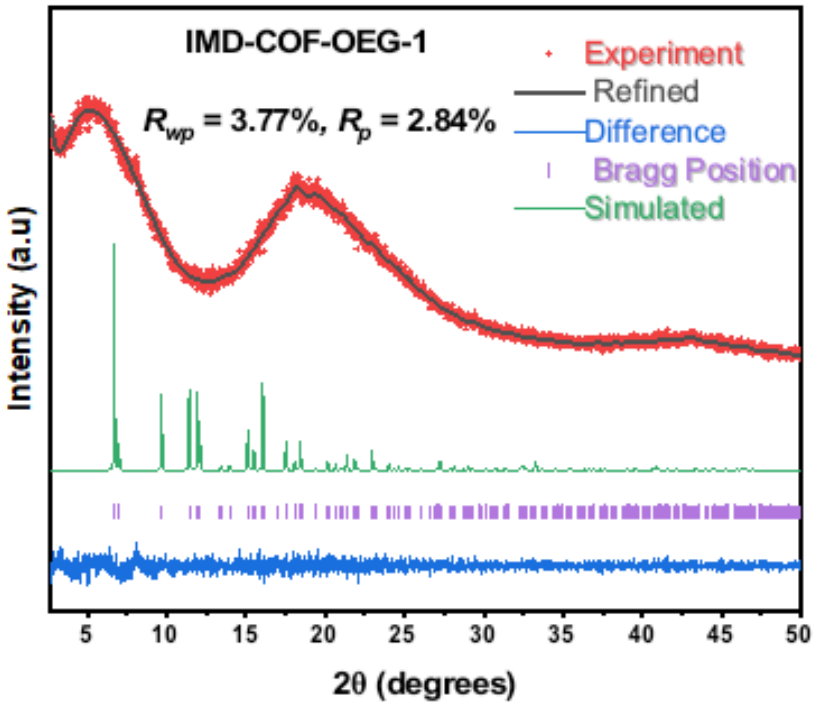

Figure 4.5.5. Crystal structures of IMD-COF-OEG-1. Experimental diffraction patterns (red), profiles calculated from Pawley fitting (black) showing the residual (blue), and pattern simulated from the structural model with ABC stacking (green). Reflection positions are shown by tick marks (purple).

Table 4.5.2. Fractional atomic coordinates for the unit cell of IMD-COF-OEG-1.

Space group: R3 a= b= 25.3843 Å, c= 16.5506 Å α= β= 90°, γ= 120°							
Atom	**X**	**Y**	**Z**	**Atom**	**X**	**Y**	**Z**
C1	0.39603	0.70537	0.11195	C41	0.60322	0.30261	0.13631
C2	0.35771	0.7307	0.11663	C42	0.63348	0.26919	0.13994
H3	0.44352	0.73552	0.09961	H43	0.55405	0.27847	0.13198
C4	0.06086	0.62954	0.15873	C44	0.93732	0.35476	0.0928
C5	0.05746	0.57346	0.14424	C45	0.94084	0.40914	0.11837
C6	0.00092	0.51897	0.14658	C46	0.99801	0.46223	0.12826

C7	0.94726	0.5212	0.16387	C47	0.05215	0.45965	0.11622
C8	0.95154	0.57819	0.17599	C48	0.04762	0.40497	0.08837
C9	0.00802	0.63298	0.17551	C49	0.99041	0.35195	0.07511
C10	0.10948	0.5691	0.13079	C50	0.88875	0.41348	0.13285
C11	0.10823	0.51473	0.12539	C51	0.89144	0.46564	0.16108
N12	0.16683	0.61527	0.12792	N52	0.83057	0.36938	0.12267
C13	0.20113	0.58804	0.12424	C53	0.79829	0.39594	0.14717
N14	0.16651	0.52542	0.12923	N54	0.83389	0.45347	0.1771
C15	0.01059	0.69386	0.19592	C55	0.98746	0.2938	0.04018
C16	0.07416	0.74952	0.18441	C56	0.92217	0.2402	0.02893
C17	0.96641	0.7036	0.14292	C57	0.01814	0.30734	-0.04296
C18	-0.00685	0.69379	0.28442	C58	1.0205	0.27163	0.09612
H19	0.10535	0.66992	0.15797	H59	0.89262	0.31552	0.08489
H20	0.91102	0.58077	0.18429	H60	0.08856	0.40419	0.07348
H21	0.08998	0.75197	0.12131	H61	0.89614	0.25221	-0.01399
H22	0.10723	0.74732	0.22631	H62	0.8978	0.2263	0.08769
H23	0.07376	0.7922	0.19817	H63	0.92252	0.19977	0.00354
H24	0.91818	0.67019	0.15655	H64	0.06678	0.34322	-0.03967
H25	0.97473	0.69958	0.07834	H65	-0.00535	0.32277	-0.08513
H26	0.97221	0.74963	0.15271	H66	0.0161	0.26594	-0.06891
H27	-0.00585	0.73691	0.30021	H67	1.01621	0.22832	0.07372
H28	0.02595	0.68947	0.3245	H68	1.00092	0.26344	0.15788
H29	0.94668	0.65563	0.29667	H69	0.06965	0.30545	0.0994
C30	0.51606	0.70149	0.16583	C70	0.51721	0.331	0.23775
C31	0.54871	0.69735	0.24142	C71	0.50342	0.35259	0.31772
O32	0.58276	0.75584	0.27663	O72	0.50012	0.31489	0.38304

C33	0.64412	0.78463	0.25142	C73	0.44856	0.25599	0.37626
H34	0.49059	0.72262	0.19082	H74	0.54865	0.31453	0.25596
H35	0.54876	0.73317	0.12051	H75	0.47611	0.29125	0.21227
H36	0.5761	0.67516	0.22988	H76	0.46183	0.35646	0.31416
H37	0.51327	0.6673	0.28568	H77	0.54156	0.39932	0.33049
H38	0.64811	0.79835	0.18709	H78	0.45659	0.2283	0.33112
H39	0.6653	0.756	0.26208	H79	0.40643	0.25706	0.36115
H40	0.6707	0.82652	0.28797	H80	0.44112	0.23239	0.43518

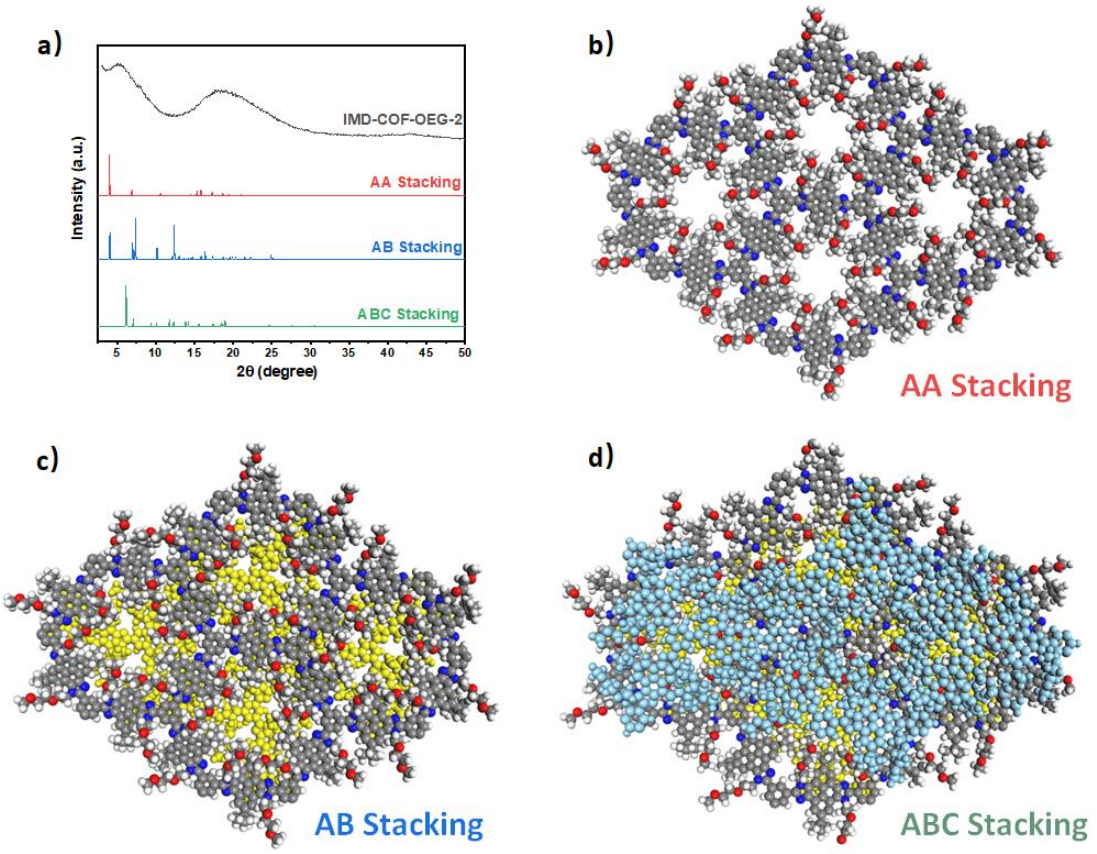

Figure 4.5.6. PXRD patterns of IMD-COF-OEG-2: observed (black) and calculated with the AA stacking mode (red), AB stacking mode (blue) and ABC stacking mode (green). Comparison of the observed and the simulated PXRD patterns suggest s that the preferable structure of IMD-COF-OEG-2 is the ABC stacking mode.

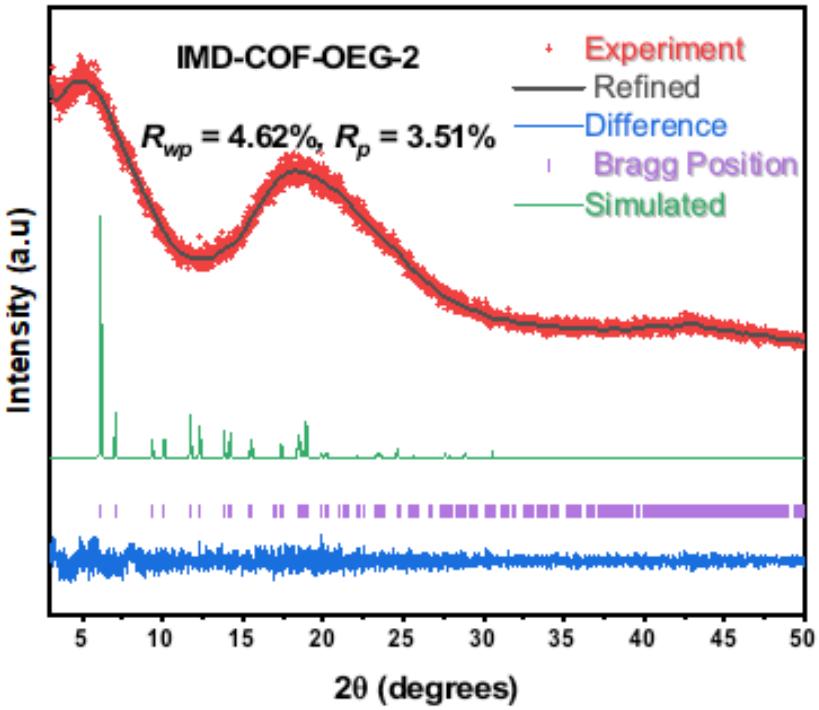

Figure 4.5.7. Crystal structures of IMD-COF-OEG-2. Experimental diffraction patterns (red), profiles calculated from Pawley fitting (black) showing the residual (blue), and pattern simulated from the structural model with ABC stacking (green). Reflection positions are shown by tick marks (purple).

Table 4.5.3. Fractional atomic coordinates for the unit cell of IMD-COF-OEG-2.

Space group: R3 a= b= 25.0425 Å, c= 19.1852 Å α= β= 90°, γ= 120°							
Atom	**X**	**Y**	**Z**	**Atom**	**X**	**Y**	**Z**
C1	0.39621	0.70828	0.15127	C48	0.60249	0.30066	0.04591
C2	0.35487	0.73114	0.15445	C49	0.63478	0.26846	0.05064
H3	0.44323	0.74035	0.13892	H50	0.55268	0.27509	0.04292
C4	0.05942	0.62634	0.14288	C51	0.9402	0.35259	0.06542
C5	0.05575	0.56901	0.13513	C52	0.942	0.40773	0.08255
C6	-0.00041	0.51635	0.11845	C53	0.99774	0.45911	0.10515

C7	0.94597	0.52142	0.11189	C54	0.05228	0.45478	0.11032
C8	0.95151	0.58022	0.11389	C55	0.05045	0.40096	0.08514
C9	0.00836	0.63376	0.12896	C56	0.99445	0.34873	0.06368
C10	0.10741	0.56262	0.14229	C57	0.88979	0.41432	0.07753
C11	0.10684	0.50804	0.13431	C58	0.89026	0.46709	0.09678
N12	0.16443	0.60861	0.15368	N59	0.83309	0.37154	0.0567
C13	0.19967	0.58185	0.15458	C60	0.79887	0.3992	0.06648
N14	0.165	0.51844	0.14815	N61	0.83154	0.45644	0.09647
C15	0.01466	0.69833	0.13375	C62	0.99078	0.28881	0.03673
C16	0.07798	0.74914	0.10742	C63	0.96431	0.27427	-0.0376
C17	0.96611	0.70359	0.08973	C64	0.05351	0.29192	0.03384
C18	0.00764	0.71207	0.20984	C65	0.9491	0.23482	0.08459
H19	0.10297	0.66542	0.15817	H66	0.89665	0.31338	0.0501
H20	0.91181	0.58413	0.10203	H67	0.09295	0.40055	0.0809
H21	0.08808	0.73698	0.05526	H68	0.99336	0.31313	-0.07315
H22	0.11604	0.75744	0.14347	H69	0.91643	0.26574	-0.03965
H23	0.07968	0.79406	0.10305	H70	0.9631	0.23218	-0.05816
H24	0.91916	0.67479	0.11089	H71	0.07528	0.30039	0.08592
H25	0.96717	0.68957	0.03503	H72	0.08542	0.3292	-0.00165
H26	0.97473	0.75162	0.08964	H73	0.04832	0.24788	0.01428
H27	0.01026	0.75748	0.215	H74	0.94655	0.19139	0.06669
H28	0.04449	0.71255	0.24257	H75	0.90138	0.22684	0.08588
H29	-0.03742	0.67637	0.23112	H76	0.96781	0.24451	0.13844
C30	0.52756	0.7108	0.16766	C77	0.51463	0.32043	0.14314
C31	0.57621	0.71613	0.21981	C78	0.50536	0.33621	0.21762
O32	0.62006	0.77964	0.22659	O79	0.49256	0.28535	0.26112

C33	0.67816	0.78807	0.24669	C80	0.4342	0.26027	0.29398
C34	0.72186	0.85579	0.26157	C81	0.38383	0.21138	0.24818
O35	0.77796	0.86295	0.2873	O82	0.32713	0.18623	0.28428
H36	0.50615	0.733	0.19723	H83	0.54507	0.30062	0.15088
H37	0.54952	0.73894	0.12037	H84	0.47106	0.28327	0.12067
H38	0.59706	0.68818	0.20403	H85	0.46993	0.35043	0.21912
H39	0.55326	0.69738	0.27077	H86	0.54923	0.37678	0.23555
H40	0.69858	0.77327	0.2049	H87	0.42185	0.29547	0.30987
H41	0.67505	0.76203	0.29441	H88	0.43569	0.23759	0.34302
H42	0.69959	0.87148	0.30048	H89	0.39637	0.1755	0.23625
H43	0.7291	0.88164	0.21212	H90	0.38218	0.2336	0.19887
C44	0.10627	0.1801	0.29841	C91	0.8613	0.7205	0.24291
H45	0.1181	0.16627	0.24819	H92	0.88762	0.72698	0.194
H46	0.06879	0.13781	0.32317	H93	0.88556	0.76443	0.27256
H47	0.14647	0.19895	0.33456	H94	0.81439	0.7124	0.23106

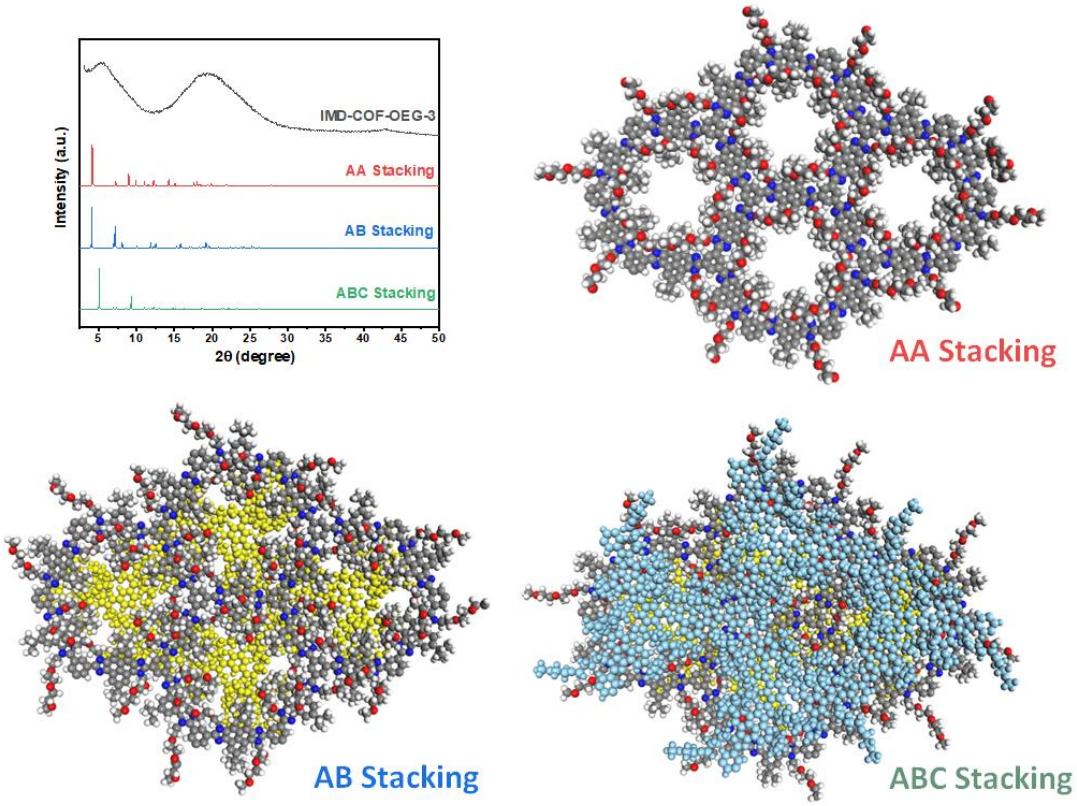

Figure 4.5.8. PXRD patterns of IMD-COF-OEG-3: observed (black) and calculated with the AA stacking mode (red), AB stacking mode (blue) and ABC stacking mode (green). Comparison of the observed and the simulated PXRD patterns suggests that the preferable structure of IMD-COF-OEG-3 is the ABC stacking mode.

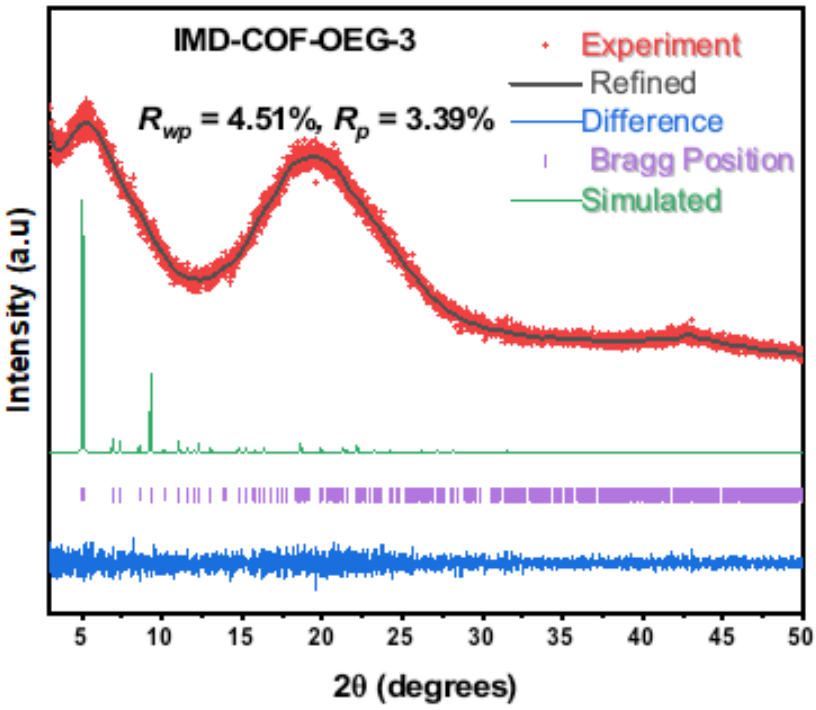

Figure 4.5.9. Crystal structures of IMD-COF-OEG-3. Experimental diffraction patterns (red), profiles calculated from Pawley fitting (black) showing the residual (blue), and pattern simulated from the structural model with ABC stacking (green). Reflection positions are shown by tick marks (purple).

Table 4.5.4. Fractional atomic coordinates for the unit cell of IMD-COF-OEG-3.

Space group: R3 a= b= 25.513 Å, c= 28.556 Å α= β= 90°, γ= 120°							
Atom	**X**	**Y**	**Z**	**Atom**	**X**	**Y**	**Z**
C1	0.3955	0.70423	0.11272	C55	0.60481	0.29338	0.08272
C2	0.35853	0.73072	0.11155	C56	0.64438	0.26965	0.08213
H3	0.44239	0.73364	0.11682	H57	0.55808	0.26208	0.08605
C4	0.06736	0.64169	0.11021	C58	0.93226	0.36546	0.08291
C5	0.06026	0.58356	0.10827	C59	0.93918	0.42306	0.08908
C6	0.0024	0.53256	0.10084	C60	0.99684	0.47406	0.09615

C7	0.95042	0.53989	0.09759	C61	0.04856	0.46656	0.09851
C8	0.95951	0.599	0.10145	C62	0.03904	0.40724	0.09582
C9	0.0175	0.65066	0.1057	C63	0.98221	0.35661	0.08583
C10	0.11012	0.57472	0.11082	C64	0.88934	0.43133	0.08791
C11	0.10627	0.5196	0.10486	C65	0.89267	0.48637	0.09111
N12	0.168	0.61825	0.11504	N66	0.83216	0.38721	0.08335
C13	0.20065	0.58991	0.11092	C67	0.79879	0.41476	0.08349
N14	0.16402	0.52852	0.10362	N68	0.83483	0.47699	0.08684
C15	0.02748	0.7159	0.10461	C69	0.97684	0.29394	0.07903
C16	0.06894	0.75134	0.06353	C70	0.91404	0.2448	0.06201
C17	-0.03116	0.71851	0.09855	C71	1.02273	0.29828	0.04215
C18	0.05707	0.74926	0.15016	C72	0.98956	0.27202	0.12533
H19	0.11234	0.68033	0.11408	H73	0.88731	0.32777	0.07674
H20	0.92235	0.60617	0.1011	H74	0.07444	0.39821	0.1025
H21	0.04743	0.72924	0.02986	H75	0.9023	0.25849	0.02855
H22	0.11358	0.75391	0.06606	H76	0.87865	0.23602	0.0883
H23	0.07738	0.79849	0.06277	H77	0.91292	0.20127	0.05593
H24	0.94542	0.6958	0.06553	H78	0.01792	0.31957	0.00984
H25	-0.02132	0.76609	0.09654	H79	1.01557	0.25288	0.03291
H26	0.93793	0.69694	0.12872	H80	0.07002	0.32559	0.05468
H27	0.10447	0.75959	0.152	H81	0.95541	0.26618	0.15205
H28	0.03183	0.72131	0.18088	H82	1.03495	0.30483	0.13928
H29	0.0581	0.79325	0.15222	H83	0.98765	0.2279	0.12056
C30	0.51557	0.69734	0.08787	C84	0.47654	0.29478	0.07639
C31	0.55509	0.73646	0.12897	C85	0.44731	0.25851	0.12148
O32	0.53704	0.77791	0.14348	O86	0.47835	0.22903	0.13714

C33	0.5564	0.79781	0.18986	C87	0.44736	0.19077	0.17543
C34	0.50511	0.76199	0.22475	C88	0.48642	0.16711	0.19634
O35	0.5285	0.76321	0.27011	O89	0.45288	0.1222	0.2305
H36	0.49404	0.71915	0.06855	H90	0.49321	0.27182	0.0531
H37	0.54422	0.69492	0.05971	H91	0.44185	0.29477	0.05296
H38	0.6029	0.7631	0.11701	H92	0.39921	0.22478	0.11337
H39	0.55265	0.70557	0.1578	H93	0.44847	0.29015	0.14902
H40	0.56835	0.84591	0.19252	H94	0.40401	0.15134	0.16374
H41	0.59764	0.79592	0.20007	H95	0.43794	0.21505	0.2037
H42	0.47928	0.71413	0.21283	H96	0.52614	0.2057	0.21341
H43	0.47206	0.77851	0.22467	H97	0.5053	0.15188	0.16763
C44	0.2694	0.44891	0.29207	C98	0.62931	0.5655	0.21234
C45	0.22828	0.38208	0.30287	C99	0.62114	0.60466	0.24818
O46	0.26393	0.35633	0.31599	O100	0.58785	0.62941	0.22765
C47	0.22689	0.29283	0.31885	C101	0.57724	0.66332	0.26154
H48	0.28777	0.47342	0.32555	H102	0.58399	0.52571	0.20459
H49	0.30917	0.45448	0.27161	H103	0.64753	0.59272	0.17985
H50	0.20086	0.3599	0.27114	H104	0.66689	0.64088	0.25922
H51	0.19702	0.37794	0.33162	H105	0.597	0.5755	0.27883
H52	0.18662	0.27902	0.34164	H106	0.55213	0.63542	0.29241
H53	0.25354	0.27377	0.33461	H107	0.54806	0.67932	0.24581
H54	0.21246	0.27258	0.28339	H108	0.6201	0.70393	0.27275

IMD-COF-OEG-1~3 show poorer crystallinity than IMD-COFs due to the crowded OEG chains in the pore structure, which reduce the interlayer π-π interaction which affects the regular stacking of each COF layer. Compared with the simulation data, the

PXRD patterns of IMD-COF-OEG-x match better with the ABC stacking mode, proving the planar slipping of the layers after introduction of the OEG chains (**Figure 4.5.4-4.5.9** and **Table 4.5.2-4.5.4**).

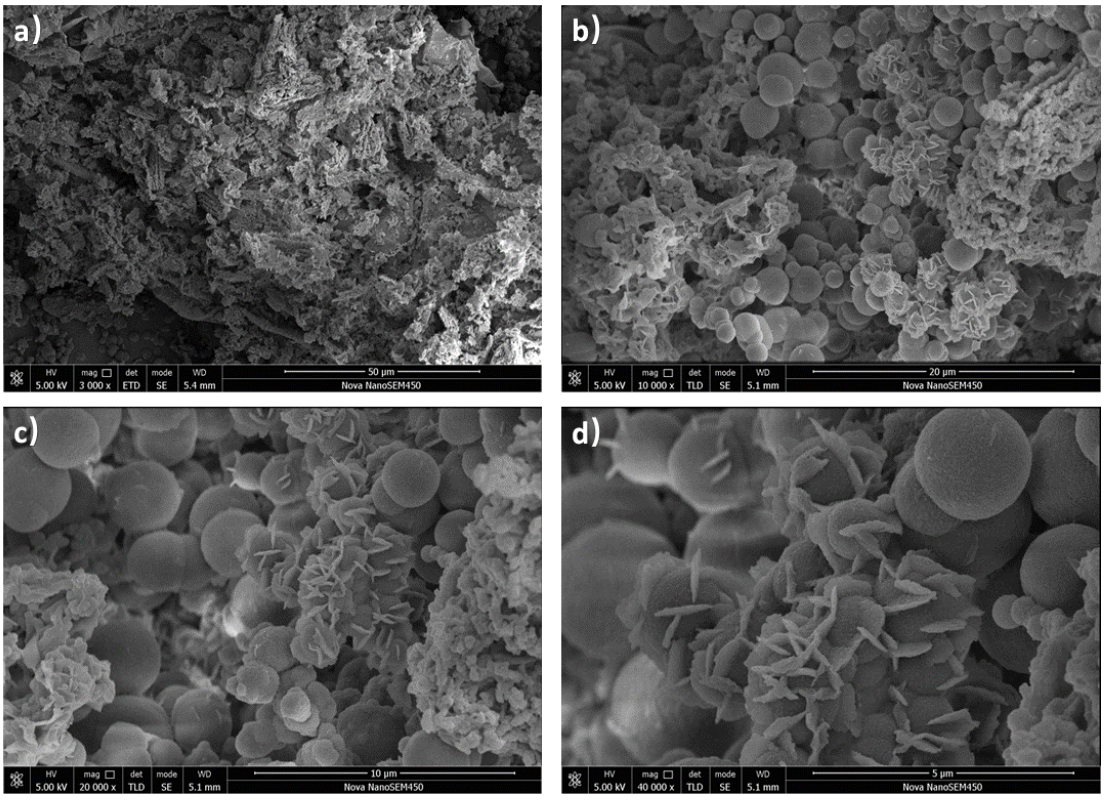

Figure 4.5.10. SEM images of IMD-COF.

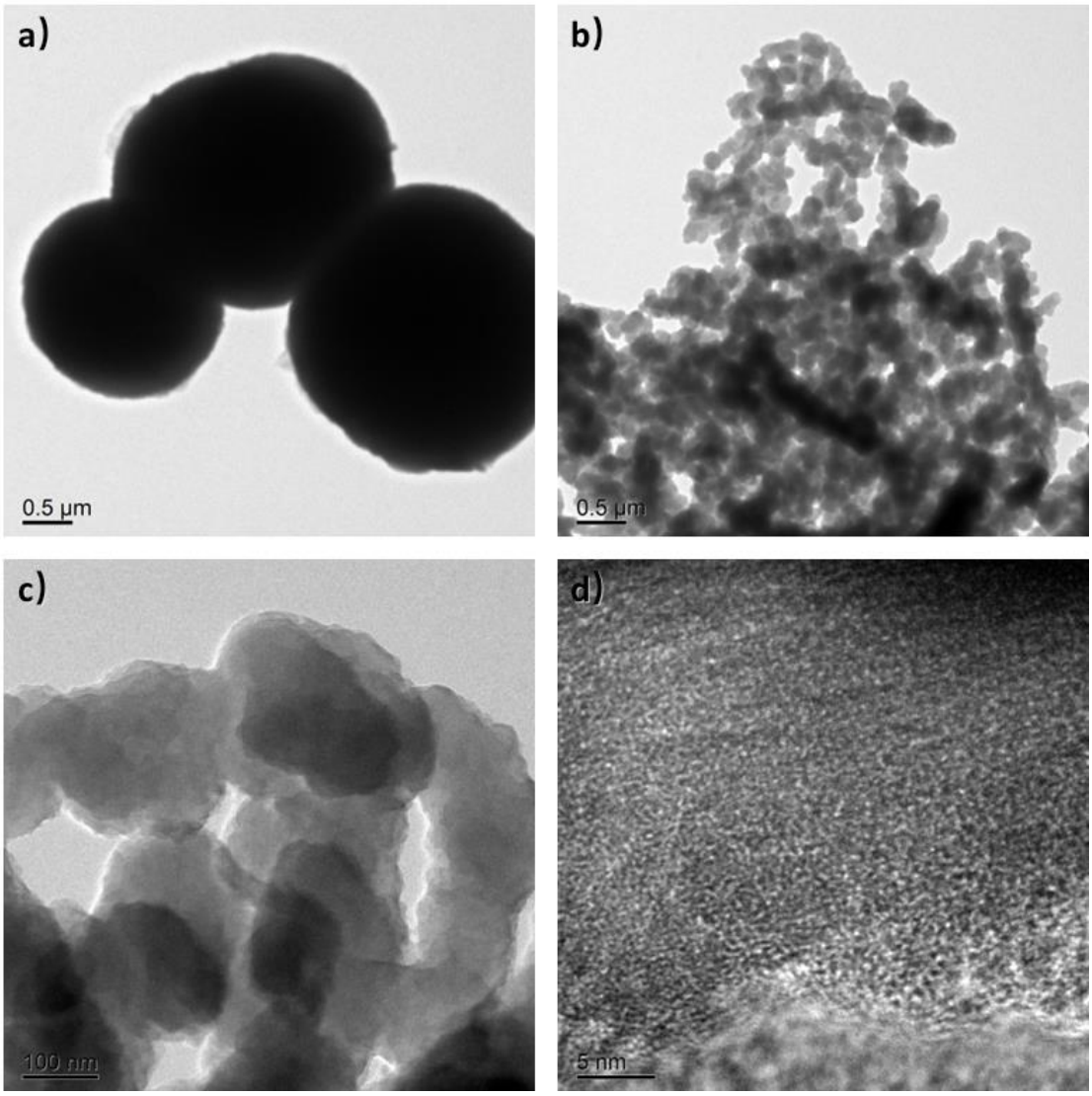

Figure 4.5.11. TEM images of IMD-COF.

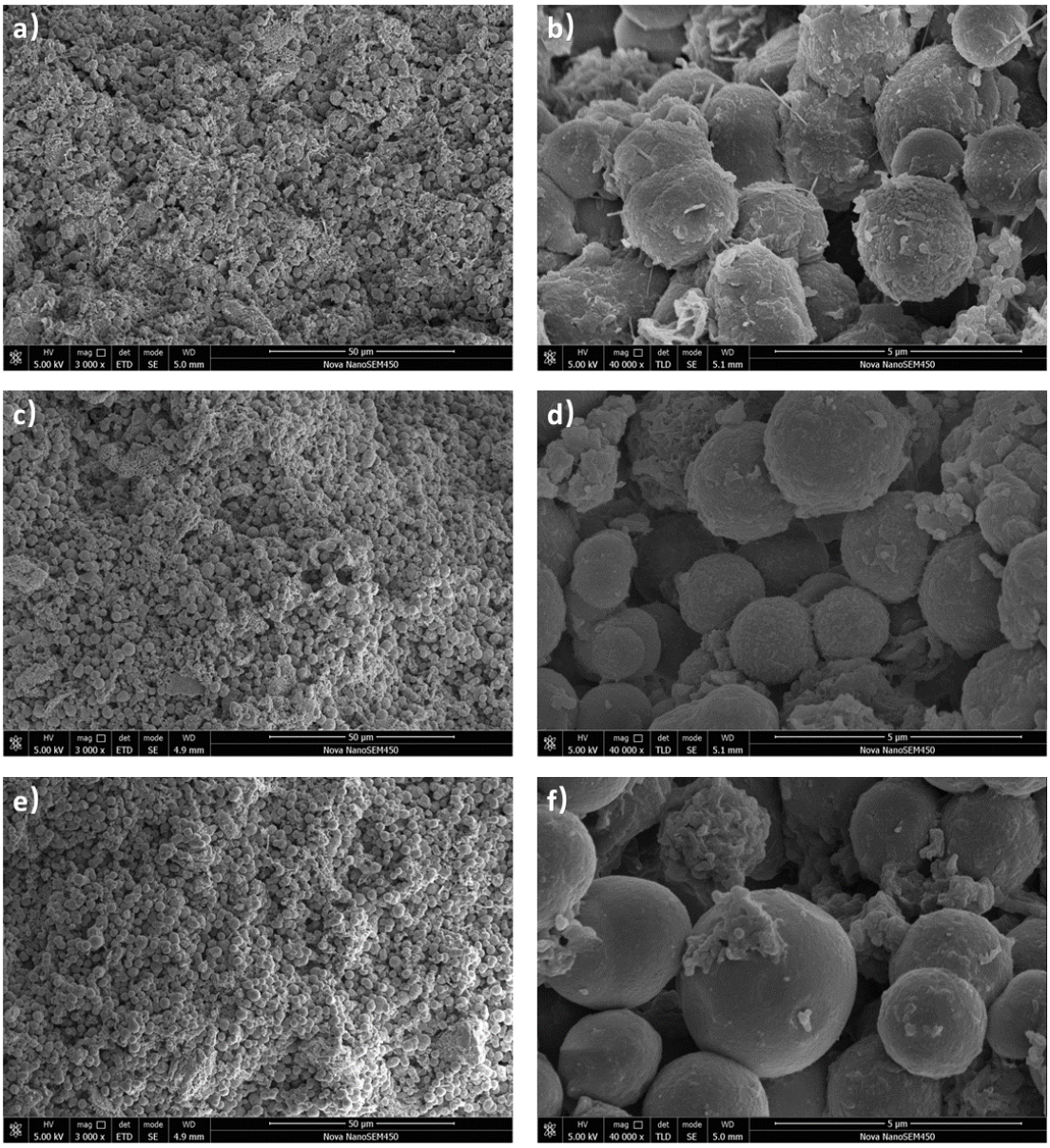

Figure 4.5.12. (a-b) SEM images of IMD-COF-OEG-1, (c-d) SEM images of IMD-COF-OEG-2, (e-f) SEM images of IMD-COF-OEG-3.

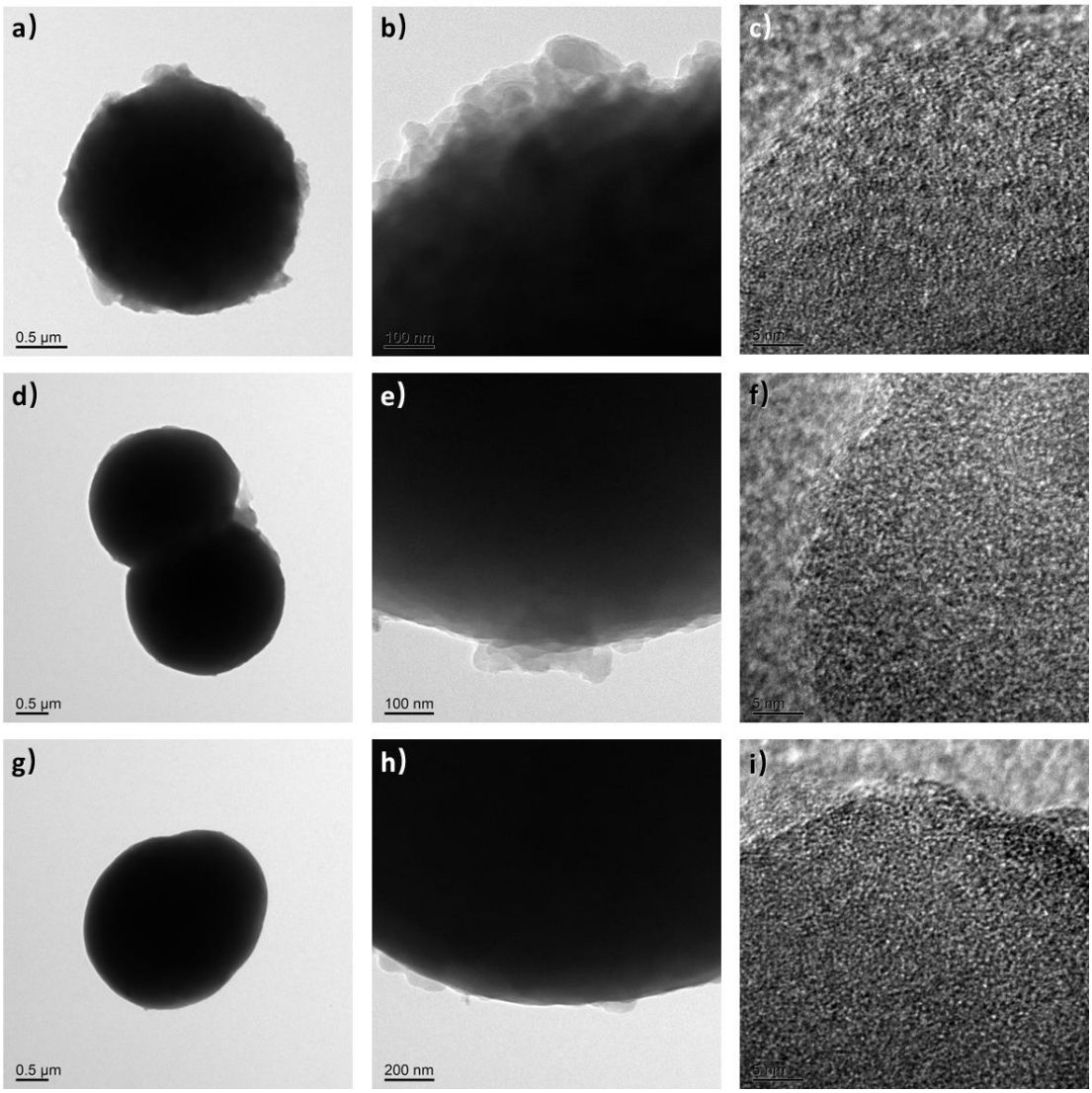

Figure 4.5.13. (a-c) SEM images of IMD-COF-OEG-1, (d-f) SEM images of IMD-COF-OEG-2, (g-i) SEM images of IMD-COF-OEG-3.

The morphologies of all the samples were investigated by scanning electron microscopy (SEM) and transmission electron microscopy (TEM). SEM and TEM images revealed a layer-assembled microsphere morphology of IMD-COF with average particle sizes of around 2 µm (**Figure 4.5.10-4.5.11**). The same morphology was observed after the post-modification reaction (**Figure 4.5.12-4.5.13**).

4.5.3 Characterization of Chemical Structures

The formation of imidazole linkages and successful graft of OEG chains can be confirmed by ^{13}C cross-polarization magic angle spinning (CP/ MAS) solid-state NMR spectroscopy. IMD-COF exhibited signals at around 127, 138, 161 ppm, corresponding

to the imidazole ring carbons. Compared with the parent IMD-COF, the OEG-anchored IMD-COF-OEG-1~3 showed additional signals at around 47, 58 and 71 ppm, which correspond to the OEG chain ethylene carbons (**Figure 4.5.14**). In addition, the intensity of the signals at 58 and 71 ppm were enhanced when increasing the size of the OEG chains, indicating the higher ratio of OEG part in the IMD-COF-OEG-3.

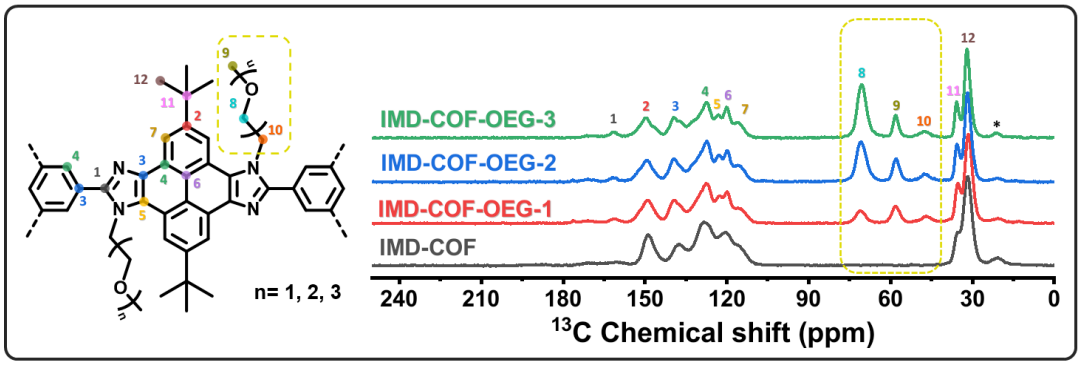

Figure 4.5.14. Solid-state ^{13}C cross-polarization magic angle spinning (CP/MAS) NMR of IMD-COF (black), IMD-COF-OEG-1 (red), IMD-COF-OEG-2 (blue), IMD-COF-OEG-3 (green). Insert is the Assignment of the ^{13}C ss-NMR signals to the respective ^{13}C in the structures of IMD-COF-OEG-x.

X-Ray photoelectron spectrometry (XPS) measurements can also confirm the elemental configuration of IMD-COFs, showing gradual enhanced O 1s from IMD-COF to IMD-COF-OEG-3 (**Figure 4.5.15**). Compared with the C 1s peak of IMD-COF, the additional sub-peak at round 286.7 eV in IMD-COF-OEG-x can be attributed to the -C-O- bond. The integral area of which was enlarged as the OEG chains increased (**Figure 4.5.16**). All of the N 1s peaks showed two sub-peaks at 398.8 eV and 400.7 eV, which belonged to saturated-N (-NH-) and unsaturated-N (=N-), respectively (**Figure 4.5.17**).

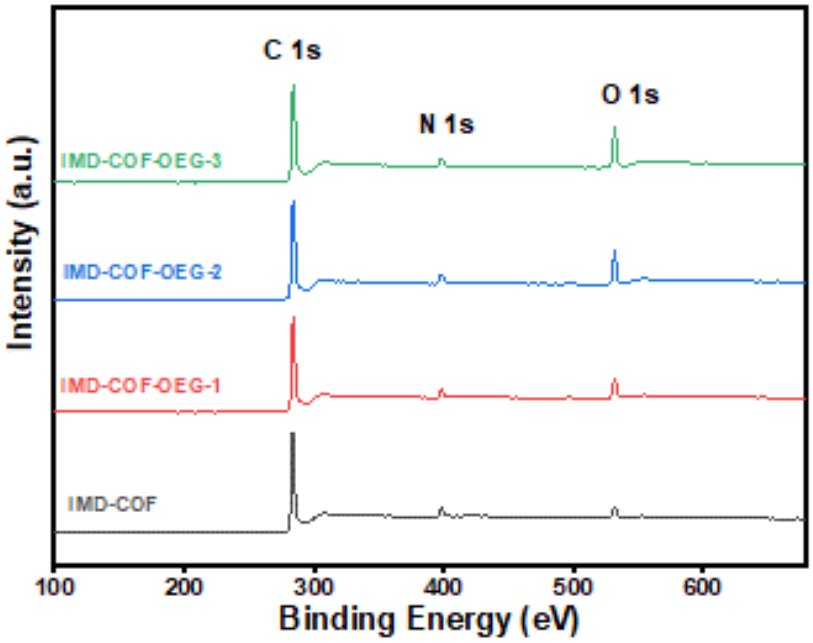

Figure 4.5.15. XPS spectra of IMD-COF (black), IMD-COF-OEG-1 (red), IMD-COF-OEG-2 (blue) and IMD-COF-OEG-3 (green).

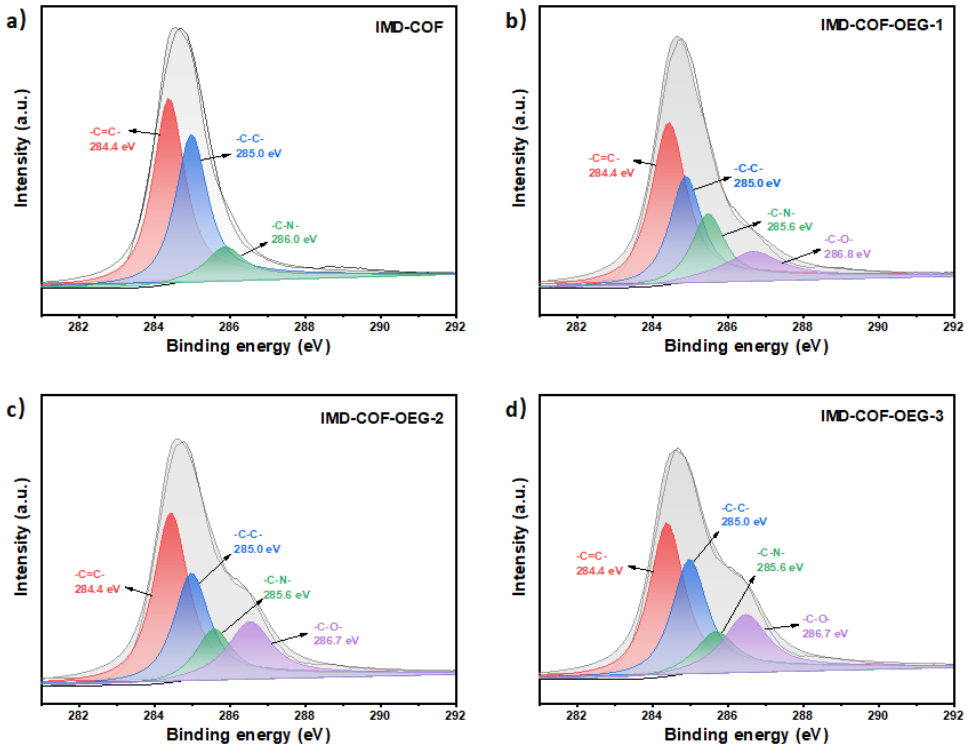

Figure 4.5.16. C 1s spectra of IMD-COFs with sub-peaks: (a) IMD-COF, (b) IMD-COF-OEG-1, (c) IMD-COF-OEG-2 and (d) IMD-COF-OEG-3.

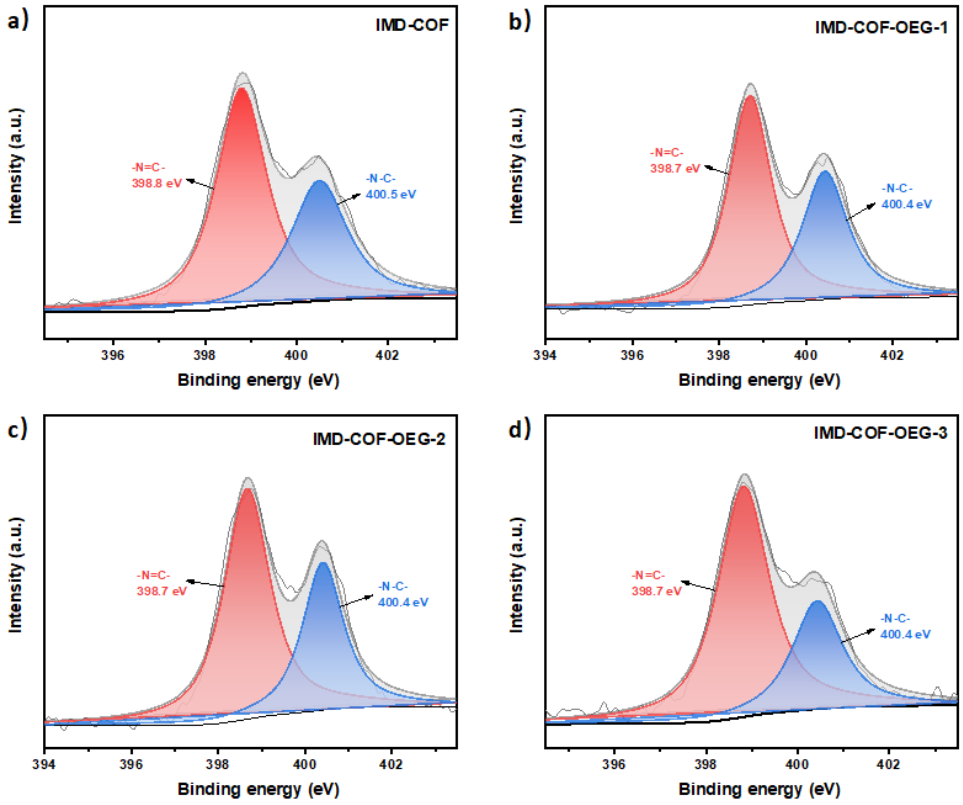

Figure 4.5.17. N 1s spectra of IMD-COFs with sub-peaks: (a) IMD-COF, (b) IMD-COF-OEG-1, (c) IMD-COF-OEG-2 and (d) IMD-COF-OEG-3.

Fourier transform infrared (FT-IR) spectra of IMD-COF show bands at 1618 cm^{-1} (*ν*-N=C-) and 3434 cm^{-1} (*ν*-N-H), which are characteristic of the imidazole ring. For IMD-COF-OEG-x, a new peak at around 1100 cm^{-1} is observed belonging to the vibration of C-O bonds in OEG chains, indicating the success of the post-modification (**Figure 4.5.18**).

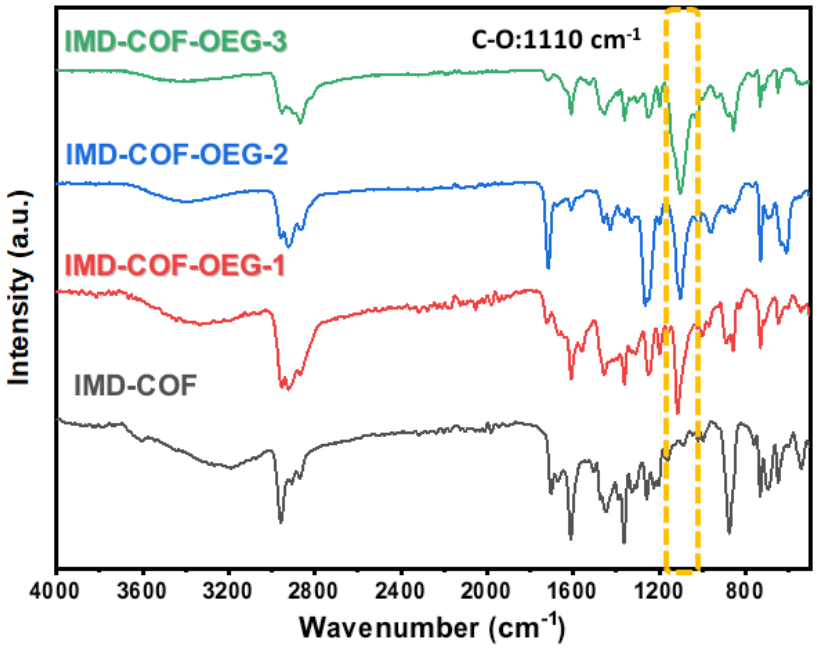

Figure 4.5.18. FT-IR spectra of IMD-COF (black), IMD-COF-OEG-1 (red), IMD-COF-OEG-2 (blue), IMD-COF-OEG-3 (green).

4.5.4 Characterization of Chemical Stability and Thermal Stability

The chemical stability of IMD-COF was tested by immersing materials in different solvents and acid or base solution for 48 h. The crystallinity of IMD-COF remains under all of these conditions, which was encouraging for post-modification reactions and lithium salts doping (**Figure 4.5.19**).

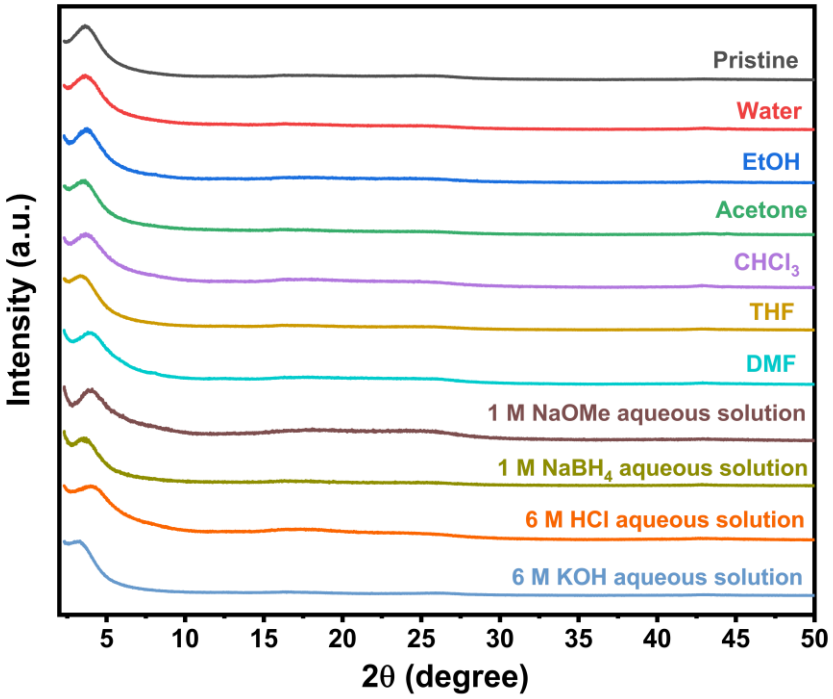

Figure 4.5.19. PXRD patterns of IMD-COF after 48 h stability tests by various solvents.

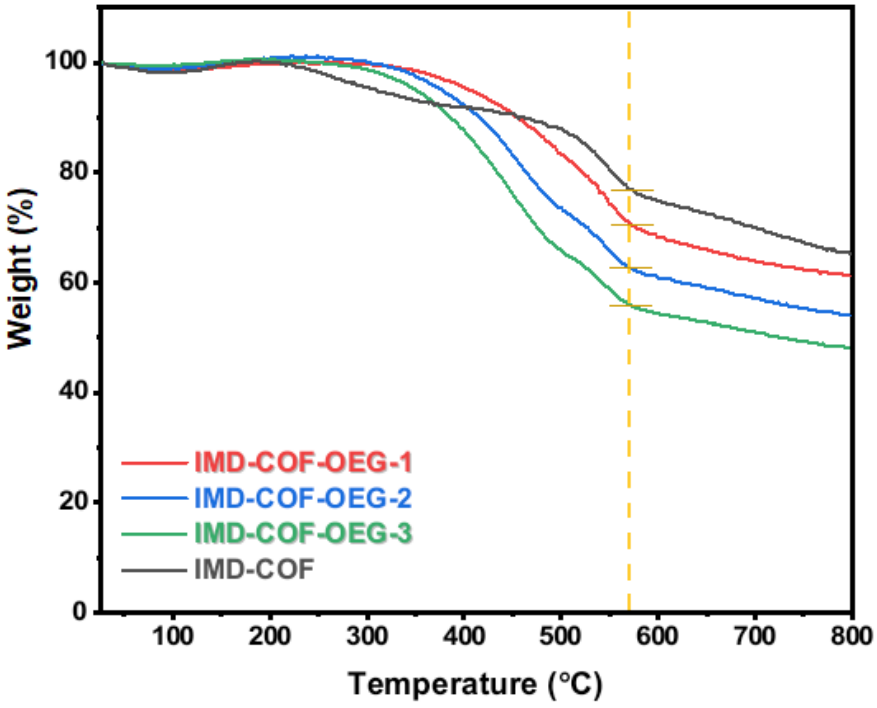

Figure 4.5.20. TGA curves of IMD-COF (black), IMD-COF-OEG-1 (red), IMD-COF-OEG-2 (blue), IMD-COF-OEG-3 (green) measured in N_2.

For the thermal stability, thermogravimetric analysis (TGA) was measured up to 800 ℃ under N_2 atmosphere for all the samples (**Figure 4.5.20**). IMD-COFs show a good thermal stability, with weight loss of 10 % at temperatures around 350 ℃, while IMD-COF-OEG-x have higher stability presumably due to the ordered π-stacking within layers stabilized by the OEG chains.[37] The onset decomposition temperatures of IMD-COF-OEG-x are around 400 ℃ from which shows the breakup of C-O bonds, causing the decomposition of OEG chains. Until the temperature is increased to 800 ℃, the residual mass of IMD-COF is about 65%, which is higher than those of IMD-COF-OEG-1 (61%), IMD-COF-OEG-2 (54%) and IMD-COF-OEG-3 (48%). Therefore, the grafting rate of OEG-x can be calculated to around 75%, which match the results from Elemental Analysis and X-ray photoelectron spectroscopy (XPS) (**Table 4.5.5** and **Table 4.5.6**).

Table 4.5.5. Elemental analysis of IMD-COF and IMD-COF-OEG-x (x=1, 2, 3). We note that theoretical values for COFs often differ substantially from experiment. There are a number of reasons for this including the presence of end groups/ surface groups, which are not accounted for in the theoretical values, and physisorbed guests in the COF pores (*e.g.*, H_2O, CO_2), that affect the sample mass.

Samples	Empirical Formula	Calculation wt%				Analysis wt%			
		%C	%H	%N	%O	%C	%H	%N	%O
IMD-COF	$(C_{15}H_{13}N_2)_n$	81.45	5.88	12.67	-	73.16	5.94	9.31	-
IMD-COFOEG-1	$(C_{18}H_{19}N_2O)_n$	77.42	6.81	10.04	5.73	81.55	7.43	8.03	-
IMD-COF-OEG-2	$(C_{20}H_{23}N_2O_2)_n$	74.30	7.12	8.67	9.91	75.14	7.53	6.53	-
IMD-COFOEG-3	$(C_{22}H_{27}N_2O_3)_n$	71.93	7.36	7.63	13.08	70.85	7.35	5.78	-

Table 4.5.6. Elemental analysis of IMD-COF and IMD-COF-OEG-x (x=1, 2, 3) from XPS calculation.

Sample	Empirical Formula	Calculation at%				Analysis at%			
		%C	%H	%N	%O	%C	%H	%N	%O
IMD-COF	$(C_{15}H_{13}N_2)_n$	**81.45**	**5.88**	**12.67**	**-**	**84.38**	**-**	**7.38**	**5.55**
IMD-COF-OEG-1	$(C_{18}H_{19}N_2O)_n$	**77.42**	**6.81**	**10.04**	**5.73**	**81.87**	**-**	**6.57**	**8.8**
IMD-COF-OEG-2	$(C_{20}H_{23}N_2O_2)_n$	**74.30**	**7.12**	**8.67**	**9.91**	**79.59**	**-**	**5.95**	**10.97**
IMD-COF-OEG-3	$(C_{22}H_{27}N_2O_3)_n$	**71.93**	**7.36**	**7.63**	**13.08**	**78.89**	**-**	**5.36**	**12.79**

Moreover, the thermal behaviours of IMD-COF and IMD-COF-OEG-1~3 were characterized by differential scanning calorimetry (DSC) measurement from -50 to 180 ℃ under N_2 atmosphere (**Figure 4.5.21**). Similar to that of IMD-COF, there are no signals for the endothermic or exothermic peak observed in the measured temperature region for IMD-COF-OEG-x. This is presumably due to the non-melting property of the cross-linked framework, indicating that anchoring in the pores of IMD-COF can restrict the endothermic glass transitions (T_g) of OEG chain efficiently, which is beneficial to the lithium conductivity.

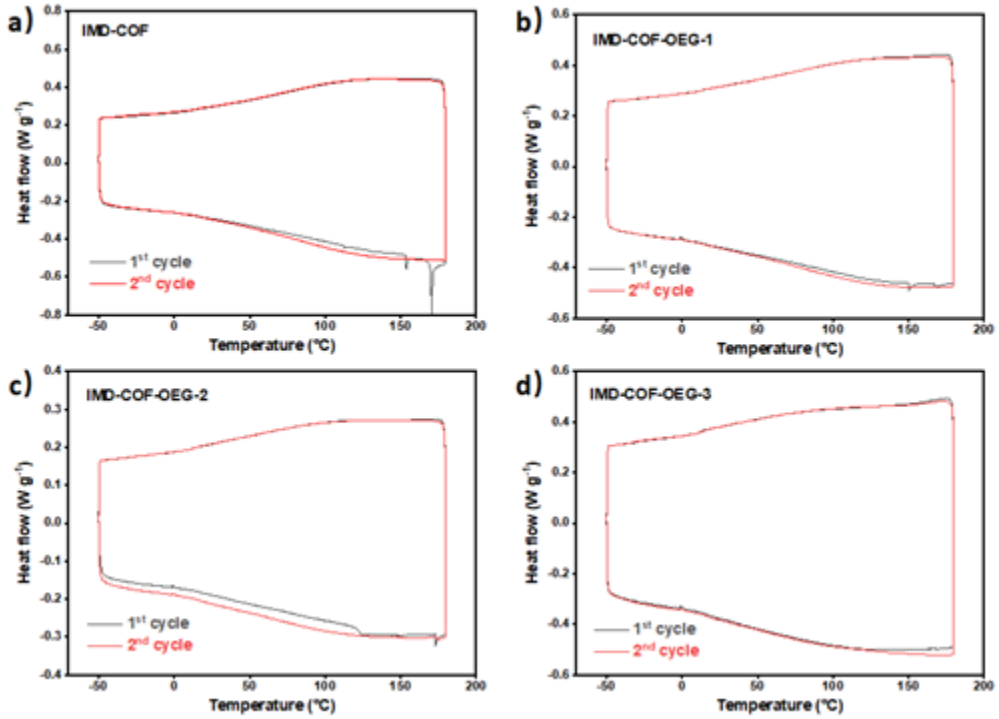

Figure 4.5.21. DSC profiles of (a) IMD-COF; (b) IMD-COF-OEG-1; (c) IMD-COF-OEG-2; (d) IMD-COF-OEG-3.

4.5.5 Characterization of Porous Properties and Gas Adsorption

The surface area and porosity of IMD-COF and IMD-COF-OEG-1~3 were measured by nitrogen adsorption-desorption analysis at 77 K (**Figure 4.5.22a**). The Brunauer-Emmett-Teller (BET) surface area of IMD-COF was calculated as 676 m^2 g^{-1} with a pore volume of 0.39 cm^3 g^{-1}. The pore size distributions were calculated using non-local density functional theory (NL-DFT) with a cylindrical pore model, showing pore size distributions for IMD-COF mainly centred at around 1.0 nm and 2.1 nm (**Figure 4.5.22b**), This is a small pore size among the reported COFs, providing a narrow channel for Li^+ transport while restricting the movement of cations. We also investigated the CO_2 and H_2 adsorption of IMD-COF, which might have benefited from the micropores. The CO_2 adsorption of IMD-COF were 1.1 and 1.8 mmol g^{-1} at 298 K and 273 K (**Figure 4.5.22c**), respectively and the H_2 adsorption of IMD-COF was 4.9 mmol g^{-1} at 77 K (**Figure 4.5.22d**).

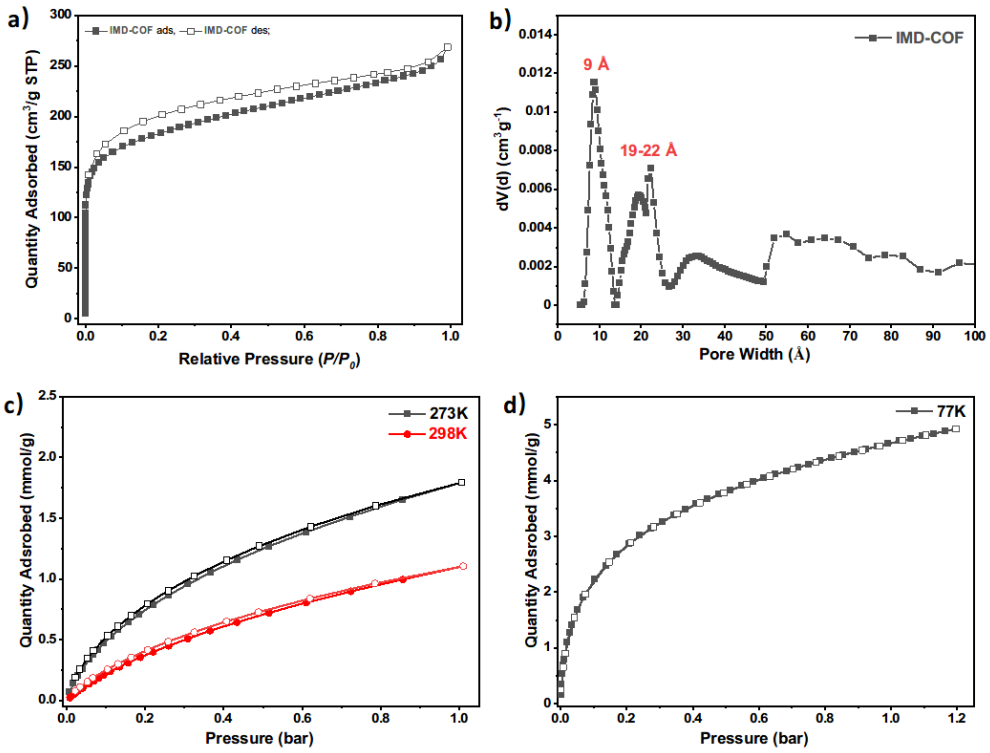

Figure 4.5.22. (a) N_2 adsorption and desorption isotherms of IMD-COF. (b) Pore size distribution of IMD-COF calculated by NLDFT method, mainly shown two pores at around 9 Å and 20 Å (Insert). The pores that possess size around 20 Å can match well with the PXRD pattern and the smaller pore that is around 9 Å could be attributed to the presence of bulky *t*-Bu groups. (c) CO_2 adsorption and desorption isotherms of IMD-COF at 273 K (black) and 298 K (red). (d) H_2 adsorption and desorption isotherms of IMD-COF at 77 K.

After post-modification, the BET surface area decreases dramatically to 114 m^2 g^{-1} for IMD-COF-OEG-1, 12 m^2 g^{-1} for IMD-COF-OEG-2 and 2 m^2 g^{-1} for IMD-COF-OEG-3 (**Figure 4.5.23**). The low BET surface area is not only from the ABC stacking of COF layers, but also from the more crowed pore environment caused by the longer OEG chains. Due to the non-porous property of IMD-COF-OEG-3, we proposed to use OEG-3 as the longest side chain in IMD-COF system. Such a high concentration of OEG chains should be beneficial for lithium conductivity.

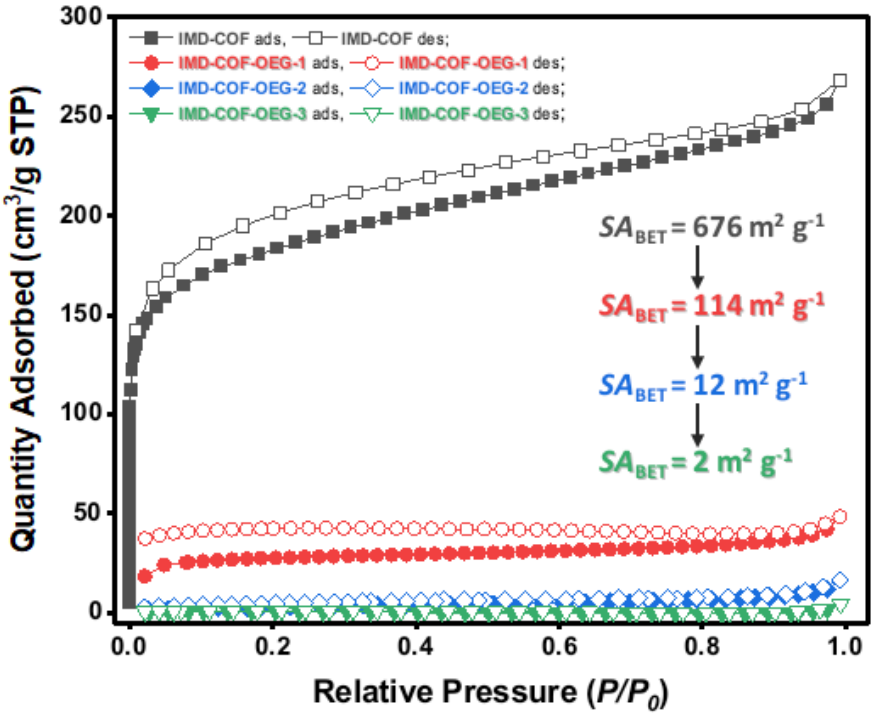

Figure 4.5.23. Nitrogen adsorption and desorption isotherms for IMD-COF (black), IMD-COF-OEG-1 (red), IMD-COF-OEG-2 (blue), IMD-COF-OEG-3 (green) recorded at 77 K (filled symbols= adsorption; open symbols= desorption).

4.5.6 Characterization of Lithium-Doping IMD-COF-OEG-x Solid-State Electrolytes

All of these results above indicate the unique properties of as-obtained IMD-COF-OEG-x that comes from our design principle and match our initial assumption about the underlying condition of the lithium-ion conductor. We then investigated the electrochemical tests of IMD-COF-OEG-x to evaluate their lithium-ion conductivity for potential applications as solid-state electrolyte materials. Firstly, all the IMD-COF-OEG-x were mixed with the 1 M $LiClO_4$ of MeOH solution in an [Li]: [O] ratio of 1:6 and stirred overnight, filtered, and washed with MeOH and dried under vacuum overnight to get Li-doped samples, namely, Li@IMD-COF-OEG-x SSE. Li@IMD-COF-PEG-8000 SSE was obtained by the same method. The FT-IR spectra was used to confirm the combination of $LiClO_4$ and IMD-COF-OEG-x (**Figure 4.5.24**).

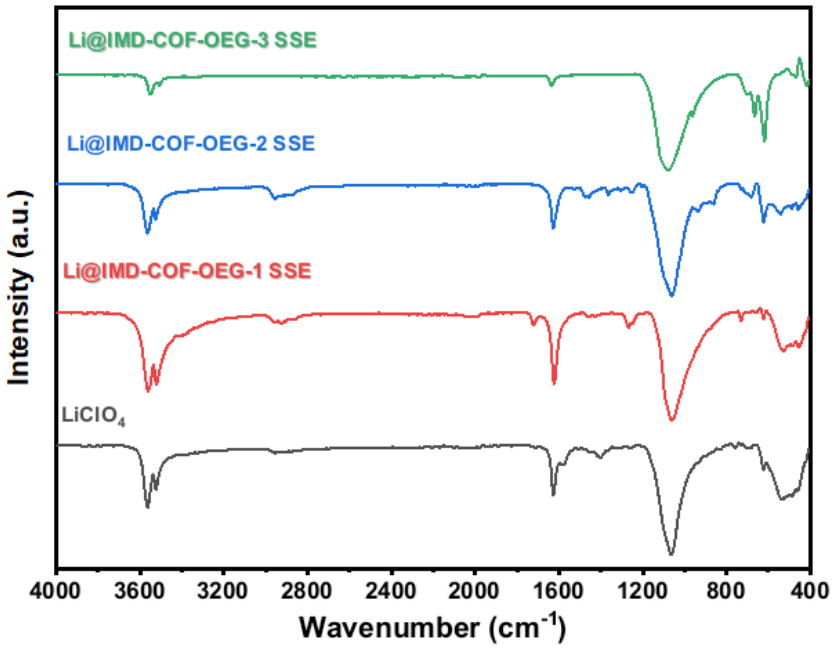

Figure 4.5.24. FT-IR spectra of LiClO4 (black) and Li@IMD-COF-OEG-x SSE: Li@IMD-COF-OEG-1 (red), Li@IMD-COF-OEG-1 (blue), Li@IMD-COF-OEG-3 (green).

Moreover, the PXRD patterns of Li@IMD-COF-OEG-x SSE are different from either IMD-COF-OEG-x or LiClO4, indicating a new formation of the uniform lithium-COF salts (**Figure 4.5.25**). These showed an irregular shape and surface of microspheres from SEM and TEM images, respectively (**Figure 4.5.26-4.5.27**). Also, the SEM and TEM images of Li@ IMD-COF/PEG-8000 SSE showed similar morphology (**Figure 4.5.28-4.5.29**).

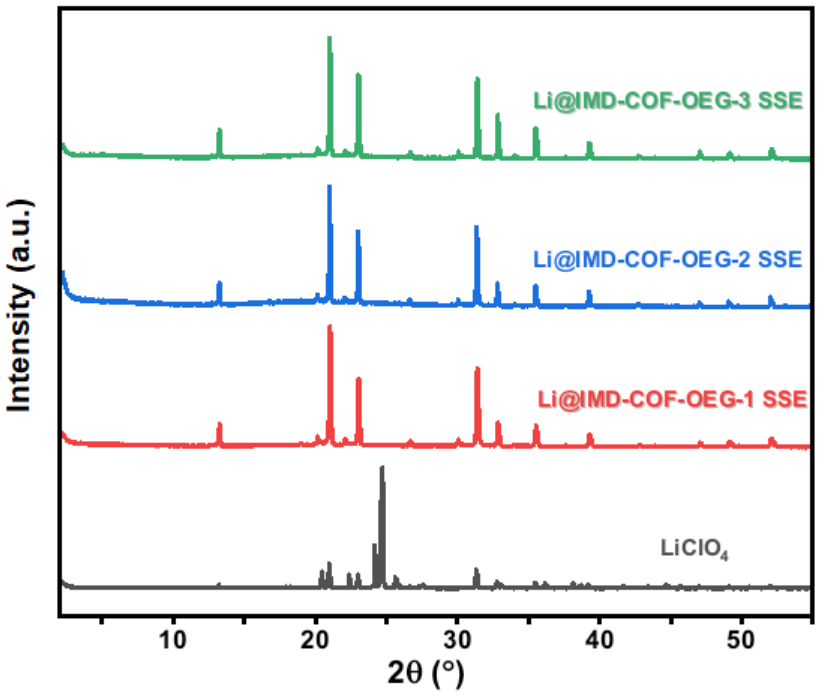

Figure 4.5.25. FT-IR spectra of LiClO4 (black) and Li@IMD-COF-OEG-x SSE: Li@IMD-COF-OEG-1 (red), Li@IMD-COF-OEG-1 (blue), Li@IMD-COF-OEG-3 (green).

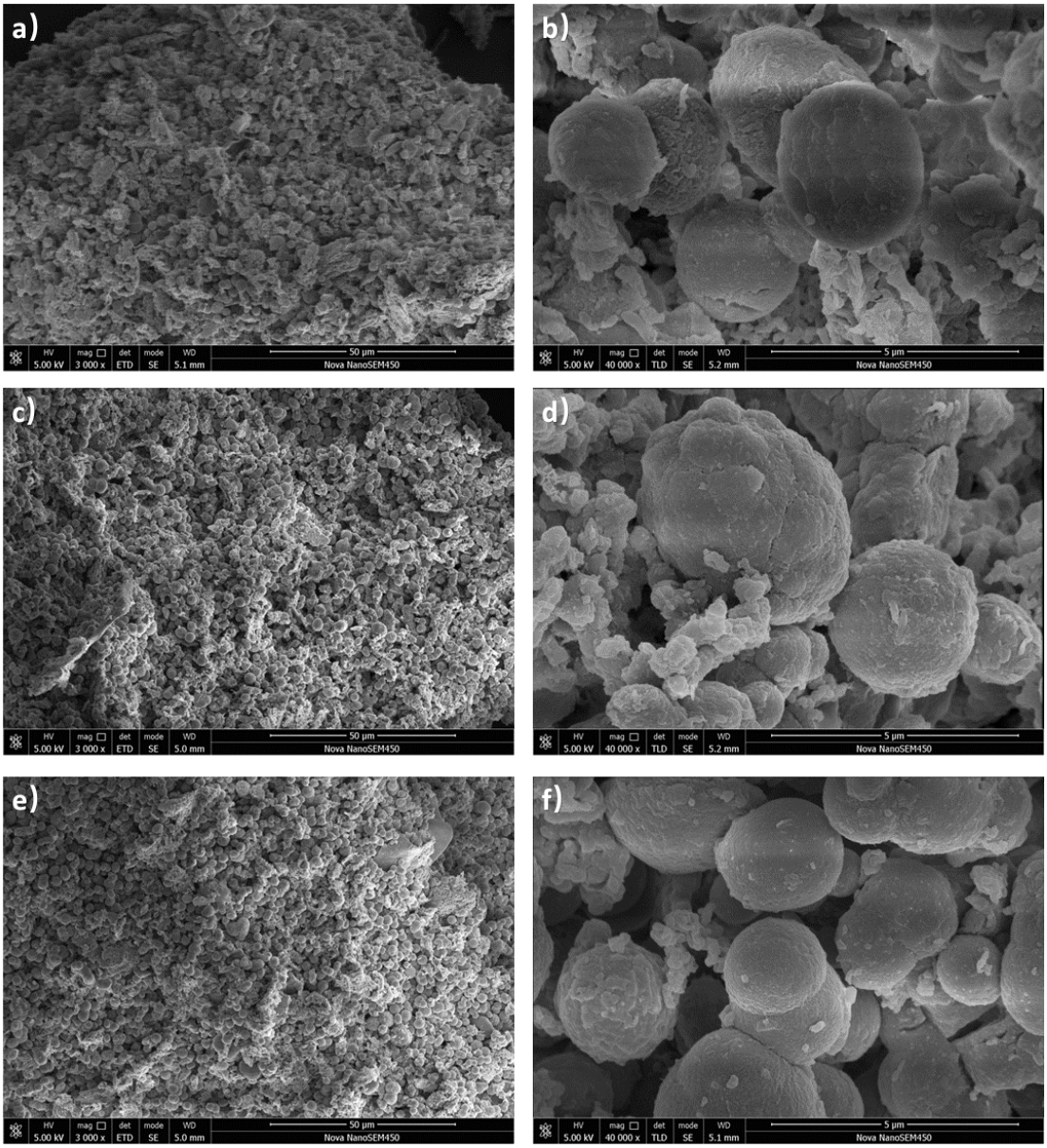

Figure 4.5.26. (a-b) SEM images of Li@IMD-COF-OEG-1, (c-d) SEM images of Li@IMD-COF-OEG-2, (e-f) SEM images of Li@IMD-COF-OEG-3.

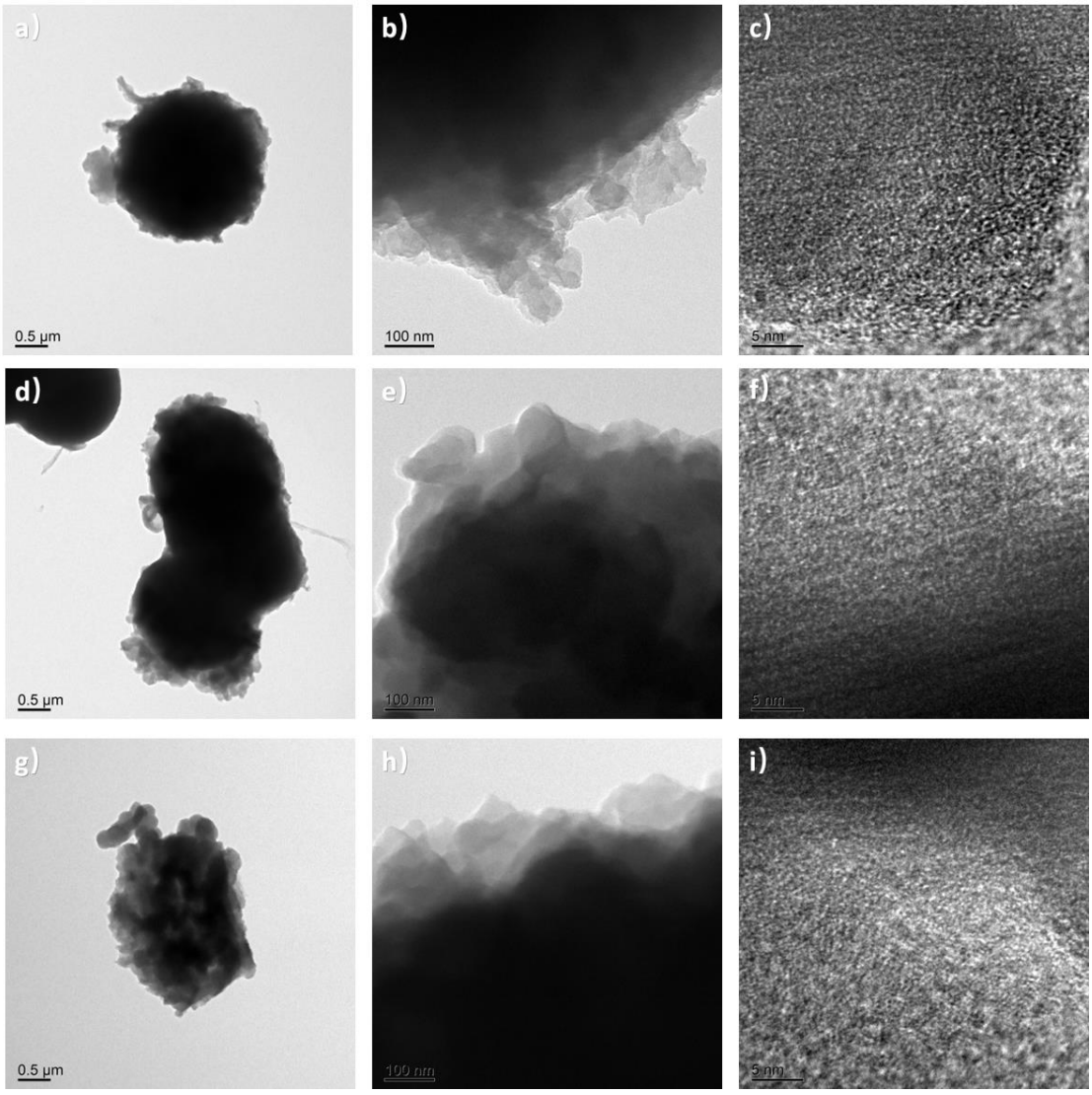

Figure 4.5.27. (a-c) TEM images of Li@IMD-COF-OEG-1, (d-f) TEM images of Li@IMD-COF-OEG-2, (g-i) TEM images of Li@IMD-COF-OEG-3.

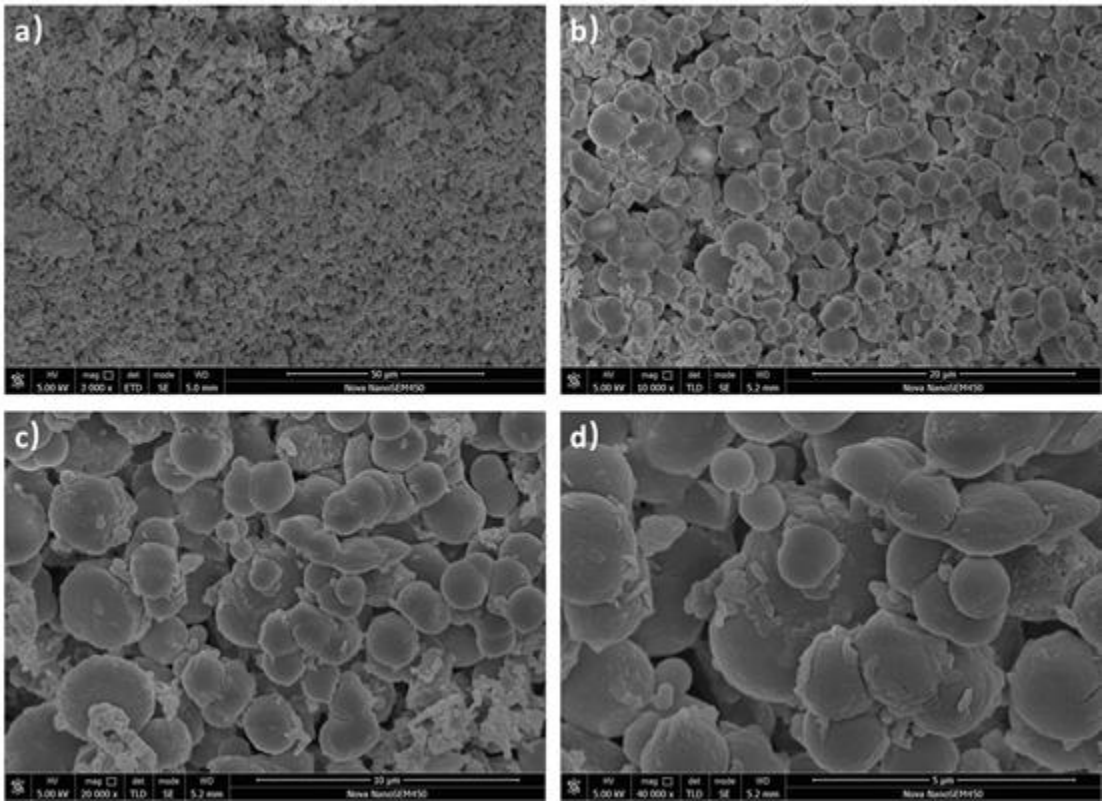

Figure 4.5.28. SEM images of Li@IMD-COF/ PEG-8000.

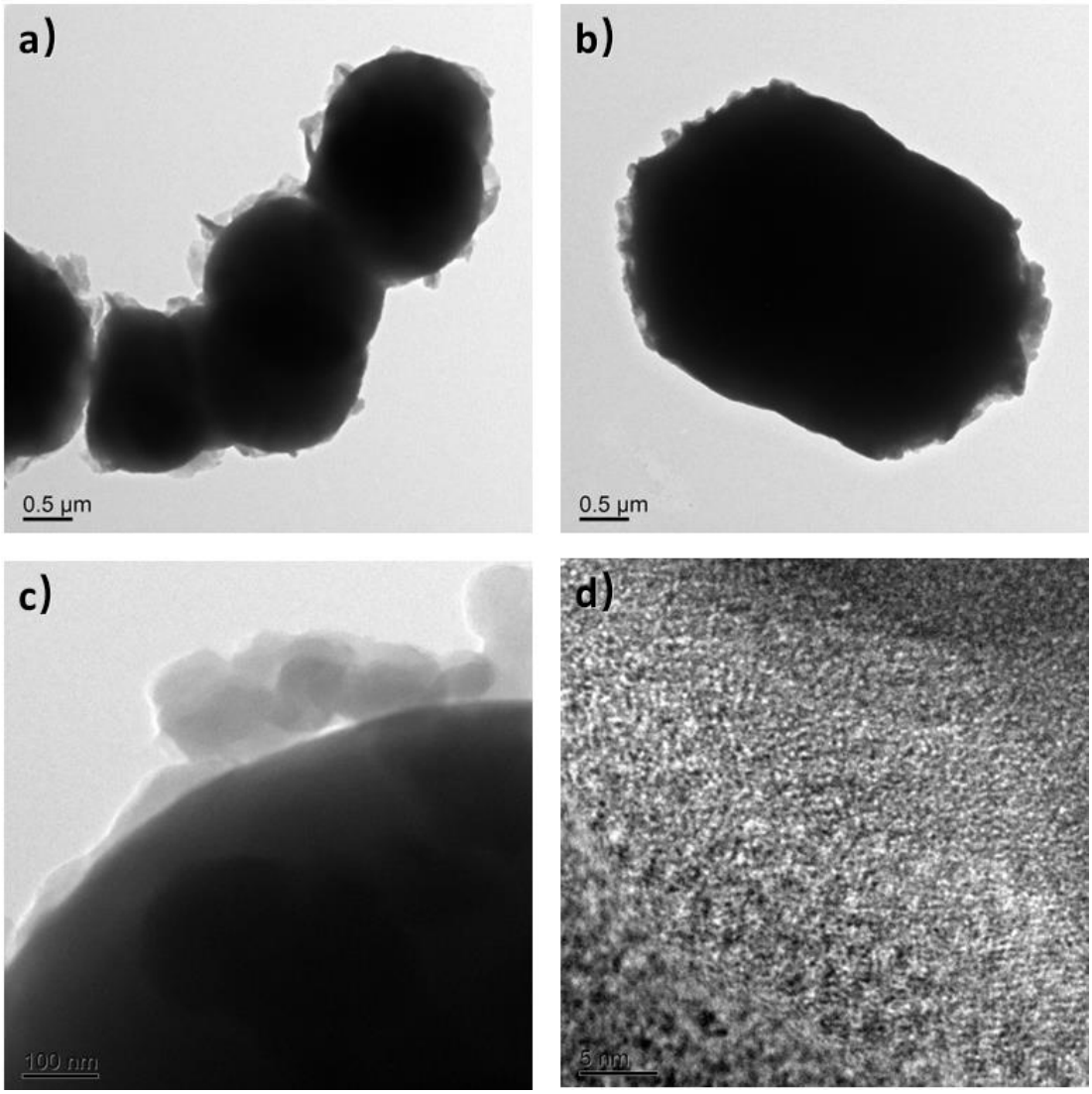

Figure 4.5.29. TEM images of Li@IMD-COF/ PEG-8000.

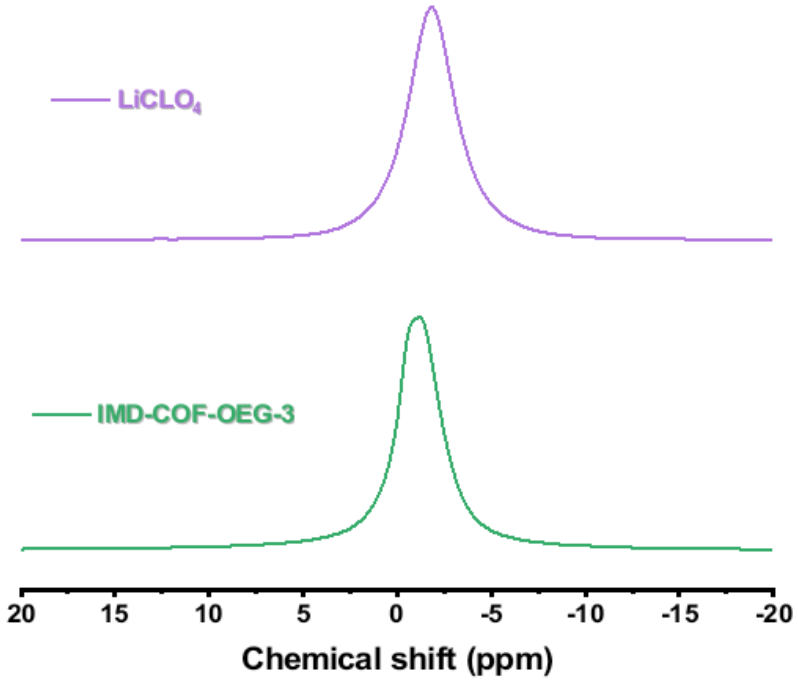

Figure 4.5.30. Solid-state ^{7}Li NMR spectra of $LiClO_4$ and IMD-COF-OEG-3.

Solid-state ^{7}Li NMR spectroscopy confirmed the dynamic behaviour of Li^+ in an OEG-grafted nanochannel within Li@IMD-COF-OEG-3 SSE. As shown in **Figure 4.5.30**, a broad peak of $LiClO_4$ can be observed due to the solid-state dipole-dipole and quadrupolar coupling between lithium sites. As the comparison, Li@IMD-COF-OEG-3 SSE shows a narrower peak with a down-field shift (0.6 ppm), implying the Li^+ species with significantly higher mobility inside. This mainly indicates the OEG-3 chains can promote the transport of Li-ions in the 1D nanochannels of IMD-COF.

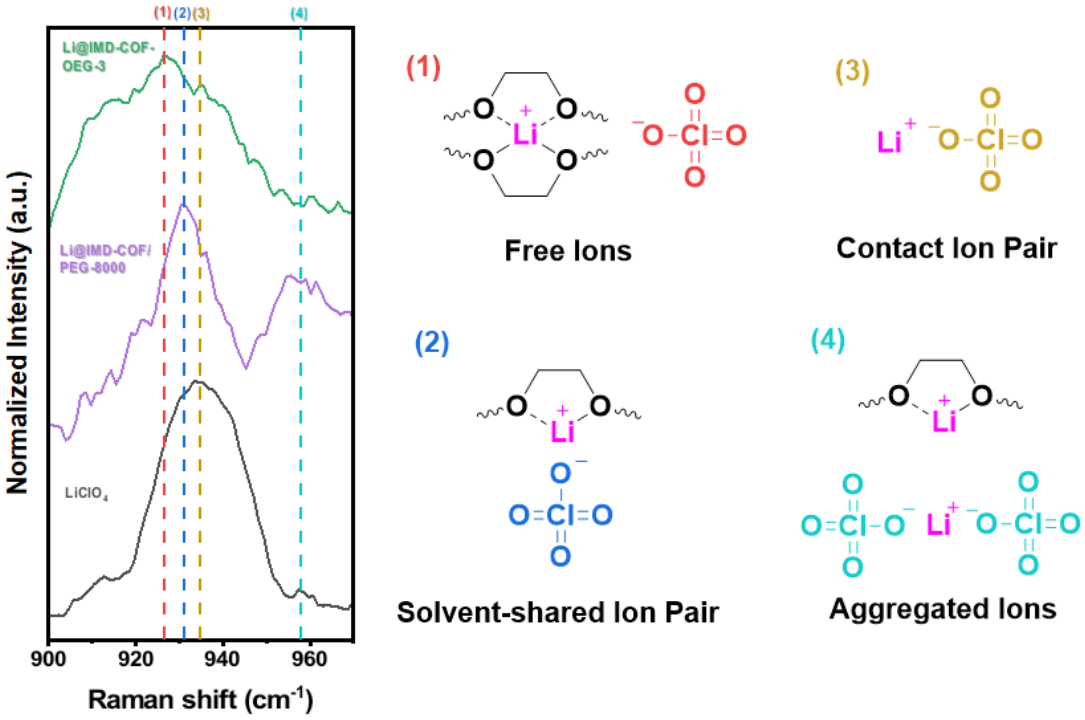

Figure 4.5.31. Raman spectra of $LiClO_4$ (black), Li@IMD/PEG-8000 (purple), Li@IMD-COF-OEG-3 (green) with the schematic of potential ion solvation structures.

The existence of perchlorate ions in different chemical environments was also observed by Raman spectra (**Figure 4.5.31**). Compared with contact ion pairs at 935 cm^{-1} of $LiClO_4$, Li@IMD-COF/PEG-8000 showed the aggregated ions at 958 cm^{-1} and solvent-shared ion pair at 931 cm^{-1} of ion pair (CIP), and free anions have distinct stretching frequencies at 927 cm^{-1} of Li@IMD-COF-OEG-3. This suggests that the Li^+ in IMD-COF-OEG-3 was well dissociated from the anions, which is beneficial for ionic conductivity.

4.5.7 Electrochemical Properties of Solid-State Electrolytes

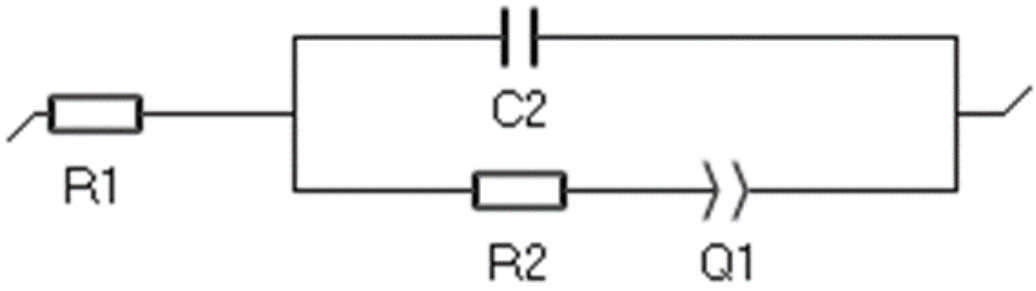

Figure 4.5.32. Equivalent circuit by *Z*-fit to fit the experimental Nyquist plots of IMD-COF-OEG-x, in which R_1 is bulk resistance, R_2 is charge-transfer resistance, C_2 is contact capacitance and Q_1 is constant phase element of double-layers.

The as-obtained samples were pressed into the solid pellets with propylene carbonate (PC) as the plasticizer, and subjected to electrochemical impedance spectroscopy (EIS) from 20 ℃ to 70 ℃ (**Figure 4.5.33-4.5.35**). The Nyquist plots of all the samples show typical curves with a semicircle in the high-frequency region and a linear tail in the low-frequency region, while the plots of IMD-COF-OEG-3 over 50 ℃ display steep spikes without the semicircles. This indicates the lowest resistance of IMD-COF-OEG-3 among all the samples. With the suitable model of equivalent circuit using a *Z*-fit method, the ion conductivity of all the samples can be calculated (**Figure 4.5.32**). With the increasing EGO chains, the Li-ion conductivity at 20 ℃ is improved from 5.63×10^{-6} S cm^{-1} of IMD-COF-OEG-1 to 2.60×10^{-5} S cm^{-1} of IMD-COF-OEG-2 and then 3.36×10^{-4} S cm^{-1} of IMD-COF-OEG-3. The performance was found to increase upon heating, affording a conductivity of 7.62×10^{-5} S cm^{-1} for IMD-COF-OEG-1, 3.31×10^{-4} S cm^{-1} for IMD-COF-OEG-2 and 4.55×10^{-3} S cm^{-1} for IMD-COF-OEG-3 at 70 ℃, respectively (**Figure 4.5.36**).

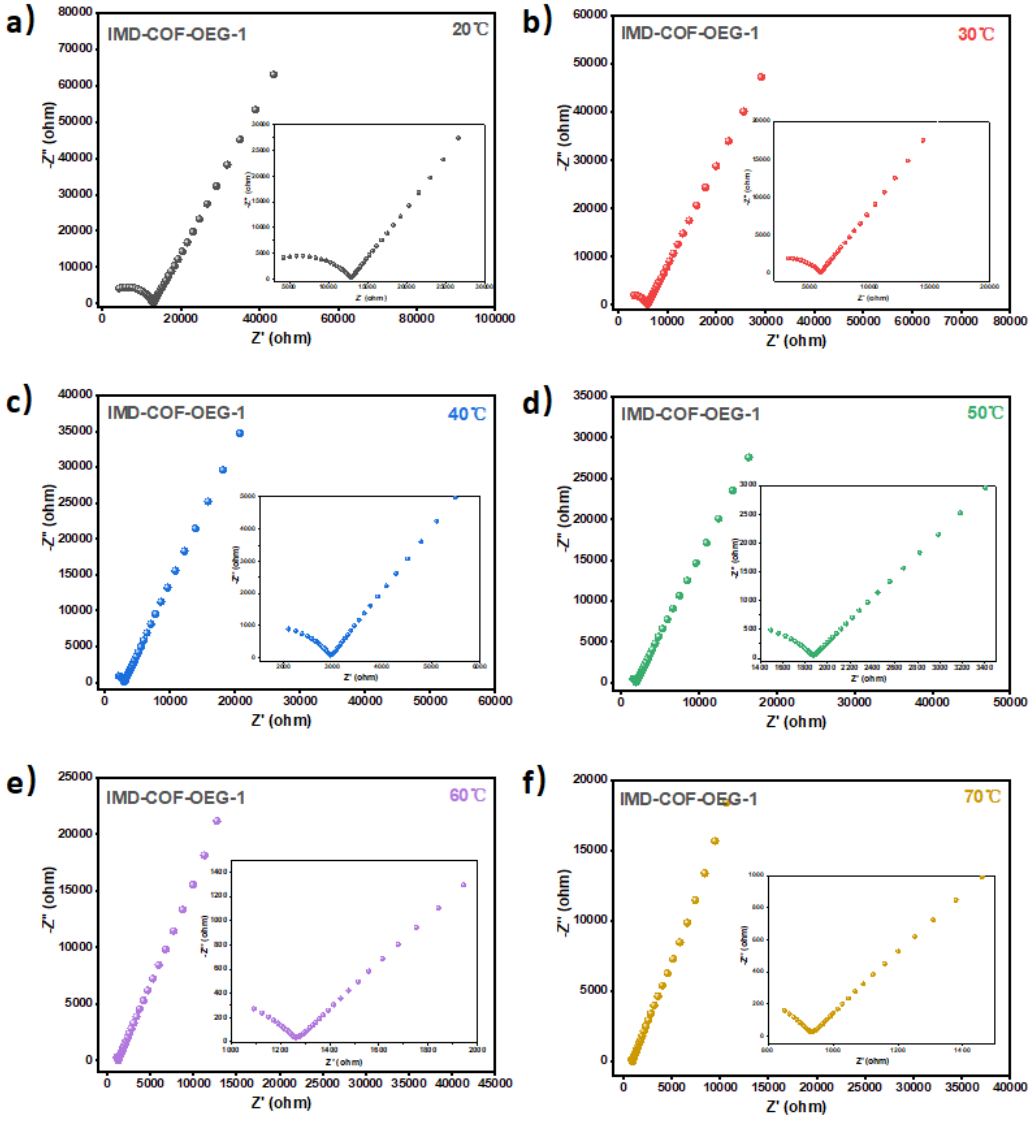

Figure 4.5.33. Nyquist plots of IMD-COF-OEG-1 obtained from variable temperature EIS measurements at (a) 20 °C, (b) 30 °C, (c) 40°C, (d) 50 °C, (e) 60°C, and (f) 70°C, insert is the enlarge of the high-frequency region.

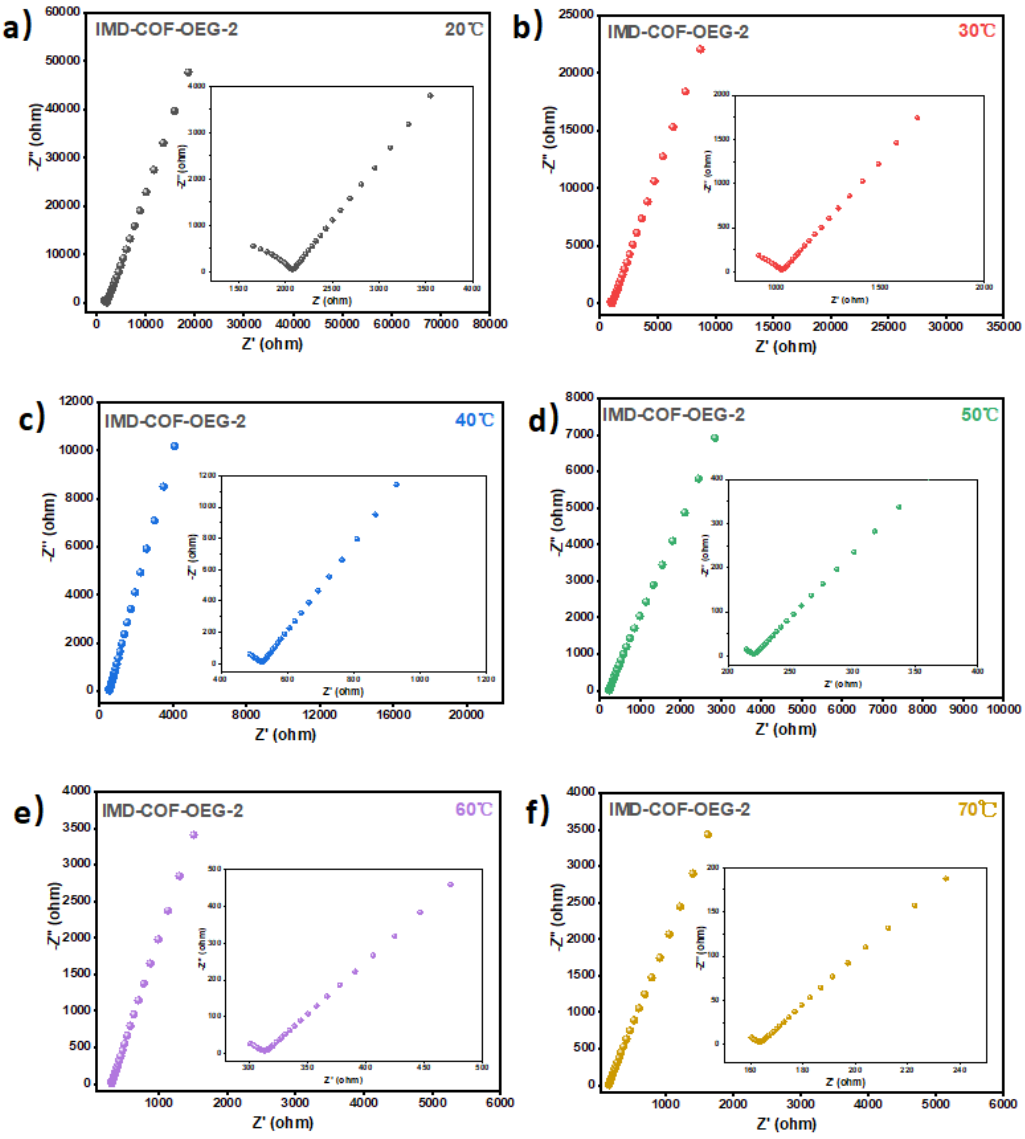

Figure 4.5.34. Nyquist plots of IMD-COF-OEG-2 obtained from variable temperature EIS measurements at (a) 20 °C, (b) 30 °C, (c) 40°C, (d) 50 °C, (e) 60°C, and (f) 70°C, insert is the enlarge of the high-frequency region.

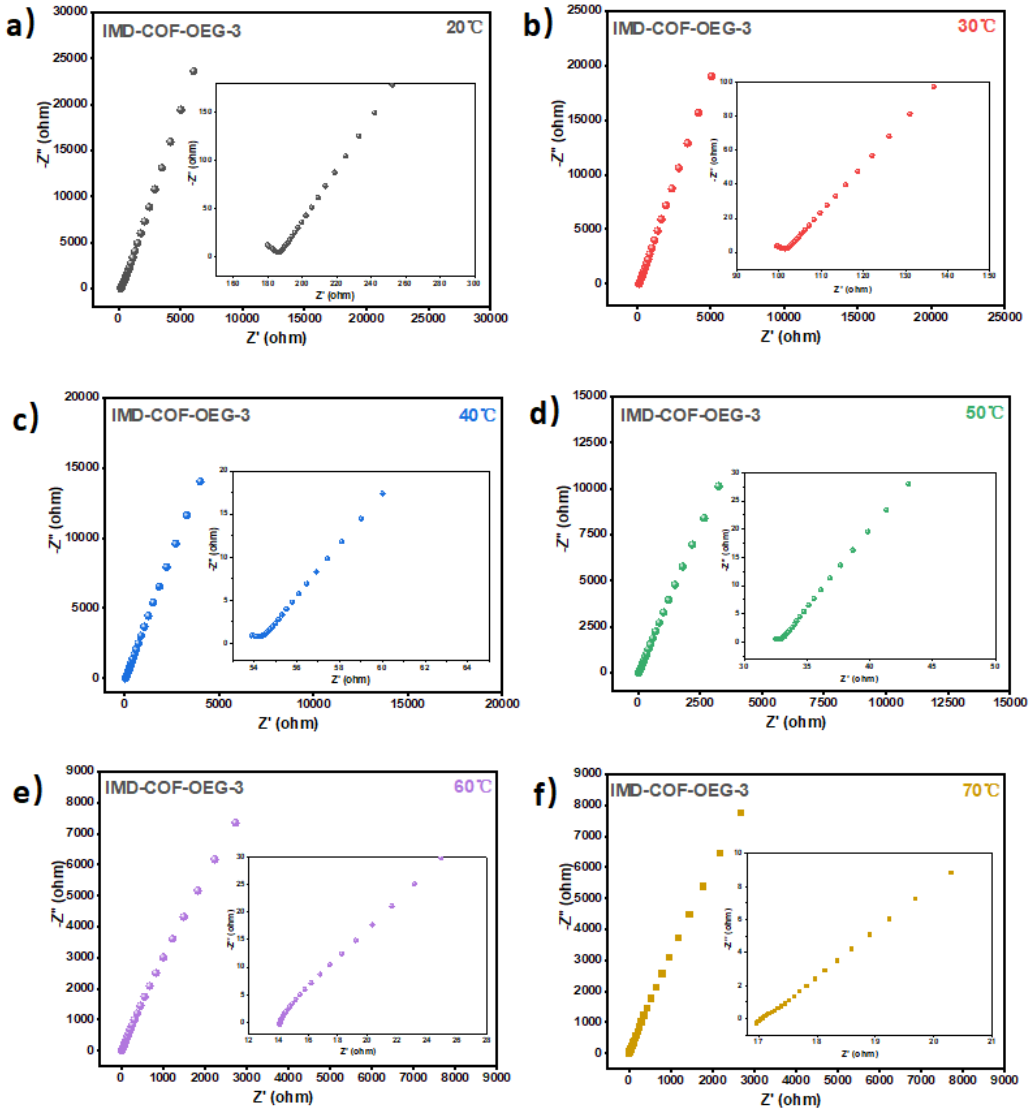

Figure 4.5.35. Nyquist plots of IMD-COF-OEG-3 obtained from variable temperature EIS measurements at (a) 20 °C, (b) 30 °C, (c) 40°C, (d) 50 °C, (e) 60°C, and (f) 70°C, insert is the enlarge of the high-frequency region.

As control experiments, pure IMD-COF and the composite (IMD-COF/PEG-8000) made by the physical mixing of IMD-COF and PEG-8000 (polyethylene glycol with a molecular weight of 8000) were used for the same doping, pelletization and measurement as well. Consequently, IMD-COF and IMD-COF-PEG-8000 exhibit the Li-ion conductivity of 2.33×10^{-6} S cm^{-1} and 4.69×10^{-6} S cm^{-1} at 20 ℃, respectively, indicating both OEG chains and IMD-COF network play crucial roles in the fast Li-ion transport (**Figure 4.5.37**).

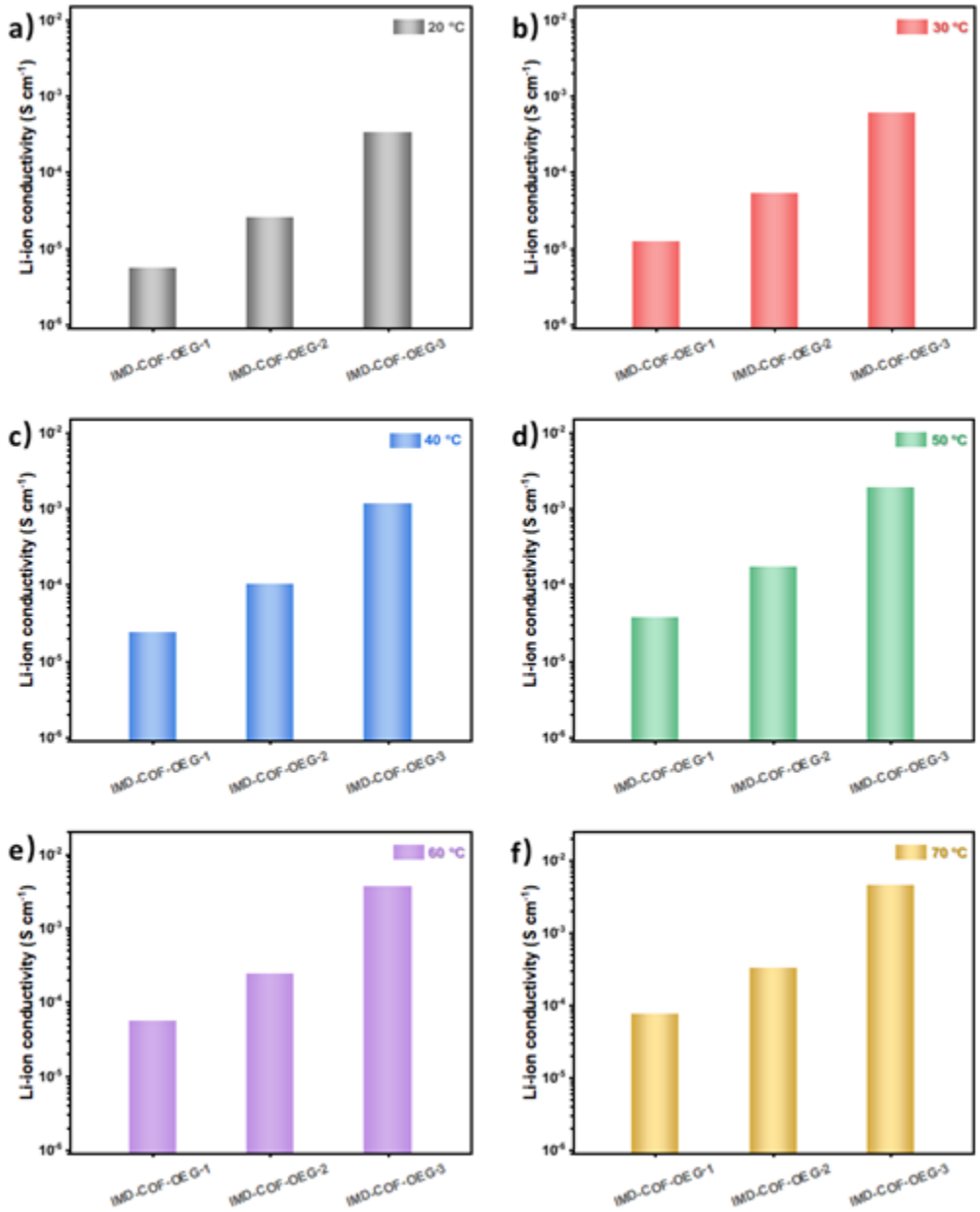

Figure 4.5.36. Comparisons of Li-ion conductivity as a function of temperature within IMD-COF-OEG-x studied: (a) 20 °C, (b) 30 °C, (c) 40 °C, (d) 50 °C, (e) 60 °C, (f) 70 °C.

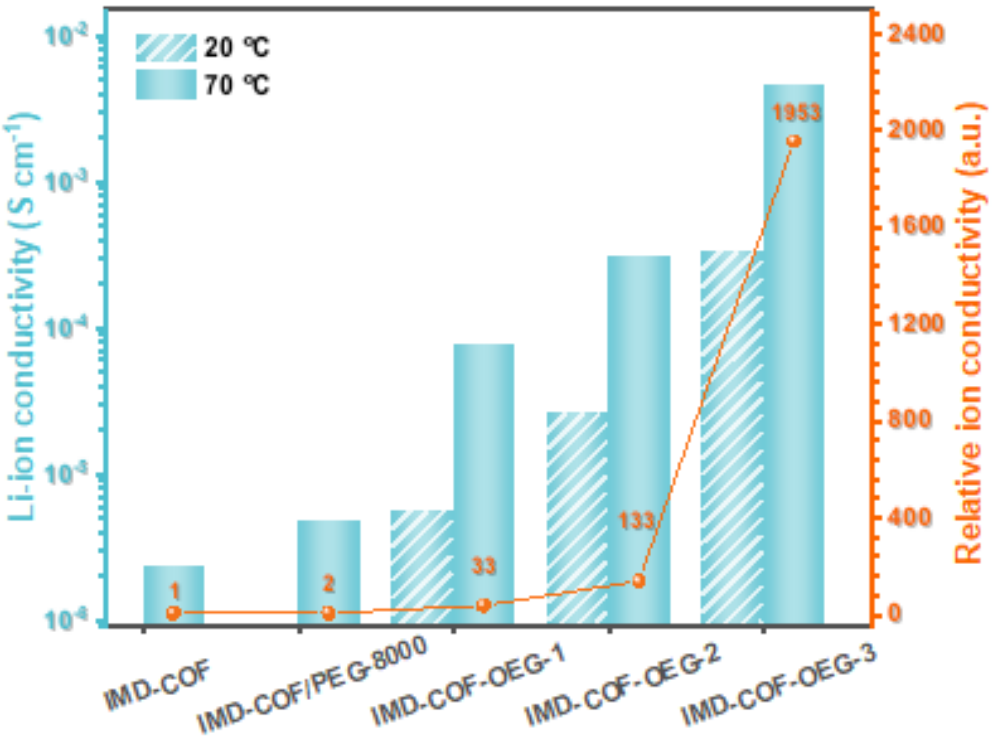

Figure 4.5.37. Comparison of the ion conductivity of IMD-COF, IMD-COF-PEG-8000 and IMD-COF-OEG-x.

As the comparison, the performance of pure PEO materials was test. The Arrhenius plots of PEO-based materials shows an activation energy of 0.435 eV at high temperature, however, a following mutation point appears at the T_g of PEO due to the phase transfer of PEO-base electrolytes, which causes the low ionic conductivity (**Figure 4.5.38**). The Arrhenius plots of all the IMD-COF-OEG-x exhibit a linear sloping profile with a low activation energy for ion hopping of 0.45 eV, which illustrates the efficient prevention of crystallization of OEG chains by anchoring into the pores of IMD-COF, implying a fast ion conduction pathway introduced by the OEG chains (**Figure 4.5.39-4.5.41**).[21]

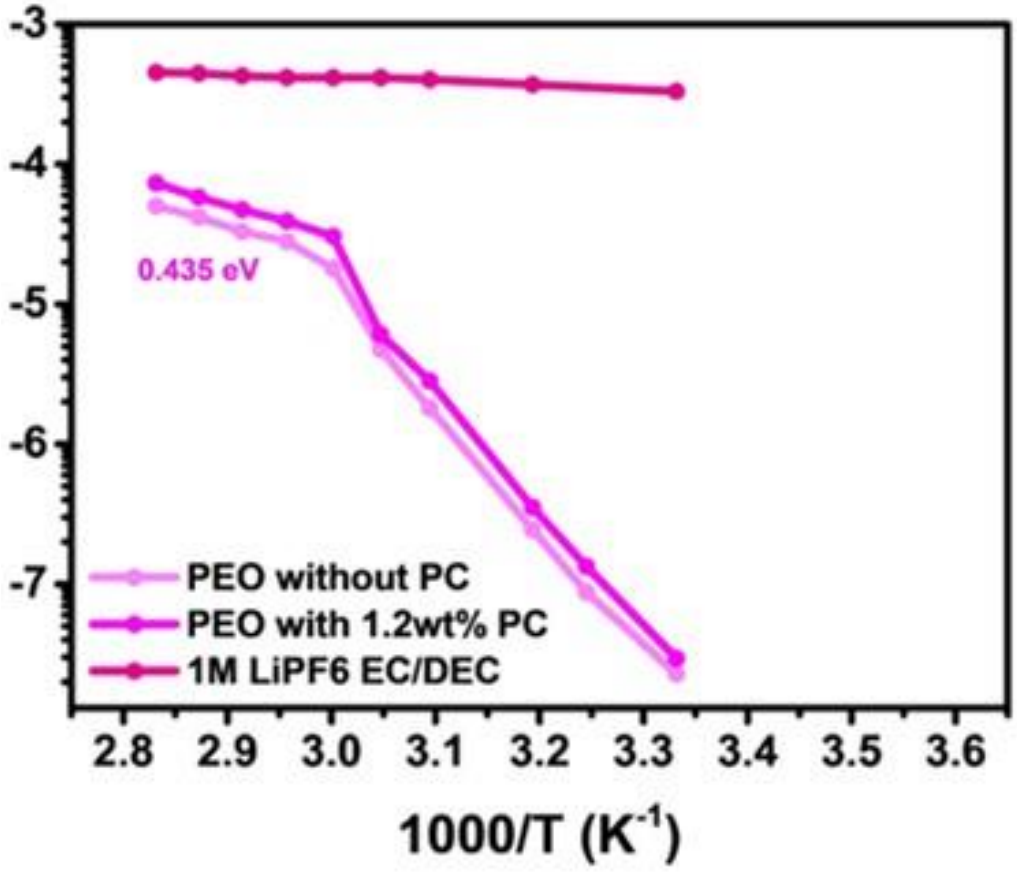

Figure 4.5.38. Arrhenius behaviour of PEO, PEO with PC and $LiPF_6$ as conductivity increased with temperature. (This figure is reprinted from ref. 31).

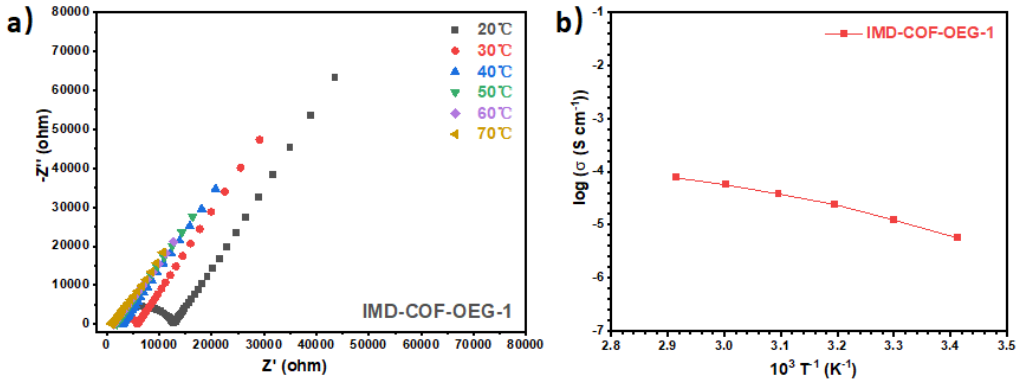

Figure 4.5.39. a) Overlaid Nyquist plots of IMD-COF-OEG-1 obtained from variable temperature EIS highlighting. b) Arrhenius behaviour of IMD-COF-OEG-1 as conductivity increased with temperature.

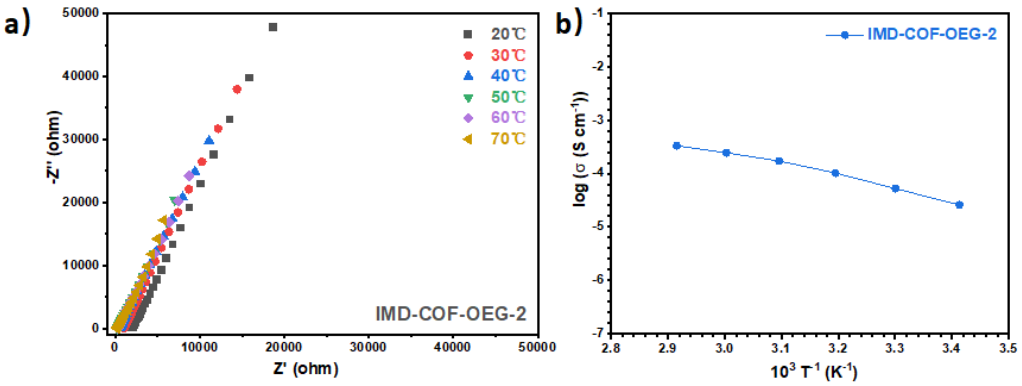

Figure 4.5.40. a) Overlaid Nyquist plots of IMD-COF-OEG-2 obtained from variable temperature EIS highlighting. b) Arrhenius behaviour of IMD-COF-OEG-2 as conductivity increased with temperature.

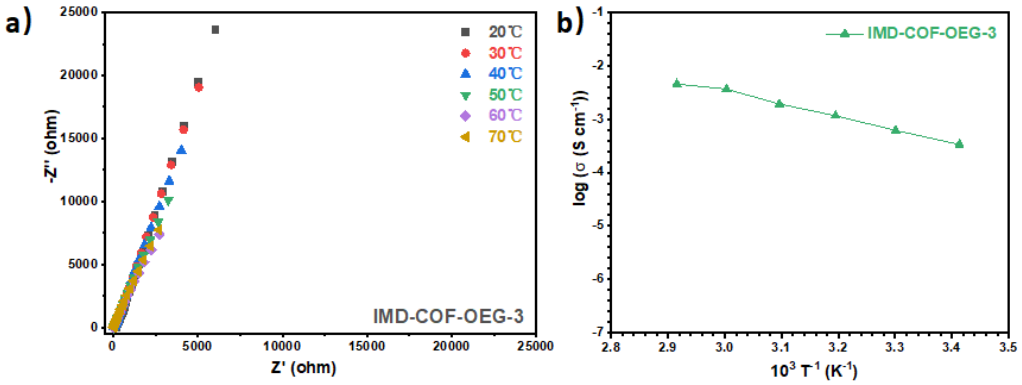

Figure 4.5.41. a) Overlaid Nyquist plots of IMD-COF-OEG-3 obtained from variable temperature EIS highlighting. b) Arrhenius behaviour of IMD-COF-OEG-3 as conductivity increased with temperature.

Among all the Debye plots, IMD-COF-OEG-3 has the peak appearing with the highest frequency, indicating the fastest relaxation process due to the longer OEG chains (**Figure 4.5.42b**).[38]

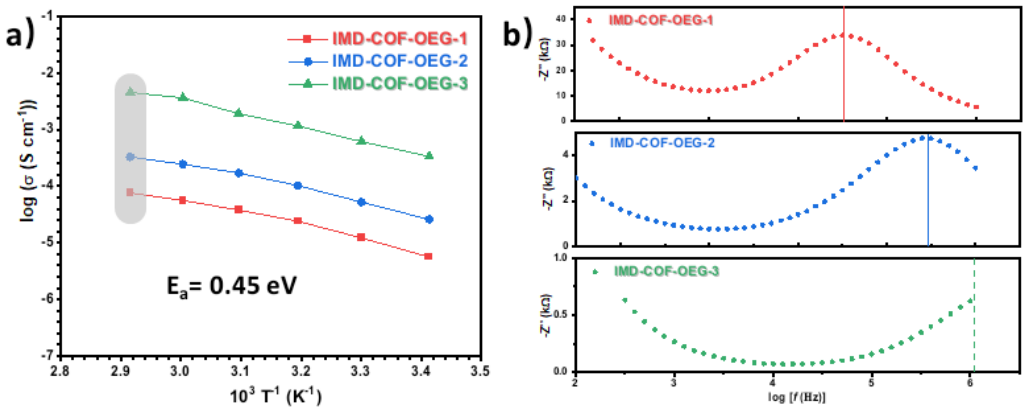

Figure 4.5.42. a) Arrhenius plot of ionic conductivity as a function of temperature: IMD-COF-OEG-1 (red), IMD-COF-OEG-2 (blue), IMD-COF-OEG-3 (green). b) Representative Debye plots of imaginary impedance as a function of log *f*: IMD-COF-OEG-1 (red), IMD-COF-OEG-2 (blue), IMD-COF-OEG-3 (green).

Having identified IMD-COF-OEG-3 as the best Li-ion conductor among all the IMD-COF-x, we then constructed both asymmetric and symmetric cells for the further tests. DC polarization and AC impedance measurement in a Li | IMD-COF-OEG-3| Li symmetric cell was taken to evaluate the contribution of lithium ions in the whole ion migration fraction. By BE method, the average lithium transference number of IMD-COF-OEG-3 was determined to be 0.83 at 20 ℃, which is a high value for suggesting that IMD-COF-OEG-3 is conductive for lithium cations rather than the anion (**Figure 4.5.43**).

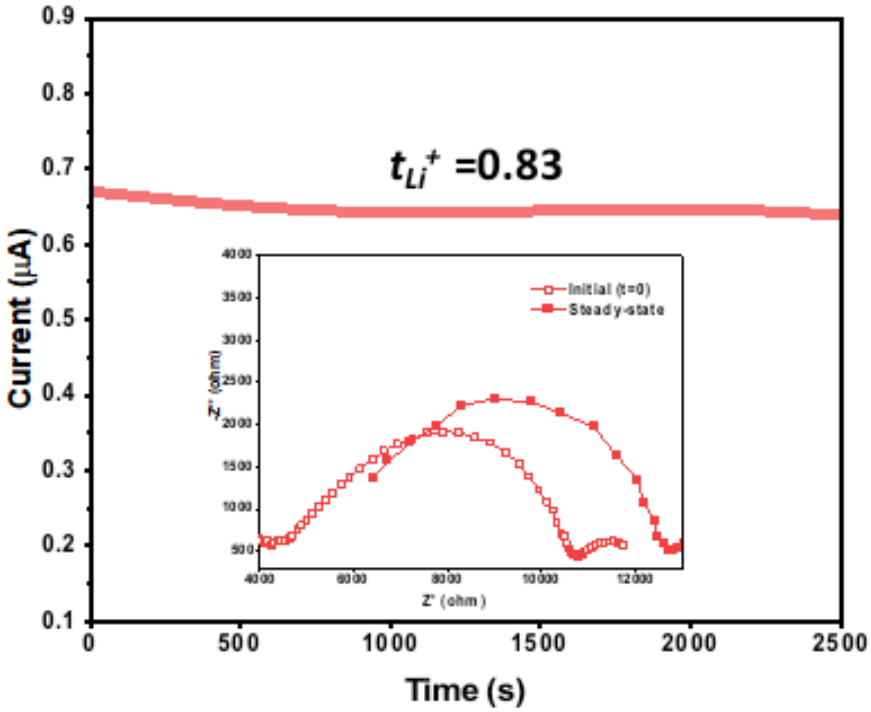

Figure 4.5.43. Lithium transference number of IMD-COF-OEG-3 calculated using the Bruce-Vincent-Evans technique.

From the Li-ion conductivity (σ) and Li^+ transference number at near room temperature, IMD-COF-OEG-3 showed a better comprehensive performance than many state-of-the-art COF-based SSEs (**Figure. 4.5.44** and **Table. 4.5.7**).[16, 18, 21, 22, 30, 38-45]

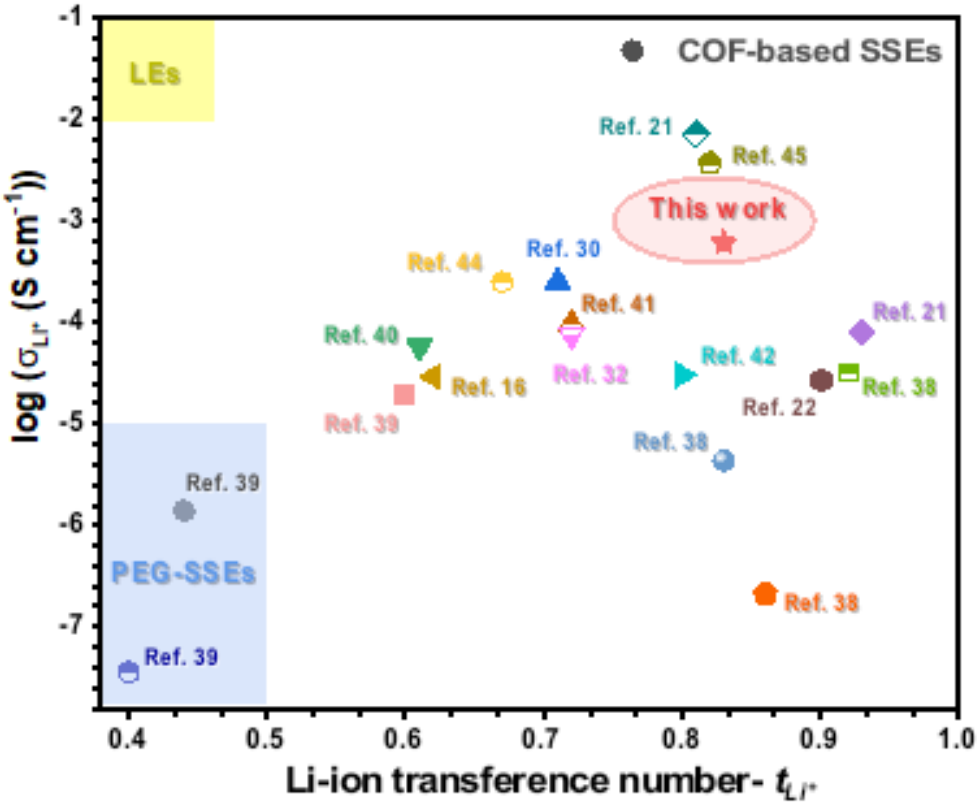

Figure 4.5.44. Comparison of the Li-ion conductivity (σ) and Li^+ transference number (t^+) at near room temperature with those COF-based SSEs reported in the literature.

Table 4.5.7. Comparison of the major performances of IMD-COF-OEG-x with other inorganic electrolytes and COF-based Li^+ SSEs

Description			σ_{Li}[a]	E_a	t_{Li+}	EW[b]	Ref.
Materials	Li salt	Plasticizer	(S cm^{-1})	(eV)		(V)	
$LiClO_4$@COF-5	$LiClO_4$	/	2.6×10^{-4}	0.037	/	/	**[4]**
PEG-Li^+@COF-300	$LiClO_4$	/	1.40×10^{-6}	0.20	0.44	/	**[5]**
Li^+@TPB-BMTP-COF	$LiClO_4$	/	6.04×10^{-6}	0.87	/	/	**[6]**
Li^+@$[TEO]_{0.5}$-TPB-DMTP-COF	$LiClO_4$	/	1.31×10^{-5}	0.68	/	/	**[7]**
COF-PEO-9-Li	LiTFSI	/	~1.0×10^{-6}	/	/	5.2	**[8]**
PEG-Li^+@EB-COF-ClO_4	$LiClO_4$	/	1.93×10^{-5}	0.21	0.60	/	**[5]**
PVDF/H-COF-1@10	$LiClO_4$	/	2.5×10^{-4}	/	0.71	4.3	**[9]**

Li-CON-TFSI	LiTFSI	/	5.74×10^{-5}	0.34	0.61	3.8	**[10]**
dCOF-ImTFSI-60@Li	LiTFSI	/	9.74×10^{-5}	0.28	0.72	5.3	**[11]**
Im-COF-TFSI@Li	LiTFSI	/	2.92×10^{-5}	0.32	0.62	4.2	**[12]**
ICOF-2	/	55% wt. PC	3.05×10^{-5}	0.24	0.80	4.5	**[13]**
$LiPF_6$-EC-DMC@CD-COF-Li	$LiPF_6$	EC+DMC (v/v = 1:1)	2.7×10^{-3}	0.26	/	/	**[14]**
H-Li-ImCOF			5.3×10^{-3}	0.12	0.88		
CH_3-Li-ImCOF	/	20% wt. PC	8.0×10^{-5}	0.27	0.93	4.5	**[15]**
CF_3-Li-ImCOF			7.2×10^{-3}	0.10	0.81		
TpPa-SO_3Li	/	/	2.7×10^{-5}	0.18	0.90	4.0	**[16]**
Tp-PaSO_3Li-COF	/	EC+DMC (v/v = 1:1)	1.6×10^{-3}	0.13	0.94	/	**[17]**
LiCON-1	/	/	2.13×10^{-7}	0.25	0.86	4.2	**[18]**
LiCON-2			4.36×10^{-6}	0.22	0.83	3.8	
LiCON-3			3.21×10^{-5}	0.13	0.92	4.3	
Ge-COF-1	$LiPF_6$	EC+DEC (v/v = 1:1)	1.1×10^{-6}	0.26	/	/	**[19]**
EC/DEC@Ge-COF-1			1.6×10^{-5}	0.24	/		
$LiPF_6$@Ge-COF-1			2.5×10^{-4}	0.29	0.67		
EC/DEC@ACOF	$LiPF_6$	EC+DEC (v/v = 1:1)	1.3×10^{-4}	0.15	/	/	**[20]**
LE@ACOF			3.7×10^{-3}		0.82		
Q-COF	LiTFSI	/	7.5×10^{-5}	0.15	0.72	5.6	**[21]**
Li_6PS_5Cl	/	/	4.6×10^{-4}	0.33	1.00	/	**[22]**
$Li_{10}GeP_2S_{12}$	/	/	1.2×10^{-2}	0.25	1.00	/	**[23]**
$Li_7P_3S_{11}$	/	/	4.1×10^{-3}	0.15	1.00	/	**[24]**
MIT-20-LiCl	/	~70 wt % PC	1.31×10^{-5}	0.32	0.66	/	**[25]**
IMD-COF-OEG-3	**$LiClO_4$**	**~20 wt % PC**	**3.36×10^{-4}**	**0.45**	**0.83**	**5.1**	**This work**

σ_{Li}[a], the ionic conductivity near room temperature. EW[c] represent the electrochemical window of different COF-based SSEs

Linear sweep voltammetry (LSV) of the Li | IMD-COF-OEG-3 SSE| stainless steel asymmetric cell shows an electrochemical stability up to 5.1 V versus Li/Li^+ (**Figure 4.5.45a**), which can also be further confirmed by the electrochemical stability windows in the range of 2-5 V versus Li/Li^+ observed from cyclic voltammetry (CV) curve (**Figure 4.5.45b**).[31] A potentiostatic hold experiment was also carried out to evaluate the oxidative stability of IMD-COF-OEG-3 (**Figure 4.5.45c**).[32] The current density of IMD-COF-OEG-3 remained low at the voltage below 4.8 V while it increased dramatically when the voltage was up to 5.2 V, proving a similar result with CV and LSV tests.

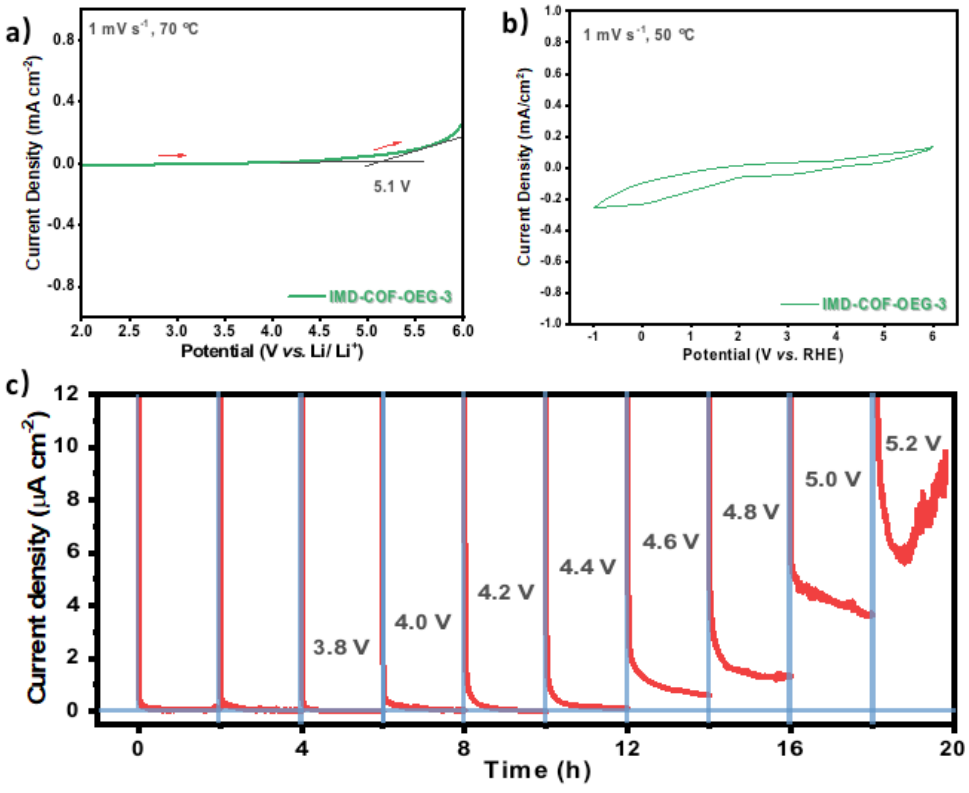

Figure 4.5.45. a) LSV curves of IMD-COF-OEG-3 SSE at 1 mV s^{-1} under 50 ºC. b) Cyclic voltammogram of the Stainless steel/ IMD-COF-OEG-3 SSE/ Li cell at the scan rate of 50 mV S^{-1} under 50 ℃. c) Potentiostatic hold tests of the IMD-COF-OEG-3 SSE for 2 h at different voltages at 50 ºC.

Furthermore, a long-term reversibility of Li plating-stripping cycling based on IMD-COF-OEG-3 was investigated in the symmetric cells. As shown in **Figure 4.5.46a**, IMD-COF-OEG-3 demonstrated a stable behaviour without an appreciable increase and an irreversible fluctuation of over-potential during the cycling at the current density of 0.05 mA cm^{-2} over 560 h under 35 °C.[31] Also, the inset figures of the enlarged voltage profiles of 100-150, 250-300, and 400-450 h display a relatively steady voltage hysteresis, demonstrating the effectiveness of IMD-COF-OEG-3 in preventing lithium dendrite growth (**Figure 4.5.46b-d**).

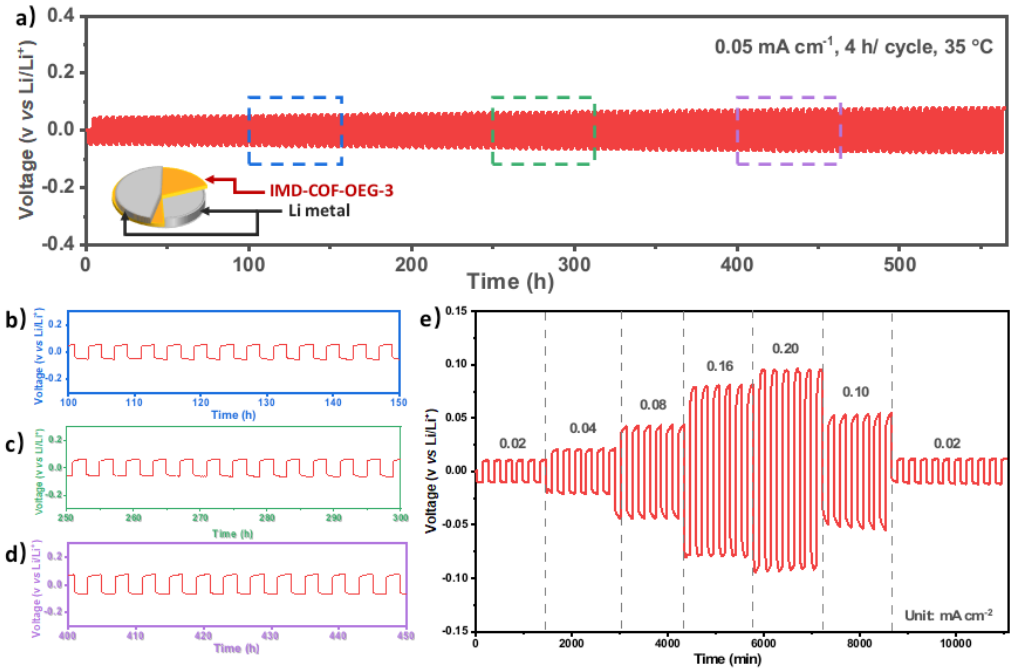

Figure 4.5.46. a) Long-term Li plating-stripping cycles of IMD-COF-OEG-3 SSE based symmetrical lithium metal cell. Magnified view of the Li plating-stripping test between 100-150 h (b), 250-300 h (c) and 400-450 h (d), highlighted by the blue, green, purple box in (a), respectively. e) Rate performance of symmetric Li-metal battery with a current density from 0.02 to 0.20 mA cm^{-2}.

The rate performance of the symmetric cell at different current densities was shown by the time-dependent voltage profile (**Figure 4.5.46e**).[46] Small polarization potentials of 11, 21, 43, 79, 96, and 52 mV are observed for 0.02, 0.04, 0.08, 0.16, 0.20 and 0.10 mA cm^{-2}, respectively, and when the current density was modified back to 0.02 mA cm^{-2}, the polarization potential still kept the same value as what it was as before (11 mV).

This indicates good interfacial compatibility of IMD-COF-OEG-3 with lithium metal electrodes.

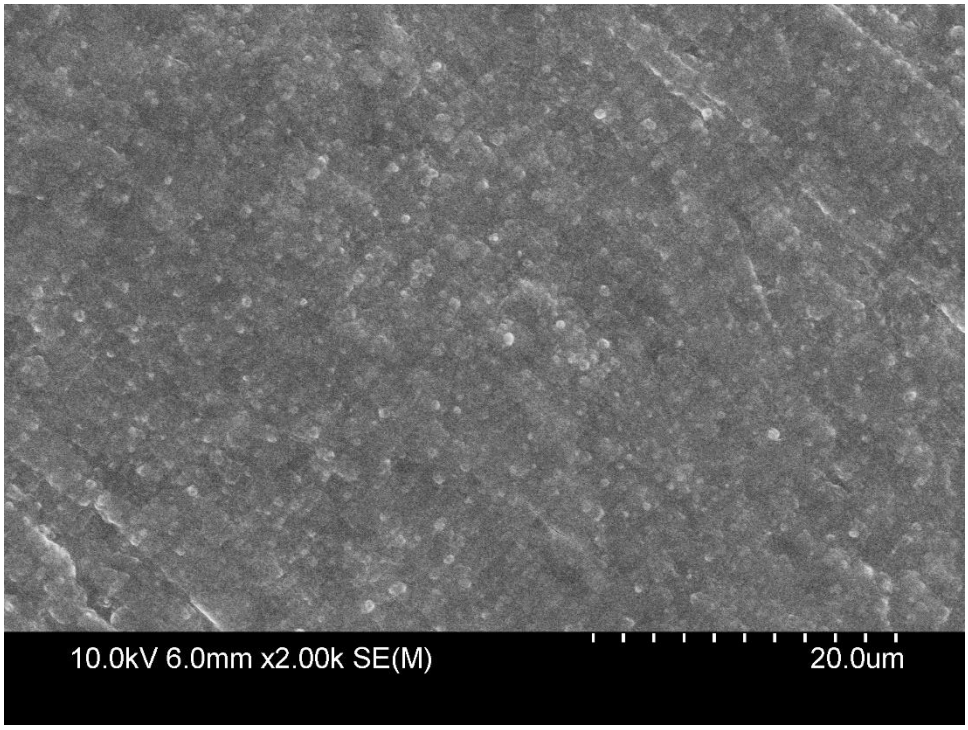

Figure 4.5.47. Smooth surface of the Li metal electrode after the cycling test.

The clean and smooth surface of Li metal electrode after cycling was confirmed by SEM (**Figure 4.5.47**), implying the homogeneous Li-ion migration through IMD-COF-OEG-3 SSE. All the test results shown above demonstrate the promising potential of IMD-COF-OEG-3 as a solid-state electrolyte for Li-ion batteries.

4.6 Conclusions

In a conclusion, we have rationally designed robust oligo-ethylene glycol-anchored Imidazole-linked COFs with three different degrees of OEG chains for emergent lithium-ion conduction. A change of the stacking model from AA to ABC can be observed after the post-modification reaction of IMD-COF. As a design principle, the advantages of these oligo-ethylene glycol-anchored IMD-COFs as solid-state electrolytes for lithium-ion conductivity can be summarized as: 1) Robust imidazole linkages enhances the stability of the framework, 2) 1D nanochannel provides the pathway for lithium-ion transport; 3) OEG chains induce the transport of lithium-ions

and improve the carrier density in the nanochannels, 4) the porous skeleton prevents the crystallization of OEG chains, and 5) the micropore structure with *tert*-butyl groups inside reduces the migration of anions, improving the lithium-ion transference number. All these features work co-operatively, leading to high lithium-ion conductivity as a solid-state electrolyte. IMD-COF-OEG-3 SSE exhibits a high lithium-ion conductivity with a high Li^+ transference number, low activation energy, and high stability during a Li plating-stripping cycling over 560 h. This work opens up a novel avenue for the design of COF-based SSEs for the next-generation high-performance solid-state batteries.

4.7 References

1. Manthiram, A.; Yu, X.; Wang, S., Lithium battery chemistries enabled by solid-state electrolytes. *Nat. Rev. Mater.* **2017,** *2* (4), 1-16.
2. Choi, J. W.; Aurbach, D., Promise and reality of post-lithium-ion batteries with high energy densities. *Nat. Rev. Mater.* **2016,** *1* (4), 1-16.
3. Janek, J.; Zeier, W. G., A solid future for battery development. *Nat. Energy* **2016,** *1* (9), 1-4.
4. Cheng, X.-B.; Zhang, R.; Zhao, C.-Z.; Zhang, Q., Toward safe lithium metal anode in rechargeable batteries: a review. *Chem. Rev.* **2017,** *117* (15), 10403-10473.
5. Cheng, X.; Pan, J.; Zhao, Y.; Liao, M.; Peng, H., Gel polymer electrolytes for electrochemical energy storage. *Adv. Energy Mater.* **2018,** *8* (7), 1702184.
6. Lightfoot, P.; Mehta, M.; Bruce, P., Crystal structure of the polymer electrolyte poly (ethylene oxide) 3: LiCF3SO3. *Science* **1993,** *262* (5135), 883-885.
7. Croce, F.; Appetecchi, G.; Persi, L.; Scrosati, B., Nanocomposite polymer electrolytes for lithium batteries. *Nature* **1998,** *394* (6692), 456-458.
8. Xue, Z.; He, D.; Xie, X., Poly (ethylene oxide)-based electrolytes for lithium-ion batteries. *J. Mater. Chem. A.* **2015,** *3* (38), 19218-19253.
9. Khurana, R.; Schaefer, J. L.; Archer, L. A.; Coates, G. W., Suppression of lithium dendrite growth using cross-linked polyethylene/poly (ethylene oxide) electrolytes: a

new approach for practical lithium-metal polymer batteries. *J. Am. Chem. Soc.* **2014,** *136* (20), 7395-7402.

10. Gadjourova, Z.; Andreev, Y. G.; Tunstall, D. P.; Bruce, P. G., Ionic conductivity in crystalline polymer electrolytes. *Nature* **2001,** *412* (6846), 520-523.

11. Xu, W.; Pei, X.; Diercks, C. S.; Lyu, H.; Ji, Z.; Yaghi, O. M., A metal–organic framework of organic vertices and polyoxometalate linkers as a solid-state electrolyte. *J. Am. Chem. Soc.* **2019,** *141* (44), 17522-17526.

12. Xu, K., Electrolytes and interphases in Li-ion batteries and beyond. *Chem. Rev.* **2014,** *114* (23), 11503-11618.

13. Cote, A. P.; Benin, A. I.; Ockwig, N. W.; O'Keeffe, M.; Matzger, A. J.;Yaghi, O. M., Porous, crystalline, covalent organic frameworks. *Science* **2005,** *310* (5751), 1166-1170.

14. Zhao, X.; Chen, Y.; Wang, Z.; Zhang, Z., Design and application of covalent organic frameworks for ionic conduction. *Polym. Chem.* **2021**, *12*, 4874-4894.

15. Huang, W.-H.; Li, X.-M.; Yang, X.-F.; Zhang, X.-X.; Wang, H.-H.; Wang, H., The recent progress and perspectives on metal-and covalent-organic framework based solid-state electrolytes for lithium-ion batteries. *Mater. Chem. Front.* **2021,** *5* (9), 3593-3613.

16. Li, Z.; Liu, Z.-W.; Mu, Z.-J.; Cao, C.; Li, Z.; Wang, T.-X.; Li, Y.; Ding, X.; Han, B.-H.; Feng, W., Cationic covalent organic framework based all-solid-state electrolytes. *Mater. Chem. Front.* **2020,** *4* (4), 1164-1173.

17. Shan, Z.; Wu, M.; Du, Y.; Xu, B.; He, B.; Wu, X.; Zhang, G., Covalent Organic Framework-Based Electrolytes for Fast Li^+ Conduction and High-Temperature Solid-State Lithium-Ion Batteries. *Chem. Mater*. **2021,** *33* (13), 5058-5066.

18. Gao, Z.; Liu, Q.; Zhao, G.; Sun, Y.; Guo, H., Covalent organic frameworks for solid-state electrolytes of lithium metal batteries. *J. Mater. Chem. A.* **2022,** *10* (14), 7497-7516.

19. Xu, Q.; Tao, S.; Jiang, Q.; Jiang, D., Designing Covalent Organic Frameworks with a Tailored Ionic Interface for Ion Transport across One-Dimensional Channels. *Angew. Chem., Int. Ed*. **2020,**59, 4557-4563.

20. Liu, Z.; Zhang, K.; Huang, G.; Xu, B.; Hong, Y. l.; Wu, X.; Nishiyama, Y.; Horike, S.; Zhang, G.; Kitagawa, S., Highly Processable Covalent Organic Framework Gel Electrolyte Enabled by Side-Chain Engineering for Lithium-Ion Batteries. *Angew. Chem., Int. Ed*. **2022,** *61*, e202110695.

21. Hu, Y.; Dunlap, N.; Wan, S.; Lu, S.; Huang, S.; Sellinger, I.; Ortiz, M.; Jin, Y.; Lee, S.-h.; Zhang, W., Crystalline lithium imidazolate covalent organic frameworks with high Li-ion conductivity. *Journal of the American Chemical Society* **2019,** *141* (18), 7518-7525.

22. Jeong, K.; Park, S.; Jung, G. Y.; Kim, S. H.; Lee, Y.-H.; Kwak, S. K.;Lee, S.-Y., Solvent-free, single lithium-ion conducting covalent organic frameworks. *J. Am. Chem. Soc.* **2019,** *141* (14), 5880-5885.

23. Xie, Z.; Wang, B.; Yang, Z.; Yang, X.; Yu, X.; Xing, G.; Zhang, Y.;Chen, L., Stable 2D heteroporous covalent organic frameworks for efficient ionic conduction. *Angew. Chem., Int. Ed.* **2019,** *58* (44), 15742-15746.

24. Xu, Q.; Tao, S.; Jiang, Q.; Jiang, D., Ion conduction in polyelectrolyte covalent organic frameworks. *J. Am. Chem. Soc.* **2018,** *140* (24), 7429-7432.

25. Li, X.; Loh, K. P., Recent progress in covalent organic frameworks as solid-state ion conductors. *ACS Mater. Lett.***2019,** *1* (3), 327-335.

26. Wu, X.; Hong, Y.-l.; Xu, B.; Nishiyama, Y.; Jiang, W.; Zhu, J.; Zhang, G.; Kitagawa, S.; Horike, S., Perfluoroalkyl-functionalized covalent organic frameworks with superhydrophobicity for anhydrous proton conduction. *J. Am. Chem. Soc.* **2020,** *142* (33), 14357-14364.

27. Zhao, X.; Pachfule, P.; Thomas, A., Covalent organic frameworks (COFs) for electrochemical applications. *Chem Soc Rev.* **2021,** *50* (12), 6871-6913.

28. Zhou, T.; Huang, X.; Ding, N.; Lin, Z.; Yao, Y.; Guo, J., Porous polyelectrolyte frameworks: synthesis, post-ionization and advanced applications. *Chem Soc Rev*.**2022**, *51*, 237-267.

29. Guo, D.; Shinde, D. B.; Shin, W.; Abou-Hamad, E.; Emwas, A. H.; Lai, Z.; Manthiram, A., Foldable Solid-state Batteries Enabled by Electrolyte Mediation in Covalent Organic Frameworks. *Adv. Mater.* **2022**, 2201410.

30. Dong, D.; Zhang, H.; Zhou, B.; Sun, Y.; Zhang, H.; Cao, M.; Li, J.; Zhou, H.; Qian, H.; Lin, Z., Porous covalent organic frameworks for high transference number polymer-based electrolytes. *Chem. Comm.* **2019,** *55* (10), 1458-1461.

31. Strauss, M. J.; Hwang, I.; Evans, A. M.; Natraj, A.; Aguilar-Enriquez, X.; Castano, I.; Roesner, E. K.; Choi, J. W.; Dichtel, W. R., Lithium-Conducting Self-Assembled Organic Nanotubes. *J. Am. Chem. Soc.* **2021,** *143* (42), 17655-17665.

32. Niu, C.; Luo, W.; ai, C.; Yu, C.; Xu, Y., High-Voltage-Tolerant Covalent Organic Framework Electrolyte with Holistically Oriented Channels for Solid-State Lithium Metal Batteries with Nickel-Rich Cathodes. *Angew. Chem., Int. Ed.* **2021,** *60* (47), 24915-24923.

33. Zhao, G.; Xu, L.; Jiang, J.; Mei, Z.; An, Q.; Lv, P.; Yang, X.; Guo, H.; Sun, X., COFs-based electrolyte accelerates the Na+ diffusion and restrains dendrite growth in quasi-solid-state organic batteries. *Nano Energy* **2022,** *92*, 106756.

34. Wang, P.-L.; Ding, S.-Y.; Zhang, Z.-C.; Wang, Z.-P.; Wang, W., Constructing robust covalent organic frameworks via multicomponent reactions. *J. Am. Chem. Soc.* **2019,** *141* (45), 18004-18008.

35. Zhang, G.; Hong, Y.-; Nishiyama, Y.; Bai, S.; Kitagawa, S.; Horike, S., Accumulation of glassy poly (ethylene oxide) anchored in a covalent organic framework as a solid-state Li^+ electrolyte. *J. Am. Chem. Soc.* **2018,** *141* (3), 1227-1234.

36. Wang, Y.; Zhang, K.; Jiang, X.; Liu, Z.; Bian, S.; Pan, Y.; Shan, Z.; Wu, M.; Xu, B.; Zhang, G., Branched Poly (ethylene glycol)-Functionalized Covalent Organic Frameworks as Solid Electrolytes. *ACS Appl. Electron. Mater.* **2021,** *4* (10), 11720-11725.

37. Zhou, T.; Wang, L.; Huang, X.; Unruangsri, J.; Zhang, H.; Wang, R.; Song, Q.; Yang, Q.; Li, W.; Wang, C., PEG-stabilized coaxial stacking of two-dimensional covalent organic frameworks for enhanced photocatalytic hydrogen evolution. *Nat. Commun.* **2021,** *12* (1), 1-12.

38. Li, X.; Hou, Q.; Huang, W.; Xu, H.-S.; Wang, X.; Yu, W.; Li, R.; Zhang, K.; Wang, L.; Chen, Z., Solution-processable covalent organic framework electrolytes for all-solid-state Li-organic batteries. *ACS Energy Lett.***2020,** *5* (11), 3498-3506.

39. Guo, Z.; Zhang, Y.; Dong, Y.; Li, J.; Li, S.; Shao, P.; Feng, X.; Wang, B., Fast ion transport pathway provided by polyethylene glycol confined in covalent organic frameworks. *J. Am. Chem. Soc.* **2019,** *141* (5), 1923-1927.

40. Chen, H.; Tu, H.; Hu, C.; Liu, Y.; Dong, D.; Sun, Y.; Dai, Y.; Wang, S.; Qian, H.; Lin, Z., Cationic covalent organic framework nanosheets for fast Li-ion conduction. *J. Am. Chem. Soc.* **2018,** *140* (3), 896-899.

41. Li, Z.; Liu, Z. W.; Li, Z.; Wang, T. X.; Hao, F.; Ding, X.; Feng, W.; Han, B. H., Defective 2D covalent organic frameworks for postfunctionalization. *Adv. Funct. Mater.* **2020,** *30* (10), 1909267.

42. Du, Y.; Yang, H.; Whiteley, J. M.; Wan, S.; Jin, Y.; Lee, S. H.; Zhang, W., Ionic covalent organic frameworks with spiroborate linkage. *Angew. Chem., Int. Ed.* **2016,** *55* (5), 1737-1741.

43. Li, J.; Zhang, F.-Q.; Li, F.; Wu, Z.; Ma, C.; Xu, Q.; Wang, P.; Zhang, X.-M., A pre-synthetic strategy to construct single ion conductive covalent organic frameworks. *Chem. Comm.* **2020,** *56* (18), 2747-2750.

44. Ashraf, S.; Zuo, Y.; Li, S.; Liu, C.; Wang, H.; Feng, X.; Li, P.; Wang, B., Crystalline anionic germanate covalent organic framework for high CO_2 selectivity and fast Li ion conduction. *Chem. Eur. J.***2019,** *25* (59), 13479-13483.

45. Li, X.; Tian, Y.; Shen, L.; Qu, Z.; Ma, T.; Sun, F.; Liu, X.; Zhang, C.; Shen, J.; Li, X., Electrolyte interphase built from anionic covalent organic frameworks for lithium dendrite suppression. *Adv. Funct. Mater.* **2021,** *31* (22), 2009718.

46. Zhang, W.; Zhang, J.; Liu, X.; Li, H.; Guo, Y.; Geng, C.; Tao, Y.; Yang, Q. H., In-situ Polymerized Gel Polymer Electrolytes with High Room-Temperature Ionic Conductivity and Regulated Na^+ Solvation Structure for Sodium Metal Batteries. *Adv. Funct. Mater.* **2022**, 2201205.

Chapter 5

Summary & Outlook

The studies of covalent organic frameworks have mainly focussed on boronate- or imine-linked COFs, which are easy to prepare with high crystallinity and high surface areas. However, these linkages are unstable, and non-conjugated in the case of the boronate linkage. The bulk structures have poor processability which limits their further development and practical applications in energy and environment fields.[1-3] In this thesis, we studied the design and development of new COF systems with novel linkages to address these issues, namely, improving the conjugation, stability and processability.

In **Chapter 2**, a new fluorindine-based COF (**FL-COF**) was prepared by using a temperature gradient condensation of 2, 5-dihydroxy-1, 4-benzoquinone and an aromatic *o*-diamine compound as the monomers. Compared with other kinds of ladder-type COFs, FL-COF shows a better crystallinity with an ABC stacking mode. The fluorindine-linkage is a redox-active site with a ladder-type structure and allows reversible four-electron redox processes and fast inter- and intra-layer charge transfer.[4] FL-COF achieved an excellent capacitance of 393 F g^{-1} at 0.5 A g^{-1} with high energy and power densities reaching 50.28 Wh kg^{-1} and 39.79 kW kg^{-1} respectively, which is highly competitive among previously reported COF-based electrodes in supercapacitors.[5]

However, the crystallinity of FL-COF is lower than imine-based COFs due to the poor reversibility of the multi-step reaction used to install the fluorindine linkages. Therefore, the design of new COF linkages based on a reaction with an initial reversible step should be considered.[6] With this in mind, we then decided to investigate multicomponent reactions to prepare stable and crystalline COFs because they can combine initial reversible covalent bond-forming steps to confer crystallinity with following irreversible steps that confers stability. Also, due to the introduction of a third component, multicomponent reactions can be an efficient method to achieve structural diversification and functionalization of COFs. Furthermore, the COF systems from multicomponent reactions can be greatly extended by the diverse monomers available.[7]

In **Chapter 3**, we developed a simple and efficient multicomponent Doebner reaction route to stable, porous and crystalline quinoline-linked covalent organic frameworks (**Qu-COFs**). The successful Qu-COFs can be made by both one-pot synthesis and post-synthetic modification with different monomers. These Qu-COFs show good crystallinity and chemical stability, and can be easily exfoliated to Qu-CONs under mild basic conditions. We believe the exfoliation is mediated by the unique quinoline-4-carboxylic acid motif installed using this approach which reduces the π-π stacking interaction and provide active-sites for ion insertion leading to the repulsion of the COF layers.[8] Qu-CONs exhibited excellent performance for cadmium capture from water, with high capacity, quick adsorption rates and good selectivity. The multicomponent Doebner reaction provides COFs with active-sites for metal-ions insertion, adsorption and transportation, and will serve as a guide for future design of COF materials for these applications.[9]

Encouraged by these results, we designed robust oligo-ethylene glycol-anchored imidazole-linked COFs with three different OEG chain sizes for emergent lithium-ion conduction.[10] The initial imidazole-linked COF (IMD-COF) with good stability and crystallinity was synthesized from a multicomponent Debus-Radziszewski reaction. The as-obtained IMD-COF was reacted with oligo-ethylene glycol (OEG) bromides of different chain lengths to form IMD-COF-OEG-1~3. A change in the stacking model from AA to ABC was observed after the post-modification reaction, which is proposed to be the disturbance from the free OEG chains. As a design principle, the 1D nanochannels of IMD-COF prevent the crystallization of OEG chains and provide a pathway for lithium-ion transport. The OEG chains induce the transport of lithium-ions and improve the carrier density in the nanochannels. Also, the micropore structure from ABC stacking model with tert-butyl groups inside reduces the migration of cations to improve lithium-ion transference number. IMD-COF-OEG-3 exhibits a high lithium-ion conductivity (3.36×10^{-4} S cm^{-1} at 20 ℃ and 4.55×10^{-3} S cm^{-1} at 70 ℃) with high Li^+ transference number (0.83), low activation energy (0.45 eV), high potential window (up to 5.1 V) and high stability during a Li plating-stripping cycling over 560 h,

indicating an enhanced performance compared with traditional PEG electrolytes and liquid electrolytes.[11]

Overall, we present a series of fully π-conjugated robust COFs with fluorindine-, quinoline- and imidazole-linkages, with applications as electrodes for supercapacitor, nanosheets for selective ion adsorption, and solid-state electrolytes for lithium-ion batteries, respectively. By using traditional solvothermal synthesis, all the COFs made in this thesis are still needed to use toxic organic solvents that are not environmentally friendly, thus optimizing the reaction conditions should been a necessary direction in the future. Developing a general method for the synthesis of stable and easy exfoliated COF systems with suitable linkages is a challenge, however, the findings of this thesis will encourage the development of the area of stable COFs with novel linkages to enable efficient electrode and electrolyte materials in energy storage devices.

Covalent organic frameworks are an emerging class of materials that bridge the gap between organic chemistry and materials science, and have many important developments during these 15 years. One highlight is the discovery of new reactions and methods that can link various organic building blocks to form novel COFs. Therefore, understanding the process of the reactions and crystallization can be the key for designing new linkages of crystalline robust COFs.[12] However, the chemical stability of 3D COFs without interlayer π-π stacking is perceived as more problematic than 2D COFs, which still requires further studies in the future.[6] Also, the poor processability can be another challenge of COFs for specific applications. Thus, finding a clever way to exfoliate COFs with high efficiency and high quality to overcome the processability barrier would be a big step toward application of COF materials in many specific applications.[13] We anticipate that there will be an increasing number of works that concentrate on the COF linkage engineering and promote development of COF research field in the future.

References

1. Geng, K. Y.; He, T.; Liu, R. Y.; Dalapati, S.; Tan, K. T.; Li, Z. P.; Tao, S. S.; Gong, Y. F.; Jiang, Q. H.; Jiang, D. L., Covalent Organic Frameworks: Design, Synthesis, and Functions. *Chem. Rev.* **2020,** *120* (16), 8814-8933.

2. Haase, F.; Lotsch, B. V., Solving the COF trilemma: towards crystalline, stable and functional covalent organic frameworks. *Chem Soc Rev.* **2020,** *49* (23), 8469-8500.

3. Evans, A. M.; Strauss, M. J.; Corcos, A. R.; Hirani, Z.; Ji, W.; Hamachi, L. S.; Aguilar-Enriquez, X.; Chavez, A. D.; Smith, B. J.; Dichtel, W. R., Two-Dimensional Polymers and Polymerizations. *Chem. Rev.* **2021,** *122* (1), 442-564.

4. Scherf, U., Ladder-type materials. *J. Mater. Chem.* **1999,** *9* (9), 1853-1864.

5. Kong, L. J.; Zhong, M.; Shuang, W.; Xu, Y. H.; Bu, X. H., Electrochemically active sites inside crystalline porous materials for energy storage and conversion. *Chem Soc Rev.* **2020,** *49* (8), 2378-2407.

6. Li, X. L.; Cai, S. L.; Sun, B.; Yang, C. Q.; Zhang, J.; Liu, Y., Chemically Robust Covalent Organic Frameworks: Progress and Perspective. *Matter.* **2020,** *3* (5), 1507-1540.

7. Li, Y. S.; Chen, W. B.; Xing, G. L.; Jiang, D. L.; Chen, L., New synthetic strategies toward covalent organic frameworks. *Chem Soc Rev.* **2020,** *49* (10), 2852-2868.

8. Li, J.; Jing, X. C.; Li, Q. Q.; Li, S. W.; Gao, X.; Feng, X.; Wang, B., Bulk COFs and COF nanosheets for electrochemical energy storage and conversion. *Chem Soc Rev.* **2020,** *49* (11), 3565-3604.

9. Rodriguez-San-Miguel, D.; Montoro, C.; Zamora, F., Covalent organic framework nanosheets: preparation, properties and applications. *Chem Soc Rev.* **2020,** *49* (8), 2291-2302.

10. Zhao, X. J.; Pachfule, P.; Thomas, A., Covalent organic frameworks (COFs) for electrochemical applications. *Chem Soc Rev.* **2021,** *50* (12), 6871-6913.

11. Gao, Z.; Liu, Q.; Zhao, G.; Sun, Y.; Guo, H., Covalent organic frameworks for solid-state electrolytes of lithium metal batteries. *J. Mater. Chem. A.* **2022,** *10* (14), 7497-7516.

12. Zou, X., Xiaodong Zou answers questions about 15 years of research on covalent organic frameworks. *Nat. Commun.* **2020,** *11* (1), 5330.
13. Kreutzer, J.; Liu, Y., Yi Liu answers questions about 15 years of research on covalent organic frameworks. *Nat. Commun.* **2020,** *11* (1), 5333.